

# **Sectional-based PBE-MMC-LES methodology for simulating flame synthesis of particulates with fractal morphology**

von der  
Fakultät Energie-, Verfahrens- und Biotechnik  
der Universität Stuttgart  
zur Erlangung der Würde eines  
Doktors der Ingenieurwissenschaften  
(Dr.-Ing.) genehmigte Abhandlung

vorgelegt von  
**Gregor Neuber**  
aus Berlin, Deutschland

Hauptberichter: Herr Prof. Dr. Andreas Kronenburg  
Mitberichter: Herr Prof. Dr. Peter Gerlinger  
Vorsitzender Herr Prof. Dr. Damian Vogt

Tag der mündlichen Prüfung: 06. Mai 2022

Institut für Technische Verbrennung  
der Universität Stuttgart  
2022



To my gracious wife Frederike



# Erklärung

Hiermit versichere ich:

1. dass ich meine Arbeit selbständig verfasst habe,
2. dass ich keine anderen als die angegebenen Quellen benutzt und alle wörtlich oder sinngemäß aus anderen Werken übernommenen Aussagen als solche gekennzeichnet habe,
3. dass die eingereichte Arbeit weder vollständig noch in wesentlichen Teilen Gegenstand eines anderen Prüfungsverfahrens gewesen ist,
4. dass das elektronische Exemplar mit den anderen Exemplaren übereinstimmt.

Rostock, September 2021

Gregor Neuber



# Preface

Parts of this thesis have been published in the archival literature. The background and theoretical developments given in Chapters 2, 3 and 4 have been modified with respect to the originally published texts and have been significantly extended to ensure completeness, coherence and consistency of the present manuscript.

The relevant papers are:

1. Gregor Neuber, Frederik Fuest, Jonas Kirchmann, Andreas Kronenburg, Oliver T. Stein, Sebastian Galindo-López, Matthew J. Cleary, Robert S. Barlow, Bruno Cori-ton, Jonathan H. Frank, Jeffrey A. Sutton (2019). *Sparse-Lagrangian MMC modelling of the Sandia DME flame series*, *Combust. Flame* (208), 110–121.

<https://doi.org/10.1016/j.combustflame.2019.06.026>

Author's contribution: programming (100%), simulation data generation (100%), scientific originality (30%)

2. Gregor Neuber, Andreas Kronenburg, Oliver T. Stein, Matthew J. Cleary, (2017). *MMC-LES modelling of droplet nucleation and growth in turbulent jets*. *Chem. Eng. Sci.* 167, 204–218.

<https://doi.org/10.1016/j.ces.2017.04.008>

Author's contribution: programming (100%), simulation data generation (100%), scientific originality (30%)

3. Gregor Neuber, Carlos E. Garcia, Andreas Kronenburg, Benjamin A. O. Williams, Frank Beyrau, Oliver T. Stein, Matthew J. Cleary (2019). *Joint experimental and numerical study of silica particulate synthesis in a turbulent reacting jet*, *Proc. Combust. Inst.* (37), 1213–1220.

<https://doi.org/10.1016/j.proci.2018.06.07>

Author's contribution: programming (100%), simulation data generation (100%), scientific originality (20%)

4. Gregor Neuber, Andreas Kronenburg, Oliver T. Stein, Carlos E. Garcia, Benjamin A. O. Williams, Frank Beyrau, Matthew J. Cleary (2021). *Sparse-Lagrangian PDF Modelling of Silica Synthesis from Silane Jets in Vitiated Co-flows with varying Inflow conditions*, *Flow, Turbulence and Combustion*. (106), 1167–1194.

<https://doi.org/10.1007/s10494-020-00140-2>

Author's contribution: programming (100%), simulation data generation (100%), scientific originality (50%)

# Summary

The objective of the work at hand is to develop an efficient methodology for simulating the flame synthesis of particulates with fractal morphology using a sparse-Lagrangian particle method. Flame synthesis involves precursor chemistry in the gas phase and aerosol processes such as particulate formation, surface growth and agglomeration. Flame synthesis for the production of particulates is widely used in the manufacturing industry. For example, particulates with fractal morphology are used in the chemical industry to produce dyes and pigments, in medical technology to produce pharmaceuticals, and in the semiconductor industry to produce wafers. The continuously increasing demands with respect to fractal shape and to size (e.g. narrow size distributions of spherical particulates) as well as on the chemical purity pose significant requirements for the manufacturing process. To meet these requirements, it is necessary to understand the formation process. A fast and cost-effective way to gain insight into the thermophysical processes involved in particulate formation is the use of numerical simulation techniques, which help to make valid predictions for optimising the manufacturing process. Currently, available simulation methods for the simulation of real problems of industrial dimensions - usually found in reactive turbulent flows - require an enormous computational effort. In the present work, a sparse-Lagrangian stochastic particle method is presented as a very efficient approach for the numerical simulation of aerosol dynamics. Compared to conventional stochastic particle based approaches, this method achieves qualitatively equivalent results with significantly less computational effort.

It is of utmost importance to validate the newly created simulation framework and to prove the method to be capable of covering a wide range of possible applications. To do so, the work starts with presenting the basic methodological and numerical principles. This is followed by the presentation of the numerical treatment of reactive turbulent flows and the modelling of aerosol processes. The presentation includes the description of a very efficient sparse-Lagrangian stochastic particle method, the so-called generalised form of the Multiple Mapping Conditioning (MMC) model. Additionally, the models for describing the inception, size growth and agglomeration of particulates with fractal morphology are explained in detail. In this work, the particle size distribution is described using a sectional method, which is far more efficient than a direct Monte Carlo method and more accurate than the common approach using a moment-based method. It is further shown how the numerical simulation of aerosol dynamic processes can be coupled with the generalised form of the MMC method.

In a first step, results are presented with respect to the simulation of the entire tur-

bulent Sandia DME flame series, showing that the MMC method can correctly predict trends with a single universal set of numerical parameters for a flame without particulates. This is worth emphasising, as many good results in the field of turbulent reactive flame simulation can often only be achieved if the numerical parameters are adapted to the flame configuration under investigation. Simulation results obtained with a newly developed stochastic particle mixing time scale model show that excellent prediction accuracies of the implemented numerical methods can be achieved for both conditional and unconditional averages.

Second, a discussion of the results includes a quantification of the errors that would arise if the sub-grid contributions of aerosol processes were not taken into account, showing that they are by no means negligible. This quantification was performed on the basis of a numerical study of a jet flow in which nucleation and condensation of small liquid droplets occur due to the mixing of a hot jet with a cold co-flow. Here it is shown that interactions between turbulence and nucleation can modify averaged nucleation rates by more than 250%.

This work culminates in the discussion of simulation results of a flame configuration, which was developed especially for this investigation, where a turbulent cold jet doped with silane issues into a hot oxygen-containing co-flow stream. The numerical data are compared with experimentally obtained optical measurements. In order to extend the range of operating conditions, various boundary conditions such as the precursor doping, the temperature of the co-flow stream and the Reynolds number of the jet were varied both in the experiment and for the simulation, respectively. Thus, it is shown that the application of a stochastic PDF model simulating the finite rate chemistry and aerosol processes to a real laboratory-sized flame configuration using a sectional particulate size distribution can reproduce the trends satisfactorily. A concluding discussion highlights remaining uncertainties and points to a number of possible pathways of development for future scientific investigations.

# Zusammenfassung

Das Ziel der vorliegenden Arbeit ist die Entwicklung einer effizienten Methodik zur Simulation der Flammensynthese von Partikeln mit fraktaler Morphologie unter Verwendung einer dünn besetzten Lagrange-Partikelmethode. Die Flammensynthese umfasst die Vorläuferchemie in der Gasphase und Aerosolprozesse wie Partikelbildung, Oberflächenwachstum und Agglomeration. Die Flammensynthese zur Herstellung von Partikeln ist in der Industrie weit verbreitet. So werden beispielsweise Partikel mit fraktaler Morphologie in der chemischen Industrie zur Herstellung von Farbstoffen und Pigmenten, in der Medizintechnik zur Herstellung von Pharmazeutika und in der Halbleiterindustrie zur Herstellung von Wafern verwendet. Die ständig steigenden Anforderungen in Hinblick auf die fraktale Form, Größe und chemische Reinheit stellen enorme Anforderungen an den Herstellungsprozess. Um diese Anforderungen zu erfüllen, ist es notwendig, den Entstehungsprozess zu verstehen. Eine schnelle und erschwingliche Möglichkeit, Einblick in die thermophysikalischen Vorgänge bei der Partikelbildung zu erhalten, ist der Einsatz numerischer Simulationsverfahren, die helfen, valide Vorhersagen zur Optimierung des Herstellungsprozesses zu treffen. Mit den derzeit zur Verfügung stehenden Simulationsverfahren zur Simulation von turbulenten Partikelbildungsprozessen sind für reale Probleme industrieller Dimensionen, die häufig in reaktiven turbulenten Strömungen auftreten, nur mit enormem Rechenaufwand zu realisieren. In der vorliegenden Arbeit wird ein dünn-besetztes, stochastisches Lagrange-Partikelverfahren als eine effiziente Methode für die numerische Simulation der Aerosoldynamik vorgestellt. Im Vergleich zu konventionellen Ansätzen werden mit dieser Methode qualitativ gleichwertige Ergebnisse bei deutlich geringerem Rechenaufwand erzielt.

Es ist von eminenter Bedeutung, das neu entwickelte Simulationsverfahren zu validieren und zu beweisen, dass die Methode in der Lage ist, ein breites Spektrum möglicher Anwendungsbereiche abzudecken. Zunächst werden dazu die grundlegenden methodischen und numerischen Prinzipien vorgestellt. Weiterhin werden die Modelle zur Modellierung von Aerosolprozessen und zur numerischen Behandlung von reaktiven turbulenten Strömungen vorgestellt. Die Darstellung umfasst die Beschreibung einer sehr effizienten dünn besetzten stochastischen Partikelmethode, der sogenannten verallgemeinerten Form des Multiple Mapping Conditioning (MMC) Modells. Zusätzlich werden die Modelle zur Beschreibung der Entstehung, des Größenwachstums und der Agglomeration von Partikeln mit fraktaler Morphologie detailliert erläutert. In dieser Arbeit wird die Partikelgrößenverteilung mit einer sektionalen Methode beschrieben, die weitaus effizienter als eine direkte Monte-Carlo-Methode und genauer als der übliche Ansatz mittels einer momentbasierten Methode ist. Es wird weiterhin gezeigt, wie diese Modelle mit

der verallgemeinerten Form der MMC-Methode gekoppelt werden können.

In einem ersten Schritt werden Ergebnisse in Bezug auf die erste Simulation der gesamten turbulenten Sandia-DME-Flammenserie vorgestellt, die zeigen, dass die MMC-Methode Trends mit einem einzigen allgemeingültigen Satz an numerischen Parametern korrekt für eine Flamme ohne Partikel vorhersagen kann. Dies ist hervorzuheben, da viele gute Ergebnisse im Bereich der Simulation turbulenter reaktiver Flammen bislang nur dann erzielt werden konnten, wenn die numerischen Parameter an die untersuchte Flammenkonfiguration angepasst werden. Simulationsergebnisse, die mit einem neu entwickelten stochastischen Partikelmischungszeitskalenmodell erzielt werden, zeigen, dass die implementierten numerischen Methoden sowohl für bedingte als auch für unbedingte Mittelwerte eine ausgezeichnete Vorhersagegenauigkeit erreichen können.

Anschließend beinhaltet eine Diskussion der Ergebnisse eine Quantifizierung der Fehler, die sich ergeben würden, wenn für die Aerosolprozesse die Beiträge unterhalb der Filterweite nicht berücksichtigt würden, wodurch gezeigt werden kann, dass diese keineswegs vernachlässigbar sind. Diese Quantifizierung konnte anhand einer numerischen Studie einer Strahlströmung durchgeführt werden, in der es durch die Vermischung eines heißen Strahls mit einer kalten Hüllströmung zur Nukleation und Kondensation von kleinen Flüssigkeitstropfen kommt. Hier wird gezeigt, dass Wechselwirkungen zwischen Turbulenz und Nukleation die gemittelten Nukleationsraten um mehr als 250% variieren lassen können.

In einem dritten Schritt werden Simulationsergebnisse einer speziell für diese Untersuchung entwickelten Flammenkonfiguration diskutiert. Hier strömt ein turbulenter kalter mit Silan versehener Freistrahler in einen heißen sauerstoffhaltigen Hüllstrom. Die numerischen Daten werden mit experimentell gewonnenen optischen Meßwerten verglichen. Verschiedene Randbedingungen, wie die Vorläuferkonzentration, die Temperatur des Hüllstroms und die Reynoldszahl des Freistrahls, wurden sowohl im Experiment, als auch für die Simulationen variiert, um den Bereich der Einflussfaktoren zu erweitern. Die numerischen Ergebnisse liefern eine gute Übereinstimmung mit den gemessenen Signalen, und es wird gezeigt, dass die Anwendung eines stochastischen PDF-Modells, das die Chemie und die Aerosolprozesse mit einer sektionalen Methode an einer realen Flammenkonfiguration in Laborgröße simuliert, die Trends zufriedenstellend reproduzieren kann. Eine abschließende Diskussion zeigt verbleibende Unsicherheiten auf und weist auf eine Reihe möglicher Pfade der Entwicklung für zukünftige wissenschaftliche Untersuchungen hin.

# Acknowledgements

First and foremost, I would like to thank my supervisor, Prof. Dr. Andreas Kronenburg, who patiently supported my ideas and aspirations and whose indepth knowledge of the field contributed significantly to the success of this thesis. I thank him for the trust he has placed in me and for the great guidance he offered me in exploring both teaching and science.

I would also thank Prof. Dr. Peter Gerlinger for being the examiner of my thesis and Prof. Dr. Damian Vogt for being the chairmen of the examination.

During my time at the Institute of Combustion Technology at the University of Stuttgart, I met a number of terrific people, to whom I am truly grateful.

I would like to thank Dr. Oliver T. Stein for the many fruitful and enjoyable scientific discussions and personal conversations. I would like to thank my teammate Jonas Kirchmann for all the fruitful discussions, to which I will always look back with pleasure. I would also like to thank Carmen Straub and Son Vo for their constructive consultations. My thanks also go to Dirk Dietzel and Benedikt Heine for their extraordinary efforts on behalf of the Institute's computing infrastructure, without which this work would not have come about in this form. I would also like to thank all my other colleagues Dr. Giovanni Luigi Tufano, Dr. Gregor Olenik, Dr. Niko Seubert, Dr. Bosen Wang, Marvin Sontheimer, Jan Gärtner, Prof. Dr. Santanu De, Gizem Inci, Milena Smiljanic, Dr. Satoshi Ukai, Nadezhda Iaroslavtceva, Daniel Loureiro, Tien Duc Luu, Dr. Songbai Yao and Jacqueline Yang for a truly wonderful time. I would also like to thank Ms Ricarda Schubert for her patient support in all administrative matters.

My special thanks go to Dr. Carlos Enol Garcia for conscientiously conducting the experimental study at Imperial College London, on which I was able to validate my numerical data. In the same way, I would like to thank Dr. Benjamin A. O. Williams and Prof. Dr. Frank Beyrau for their excellent collaboration in designing the investigated flow configuration and in interpreting the measured signals.

During my doctoral studies, I was granted the opportunity of a scientific exchange with the School of Aerospace, Mechanical and Mechatronic Engineering of the University of Sydney; an experience I am very grateful for. I would like to thank Prof. Dr. Andreas Kronenburg and Prof. Dr. Matthew J. Cleary for their effort and commitment in organising this exchange. I would also like to thank Prof. Dr. Matthew J. Cleary for his trust in me regarding my implementations for the mmcFoam source code. Special thanks go to Dr. Sebastian Galindo-López for his tremendous effort in completely redesigning the mmcFoam source code, whose work greatly facilitated my new implementations. Due to

his support in crucial implementations and the many fruitful discussions about the MMC method and its flavours, the time in Sydney remains unforgettable. Furthermore, Prof. Dr. Asaad Masri, Dr. Fatemeh Salehi as well as my roommates Zhijie Huo and Longfei Zhao made my stay in Sydney extremely enjoyable, for which I would like to express my sincere gratitude.

I owe special thanks to my gracious and loving wife Frederike, to whom I dedicate this work, for her support and for always believing in me.

Rostock, Germany, October 2022

Gregor Neuber

# Contents

<b>Preface</b>	<b>III</b>
<b>Summary</b>	<b>V</b>
<b>Zusammenfassung</b>	<b>VII</b>
<b>Acknowledgements</b>	<b>IX</b>
<b>Table of Contents</b>	<b>XIII</b>
<b>List of Figures</b>	<b>XV</b>
<b>List of Tables</b>	<b>XVII</b>
<b>Nomenclature</b>	<b>XIX</b>
<b>1 Introduction</b>	<b>1</b>
1.1 Motivation . . . . .	5
1.2 Aim of the dissertation . . . . .	7
1.3 Thesis outline . . . . .	8
<b>2 Theoretical background</b>	<b>11</b>
2.1 Conservation equations . . . . .	11
2.2 Combustion . . . . .	13
2.2.1 Reaction kinetics . . . . .	13
2.2.2 Combustion modes . . . . .	14
2.3 Turbulence . . . . .	15
2.4 Aerosols . . . . .	16
2.4.1 Properties of particulates . . . . .	17
2.4.2 Aerosol dynamics . . . . .	19
2.4.3 Particulate conservation equation . . . . .	20
<b>3 Modelling</b>	<b>25</b>
3.1 Modelling of turbulent flows . . . . .	25
3.1.1 Large Eddy Simulation . . . . .	25
3.1.1.1 Smagorinsky-Model . . . . .	28

3.1.1.2	$\sigma$ -Model . . . . .	29
3.1.2	Detached Eddy Simulation . . . . .	29
3.2	Modelling of turbulent combustion . . . . .	30
3.2.1	Flamelet Model . . . . .	30
3.2.2	Conditional Moment Closure . . . . .	32
3.2.3	Transported Probability Density Function models . . . . .	33
3.2.3.1	Mixing models . . . . .	35
3.2.4	Multiple Mapping Conditioning for modelling turbulent reacting flows . . . . .	37
3.2.4.1	Generalised MMC . . . . .	39
3.2.4.2	Sparse-Lagrangian FDF methods . . . . .	40
3.2.4.3	Sparse-Lagrangian MMC . . . . .	41
3.2.4.4	Density coupling . . . . .	44
3.3	Modelling of aerosol dynamics . . . . .	45
3.3.1	Direct Monte-Carlo methods . . . . .	46
3.3.2	Population balance equation modelling . . . . .	46
3.3.2.1	Moment methods . . . . .	47
3.3.2.2	Sectional methods . . . . .	48
3.3.3	Aerosol dynamic modelling . . . . .	51
3.3.3.1	Particulate Formation . . . . .	51
3.3.3.2	Surface growth . . . . .	54
3.3.3.3	Coagulation . . . . .	55
3.3.4	Incorporation into the sparse-Lagrangian MMC framework . . . . .	60
<b>4</b>	<b>Incorporation of polydispersed particulates simulation into a variable density flow solver</b>	<b>63</b>
4.1	OpenFOAM . . . . .	63
4.2	Incorporation of the MMC method into the OpenFOAM framework . . . . .	64
4.2.1	Density Coupling . . . . .	65
4.2.1.1	FlameletCurves . . . . .	65
4.2.1.2	KernelEstimation . . . . .	65
4.2.2	Mixing operation . . . . .	66
4.2.3	Boundary conditions . . . . .	67
4.3	Incorporation of the aerosol dynamics into the MMC framework . . . . .	69
<b>5</b>	<b>Application of the Multiple Mapping Conditioning model to particulate laden flows</b>	<b>73</b>
<b>6</b>	<b>Conclusion &amp; Outlook</b>	<b>155</b>
6.1	Conclusion . . . . .	155
6.2	Outlook . . . . .	156
	<b>Bibliography</b>	<b>161</b>
	<b>Appendix</b>	<b>183</b>

---

<b>A Silane combustion reaction mechanism</b>	<b>183</b>
<b>B Data storage</b>	<b>197</b>



# List of Figures

2.1	Transmission electron microscope image of silica particulates and a soot agglomerate . . . . .	17
2.2	Schematic representation of aerosol dynamics processes . . . . .	20
2.3	Time evolution of a particulate size distribution . . . . .	21
3.1	Distribution of coagulated particulates to the two adjacent sections . . . . .	49
3.2	Particulate inception rate and particulate number density for perfectly stirred reactor simulations . . . . .	53
3.3	Volumetric surface growth rate for particulates using different growth rate formulations . . . . .	55
3.4	Collision kernel dependence on particulate size . . . . .	58
3.5	Decay of normalised particulate number density assuming different fractal dimensions . . . . .	58
3.6	Time evolution of mass mean diameter for particulates with different fractal dimension . . . . .	59
3.7	Time evolution of particulate number density for PSR simulations . . . . .	60
4.1	Temperature profiles of flamelet equation solutions . . . . .	66
4.2	Representation of the k-d tree here with $k = 2$ . . . . .	67
4.3	Instantaneous velocity field and q-criterion of a pipe flow. . . . .	68
4.4	Mean and RMS of axial velocity of the Sandia DME D flame configuration . . . . .	69
4.5	Flow chart of the mmcPbeFoam solver . . . . .	71
5.1	Stochastic particle temperature conditioned on mixture fraction. . . . .	75
5.2	Profiles of standard deviation of stochastic particle CO mole fraction conditioned on mixture fraction. . . . .	75
5.3	Droplet number density and count mean droplet diameter as function of the DBP mole fraction . . . . .	77
5.4	Contour plots of the normalised elastic light scattering signal . . . . .	79
5.5	Mean elastic light scattering signal along the centerline for cases with different boundary conditions. . . . .	82



# List of Tables

A1	Case and code used to produce results of Neuber <i>et al.</i> [1]. . . . .	197
A2	Case and code used to produce results of Neuber <i>et al.</i> [2] . . . . .	197
A3	Case and code used to produce results of Neuber <i>et al.</i> [3]. . . . .	197
A4	Case and code used to produce results of Neuber <i>et al.</i> [4]. . . . .	197



# Nomenclature

## Acronyms

CD	Coalescence-Dispersion
CDS	Central Differencing Scheme
CFD	Computational Fluid Dynamics
CFL	Courant-Friedrichs-Lewy
CMC	Conditional Moment Closure
DNS	Direct Numerical Simulation
DSD	Droplet Size Distribution
ELS	Elastic Light Scattering
FDF	Filtered Probability Density Function
FVM	Finite Volume Method
(ID)DES	(Improved Delayed) Detached Eddy Simulation
LES	Large Eddy Simulation
LIF	Laser Induced Fluorescence
MC	Monte Carlo
MC	Mapping Closure
MMC	Multiple Mapping Conditioning
ODE	Ordinary Differential Equation
OpenFOAM	Open source Field Manipulation and Operation
PBE	Population Balance Equation
PDE	Partial Differential Equation
PDF	Probability Density Function
PISO	Pressure-Implicit with Splitting of Operators
PSD	Particulate Size Distribution
PSR	Perfectly Stirred Reactor
RANS	Reynolds-averaged Navier-Stokes
RMS	Root Mean Square
SGS	Sub-Grid Scale
TEM	Transmission Electron Microscope
TVD	Total Variation Diminishing

## Latin letters

$A$	area	$[\text{m}^2]$
$B_{kl}$	diffusion coefficient tensor	$[\text{m}^2/\text{s}]$
$c_\alpha$	concentration of species $\alpha$	$[\text{kmol}/\text{m}^3]$
$C_s$	Smagorinsky constant	$[-]$
$c_p$	mixture specific heat capacity	$[\text{J}/\text{kg K}]$
$d_{p,q}^2$	effective square distance between mixing particles	$[\text{m}^2]$
$dx_i^{p,q}$	particle pair mixing distance in the spatial direction $i$	$[\text{m}]$
$d_c$	collision diameter	$[\text{m}]$
$\mathcal{D}_\alpha$	molecular diffusivity	$[\text{m}^2/\text{s}]$
$D_t$	turbulent diffusivity	$[\text{m}^2/\text{s}]$
$D_p$	particulate diffusivity	$[\text{m}^2/\text{s}]$
$D_f$	fractal dimension	$[-]$
$E_{\alpha,i}$	activation energy in reaction $i$	$[\text{kJ}/\text{kmol}]$
$\mathcal{F}_{sgs}$	mass-weighted filtered density function	$[-]$
$\mathcal{F}_Y$	species PDF	$[-]$
$\mathcal{F}_M$	major species PDF	$[-]$
$\mathcal{F}_\xi$	reference variable PDF	$[-]$
$f$	passive scalar e.g. mixture fraction	$[-]$
$g_i$	gravitational acceleration in spatial direction $i$	$[\text{m}/\text{s}^2]$
$h$	enthalpy	$[\text{kJ}/\text{kg}]$
$G$	volumetric growth rate	$[\text{m}^3/\text{s}]$
$G$	LES filter function	$[1/\text{m}]$
$h_f^0$	enthalpy of formation at standard conditions	$[\text{kJ}/\text{kg}]$
$h_s$	sensible enthalpy	$[\text{kJ}/\text{kg}]$
$J_j^\alpha$	diffusive flux of species $\alpha$ in spatial direction $j$	$[1/\text{m}^2 \text{s}]$
$J_j^h$	diffusive flux of enthalpy in spatial direction $j$	$[1/\text{m}^2 \text{s}]$
$J_j^{sgs}$	subgrid-scale scalar flux	$[\text{kg}/\text{m}^2 \text{s}]$
$k_{fi}$	rate coefficients of forward reaction	$[1/\text{s}]$
$k_{ri}$	rate coefficients of reverse reaction	$[1/\text{s}]$
$k$	turbulent kinetic energy	$[\text{m}^2/\text{s}^2]$
$k_B$	Boltzmann constant	$[\text{kJ}/\text{kg}]$
$k_f$	fractal prefactor	$[-]$
$\ell_0$	integral length scale or turbulence macroscale	$[\text{m}]$

$\ell_\lambda$	Taylor microscale	[m]
$\ell_K$	Kolmogorov microscale	[m]
$L$	characteristic width of the flow or macroscale	[m]
$m$	mass	[kg]
$M$	molar mass	[kg/kmol]
$n$	mole number	[mol]
$n$	volume based particulate size distribution function	[–]
$n_d$	diameter based particulate size distribution function	[1/m <sup>3</sup> ]
$N_{sp}$	total number of species	[–]
$N_p$	number of primary particulates	[–]
$N_i$	particulate number density of particulates of size $v_i$	[1/m <sup>3</sup> ]
$\dot{N}$	inception/nucleation rate	[1/m <sup>3</sup> s]
$p$	pressure	[Pa]
$\tilde{P}$	probability	[–]
$p$	pressure	kg/m s <sup>2</sup>
$\dot{q}$	heat release	[kJ/s]
$q_\phi$	production/destruction of scalar	[–]
$Q_r$	reaction rate	[kmol/s]
$Q_\alpha$	conditionally filtered mass fraction of species $\alpha$	[–]
$Q_h$	conditional enthalpy	[J]
$\mathcal{R}_u$	universal gas constant	[kJ/kmol K]
$R_g$	radius of gyration	[m]
$S_{ij}$	strain rate tensor	[1/s]
$t$	time	[s]
$t_K$	Kolmogorov time scale	[s]
$T$	temperature	[K]
$u_0$	integral velocity scale	[m/s]
$u_K$	Kolmogorov velocity scale	[m/s]
$u_i$	velocity in spatial direction $i$	[m/s]
$v$	volume	[m <sup>3</sup> ]
$v'_{\alpha,r}$	stoichiometric coefficient of reactants for species $\alpha$	[–]
$v''_{\alpha,r}$	stoichiometric coefficient of reactants for species $\alpha$	[–]
$x_\alpha$	mole fraction of species $\alpha$	[–]
$Y_\alpha$	mass fraction of species $\alpha$	[–]
$Z_e$	element mass fraction of an element $e$	[–]

## Greek letters

$\Delta$	filter width	[m]
$\delta_{ij}$	Kronecker delta	[-]
$\beta$	temperature exponent of the Arrhenius law	[-]
$\beta_{ij}$	collision kernel	[1/m <sup>3</sup> s]
$\eta$	mixture fraction sample space	[-]
$\kappa$	thermal conductivity of mixture	[W/m K]
$\kappa$	wave number	[1/m]
$\lambda$	heat diffusion coefficient	[m <sup>2</sup> /s]
$\lambda$	mean free path of molecules	[m]
$\mu$	dynamic viscosity	[Pa s]
$\mu_t$	eddy viscosity	[Pa s]
$\nu$	kinematic viscosity	[m <sup>2</sup> /s]
$\nu_t$	turbulent kinematic viscosity	[m <sup>2</sup> /s]
$\chi$	scalar dissipation rate	[1/s]
$\xi$	mixture fraction	[-]
$\tilde{\xi}$	filtered mixture fraction	[-]
$\rho$	density	[kg/m <sup>3</sup> ]
$\tau_E$	Eulerian mixing time scale	[s]
$\tau_L$	Lagrangian mixing time scale	[s]
$\tau_{ij}$	viscous stress tensor	[N/m <sup>2</sup> ]
$\tau_{ij}^{sgs}$	subgrid-scale Reynolds stress	[N/m <sup>2</sup> ]
$v_F$	moles of fuel	[-]
$v_O$	moles of oxidizer	[-]
$v_P$	moles of products	[-]
$v'_{\alpha i}$	stoichiometric coefficients of reactants side	[-]
$v''_{\alpha i}$	stoichiometric coefficients of products side	[-]
$\phi, \Phi$	scalar quantity	[-]
$\phi$	scalar vector	[-]
$\psi_\eta$	fine-grained PDF	[-]
$\dot{\omega}_\alpha$	reaction rate of species $\alpha$	[kg/m <sup>3</sup> s]
$\dot{\omega}_\phi$	reaction rate of species or enthalpy source term	[kg/m <sup>3</sup> s], [kJ/m <sup>3</sup> s]
$\Omega$	kernel function	[-]

**Subscripts, Superscripts and Operators**

$(\cdot)_t$	turbulent property
$(\cdot)_{\text{Fu}}$	fuel property
$(\cdot)_{\text{Ox}}$	oxidiser property
$(\cdot)_{\text{Pr}}$	product property
$(\cdot)_0$	reference property
$(\cdot)_{\text{ref}}$	reference property
$(\cdot)_p, (\cdot)^p$	property on the stochastic particle
$(\cdot)_i, (\cdot)_j, (\cdot)_k$	property in spatial direction $i, j, k$
$(\cdot)_\alpha$	property related to species $\alpha$
$(\cdot)_{\text{tot}}$	property related to the total quantity
$(\cdot)'$	unconditional fluctuation
$(\cdot)''$	density weighted fluctuation
$(\cdot)'''$	conditional fluctuation
$(\cdot)_{\text{sgs}}, (\cdot)^{\text{sgs}}$	sub-grid scale quantity
$(\cdot)_E, (\cdot)^E$	property related to the Eulerian scheme
$(\cdot)_L, (\cdot)^L$	property related to the Lagrangian scheme
$\overline{(\cdot)}$	time average
$\widetilde{(\cdot)}$	Favre (density-weighted) filtered average
$\langle \phi   \psi \rangle$	quantity $\phi$ conditioned on quantity $\psi$
$\langle \cdot \rangle$	expectation or average

**Dimensionless quantities**

Le	Lewis number
Re	Reynolds number
Sc	Schmidt number
Pr	Prandtl number
Kn	Knudsen number



# Chapter 1

## Introduction

The formation of suspended particulates<sup>1</sup> from the gas phase is widespread both in nature and in industry. Examples of such processes are the nucleation of droplets leading to the formation of, for example, raindrops or medical agents, and the flame synthesis of solid particulates for industrial commodities such as pigments, reinforcing materials, pharmaceuticals or surface coatings used in the semiconductor industry [5]. Technical progress is expanding the range of applications for particulates enormously: They are used for the production of pharmaceuticals, detergents, composite materials and substances in the semiconductor industry. In this context, the requirements on product quality, such as chemical purity, optical properties and particulate morphology are becoming increasingly important.

In addition to these intended production possibilities, there is also an undesired formation of particulates, such as soot formation, which occurs during the combustion process of fossil and synthetic fuels for power generation and in the mobility sector. Several million tons of particulates are produced per year by the energy sector [6]. In this context the World Health Organization (WHO) reports over three million premature deaths due to particulates suspended into the atmosphere [7]. Carbon dioxide is of course the main driver of global climate change, but in addition, soot also contributes massively to the temperature rise [6]. Additionally, soot is a very toxic substance for humans and animals as it causes respiratory diseases. For these reasons, it is necessary to reduce the emission of soot from combustion processes as much as possible.

For desired particulate formation and especially for the development of new applications, it is important to achieve the transition from laboratory conditions to industrial scale without affecting product quality. In the case of undesirable

---

<sup>1</sup>In order to avoid ambiguities, this study strictly distinguishes between *particulates*, which represent the physical nanoparticles in the gas phase and stochastic *particles*, which are computational elements for solving the governing differential equations in the Lagrangian sense. In this context, the term *particulates* is used uniformly for solid particulates and liquid droplets.

---

particulate formation, it is equally important to understand the processes and conditions under which they are formed so that it is possible to modify the process to prevent or reduce their formation. These principles require a comprehensive understanding of the thermophysical processes involved in the production and formation of organic or inorganic particulates. Besides the experimental investigation of these processes, numerical simulation is an efficient and cost-effective way to gain insight into the formation process. Accordingly, through comparison with experimental data, the numerical simulation of aerosol processes represents an excellent possibility to understand the inherent processes of particulate synthesis and thus to gain control over the formation process achieving intended particulate properties or preventing undesired particulate formation. However, to cover all important physical processes, models are needed for the chemical and physical processes to represent particulate formation, particulate interactions and interaction with the surrounding gas phase as well as their transport in a laminar or turbulent environment.

Depending on the specific application, the particulates can be characterised by different intrinsic properties, such as particulate size, particulate morphology, chemical composition or particulate velocity. Through interaction with the surrounding phase or collision with other particulates, these intrinsic properties can change, leading to an evolution of the properties as well as a variation in physical space. The level of detail determines how many intrinsic properties should be considered. If only a few particulates are considered, these intrinsic properties can be accounted for on each individual particulate. Since the positions and component composition of each primary particulate is known, the particulates' morphology such as fractal structure or particulate size can be derived from this information.

However, if a very large number of particulates is considered, it is reasonable to take a continuum-theoretical point of view and consider the particulate average number density as a descriptive variable and thus describe the change in intrinsic properties at a specific location and time. This leads to a description of the aerosol by a particulate property distribution in space and time. Which particulate properties are to be determined depends on the problem to be investigated. In general, the more particulate properties that are taken into account, the more complex the equation to be solved for the particulate property balance becomes. In the present work, the particulate size is the particulate property under investigation. The spatial and temporal evolution of the particulate property distribution is described by the population balance equation (PBE) [8].

In devising methods to solve the PBE, it can be distinguished between direct Monte Carlo methods [9, 10], moment methods [11] and sectional methods [12]. Direct Monte Carlo methods use a large number of stochastic particles to reconstruct the statistics of aerosol interactions, including direct modelling of collisions

and agglomeration, making this approach computationally intensive and thus inaccessible for simulating non-academic problems [9, 13, 14]. Moment methods, of which there are many varieties, mathematically reduce the particulate size distribution to its moments. Typically only the first two or three moments are required leading to a method with low computational cost. A compromise in terms of computational requirements is the sectional method, in which the particulate size distribution is approximated by a finite number of grid points. Implementation may be conceptually quite simple as the governing equations for gaseous species and particulates are solved in the same way and the description of the transition between the phases is straightforward. The significant advantage of this method is that it does not require any assumptions about the shape of the PSD, as needed for the Moment Methods, and their implementation is very intuitive. The reader is referred to references [15, 16, 17, 18] for comprehensive reviews of the different flavours of PBE methods in reactive flows.

Very often the carrier phase which surrounds the particulates behaves turbulently. Turbulence can be understood as the irregular motion of a fluid with turbulence occurring over a wide range of spatial and temporal size scales. In many engineering problems, numerical simulation offers promising approaches for the modelling of turbulent flows. The accurate simulation of turbulent processes is a crucial challenge in computational fluid dynamics. In order to meet this challenge, a number of turbulence treatment methods have been developed over the last decades.

Although Direct Numerical Simulation (DNS) represents the most accurate form of flow calculation, due to its ability to represent the entire turbulent frequency spectrum, it is only applicable for purely academic investigations in the near future due to the exorbitant calculation requirements, see [19]. The Reynolds-averaged Navier-Stokes equations (RANS) are a dichotomy to DNS, since they treat any turbulence purely statistically. Since a statistical approach is too imprecise, the associated uncertainties are not clear even for relatively simple problems [20]. Large-Eddy Simulation (LES) represents a compromise; the large energy-carrying eddies are resolved, while the eddies that cannot be resolved are still subject to a purely statistical treatment. This scale separation is particularly problematic in the treatment of turbulent, reactive flows, since molecular mixing and chemical reaction take place at the molecular level and thus below the grid resolution. To solve this problem, averaging or filtering algorithms are applied to the flow governing equations, whereby the interactions of turbulence with molecular processes now occur as unclosed terms. In the past, a substantial effort has been made to develop closure models for the treatment of turbulent, reactive flows. In this context, the closure of the terms for the formation of the reactive variables poses a major challenge since they are of a strongly non-linear nature [21, 22].

The most prominent closure models that aim at closing the highly non-linear

turbulence-chemistry interactions are the flamelet model [23], the Conditional Moment Closure (CMC) [24] and the transported Probability Density Function (PDF) models [25]. The basic idea behind the flamelet approach is that a turbulent flame can be seen as a collection of thin stretched laminar flame elements embedded into a turbulent flow. The Conditional Moment Closure model is based on a parametrisation with the help of a conditioning variable and solves transport equations of the conditioned reactive scalars. Flamelet approaches and CMC are very efficient and their application is suitable for cases where the composition can be parameterised by the conditioning variable. This restriction does not apply to transported PDF models, since these are formally derived in a more general way. Here, no filtering or averaging is necessary, so that the highly nonlinear turbulence-chemistry interactions appear in closed form.

In most cases, the transported PDF model is implemented through a stochastic Monte Carlo method [26] involving a set of Lagrangian particles<sup>2</sup>. The closure problem is then shifted towards the modelling of the molecular mixing which can be emulated by a Lagrangian micro-mixing model. A variety of stochastic mixing models with their specific advantages and disadvantages are available in the literature [27, 28, 29]. For these conventional mixing models tens or hundreds of stochastic particles are required for an adequate modelling of the molecular mixing.

The Multiple Mapping Conditioning (MMC) combustion model shares the ideas of PDF and CMC models, as it aims to combine the formal general formulation and the efficient parametrisation procedure. MMC constitutes rather a whole framework than a (mixing) model. There are different flavours of the MMC framework available, of which the stochastic MMC model is the most advanced. In the context of LES the MMC model is denoted as MMC-LES. Yet, the mixing model used through MMC-LES emulates the molecular mixing of particles which are close to each other in physical space and a reference space, on which the composition can be parameterised. Through the additional localisation process, MMC allows a substantial reduction of the required stochastic particle number and the model development stranded into the formulation of a sparse-Lagrangian MMC-LES in which only a few stochastic particles per Eulerian grid cell are required. Since the computational requirements scale linearly with the number of stochastic particles, the MMC model is a highly efficient alternative compared to conventional mixing model calculations [28]. Subramaniam & Pope [27] defined requirements for micro-mixing models and as one of the few, the MMC framework allows the fulfilment of all requirements, thus, constituting

---

<sup>2</sup>Once again, the reader is reminded that this thesis strictly distinguishes between the stochastic *particles*, which are computational elements for solving the governing differential equations in the Lagrangian sense, and *particulates*, which represent the physical nanoparticles in the gas phase.

an efficient and reliable numerical scheme for the modelling of turbulent combustion. It is yet to be seen whether these advantages can also be used for the reliable and efficient solution of more complex problems, e.g. those involving aerosol dynamics.

## 1.1 Motivation

In the context of Large-Eddy Simulations (LES) the most common methods for the solution of the PSD are the monodisperse model introduced by Kruis *et al.* [30] and the different flavours of the method of moments [31]. When the monodisperse model [32, 33] or the moment method [34, 35] for the solution of the PSD is combined with a flamelet model for the gaseous reactive species, predictions of particulate formation are good, albeit uncertainties with respect to the parameterisation of the flamelets for both kinetically fast gaseous species and kinetically slow aerosol species remain.

So far, only a few flame synthesis studies have combined LES [36, 37] with the sectional method. These have all neglected turbulence interactions with aerosol nucleation and growth despite clear evidence from Direct Numerical Simulation (DNS) studies [38] that such contributions are typically not small. A good approximation of the particulate size distribution requires an adequate resolution by a reasonable number of sections. The numerical treatment of a reasonable number of sections requires an enormous computational effort, which is not insignificant with LES. Especially in the context of turbulent combustion processes, the additional processing of the aerosol phase with a sectional method is not easily feasible. However, due to its efficiency compared to conventional modelling approaches, the MMC method would allow a sectional method to be considered within the framework of an LES, since the individual sections are mathematically equivalent to the transported reactive scalars of the classical PDF approach. Yet it would first have to be shown that the MMC method can also be used to describe aerosol processes.

Independent of the PBE solution method, some specific closure problems arise during the modelling process of particulate matter in turbulent environments since the particulate formation process is often much slower than the chemical processes involved. Thus, additionally to the separation of the time scales for the turbulence, a separation of the time scales for the particulate synthesis process has to be considered. Universal and convincing modelling strategies for accurate predictions are not yet well established. Temporally and/or spatially averaged conservation equations can be derived, but the key challenge for turbulent flows is the closure of the averaged nucleation, growth and agglomeration terms due to their highly non-linear dependence on instantaneous and

local thermodynamic properties. It is reasonable to assume that simplified approaches that neglect the interactions between turbulence, chemistry and aerosol (e.g. the model of the perfectly stirred reactor) may be sufficient for some flow conditions [39, 40]. However, most applications of practical interest feature distinctly inhomogeneous conditions, such as turbulent jets, and modelling of the large and small (i.e. subgrid) scale inhomogeneities is of paramount importance for accurate predictions.

Since a decisive reduction of unwanted soot formation in the turbulent combustion process would contribute greatly to reducing the negative impact on the ecosystem and the human body, considerable efforts have been made in recent years to fully understand and numerically reproduce soot formation. However, problems continue to be encountered in this process because the initial soot formation is chemically very complex and established methods for the solution of the PBE in turbulent, reacting environments are comparatively inaccurate due to their rigorous assumptions or presuppositions. Many investigations for example have failed to correctly predict the soot formation and the numerical results can deviate by up to an order of magnitude from measurements [41, 42, 43]. Many experimental and numerical investigations are often limited to only one or two flame configurations, and there is a high probability that the numerical models used are adjusted to these few flame configurations and therefore no statement can be made about the general validity of the methods. For this reason, it is necessary to investigate flame series with many different boundary conditions and to validate the developed numerical method on these entire flame series with a single universal parameter set.

Such a flame series was experimentally studied at Imperial College London [44]. One focus of the study was the experimental investigation of flame synthesis of silica particulates from silane in a turbulent jet configuration under varying boundary conditions. Although much experimental and numerical research has focused on the formation of soot, this study investigated the formation of silicon particulates because it was assumed that the precursor chemistry is easier and with less uncertainty to model than that of soot. Nevertheless, the knowledge derived from the silane study acquires a general character and the numerical models can be equally applied to problems with a different fuel. A validation of the numerical methods shall provide insights into the general requirements for the modelling of particulate-laden turbulent flows. It has been shown that the final product properties, such as particulates' size, shape and chemical purity, are significantly influenced by precursor reactions leading to particulate formation [45] and interparticulate interactions [46]. Especially in turbulent flows, which are necessary to enable a high product throughput, the prediction of these interactions is a challenge.

The existing experimental databases provide some understanding of the

physics of particulate dynamics and their resulting characteristics [15, 47, 48], but do not usually provide all necessary correlations between hydrodynamic and thermodynamic quantities needed for model development. This is particularly true for small scale turbulence effects on precursor chemistry, particulate nucleation, growth and agglomeration. As a consequence, although there has been some success in modelling the evolution of aerosol particulate size distributions (PSD) in laminar flames [49, 47, 50, 15], turbulent flame synthesis modelling efforts have been less successful [41] and require far too much computational demands [51, 52] to be applied for industrial purposes. For this reason, it is necessary to develop a robust numerical approach that can efficiently and reliably model aerosol processes in turbulent, reactive flows so that it can be integrated into everyday industrial applications.

## 1.2 Aim of the dissertation

Taking into account the efficiency considerations and the shortcomings and drawbacks of the currently established numerical models for particulate flame synthesis, this work intends to address the existing problems in the modelling of reactive turbulent flames, the efficient treatment of the chemical reaction and the correct prediction of the particulate matter in the turbulent carrier medium. In this sense, this work aims to combine established standard models into a comprehensive framework and to validate them on the basis of a complete series of flames, thus investigating their generality.

The following topics are the subject of this study:

- Investigation of a sparse-Lagrangian MMC-LES approach to model the combustion of a synthetic fuel for a complete flame series with increasing jet Reynolds number. A comprehensive model and stochastic numerical solution scheme for predicting combustion in a turbulent flow of varying density is presented. In a first step, the investigation of a pure gas phase flow was essential to revise the MMC modelling of the turbulence-chemistry interactions, as the modelling approach was not fully validated at the beginning of the thesis. New findings in modelling the time scales for mixing at the molecular level are included and results are compared with previously proposed mixing time scale models.
- Implementation of a sectional method for modelling the particulate size distribution in a turbulent non-reactive flow as a second step towards a comprehensive particulate modelling strategy. Based on the already existing concept for the modelling of turbulent combustion, the MMC-LES approach

is supplemented by a sectional method for the description of the particulate size distribution. With this novel combined PBE-MMC-LES approach, the properties of the aerosol can now be predicted for any spatial location and at any time without restriction on the instantaneous thermodynamic state of the gas phase. Standard models are used for the prediction of nucleation and size growth. Applying this combined approach to a non-reactive turbulent flow and comparing the results against conventional stochastic PDF methods, it becomes clear that the MMC framework can also be used to model aerosol dynamics. Furthermore, it needs to be investigated whether the sub-filter contributions should not be neglected and are crucial for correct numerical predictions.

- Validation of the PBE-MMC-LES approach by comparison to a turbulent reacting flow for the prediction of a particulate size distribution of particulates with fractal morphology. Here, established standard models for the modelling of particulate inception, volumetric size growth and agglomeration are applied. In order to show that the applied numerical methods and calibrated parameters are not adjusted to a single flame configuration but rather possess a certain general validity, the PBE-MMC-LES approach is validated against a complete turbulent and reacting flame series with varying boundary conditions and precursor dopings.

### 1.3 Thesis outline

This thesis can be structurally divided into six chapters. The second chapter presents the governing equations for the description of reactive, turbulent flows. The basics with regard to reaction kinetics and combustion modes are also presented. Furthermore, an introduction to the theory of turbulence is made and the basics for the description of aerosols and their inherent processes are given. The third chapter focuses on the numerical modelling of turbulent, reactive flows involving flame particulate synthesis. The basics of turbulence modelling are followed by the presentation of closure models of the turbulence-chemistry interactions with emphasis on the generalised sparse-Lagrangian Multiple Mapping Conditioning (MMC) model. This is followed by modelling strategies of aerosols including the presentation of models for particulate inception, surface growth and agglomeration. The fourth chapter presents the code in which the combined PBE-MMC-LES model framework has been incorporated and discusses specific numerical challenges which arise with the application of a sparse particle method. The fifth chapter presents results of different investigations of turbulent flow configurations which have been made to validate the combined PBE-MMC-LES. In a first step the MMC-LES approach is validated against the entire

---

turbulent Sandia DME flames series which has been extended by two additional configurations compared to previous publications. In a second step the sectional approach has been combined with the MMC-LES method and has been applied to predict particulate number densities in a non-reacting turbulent jet flow. This is followed by the presentation of numerical results from simulations of a novel particulate laden flame configuration for different boundary conditions. The last chapter summarises the knowledge obtained and provides an outlook on possible future scientific investigations.



# Chapter 2

## Theoretical background

In this chapter, the mathematical fundamentals are presented, which allow to describe the temporal and spatial evolution of fluid elements in turbulent flows. Starting from the basic governing transport equations, combustion processes are discussed together with turbulence phenomena. This chapter also includes the characterisation of particulates which are transported in turbulent and reacting flows.

### 2.1 Conservation equations

To adequately describe a reactive gas flow, conservation equations for mass, momentum, enthalpy and reactive species are needed. A thorough derivation of these conservation equations can be found in several relevant textbooks on the subject, e.g. in the books by Pope [26] as well as Poinso & Veynante [53] and this section summarises the derivations presented there.

The conservation of mass is determined by the continuity equation given by

$$\frac{\partial \rho}{\partial t} + \frac{\partial \rho u_j}{\partial x_j} = 0. \quad (2.1)$$

The momentum conservation is described by

$$\frac{\partial \rho u_i}{\partial t} + \frac{\partial \rho u_i u_j}{\partial x_j} = -\frac{\partial p}{\partial x_i} + \frac{\partial \tau_{ij}}{\partial x_j} + \rho g_i. \quad (2.2)$$

In the present work only ideal gases are considered, which are classical Newtonian fluids. For this reason the viscous shear tensor  $\tau_{ij}$  can be expressed by

$$\tau_{ij} = \mu \left( \frac{\partial u_j}{\partial x_i} + \frac{\partial u_i}{\partial x_j} \right) - \frac{2}{3} \mu \frac{\partial u_k}{\partial x_k} \delta_{ij}. \quad (2.3)$$

The conservation equation for a reactive species mass fraction  $Y_\alpha$  is given by

$$\frac{\partial \rho Y_\alpha}{\partial t} + \frac{\partial \rho Y_\alpha u_j}{\partial x_j} = -\frac{\partial J_j^\alpha}{\partial x_j} + \dot{\omega}_\alpha(\mathbf{Y}, T), \quad (2.4)$$

where  $\mathbf{Y} = \{Y_1, \dots, Y_{N_{sp}}\}$  represents the whole species composition of the reactive mixture into consideration. The diffusion flux  $J_j^\alpha$  is modelled by applying Fick's first law of diffusion [54] in its simplest form

$$J_j^\alpha = -\rho D_\alpha \frac{\partial Y_\alpha}{\partial x_j}. \quad (2.5)$$

With the definition of the Schmidt number

$$\text{Sc}_\phi = \frac{\mu}{\rho D_\phi} \quad (2.6)$$

which is a measure for the ratio of momentum diffusion to scalar diffusion the species conservation equation becomes

$$\frac{\partial \rho Y_\alpha}{\partial t} + \frac{\partial \rho Y_\alpha u_j}{\partial x_j} = \frac{\partial}{\partial x_j} \left( \frac{\mu}{\text{Sc}_\alpha} \frac{\partial Y_\alpha}{\partial x_j} \right) + \dot{\omega}_\alpha(\mathbf{Y}, T). \quad (2.7)$$

In multicomponent reacting flows the conservation equation of energy is usually based on enthalpy and takes the form

$$\frac{\partial \rho h}{\partial t} + \frac{\partial \rho h u_j}{\partial x_j} = \frac{\partial p}{\partial t} + \tau_{ij} \frac{\partial u_i}{\partial x_j} - \frac{\partial J_j^h}{\partial x_j} + \dot{q}, \quad (2.8)$$

where  $\dot{q}$  is the source term, which accounts for (external) heat sources such as radiation or spark ignition. The term  $J_j^h$  denotes the diffusive flux of enthalpy and contains a contribution from heat diffusion in the form of Fourier's law and from diffusion of species with different enthalpies and takes the form

$$J_j^h = -\lambda \frac{\partial T}{\partial x_j} + \rho D \sum_{\alpha=1}^{N_{sp}} h_\alpha \frac{\partial Y_\alpha}{\partial x_j} = -\frac{\mu}{\text{Pr}} \frac{\partial h}{\partial x_j} + \mu \left( \frac{1}{\text{Sc}_h} - \frac{1}{\text{Pr}} \right) \sum_{\alpha=1}^{N_{sp}} h_\alpha \frac{\partial Y_\alpha}{\partial x_j}, \quad (2.9)$$

where  $\lambda$  is the heat diffusion coefficient and Pr is the Prandtl number, which is defined as the ratio of momentum diffusivity and thermal diffusivity

$$\text{Pr} = \frac{\nu}{D_{th}} = \frac{\mu c_p}{\lambda}. \quad (2.10)$$

Another important dimensionless quantity is the Lewis number,

$$\text{Le}_\phi = \frac{\mathcal{D}_{th}}{\mathcal{D}_\phi} = \frac{\text{Sc}_\phi}{\text{Pr}} = \frac{\lambda}{\rho c_p \mathcal{D}_\phi}, \quad (2.11)$$

which is defined as the ratio of thermal diffusivity to mass diffusivity and used to characterise flows with simultaneously occurring mass and heat transfer. For many applications the species specific Lewis numbers are distributed around unity and thus for the mixture a unity Lewis number assumption,  $\text{Le}_\phi = \text{Le} = 1$ , leads to the omission of the last term in Eq. (2.9). With this simplification and neglecting pressure variations in time the energy conservation equation based on the species enthalpy takes the form

$$\frac{\partial \rho h}{\partial t} + \frac{\partial \rho h u_j}{\partial x_j} = \frac{\partial}{\partial x_j} \left( \frac{\mu}{\text{Sc}_h} \frac{\partial h}{\partial x_j} \right) + \dot{q}. \quad (2.12)$$

Equations (2.7) and (2.12) have a structurally comparable form and can therefore be combined for a reactive scalar vector  $\boldsymbol{\phi} = \{Y_1, \dots, Y_{N_{sp}}, h\}$

$$\frac{\partial \rho \boldsymbol{\phi}}{\partial t} + \frac{\partial \rho u_j \boldsymbol{\phi}}{\partial x_j} = \frac{\partial}{\partial x_j} \left( \frac{\mu}{\text{Sc}_\phi} \frac{\partial \boldsymbol{\phi}}{\partial x_j} \right) + \dot{\omega}_\phi(\boldsymbol{\phi}, T), \quad (2.13)$$

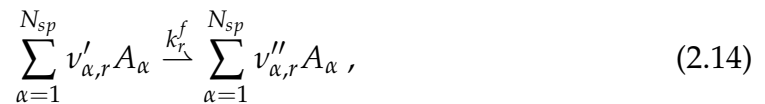
with  $\dot{\omega}_h = \dot{q}$  being the enthalpy source term.

## 2.2 Combustion

### 2.2.1 Reaction kinetics

In the previous section, the Navier-Stokes equations for the description of reactive multi-component flows were presented. A term that has not been further elaborated so far is the source term for the reactive scalar vector  $\mathbf{Y} = \{Y_1, \dots, Y_{N_{sp}}\}$ , which describes the conversion of the species.

The chemical conversion of a precursor species to product species in a multi-species environment can be represented by a system of many elementary reactions. A general form of an elementary forward reaction is

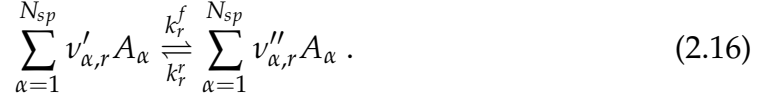


where  $\nu'_{\alpha,r}$  and  $\nu''_{\alpha,r}$  are the stoichiometric coefficients of the reactants and products with respect to the reaction  $r$  in consideration and  $A_\alpha$  stands for the species  $\alpha$ .

A similar expression can be written for the reverse reaction

$$\sum_{\alpha=1}^{N_{sp}} v'_{\alpha,r} A_{\alpha} \xrightarrow{k_r^r} \sum_{\alpha=1}^{N_{sp}} v''_{\alpha,r} A_{\alpha} . \quad (2.15)$$

For a system of elementary reactions considering forward and reverse reactions the  $r^{\text{th}}$  reaction becomes



Thus, the reaction rate  $Q_r$  for the  $r^{\text{th}}$  can be written as

$$Q_r = k_r^f \prod_{\alpha=1}^{N_{sp}} c_{\alpha}^{v'_{\alpha,r}} - k_r^r \prod_{\alpha=1}^{N_{sp}} c_{\alpha}^{v''_{\alpha,r}} \quad (2.17)$$

with the forward and reverse reaction rates coefficients  $k_r^f$  and  $k_r^r$ . To model the strong temperature dependence of the reaction rate coefficients, Svante Arrhenius [55] proposed an equation which was later subject to some modifications and finally resulted in

$$k_r = \mathcal{A}_r T^{\beta_r} \exp\left(\frac{E_{a,r}}{\mathcal{R}_u T}\right) , \quad (2.18)$$

where  $\mathcal{A}_r$  is the so-called pre-exponential factor of the reaction rate coefficient  $r$ ,  $\beta_r$  is a parameter accounting for the temperature dependence of the pre-exponential factor,  $E_{a,r}$  is the activation energy and  $\mathcal{R}_u$  is the universal gas constant. Finally, the reaction source term in Eq. (2.7) of species  $\alpha$  in a system of  $N_r$  reactions can be developed

$$\dot{\omega}_{\alpha}(Y, T) = M_{\alpha} \sum_{r=1}^{N_r} (v'_{\alpha,r} - v''_{\alpha,r}) Q_r . \quad (2.19)$$

## 2.2.2 Combustion modes

In order to examine and understand the combustion processes in more detail, it is common practice to typify the combustion mode based on the mixing of fuel and oxidiser prior to combustion. In the case of non-premixed combustion, the fuel and oxidiser are present in two separate streams and fuel conversion takes place during the mixing process. In premixed combustion, on the other hand, a combustible mixture of fuel and oxidiser is already present during the chemical conversion process [53].

In the case of non-premixed combustion the chemical reaction can only take place in a limited flammability limit around stoichiometry. Since the chemical time scales are usually below the time scales for mixing, this combustion mode is largely dependent on the mixing process itself [23]. Given that the mixing process is determined by external boundary conditions, this combustion mode is easy to control and therefore preferable for safety-critical applications [54]. Here, the mixture fraction is a key variable to quantify the progress of mixing in a flame. For a simple application with only one fuel (F) and one oxidiser (Ox) stream, the mixture fraction can be defined by

$$Z = \frac{Z_e - Z_{e,\text{Ox}}}{Z_{e,\text{F}} - Z_{e,\text{Ox}}}, \quad (2.20)$$

with  $Z_e$  is the elemental mass fraction of element  $e$ . Assuming equal Schmidt numbers for all species in the system and in conjunction with Eq. (2.13) a conservation transport equation for the mixture fraction can be developed

$$\frac{\partial \rho Z}{\partial t} + \frac{\partial \rho u_j Z}{\partial x_j} = \frac{\partial}{\partial x_j} \left( \frac{\mu}{\text{Sc}_Z} \frac{\partial Z}{\partial x_j} \right). \quad (2.21)$$

This conservation equation does not contain any source term, since the mixture fraction is dependent on elements, which are conserved during the combustion process.

Among these two main combustion modes, partially premixed combustion operates between these two limiting conditions and allows a wider range of applications. In fact, due to practical limitations, premixed combustion often results in a non-homogeneous mixture of fuel and oxidiser. In addition to these technical shortcomings, compositional inhomogeneity may be desirable, as novel combustion technologies take advantage of this inhomogeneity to achieve reduced emissions [56].

## 2.3 Turbulence

The occurrence of turbulence plays an essential role in many natural and industrial processes. In this section, the basic fluid-physical processes with regard to turbulence formation and the general turbulence properties are presented. Bradshaw's definition of turbulence [57] names its essential characteristics:

"Turbulence is a three dimensional time dependent motion in which vortex stretching causes velocity fluctuations to spread to all wavelengths between a minimum determined by viscous forces and a maximum determined by the boundary conditions. It is the usual state of

fluid motion except at low Reynolds numbers."

Peter Bradshaw [57]

Turbulence is therefore inherently three-dimensional and unsteady. Within turbulent structures, vortices exist that occur across a broad range of almost all time and velocity scales and are superimposed on the main flow. The large scales are determined by the geometry, while the smallest scales result from viscous forces in the fluid.

The importance of the correct treatment of turbulence becomes clear when considering that the presence of turbulence is the rule rather than the exception and is found in practically all technical applications. Due to the fluctuating motion of the fluid elements and the resulting increased momentum exchange of a turbulent flow, it is characterised by a significantly increased dissipation, which can exceed the molecular one by several orders of magnitude. This pseudo-viscosity - also known as turbulent viscosity - is responsible for the increased viscous dissipation and energy loss of turbulent flows. Furthermore, coherent turbulent structures cause vibrations, noise and more importantly an enhanced mixing.

Turbulence consists of a conglomerate of many intertwined vortices of different sizes and lifetimes. There is no exact definition of what a vortex is; it can however be understood as a turbulence cluster of the size  $l$ , which in turn can contain smaller vortices. The large, energy-containing vortices with the characteristic length  $l_0$  and the characteristic velocity  $u_0 = u(l_0)$ , are mostly dependent on the dimension of the geometry or dominant coherent structures. They obtain their kinetic energy from the existing velocity gradients of the main flow. Based on this, a continuous vortex decay to smaller and smaller scales takes place until the smallest vortices dissipate into heat by viscous effects.

To quantify the degree of turbulence, the Reynolds number is usually used

$$\text{Re}_{L_{\text{ref}}} = \frac{U_{\text{ref}} L_{\text{ref}}}{\nu} = \frac{\rho U_{\text{ref}} L_{\text{ref}}}{\mu}, \quad (2.22)$$

where  $U_{\text{ref}}$  is a reference velocity, e.g. a bulk velocity, and  $L_{\text{ref}}$  is characteristic reference length scale, e.g. a boundary layer thickness  $\delta$  or a nozzle diameter  $D$ .

## 2.4 Aerosols

An aerosol consists of a suspension of solid particulates or liquid droplets. The suspended solid particulates or liquid droplets are generally referred to as particulate matter or just particulates, regardless of their morphological structure or aggregate state.

### 2.4.1 Properties of particulates

Particulate size, shape, number density and chemical composition of the particulates are the aerosol properties of most interest. For certain applications, particulate charge and optical properties are also important. Particulate matter can be grouped into three categories according to particulate size: coarse particulates ( $PM_{10}$ ) with a diameter of  $10\mu\text{m}$  or less, fine particulates ( $PM_{2.5}$ ) with a diameter of  $2.5\mu\text{m}$  and ultrafine particulates with a diameter of less than  $100\text{ nm}$ .

It is conventional to assume the sphericity of liquid droplets. These droplets can change their size due to surface growth and coalescence, i.e. colliding and merging with other droplets or molecules. Due to the liquid state of the suspended droplets and the surface tension involved, the sphericity is maintained. Thus, for spherical droplets, the particulate diameter is an unequivocal size specification. However, in many applications solid agglomerates are formed which consist of many different individual particulates, the so-called primary particulates. If the temperature around the particulate remains below the melting temperature, no coalescence is observed and the primary particulates within an agglomerate remain distinct. Thus, often these particulates are not spherical, therefore excluding the size determination via the diameter alone. Therefore, the particulate volume and sometimes also the aggregated particulate surface area is a useful size parameter. In Fig. 2.1 silica and soot particulates of fractal-like morphology are shown and there it can be seen that the agglomerates consist of many small individual primary particulates and the neck formation or coalescence contributes little or negligibly to the shape of the agglomerates.

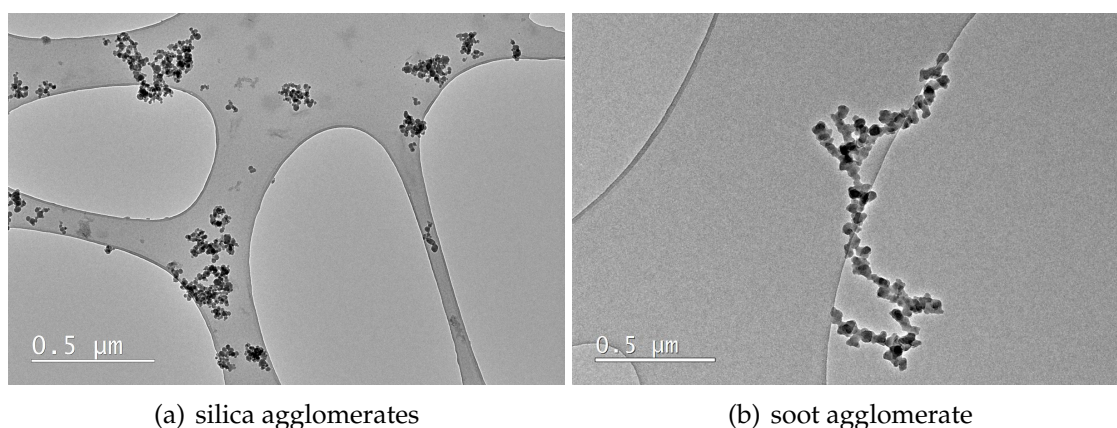


Figure 2.1: Transmission electron microscope (TEM) image of (a) silica particulates and (b) a soot agglomerate. The large empty areas correspond to holes in the carbon film of the TEM grid, used for mechanical support during imaging. Courtesy to Carlos E. Garcia Gonzalez for providing the TEM pictures.

Since in reality all particulates are differently shaped, a modelling description of the particulates' geometry can be performed using a statistical approach. Considering that an agglomerate consists of  $N_p$  primary particulates with diameter  $d_{p,0}$  and volume  $v_{p,0}$ , the shape can be described by the power law of agglomerates [12]

$$N_p = \frac{v_p}{v_{p,0}} = k_f \left( \frac{R_g}{d_{p,0}/2} \right)^{D_f}, \quad (2.23)$$

with  $v_p$  being the total volume of the particulate,  $R_g$  being the radius of gyration and  $k_f$  and  $D_f$  are the fractal prefactor and fractal dimension, respectively. Variations in primary particulate size exist, but this is usually neglected during model development. It is important to note that the power law of agglomerates is a statistical description of the particulate shape which is only valid by considering many particulates (usually more than 1000) with the same value for  $N_p$ . Nevertheless, in favour of simpler model developments, the power law for agglomerates is mostly applied for arbitrary particulate sizes, i.e. also already starting from the primary particulate. The fractal dimension is a measure of the compacity of the agglomerate and a function of the inner-agglomerate arrangement of the primary particulates, such that for  $D_f = 3$  the agglomerate would be a sphere and for  $D_f = 1$  one would consider chain-like structures. The fractal prefactor  $k_f$  is dependent on the physical definition of the radius of gyration  $R_g$ , the process and Knudsen number under which the agglomerate has been formed [12]. Usually, the fractal prefactor has a value between 0.5 and 2.5. The radius of gyration is commonly defined by

$$R_g = \sqrt{\frac{\sum_{i=1}^{N_p} m_p r_i^2}{\sum_{i=1}^{N_p} m_p}}, \quad (2.24)$$

where  $m_p$  is the mass of the primary particulate and  $r_i$  is the distance from the  $i^{\text{th}}$  primary particulate to the centre of mass of the whole agglomerate.

The diameter of particulates ranges from molecule clusters with a diameter of around 1 nm to dust particulates or nucleated droplets of diameter 100  $\mu\text{m}$ , which corresponds to a variation of  $10^5$  in particulate size and  $10^{15}$  in particulate mass. This variation over a wide size or mass range causes difficulties for modelling, since small particulates still behave like large molecular clusters and have only limited feedback effects on the flow, and large particulates must be treated as inertial particulates, i.e. due to their momentum they follow a trajectory that is related to the flow physical conditions [12].

The behaviour of particulate with respect to momentum, mass and heat exchange with the carrier fluid usually depends on the relation of the size of the

particulate and a characteristic length scale. This relation is expressed by the Knudsen number

$$\text{Kn} = \frac{2\lambda}{d_c}, \quad (2.25)$$

where  $d_c = d_{p,0}N_p^{1/D_f}$  is the collision diameter of the agglomerate and  $\lambda$  is the mean free path of the gas molecules, which can be calculated by kinetic theory of gases and is a function of pressure, temperature and the mean size of the gas molecules.

For high Knudsen numbers ( $\lambda/d_c \gg 1$ ) the number of collisions of gas molecules with a particulate is low due to the small particulate diameter. Most of the gas molecules in the vicinity of the particulate remain unaffected by the presence of the particulate and collisions are rather rare incidents. The mass, momentum and energy exchange between particulates and the surrounding gas can be described using molecular collision theory, which is why this area is also known as the free molecular regime.

For small Knudsen numbers ( $\lambda/d_c \ll 1$ ), the particulate size is much larger than the mean free path of the molecules, which increases the number of collisions drastically. Considering these size relations, the gas behaves as a continuum with the particulate as spatial boundary. For this reason the region is also called continuum regime. The transition region between these size ranges is also called transition regime.

Since particulates scatter light, this feature allows the determination of particulate number densities or concentration by applying optical measuring methods, which do not invasively interfere with the flow. A theory describing this scattering process is the Mie theory, which gives solutions of the Maxwell equations under the assumption of spherical particulates [58]. The amount of scattered light is dependent on the number density, the size and the morphology of the particulates. The scattering laws for different particulate sizes are summarised in [59].

### 2.4.2 Aerosol dynamics

Aerosol dynamics generally include particulate formation, surface growth and shrinkage, coagulation, fragmentation and sintering. The most important ones are depicted in Fig. 2.2 for solid particulate matter. Depending on whether a liquid or solid aerosol is considered, the terminology of the respective sub-processes differs, which unfortunately is not consistently complied with in the literature. Therefore, the terminology adopted in this work shall be outlined here. First, so-called primary particulates are formed from the gas phase. Particulate formation for a liquid particulate matter is called nucleation and that of solids is called particulate inception. Surface growth and shrinkage in the context of liq-

uid particles is usually referred to as condensation and evaporation, while for solid particulates the terms sublimation and deposition are used. Coagulation generally refers to the process of particulate collisions. When particulates collide, they can form larger particulates, and a distinction in terminology is made based on the aggregate state of the particulates. Coalescence refers to the merging of liquid droplets into larger liquid droplets which are assumed to maintain their sphericity. The surface area of the formed particulates is now smaller than the sum of the individual particulates, thus a reduction of the surface area results. Since solid particulates usually exhibit a certain morphological structure, they are referred to as agglomerates. Consequently, the unification of agglomerates is called agglomeration and the surface area remains unaltered. In many studies, a classification is made between agglomerates and aggregates to account for the phenomenon that aggregates are very densely packed agglomerates. However, this distinction is not made in the present thesis. Fragmentation of agglomerates refers to the separation of larger solid particulates into two or more smaller fragments. Depending on whether the temperature of the surrounding gas phase is in the range of the melting temperature, sintering of the agglomerates can occur, which leads to a change of their morphology, as well as, in a limiting case, to the formation of spherical liquid droplets. It is important to note that all the described phenomena can happen simultaneously.

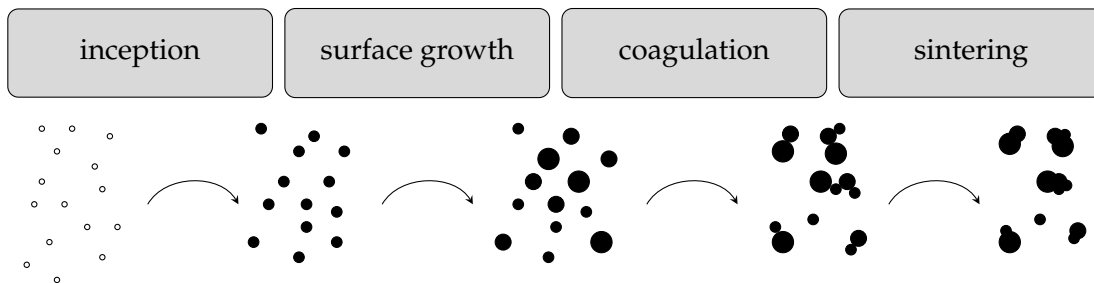


Figure 2.2: Schematic representation of aerosol dynamics processes.

### 2.4.3 Particulate conservation equation

Often there is no interest in the individual particulates but rather in the particulate size distribution at a certain location at a certain time, suggesting a description of the particulates via the particulate size distribution function  $n$ , which has the units

$$n \equiv l^{-3}L^{-3}, \quad (2.26)$$

where  $l$  refers to the length scale of the particulate matter and  $L$  refers to a length scale of the surrounding gas phase. This relation is valid when considering the

particulate volume as an intensive particulate property. Alternatively, if the particulate diameter  $d$  is used to determine the particulate size distribution function  $n_d$ , the above equation would become

$$n_d \equiv l^{-1}L^{-3} . \quad (2.27)$$

The particulate size distribution function  $n$  allows to determine the number of particulates per unit gas volume for the particulate volume range  $v_p$  to  $v_p + dv$  by

$$dN_i = n(v_i) dv , \quad (2.28)$$

with  $N_i$  being the particulate number density of particulates of size  $v_i$ . Figure 2.3 illustrates the derivation of the particulate number density  $N_i$  from the particulate size distribution function  $n(v_i)$ . The spatial and temporal evolution of the

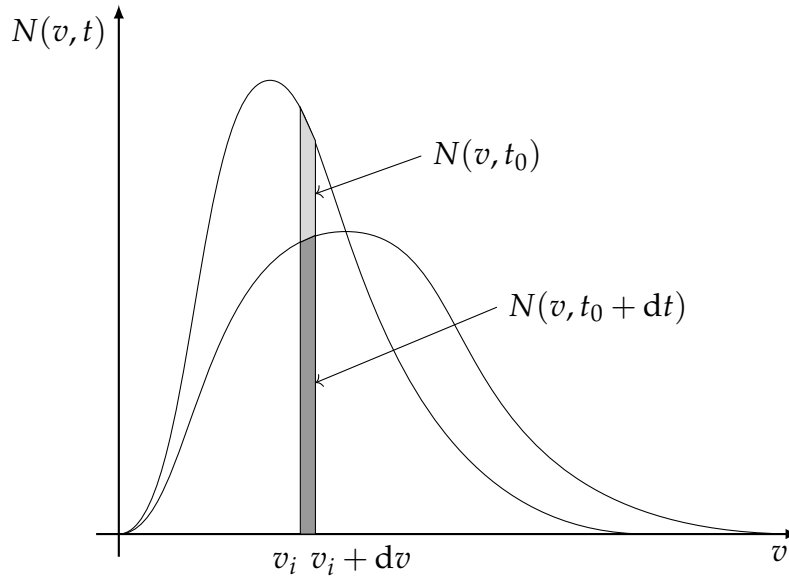


Figure 2.3: Time evolution of a particulate size distribution (sketch following Rigopoulos [17])

particulate number density can be described by the discrete or continuous Population Balance Equation (PBE).

The starting point of PBE modelling was set in 1917 by the Polish scientist Marian von Smoluchowski, who derived a discrete balance equation for the particulate number density  $N_i$  for particulates of size  $v_i$ , to calculate coagulation

problems [60]. Thus the Smoluchowski equation

$$\frac{dN_i}{dt} = \frac{1}{2} \sum_{j=1}^{i-1} \beta_{j,i-j} N_j N_{i-j} - \sum_{j=1}^{\infty} \beta_{ij} N_i N_j, \quad (2.29)$$

describes the time evolution of particulates of discrete sizes. The factor 1/2 in the source term prevents double counting of coagulation events for particulates smaller than size  $v_i$ . In Eq. (2.29) the coagulation kernel  $\beta_{ij}$  describes the coagulation frequency of a particulate of size  $v_i$  with another particulate of size  $v_j$ . The coagulation kernel is strongly size-dependent and a number of models exists in the literature, of which some are presented in Chapter 3. The original version of the Smoluchowski equation, which only considered coagulation, has been transformed into its current integral-differential formulation [61], including particulate convection and diffusional transport, as well as particulate formation, surface processes and coagulation [62, 63] and takes the form

$$\begin{aligned} \frac{\partial N(v, x_i, t)}{\partial t} + \frac{\partial u_j N(v, x_i, t)}{\partial x_j} &= \frac{\partial}{\partial x_j} \left( D_p \frac{\partial N(v, x_i, t)}{\partial x_j} \right) \\ &+ \dot{N} \delta(v - v_0) - \frac{\partial G(v) N}{\partial v} \\ &+ \frac{1}{2} \int_0^v \beta(v - v', v') N(v - v', t) N(v', t) dv' \\ &- \int_0^{\infty} \beta(v, v') N(v, t) N(v', t) dv', \quad (2.30) \end{aligned}$$

where the last four terms on the right hand side account for particulate formation, surface processes and birth and death of particulates due to coagulation. Additional source terms for particulate fragmentation and sintering are available in the relevant literature [17] and may be added to the PBE, but this is out of scope for this thesis. In Eq. (2.30),  $D_p$  is the particulate diffusivity, which is given by [12]

$$D_p = \frac{k_B T}{3\pi\mu d_c}. \quad (2.31)$$

It is important to note that the particulate number density is based on the particulates volume as an internal coordinate. Equally, another internal coordinate could be used, e.g. the particulates diameter, the surface area or the charge number. It is advantageous to use the particulate volume as the internal coordinate, as this is the conserved property and the balance equation can be treated largely independently of the morphological structure of the particulates. Under homogeneous conditions an analytical solution of the PBE equation can be found for simple coagulation problems [64, 65, 66, 67]. For inhomogeneous conditions, the solution

of an analytical approach is not possible and the solution of the PBE requires other approaches, such as the Method of Moments or the Sectional Method, which will be discussed in Chapter 3.



# Chapter 3

## Modelling

This chapter describes the modelling aspects of the particulate flame synthesis and the simulation of combustion processes in turbulent flows. First, the transport equations discussed so far are derived for turbulent flows and the associated challenges, especially for reactive flows, are explained. Then, methods to cope with these challenges are presented, with special emphasis on Multiple Mapping Conditioning (MMC) in the context of Large Eddy Simulation (LES). In a second part, methods for modelling particulate synthesis are presented and its integration into the MMC framework is explained.

### 3.1 Modelling of turbulent flows

There are many different approaches to simulate turbulent flows. The approaches differ in the degree of detail rendered and the required computational effort as an antagonistic dependency. The direct numerical simulation (DNS) avoids any kind of turbulence modelling and thus reproduces the complete turbulent energy spectrum [26]. The Reynolds-averaged Navier-Stokes (RANS) equations are the basis of all statistical turbulence models. Contrary to the efforts of direct numerical simulation to represent the entire turbulent spectrum, all the turbulence is modelled here [26]. Large eddy simulations (LES) are conceptually located between these two turbulence modelling approaches. In the following section, the model characteristics of the LES will be presented, together with closure models for the sub-grid viscosity.

#### 3.1.1 Large Eddy Simulation

In deriving the LES model, exploitation is made of the fact that small scales have an increasingly isotropic character in the subsequent sequence of the energy cascade. Thus, a differentiation can be made between large-scale and small-scale

fluctuations, whereby the former can be represented in resolved form and the latter can be left to modelling. The actual motivation for the derivation of LES is that the model-based description of small-scale turbulence is easier than with the RANS approach due to its isotropic character. The differentiation between large structures and small-scale turbulence is mainly done by filtering. The filtering of a function  $\phi(\mathbf{r}, t)$  can be understood as local averaging over a spatial range  $\Delta$  [53]. This is achieved by the filter operation

$$\bar{\phi} = \int_G \Omega(\mathbf{r} - \mathbf{r}', \Delta(\mathbf{r})) \phi(\mathbf{r}', t) d\mathbf{r}' \quad (3.1)$$

over space  $G$  with the filter kernel function  $\Omega(\mathbf{r} - \mathbf{r}', \Delta(\mathbf{r}))$ . The choice of the filter kernel function determines whether a separation is performed in physical scale space or in wave number space. Usually the box filter

$$\Omega(\mathbf{r} - \mathbf{r}', \Delta(\mathbf{r})) = \begin{cases} \frac{1}{|\Delta|} & \text{if } |\mathbf{r} - \mathbf{r}'| \leq \frac{|\Delta|}{2} \\ 0 & \text{otherwise} \end{cases} \quad (3.2)$$

is used, which performs a scale separation in the physical space [26]. A multiple application results in an increasingly progressive damping of high-frequency flow content. In contrast, the Fourier filter performs a filtering in the wave number space, whereby the energy spectrum is cut off at a certain filter frequency. The Fourier filter has the advantage that multiple applications do not alter the energy spectrum. The filtering can be performed implicitly or explicitly. An implicit filter results from the consideration that a spatial discretisation already represents a spatial filter with the filter width  $\Delta = |\Delta| \equiv \sqrt[3]{\Delta_x \Delta_y \Delta_z}$  and scales smaller than the cell width cannot be modelled. It can be implemented without much effort and makes optimal use of the available grid resolution. Since explicit filtering represents the application of filter functions, it has the advantage of being fully under control. However, the application of explicit filtering methods implies a loss of efficiency.

Applying the filtering operation to a flow governing function  $\phi$  will result in following decomposition

$$\phi = \bar{\phi} + \phi' . \quad (3.3)$$

Here  $\bar{\phi}$  represent the large structures which can be directly modelled by the basic governing equations. The turbulent structures in the high-frequency part of the energy cascade,  $\phi'$ , are approximated by a so called sub-grid model. Due to the large density variations in flows involving combustion processes, it is convenient to perform a density-weighted filtering, which is also called Favre-filtering and

defined by

$$\tilde{\phi} = \frac{\overline{\rho\phi}}{\bar{\rho}}. \quad (3.4)$$

By applying the Favre filtering procedure to the conservation equations introduced in Sec. 2.1 one obtains the Favre-filtered conservation equations

$$\frac{\partial \bar{\rho}}{\partial t} + \frac{\partial \bar{\rho} \tilde{u}_j}{\partial x_j} = 0 \quad (3.5)$$

and

$$\frac{\partial \bar{\rho} \tilde{u}_i}{\partial t} + \frac{\partial \bar{\rho} \tilde{u}_i \tilde{u}_j}{\partial x_j} = -\frac{\partial \bar{p}}{\partial x_i} + \frac{\partial}{\partial x_j} \left( 2\mu \tilde{S}_{ij} - \frac{2}{3}\mu \tilde{S}_{kk} \delta_{ij} \right) + \frac{\partial \tau_{ij}^{sgs}}{\partial x_j} + \rho g_i \quad (3.6)$$

with  $S_{ij}$  being the filtered strain rate defined by

$$\tilde{S}_{ij} = \frac{1}{2} \left( \frac{\partial \tilde{u}_i}{\partial x_j} + \frac{\partial \tilde{u}_j}{\partial x_i} \right) \quad (3.7)$$

and  $\tau_{ij}$  being the sub-grid scale stresses given by

$$\tau_{ij}^{sgs} = \bar{\rho} (\overline{u_i u_j} - \tilde{u}_i \tilde{u}_j), \quad (3.8)$$

which is an additional term due to the filtering process that needs to be modelled for closure. The requirements on the model are low, provided that the scales to be modelled are in the universal equilibrium range [68].

Most of the common sub-grid scale models are based on the Boussinesq hypothesis [69]. The Boussinesq hypothesis states that the sub-grid stresses can be represented and formally described in analogy to the dynamic viscosity, although they are physically completely different in nature. In one case the exchange processes are caused by molecular fluctuations, in the other case the exchange processes are caused by turbulent fluctuations within a continuous medium. Thus, the apparent stresses can be described by

$$\tau_{ij}^{sgs} - \frac{1}{3} \tau_{kk}^{sgs} \delta_{ij} = -2\mu_{sgs} \left( \tilde{S}_{ij} - \frac{1}{3} \tilde{S}_{kk} \delta_{ij} \right). \quad (3.9)$$

With  $\mu_{sgs}$  a sub-grid scale viscosity is introduced. This reflects the phenomenon that the effects of turbulence are apparent in an increased viscosity and diffusion. Due to the similar formulation, the effectively occurring stresses can be calculated as the sum of laminar and turbulent stresses. The effective viscosity is now de-

defined as the sum of laminar viscosity and an additional eddy viscosity  $\mu_t$ . Using the Boussinesq hypothesis the momentum conservation equation becomes

$$\frac{\partial \bar{\rho} \tilde{u}_i}{\partial t} + \frac{\partial \bar{\rho} \tilde{u}_i \tilde{u}_j}{\partial x_j} = -\frac{\partial \bar{p}}{\partial x_i} + \frac{\partial}{\partial x_j} (\mu + \mu_{sgs}) \left( \tilde{S}_{ij} - \frac{1}{3} \tilde{S}_{kk} \delta_{ij} \right) + \rho g_i. \quad (3.10)$$

The Favre-filtered conservation equation of the scalars becomes [53]

$$\frac{\partial \bar{\rho} \tilde{\phi}_\alpha}{\partial t} + \frac{\partial \bar{\rho} \tilde{\phi}_\alpha \tilde{u}_j}{\partial x_j} = \frac{\partial}{\partial x_j} \left( \frac{\mu}{Sc_\alpha} \frac{\partial \tilde{\phi}_\alpha}{\partial x_j} \right) - \frac{\partial J_{\alpha,j}^{sgs}}{\partial x_j} + \overline{\dot{\omega}_\alpha(\phi, T)}. \quad (3.11)$$

Here the sub-grid scale scalar fluxes need to be closed by the gradient assumption model

$$J_{\alpha,j}^{sgs} = -\frac{\mu_{sgs}}{Sc_{sgs}} \frac{\partial \tilde{\phi}_\alpha}{\partial x_j}, \quad (3.12)$$

with  $Sc_{sgs}$  being the turbulent Schmidt number usually set to unity and often also denoted as  $\sigma_{sgs}$ . The gradient assumption model reflects that turbulence enhances the mixing process which results in an increased diffusion and thus leads to

$$\frac{\partial \bar{\rho} \tilde{\phi}_\alpha}{\partial t} + \frac{\partial \bar{\rho} \tilde{\phi}_\alpha \tilde{u}_j}{\partial x_j} = \frac{\partial}{\partial x_j} \left( \left( \frac{\mu}{\sigma_\alpha} + \frac{\mu_{sgs}}{\sigma_{sgs}} \right) \frac{\partial \tilde{\phi}_\alpha}{\partial x_j} \right) + \overline{\dot{\omega}_\alpha(\phi, T)}. \quad (3.13)$$

Consequently, the correct calculation of the Favre-filtered conservation equations depends also on the correct modelling of the sub-grid scale viscosity  $\mu_{sgs}$  which is also known as the eddy viscosity. A simple dimensional analysis suggests that the eddy viscosity may be expressed by

$$\mu_{sgs} = \bar{\rho} (C_m \Delta)^2 \mathcal{D}_m(\mathbf{u}), \quad (3.14)$$

with  $C_m$  being a model parameter,  $\Delta$  the filter width, which is commonly a cell size related quantity, and  $\mathcal{D}_m$  being a differential operator dependent on the velocity field. A variety of eddy viscosity models are available in the literature and two of them will be presented here.

### 3.1.1.1 Smagorinsky-Model

The Smagorinsky model [70] is probably the simplest sub-grid scale model. It is based on the Boussinesq hypothesis [69] and calculates an eddy viscosity based on a geometric dimension and the local strain tensor as follows

$$\mu^{sgs} = \rho (C_s \Delta)^2 \tilde{S}, \quad (3.15)$$

with  $\tilde{S}$  as invariant of the shear rate tensor given by  $\mathcal{D}_m = \tilde{S} = \sqrt{2\tilde{S}_{ij}\tilde{S}_{ij}}$ . The value of  $C_m = C_S$  depends on the test case under investigation; a value of  $C_S = 0.1825$  was determined for the vortex decay of isotropic turbulence [26], a standard test case for the validation of a correct reproduction of the energy cascade. The Smagorinsky model has glaring shortcomings. For one thing, the parameter  $C_S$  cannot basically represent a field constant, considering that in the far field  $S$  generally has different values than in a boundary layer. Due to the globally positive parameter  $C_S$ , an eddy viscosity is also determined in a laminar flow, which means that a transition process from a laminar to a turbulent flow cannot be reproduced. Similarly, the model based on the positive parameter has a purely dissipative effect; as a result, the dissipation energy is derived exclusively from the dissolved structures. Nevertheless, energy can also be transported in the direction of smaller wave numbers, e.g. by joining several small vortices. This backscattering process cannot be reproduced with the Smagorinsky model. Another disadvantage of the model is that the differential operator does not vanish in regions close to the wall. Therefore, the inclusion of damping functions in these regions requires further input of parameters. Such parameter specifications should be avoided, as they require a new validation effort.

### 3.1.1.2 $\sigma$ -Model

Nicoud [71] proposed the  $\sigma$ -model to remedy the model deficiencies discussed above. The model is based on singular values of the resolved velocity gradient and thus the differential operator reads

$$D_m = D_\sigma = \frac{\sigma_3(\sigma_1 - \sigma_2)(\sigma_2 - \sigma_3)}{\sigma_1^2}, \quad (3.16)$$

with  $\sigma_1, \sigma_2$  and  $\sigma_3$  being the singular values of  $\tilde{u}_i/\partial x_j$  and being subject to the condition  $\sigma_1 \geq \sigma_2 \geq \sigma_3 \geq 0$ . Although there is a physical motivation for negative values of  $C_m = C_\sigma$  to reproduce backscattering of turbulent kinetic energy, for stability reasons a positive value of  $C_\sigma = 1.5$  was found by simulating the decay of isotropic turbulence<sup>1</sup>. The  $\sigma$ -model operates without damping functions for near-wall regions and delivers excellent results for pipe and jet flows [72].

## 3.1.2 Detached Eddy Simulation

The Detached Eddy Simulation (DES) is a representative of the hybrid RANS-LES models and was developed by Spalart et al. [19]. The DES attempts to combine the respective strengths of the RANS and LES approaches. The RANS equations

<sup>1</sup>Special thanks are owed to Mr. Marian Fuchs (Upstream CFD GmbH) for providing the code of the  $\sigma$ -model and for the many fruitful discussions about turbulence modelling.

are ideally suited for the statistical description of wall bounded flows, since they have been calibrated for this specific flow regime. Furthermore, they pose low demands on the grid resolution and reflect the flow behaviour in areas of small fluctuations of the flow describing variables, for example in the far field, in a good way. However, in case of detaching flows, the range of validity is violated and the RANS models usually provide unsatisfactory results. An LES, on the other hand, achieves very good results for detached flows and is capable of covering a wide range of the energy spectrum. With respect to the enormous demands on grid resolution on the wall, the LES is severely limited in terms of industrial applicability at high Reynolds numbers. The aim of the DES is to use the RANS model in regions that can be well reproduced by the turbulence model and to apply the LES approach in regions of strongly detached vortices.

In order to ensure the physically correct representation of the boundary layer, various blending and correction functions have been incorporated into the definition of the DES length scale. The new method improves the representation of the logarithmic region of the boundary layer and is called Improved-Delayed-Detached-Eddy Simulation (IDDES), although it can also be considered as wall modelled LES. A detailed description and evaluation of the individual DES modifications can be found in the work of Mockett [73].

## 3.2 Modelling of turbulent combustion

All transport and thermodynamic equations for the description of turbulent reactive flows were presented in the previous sections. In Eq. (2.7) the highly non-linear filtered reaction source term appears, which accounts for the conversion of the reactive scalars. However, the filtered reaction source term is not equivalent to the reaction source term using filtered scalars

$$\overline{\dot{\omega}_\alpha(\mathbf{Y}, T)} \neq \dot{\omega}_\alpha(\overline{\mathbf{Y}}, \overline{T}). \quad (3.17)$$

Finding a closure model for the filtered reaction source term is one of the major challenges for the combustion community and considerable scientific efforts have been made in recent decades to find an efficient and reliable method to solve this problem. Some of the established closure models for modelling non-premixed combustion processes should be presented briefly in the following sections.

### 3.2.1 Flamelet Model

Following the remarks on flame structures [74, 75], Peters introduced a methodology based on the flamelet concept [76]. The basic idea behind the flamelet approach is that a turbulent flame can be seen as a collection of thin stretched lami-

nar flame elements embedded into a turbulent flow. This is possible because the local structure of the turbulent flame front can be considered to be similar to a laminar flamelet at size scales down to the Kolmogorov scales. Thus, the flamelet concept aims to describe the global flame structure on the basis of a non-reacting transported scalar, where the flamelets are attached to an iso-surface of this non-reacting quantity which is transported by the turbulent flow. This perspective is substantiated by the introduction of the mixture fraction concept for turbulent non-premixed flames, as it allows the decoupling of turbulent transport and flame structure. A key parameter of the flamelet approach is the scalar dissipation rate which is a measure for the reactant fluxes to the reaction zone which in turn is related to the velocity gradients of the flow.

The major outcome of the introduction of the flamelet model is that the chemical structure of the flame is now modelled independently from the flow dynamics, because now the turbulence interaction is reduced to the evolution of the flame front. The flamelet structure itself can be modelled by simplified analytical solutions (e.g. Burke-Schumann solution for infinite-fast chemistry assumption) or by generating a flamelet library applying finite rate chemistry. The latter can be determined by considering a counterflow diffusion flame and often a one-dimensional approximation is solved. Its solution is therefore only altered by strain rates and curvature effects are neglected, although they may have a considerable impact [77, 78].

Using the transport equation for the mixture fraction introduced in Sec. 2.2.2 and under steady state assumptions in the vicinity of the flame front, where the approximation  $Z(x, t) \approx Z_{st}$  holds, the flamelet equations are given by

$$-\rho\chi \frac{\partial^2 Y_\alpha}{\partial Z^2} = \dot{\omega}_\alpha, \quad (3.18)$$

where  $\chi$  is the scalar dissipation rate and modelled by  $\chi = D\nabla Z\nabla Z$  [23], where equal diffusivities for all species are assumed. If a similar equation is solved for enthalpy this set of differential equations allows the full description of mass fractions and temperature as a function of mixture fraction  $Z$ .

Thus, the major advantage of the steady flamelet approach is the decoupling of the chemistry computations from the flow simulations. Thus the finite-rate chemistry can be precomputed for a variable number of scalar dissipation rates and stored into a so-called flamelet table. The solution of this flamelet table can be retrieved during the actual flame calculation which makes this approach very efficient. For a full description of the reactive flow, an additional transport equation for the mixture fraction variance needs to be solved; for which, however, standard solution approaches are available [23].

This approach reveals its shortcomings in case of high strain rates where the chemical time scales drop to the order of the turbulent time scales because then

the flame front is not restricted to the vicinity of the iso-surface of the flame [79]. The same problem occurs in case that the chemical reaction mechanism involves also slow reactions compared to the remaining kinetics. Furthermore, additional modelling effort has to be considered in case of extensive heat losses in the flow [80]. These shortcomings can be overcome by including a reaction progress variable [81, 82] or an enthalpy defect [83, 23], but these approaches partly redeem efficiency as a significant advantage over other modelling approaches due to the increased dimensionality of the system. In the case of combustion with partial premixing, the standard flamelet approach requires an extension so that a unified model for diffusion flames and partially-premixed flames is adopted [82].

### 3.2.2 Conditional Moment Closure

The Conditional Moment Closure (CMC) method is a combustion model which was independently developed by Klimenko [84] and Bilger [85] for non-premixed combustion. The basic idea behind CMC is that reactive scalars are strongly correlated to the mixture fraction and hence reactive scalar fluctuations are correlated to fluctuations in mixture fraction space. Based on this strong correlation, the conditional fluctuations are small and this relationship can be used to provide a first order closure for the chemical reaction term. Normally, the conditional moments are referred to as  $Q_\alpha$  and are defined by

$$Q_\alpha = \langle Y_\alpha | \mathbf{Z} = \mathbf{z} \rangle , \quad (3.19)$$

where  $\mathbf{Z}$  is a multidimensional scalar space and  $\mathbf{z}$  is its sample space. Whether a quantity is a conditioned or a conditioning variable depends on the problem; in any case the sets are disjoint. The vector notation in Eq. (3.19) emphasises that conditioning is not constrained necessarily to a single conditioning variable and may allow additional conditioning to other quantities that also feature correlations with the reactive scalars. Following the same procedure as for the Reynolds and Favre averaging the instantaneous quantities can be decomposed into their conditioned mean and conditioned fluctuation

$$Y_\alpha = Q_\alpha + Y_\alpha''' . \quad (3.20)$$

Applying this decomposition to the transport equation of reactive scalars and performing a conditional averaging over the whole equation together with a high Reynolds number assumption yields the transport equation for conditional reactive scalars

$$\begin{aligned} \langle \rho | \mathbf{z} \rangle \frac{\partial Q_\alpha}{\partial t} + \langle \rho u_i | \mathbf{z} \rangle \frac{\partial Q_\alpha}{\partial x_i} - \langle \dot{\omega}_\alpha | \mathbf{z} \rangle + \langle \dot{\omega}_j | \mathbf{z} \rangle \frac{\partial Q_\alpha}{\partial Z_j} = \\ \left\langle \rho \mathcal{D}_\alpha \frac{\partial Y_j}{\partial x_i} \frac{\partial Y_j}{\partial x_i} \middle| \mathbf{z} \right\rangle \frac{\partial^2 Q_\alpha}{\partial Z_j \partial Z_j} + \left\langle \rho \mathcal{D}_\alpha \frac{\partial Y_j}{\partial x_i} \frac{\partial Y_l}{\partial x_j} \middle| \mathbf{z} \right\rangle \frac{\partial^2 Q_\alpha}{\partial Z_j \partial Z_l}. \end{aligned} \quad (3.21)$$

All terms except the first need a closure model and a guideline for the choice of the closure model can be found in the literature [24, 79]. In selecting the conditioning variables, strict attention must be paid to ensure that the conditioned fluctuations are small. The mixture fraction is the most commonly used conditioning variable in non-premixed combustion. In non-premixed flames where significant local extinction events are present a single conditioning variable is not sufficient and a double conditioning is necessary where scalar dissipation rate or sensible enthalpy are possible extensions of the conditioning vector [86, 87]. Although the derivation of the CMC method is based in the mixture fraction concept the application to partially premixed flames was suggested by Bilger [85] and the sensitive enthalpy was proposed as the conditioning variable therein.

It seems obvious to increase the number of conditioning variables in order to obtain better simulation results; however, this increases the number of unclosed terms of the transport equation of the conditional scalars, which significantly increases the modelling and computational effort. The latter is due to the fact that the transport equation for the conditional quantities include additional dimensions. However, since the conditioned quantities are subject to much smaller fluctuations in physical space than the unconditioned quantities, the calculation can be performed on a much coarser grid [79].

In recent years the interest has grown to calculate liquid fuel combustion with the CMC method and Mortensen & Bilger [88] presented a fully consistent derivation for spray combustion, which gives good results in the work of Ukai *et al.* [89, 90, 91]. Kronenburg & Bilger [92] showed the capabilities of the CMC method to model soot formation and the opportunities to account for differential diffusion effects in non-premixed flames [93, 94].

### 3.2.3 Transported Probability Density Function models

The transported Probability Density Function (PDF) is a methodology to calculate the transport of a set of reactive scalars by solving the transport equation of the one-point, one-time joint PDF of the reactive scalar vector. Thereby, the method aims to model the unresolved sub-grid scale fluctuations of the transported quantities [25]. In the context of LES, where usually Favre-filtering is applied, this

method is denoted as transported filtered density function (FDF) and accounts for the solution of the PDF of the sub-grid scalars [95, 68]. In comparison to other combustion models, this approach has the significant advantage that the reaction source term appears in a closed form and no modelling is required. However, the terms for sub-grid scalar mixing and transport are present in unclosed form and have to be modelled. Given the filter kernel  $G$  the mass weighted FDF function for the sub-grid scales becomes

$$\mathcal{F}^{sgs} = \int \rho G(\mathbf{r} - \mathbf{r}', \Delta(\mathbf{r})) \delta(\psi - \phi(\mathbf{r}', t)) d\mathbf{r} \quad (3.22)$$

with  $\psi$  being the sample space for  $\phi$  and

$$\delta(\psi - \phi(\mathbf{r}', t)) \equiv \prod_{\alpha=1}^{n_s+1} \delta(\psi_\alpha - \phi_\alpha(\mathbf{r}', t)) \quad (3.23)$$

being a multidimensional delta function [96]. Following the derivations given in Colucci *et al.* [97] the transport equation for the temporal and spatial evolution of the filtered mass density function becomes

$$\begin{aligned} \frac{\partial \mathcal{F}^{sgs}}{\partial t} + \frac{\partial \tilde{u}_i \mathcal{F}^{sgs}}{\partial x_i} + \frac{\partial \dot{\omega}_\alpha(\psi) \mathcal{F}^{sgs}}{\partial \psi_\alpha} = \\ \frac{\partial}{\partial x_i} \left( \bar{\rho} (\mathcal{D} + \mathcal{D}_t) \frac{\partial \mathcal{F}^{sgs} / \bar{\rho}}{\partial x_i} \right) - \frac{\partial^2}{\partial \psi_\alpha \psi_\beta} \left( \left\langle \bar{\rho} \mathcal{D} \frac{\partial \phi_\alpha}{\partial x_i} \frac{\partial \phi_\beta}{\partial x_i} \middle| \psi \right\rangle \mathcal{F}^{sgs} / \bar{\rho} \right) \end{aligned} \quad (3.24)$$

applying standard closure models for the conditional velocity and resolved conditional diffusive fluxes. The last term represents the conditional subfilter scalar dissipation and is unclosed, because the gradients at the sub-grid scale level are unknown. In case of detailed chemistry Eq. (3.24) is a highly dimensional differential equation and its solution in the context of LES is infeasible due to the exorbitant computational costs [79].

Here, it is common practice to apply a stochastic approach by introducing a Monte Carlo scheme, for which the computational costs scales linearly with the number of dimensions instead of exponentially. The Monte Carlo method introduces Lagrangian particles which emulate the evolution of the reactive scalars due to advection, mixing and reaction in a flow field. Stochastic particles are usually characterised by their position  $x_i^p$  and composition

$$\phi_\alpha^p = (Y_1, \dots, Y_{n_s}, h). \quad (3.25)$$

The fractional step time evolution of the transported scalars are then given by the

equivalent stochastic differential equations [96] for particle transport

$$dx_i^p = \left[ \tilde{u}_i + \frac{1}{\bar{\rho}} \frac{\partial}{\partial x_i} (\bar{\rho}(D + D_t)) \right]^p dt + \sqrt{2(D + D_t)^p} d\omega_i, \quad (3.26)$$

and the change of the composition field in time is governed by [96]

$$d\phi_\alpha^p = (S_\alpha^p + M_\alpha^p) dt, \quad (3.27)$$

where  $\omega$  is a Wiener process. To account for the slip of inertial particles an additional fractional step equation needs to be solved for the particle velocity  $u_j^p$ , but is omitted here. The term  $S_\alpha$  accounts for chemical reactions or heat loss due to radiation, and by using the Arrhenius approach or a radiation model (e.g. optically thin radiation model proposed by Grosshandler [98]), this term is now in closed form. The term  $M_\alpha$  is a mixing operator which emulates the sub-filter scalar dissipation and needs modelling. A vast variety of mixing models are available in the literature and the most common will be discussed in the next section.

### 3.2.3.1 Mixing models

To close the stochastic FDF model a Lagrangian mixing model is required and a large number of mixing models is available in the literature [99, 100, 101, 102, 103, 104, 105, 106, 107, 27, 108]. Generally the choice of an accurate and efficient mixing model is crucial for the quality of the turbulent combustion simulation since it is one of the major source of uncertainty [28]. Subramanian & Pope [27] defined characteristic properties and requirements which mixing models should provide. Among these the most important properties are (i) that the locally mean scalar composition should remain constant through the mixing process, (ii) that the decay rate of scalar variance is correctly provided and (iii) that boundedness of the mixed scalars is fulfilled. Further demands are given by the requirement of (iv) linearity of the mixing process, (v) independence on the mixing scalars themselves and (vi) locality of the mixing process in composition space, so that a Gaussian distribution is obtained for statistically homogeneous systems. One additional criterion is that (vii) the mixing model should provide dependencies on length scales of the scalar fields, as it was shown by Warhaft & Lumley [109], that the variance decay rate is dependent on the initial length scales of the scalar field. In the following, the most common mixing models are presented, as they form the fundamental basis for further developments and flavours of other mixing models.

The Interaction by Exchange with the Mean (IEM) [110] which is often also referred to as Linear Mean-Square Estimation (LMSE) [100, 101] is one of the simplest models and the distribution of the particle composition is characterised as

essentially independent of the composition of other particles. Due to its simple form and straightforward numerical implementation it is widely used in FDF combustion modelling simulations. The basic idea behind this mixing model is that the particle scalar composition  $\phi_\alpha^p$  relaxes deterministically towards the local mean  $\langle \phi_\alpha^p | x^p \rangle$  as

$$S_\alpha = \frac{d\phi_\alpha^p}{dt} = -\frac{1}{2} \frac{C_\phi}{\tau} \left( \phi_\alpha^p - \langle \phi_\alpha^p | x^p \rangle \right), \quad (3.28)$$

where  $C_\phi$  is a model parameter, which is a measure for the ratio of the mechanical time scale  $\tau$  to the time scale of turbulence  $\tau_\phi$

$$C_\phi = \frac{\tau}{\tau_\phi}. \quad (3.29)$$

The mixing model fulfils the requirements of the conservation of the scalar mean and provides the correct decay of the scalar variance. It further guarantees the boundedness and linear independence of the transported scalars. In the absence of mean scalar gradient, e.g. in homogenous turbulence, the mixing model preserves the initial shape of the scalar PDF and thus prevents the formation of a Gaussian scalar distribution, which is one of the major drawbacks for its application. Another drawback is that the operator  $\langle \phi_\alpha^p | x^p \rangle$  reverts to the composition of a finite number of stochastic particles and thus violates the principle of localness if the number of stochastic particles is not sufficiently high.

The Coalescence-Dispersion (CD) mixing model proposed by Curl [99] forms the basis of later variants of this model developed by Janicka [102] and Dopazo [101]. The mixing model aims at randomly selecting pairs of particles and then allow partially linear mixing towards their respective mean. The mixing process for particles  $p$  and  $q$  can formally be described by

$$\phi_\alpha^p(t + \Delta t) = \phi_\alpha^p(t) + \gamma \left( \bar{\phi}_\alpha^{p,q}(t) - \phi_\alpha^p(t) \right), \quad (3.30)$$

$$\phi_\alpha^q(t + \Delta t) = \phi_\alpha^q(t) + \gamma \left( \bar{\phi}_\alpha^{p,q}(t) - \phi_\alpha^q(t) \right), \quad (3.31)$$

where  $\bar{\phi}_\alpha^{p,q}(t)$  is the weighted mean of the two involved particles and  $\gamma = 1 - \exp(-C_{CD}\Delta t/\tau)$  controls the mixing extend with a mechanical timescale,  $\tau$ , and the model parameter  $C_{CD}$ , which is usually set to  $C_{CD} = 2$  for variable weights of the mixing particles. The CD model again fulfils the first three requirements of mixing models together with linearity and boundedness. However, the mixing model is neither capable of forming a Gaussian distribution nor is localness in composition space satisfied. The latter is due to the randomised particle pair selection mechanism, which is formally independent of the particle position. This problem can be counteracted by increasing the stochastic particle number and

reducing the filter width, although this cannot remedy the principle violation.

Another representative of a mixing model is the Mapping Closure (MC) [111, 112] model based on Gaussian reference fields. The ingredients of this mixing model are the application of statistically isotropic, homogeneous and time-independent Gaussian fields, where means, variances and two-point correlations functions are known, a surrogate field, where the statistics are the same as of the Gaussian fields and therefore also known; and a mapping algorithm between these two fields. Here, the conservation of scalar mean, the correct decay of scalar variance as well as the linearity and boundedness are satisfied. In addition, localness in composition space is fulfilled through the mapping algorithm, resulting in a Gaussian distributions of the scalars in statistically homogeneous flows. Drawbacks of the MC model is that the mapping procedure in multi-scalar environments violates against the principles of independence.

The Multiple Mapping Conditioning (MMC) model represents an advanced synthesis of Mapping Closure and CD models but is on the contrary conform with the requirements of linearity and independence. However, since the MMC model is not only another representative of a mixing model, but rather forms a completely new framework, it will be presented in the following section.

### 3.2.4 Multiple Mapping Conditioning for modelling turbulent reacting flows

This section is dedicated to the introduction of the Multiple Mapping Conditioning (MMC) model, which can be understood as a whole modelling framework for modelling combustion processes rather than just a model. First, the characteristics and principles of MMC are presented, followed by a description of the full generalised MMC model with its recent improvements.

The Multiple Mapping Conditioning (MMC) model was originally introduced by Klimenko & Pope [113] and unifies methods and features of Mapping Closures [114, 111, 115], CMC [84, 85] and transported probability density functions [25]. The derivation of its generalized form resulted in a comprehensive framework, which could exploit the advantages of the PDF and CMC methods and at the same time remove the restrictions of mapping closures to homogeneous flows [116]. The original Multiple Mapping Conditioning model and its theoretical structure has been extended considerably over time and the following section summarises the key publications [113, 117, 118, 119, 120, 96, 121] related to the model derivation as well as works with review character [122, 123, 124, 125].

The development of MMC is based on the same physical considerations as the flamelet approach [76] and CMC [84, 85], assuming that the attainable scalar space can be related in some way to the evolution of a low-dimensional manifold. MMC applies the concepts of Mapping Closures where a low-dimensional

reference space is associated to the transported scalars by a mapping function. The Probability Density Function distribution of that reference space is either assumed to be known or is simulated by some means such as a Markov diffusion process. MMC uses the mapping functions for modelling the degree of fluctuations of the scalars. The turbulent scalar fluctuations are conceptionally divided into *major* and *minor* scalar fluctuations and the Mapping Closure establishes the association between the reference space and the major fluctuations. The dimension of the reference space is generally only limited to the number of transported scalars, but is usually very small. In non-premixed combustion processes, for example, a reference space comprising only the mixture fraction is considered to be sufficient. The reference space represents a low-dimensional manifold which is allowed to fluctuate in any possible way, while the fluctuations of the scalars are partially or completely confined relative to this reference space, dependent of the form of MMC - conditional or probabilistic - which is applied. The conditional form occurs in either a deterministic or stochastic model implementation and assumes that the small scalars can only fluctuate jointly with the large scales, so that the conditional fluctuations are negligibly small. In contrast, the probabilistic form occurs only as a stochastic variant, where the minor scalars can fluctuate relative to the major scalars, but these fluctuations are still assumed to be small. For the probabilistic form a generalized model can be derived, which allows to remove some restrictions regarding the formalities of the derivation and thus to extend the application scope considerably.

Considered that the major species in the MMC model are reasonably selected, the joint Favre-filtered PDF  $\tilde{\mathcal{F}}_Y$  of all species of the  $n_s$ -dimensional composition space can be replaced by a marginal PDF  $\tilde{\mathcal{F}}_M(\mathbf{y}^M; x, t)$  of the major species in the reduced  $n_M$ -dimensional manifold space, where  $n_M < n_s$  is the number of major species  $\mathbf{Y}^M$ . The remaining composition space of dimension  $n_\alpha = n_s - n_M$  is associated with the minor species composition  $\mathbf{Y}^\alpha$ . Additionally to the above introduction of the marginal PDF the conditional mean of the minor species  $\mathcal{Q}^\alpha(\mathbf{y}^M; x, t) = \langle Y^\alpha | \mathbf{Y}^M = \mathbf{y}^M \rangle$  can be defined such that

$$\tilde{\mathcal{F}}_Y = \tilde{\mathcal{F}}_M \cdot \delta(\mathcal{Q}^\alpha - \mathbf{y}^\alpha). \quad (3.32)$$

This expression defines the confinement of minor species to a manifold described by major species, so that in the deterministic form of MMC there are no fluctuations of minor species over their conditional means [113]. Now the transport equation of the marginal PDF of the major species becomes

$$\frac{\partial \bar{\rho} \tilde{\mathcal{F}}_M}{\partial t} + \frac{\partial \bar{\rho} U_{Y^M} \tilde{\mathcal{F}}_M}{\partial x_i} + \frac{\partial \bar{\rho} W_k \tilde{\mathcal{F}}_M}{\partial y_k} + \frac{\partial^2 \bar{\rho} N_{kl} \tilde{\mathcal{F}}_M}{\partial y_k \partial y_l} = 0 \quad (3.33)$$

and the transport equation for the conditional expectation of the minor species is

given by

$$\frac{\partial Q_a}{\partial t} + \mathbf{U}_{\mathbf{Y}^M} \cdot \frac{\partial Q_a}{\partial x_i} + W_k \frac{\partial Q_a}{\partial y_k} - N_{kl} \frac{\partial^2 Q_a}{\partial y_k \partial y_l} = W_a, \quad (3.34)$$

where

$$N_{kl} = \left\langle \rho D \frac{\partial Y_k}{\partial x_i} \frac{\partial Y_l}{\partial x_j} \middle| \mathbf{Y}^M = \mathbf{y}^M \right\rangle / \bar{\rho}_{\mathbf{Y}^M} \quad (3.35)$$

is the conditional scalar dissipation and  $\mathbf{U}_{\mathbf{Y}^M} = \langle \mathbf{U} | \mathbf{Y}^M = \mathbf{y}^M \rangle$  is the conditional velocity and both terms require modelling. Concerning the application of the Mapping Closure within the MMC framework an  $n_r$ -dimensional reference space is introduced as a set of random variables  $\boldsymbol{\xi} = \{\xi_1, \dots, \xi_{n_r}\}$ , which are associated to the major species by a mapping function. The distribution of this reference space field is given by the joint PDF  $\tilde{\mathcal{F}}_{\boldsymbol{\xi}}(\boldsymbol{\xi}; \mathbf{x}, t)$  and it is assumed here that the reference variables are transported in a similar way to all other physical scalars and thus their statistical properties are emulated, but the reference variables only form a mathematical construct and do therefore not directly model the physical variables. Between them, however, a statistical equivalence results in this form of application.

Depending on the implementation, MMC can take a deterministic or stochastic form. In this study, the generalised form of stochastic MMC is applied and further details are provided below only for this model branch. The reader may be referred to [113, 126, 127, 128] for model development and applications of deterministic MMC.

#### 3.2.4.1 Generalised MMC

Generalised MMC is a further development of the MMC method proposed by Klimenko [129], which removes some formal restrictions of the original MMC method. Although generalized MMC would be technically possible in a deterministic variant, it generally exists only as a stochastic model. The main aspect of the generalized MMC is the subdivision of the reference space into conditioning variables  $\zeta_c$  of dimension  $n_c$  and non-conditioning variables. The former serve to emulate certain characteristics of the turbulent flow and allow mixing localization in the space of the major species manifold. The latter do not participate in the localisation process, but are used to assist in emulating the turbulent quantities. As a consequence of this subdivision, Klimenko [129] proposes to use conditioning reference variables such as mixture fraction and dissipation-like variables, which may be taken from the governing flow field. Sundaram *et al.* [130] showed that the functional form of the mixing operator is the same as for traditional trans-

ported PDF models and that a conditioning of the mixing operator on reference variables is compliant with an original PDF modelling. Consequently in MMC the conditional scalars are not directly dependent on the mixture operator, but are rather governed by the properties of the conditioned reference variables. This in fact is the generalisation of the mixing process as it shifts the problem towards a decent selection of adequate conditioning variables while unaltering the mixing operation.

A suitable reference variable in non-premixed combustion processes is the mixture fraction. But a requirement in MMC is that the conditional variables should be independent of the variables to which they are to be mapped. Thus, in MMC simulations of non-premixed combustion simulations involve actually two different but conceptual similar mixture fractions. One mixture fraction,  $Z$  is transported with the scalar vector and its evolution can be described by the set of stochastic differential equations given above. The other is a mixture fraction-like conditioning variable,  $\zeta = f$  which is governed by an Eulerian simulation which emulates the real mixture fraction of the stochastic Lagrangian particles and is used for the localisation process.

#### 3.2.4.2 Sparse-Lagrangian FDF methods

So far MMC has been introduced as a modelling framework which features a mixing model fulfilling all requirements of a high quality mixing model such as the conservation of means as much as boundedness, linearity, independence, equal treatment of all scalars and a correct dissipation of variances [27]. In fact, the MMC mixing model can significantly improve numerical results, although Klimenko [131] showed that by exorbitantly increasing the number of notional Lagrangian particles, the role of the underlying mixing model becomes more and more irrelevant and at a DNS-like resolution, where the spatial distance between the particles is infinitely small, all mixing models become effectively the same. However, such an increase in particle number does not correspond to the concept of efficiency considerations where quality results are expected at minimum costs.

Sparse-Lagrangian methods include a reduction of the stochastic particle number for the simulation of the composition space below the number of Eulerian grid cells for the calculation of the turbulent flow field, which leads to substantial savings of computational costs. The idea of sparse methods is completely independent from MMC, but it requires a high-quality mixing model, which is offered by MMC. In order to distinguish the particle density in common PDF methods from the new sparse-Lagrangian distribution of particles, it will be referred to in the following as intensive-Lagrangian particle distribution [132]. The introduction of a sparse-Lagrangian particle method also changes the interpretation of stochastic PDF methods. While intensive-Lagrangian particle methods

represent a so-called strong approximation, which may even reach the DNS limit when a massive number of particles is used [131], the interpretation of sparse-Lagrangian methods changes in the sense that they can only represent stochastic distributions of lower moments and are therefore only to be understood as weak approximations. Strong approximations are naturally weak approximations at the same time, but the opposite case is generally not given.

In intensive methods the Eulerian variables and the variables of the transported scalar vector in FDF are both associated with the Eulerian grid size  $\Delta_g$ . The characteristic filtering lengths of the sparse-Lagrangian methods  $\Delta_L$  and the Eulerian scheme  $\Delta_E$  can be applied for a weak approximation of the scalar-vector distribution. The Lagrangian filter width cannot be smaller than the Eulerian filter width, because the grid resolution does not allow a suitable scale resolution of the underlying velocity field to evolve the scale vector adequately. Actually, within a weak approximation of the scalar composition distribution the Lagrangian filter width  $\Delta_L$  can be larger than the Eulerian filter width  $\Delta_E$ , which allows the mixing of particles that are close to each other but not necessarily in the same Eulerian cell. In Lagrangian PDF methods, there are two further length scales, namely the interparticle distance  $\Delta_p$  and the mixing distance  $\Delta_m$ , where the latter is the mean distance between mixing particles, which does not necessarily coincide with the interparticle distance. Besides the fact that the mixing process produces a numerical diffusion effect that usually has to be minimized, Klimenko [133, 134, 135] stated that this diffusion effect can be interpreted as a filter function for the model and that this mixing induced diffusion does not vary with stochastic particle numbers if the characteristic mixing distance  $\Delta_m$  and the characteristic mixing time  $\tau_m$  are kept constant. An appropriate choice of a characteristic mixing distance and a characteristic mixing time is of paramount importance for modelling the correct level of diffusion and suitable models will be introduced in the next section.

### 3.2.4.3 Sparse-Lagrangian MMC

The new interpretation of the diffusive effect of the mixing model operator in sparse methods allows a reduction of the stochastic particle number within the turbulent reactive simulation. The application of a sparse method necessarily requires a high quality mixing model of which the MMC model is an example as it fulfils all key features of a mixing model. Moreover, the generalised MMC framework is a suitable candidate, as it allows for a simple and straightforward implementation of the mixing model requirements.

However, special care must be taken in deriving the mixing operator in a sparse environment. In this section, the key features of the MMC mixing model, such as the constraints on conditioning to the reference variables and the mod-

elling of appropriate mixing time scales in a sparse context, are presented. In Generalised MMC [96] the temporal and spatial evolution of the stochastic particles and the transported scalar vector,  $\phi_\alpha^p = (Y_1, \dots, Y_{n_s}, h)$ , is described by Eqs. (3.26) and (3.27). Additionally, in MMC the mixing process is subject to the supplementary requirement that the conditioning involves only the generalized reference variables  $\xi_c$ , so that

$$\langle S_I | \xi_c^p = \xi_c, \mathbf{x}^p = \mathbf{x} \rangle = 0. \quad (3.36)$$

This condition can be satisfied by selecting particles for mixing that are close to each other in a space comprising the reference space and the spatial space. This can be archived by minimising the squared distance between two particles  $p$  and  $q$  defined as

$$\hat{d}_{p,q}^2 = \sum_{i=1}^3 \left( \frac{d_{x_i}^{p,q}}{r_m / \sqrt{3}} \right)^2 + \sum_{j=1}^{n_c} \left( \frac{d_{\xi_j}^{p,q}}{\zeta_{m,j}} \right)^2, \quad (3.37)$$

where  $r_m$  is a characteristic distance in physical space and  $\zeta_{m,j}$  is a characteristic distance in reference space. The factor  $\sqrt{3}$  in the denominator is based on the assumption that the mixing distance is an isotropic quantity. In the context of non-premixed combustion, the choice of the mixture fraction  $f$  as the only conditioning variable is considered sufficient in most cases. In that case the squared mixing distance becomes

$$\hat{d}_{p,q}^2 = \sum_{i=1}^3 \left( \frac{d_{x_i}^{p,q}}{r_m / \sqrt{3}} \right)^2 + \left( \frac{d_{\tilde{f}}^{p,q}}{f_m} \right)^2. \quad (3.38)$$

Generally, the parameter  $f_m$  is a local quantity which changes with the local flow conditions. Since a locally variable mixing parameter  $f_m$  is very unfavourable with regard to the computational efficiency, it is considered as a global parameter and determined on the basis of characteristic flow conditions. Where in previous publications the parameters were selected manually [135, 132, 136], Cleary & Klimenko [96] presented a relation based on a consistent scale analysis of an iso-scalar sliver such that

$$r_m = C_m \left( \frac{d\tilde{f}}{dn} \frac{\Delta_L^3}{\Delta_E^{2-D_f}} \frac{1}{f_m} \right)^{1/D_f}, \quad (3.39)$$

with  $C_m$  being a model parameter usually set to 0.5,  $d\tilde{f}/dn$  being the gradient of the filtered LES mixture fraction across the iso-scalar sliver at a characteristic lo-

cation of the flow,  $D_f$  being the fractal dimension of the turbulent iso-scalar sliver usually set to 2.36 [96] and  $f_m$  being the mean distance in mixture fraction space between particles to be mixed. The latter was the central subject of several investigations [96, 137, 138, 139] and good results were achieved when this parameter was set to  $f_m = 0.03$ .

The Lagrangian mixing time scale determines the degree of sub-filter conditional scalar dissipation. In intensive stochastic FDF simulations where there are possibly ten or more stochastic particles in each LES cell, mixing is constrained to the particle ensemble within each cell. Thus, the particle filter time and length scales are determined from the local filter scales of the Eulerian scheme. The Eulerian mixing time scale has the form

$$\tau_E = \widetilde{f'_E} / \chi_E, \quad (3.40)$$

where  $\widetilde{f'_E}$  is the sub-grid reference mixture fraction variance and  $\chi_E$  is the scalar dissipation, respectively. For these quantities, standard models are commonly used in combustion LES investigations, which leads to

$$\widetilde{f'_E} = C_f \Delta_E^2 \nabla \tilde{f} \cdot \nabla \tilde{f}, \quad (3.41)$$

where the scaling parameter is usually set to  $C_f = 0.1$  [140], and

$$\chi_E = 2(D + D_t) \nabla \tilde{f} \cdot \nabla \tilde{f}. \quad (3.42)$$

Substitution of Eqs. (3.41) and (3.42) into Eq. (3.40) results in

$$\tau_E = \frac{C_f \Delta_E^2}{2(D + D_t)}. \quad (3.43)$$

Corresponding expressions for the Lagrangian time scale have been discussed in Vo *et al.* [138]. The C&K model was developed by Cleary & Klimenko [96] and was derived on the basis of simple geometrical reasoning that led to the time scale expression

$$\tau_{L,C\&K} = \frac{\beta C_f d_{\tilde{f}}^2}{2(D + D_t) \nabla \tilde{f} \cdot \nabla \tilde{f}}, \quad (3.44)$$

with  $\beta$  being a parameter between 1 and 3. Usually a value of  $\beta = 3$  is set, to avoid excessive numerical diffusion [96]. As  $\nabla \tilde{f}$ ,  $D$  and  $D_t$  may vary significantly within a sparse-Lagrangian approach, it has been shown that the maximum mixing time of  $\tau_{L,C\&K}^p$  and  $\tau_{L,C\&K}^q$  avoids numerical diffusion [96].

As it was shown in Vo *et al.* [138], the C&K mixing time scale model under-

predicts conditional variances and a new mixing time scale model was proposed therein. The new model attempts to account for the anisotropy of the turbulent structures at the Lagrangian filter size and has the form

$$\tau_{L,a-ISO} = \frac{C_f d_x^2}{2(\mathcal{D} + \mathcal{D}_{t,L})}, \quad (3.45)$$

where  $\mathcal{D}_{t,L}$  is a turbulent sub-grid scale diffusivity which scales to the respective Lagrangian length scales  $\mathcal{D}_{t,L} = d_x / \Delta_E \mathcal{D}_t$ . It should be noted that the a-ISO (abbreviated use for anisotropic) model has a similar form to the Eulerian mixing time given by Eq.(3.43). To avoid over predictions of Lagrangian subfilter variances the inverse mean of  $\tau_{L,a-ISO}^p$  and  $\tau_{L,a-ISO}^q$  is taken as the final mixing time.

Strict care is needed in the selection of the particle number and the parameters for the mixing model, since challenging flow conditions, such as local extinction or re-ignition, can only be adequately reproduced in a sparse context if the models are used in an appropriately consistent manner. For example, local extinction effects can be significantly overestimated if a few particles in a sparse simulation would obtain a less combustible composition and as a consequence this would lead to global extinction.

#### 3.2.4.4 Density coupling

Since in transported PDF models the reactive scalars are computed on the stochastic Lagrangian particles and not on the Eulerian grid a density feedback is required for the computation of the underlying velocity and reference variable fields. In this way, PDF methods usually suffer from stability problems due to their stochastic nature. Since sparse-Lagrangian PDF methods deliver only a weak approximation of the reactive scalar field and very few particles are available for the reconstruction of the Euler fields, the stability problem is exacerbated. At this point the characteristics of the generalised MMC method can be taken advantage of again by using the reference variables to calculate conditional means of the reactive scalars for a subsequent density calculation.

The equivalent enthalpy method [141] was developed to obtain the scalar fields from the Lagrangian scheme by solving additional transport equations. The correct scalar composition is solved for on the Lagrangian particles and an equivalent composition on the Eulerian grid can be reconstructed using the reference variables. Once the equivalent composition  $\phi_\alpha^E$  on the Eulerian scheme is known, the Eulerian density can be calculated by applying the gas equation of state. The

transport equation of the equivalent composition is given by

$$\frac{\partial \bar{\rho} \tilde{\phi}_\alpha^E}{\partial t} + \frac{\partial \bar{\rho} \tilde{u}_j \tilde{\phi}_\alpha^E}{\partial x_j} - \frac{\partial}{\partial x_j} \left( \left( \frac{\mu}{\sigma_\alpha} + \frac{\mu_{sgs}}{\sigma_{sgs}} \right) \frac{\partial \tilde{\phi}_\alpha^E}{\partial x_j} \right) = \bar{W}_\alpha^E, \quad (3.46)$$

where the source term accounts for the relaxation of the equivalent composition field to the Lagrangian composition through

$$\bar{W}_\alpha^E = \bar{\rho} \frac{\langle \tilde{\phi}_\alpha^E | \tilde{\phi}_c \rangle - \tilde{\phi}_\alpha^E}{\tau_{rel}} \quad (3.47)$$

and  $\langle \tilde{\phi}_\alpha^E | \tilde{\phi}_c \rangle$  being the Favre-filtered equivalent composition conditioned on the set of reference variables. The relaxation time occurring in the denominator depends on the problem under investigation and is usually defined as  $\tau_{rel} = 10 - 50 \Delta t$ . The problem is now shifted towards the determination of the conditioned equivalent composition field  $\langle \tilde{\phi}_\alpha^E | \tilde{\phi}_c \rangle$  and two possible solutions will be discussed in Chapter 4.2.1.

### 3.3 Modelling of aerosol dynamics

This section aims at describing the modelling of aerosol dynamic processes, such as particulate formation, particulate dispersion, inter-particulate interactions and the interaction of particulates with the surrounding gas phase. This research area has received much attention not only in atmospheric environmental research due to global warming, but also in chemical engineering due to stricter legislation regarding pollutant emissions. Besides the particulate dispersion, aerosol dynamics include particulate formation (also referred to as nucleation for liquid particulate matter), surface growth (condensation) and shrinkage (evaporation), coagulation and breakage, and sintering.

Appropriate methodologies for the theoretical description of dynamic aerosol processes are the Direct Monte-Carlo method, where all particulates under consideration are resolved, and the population balance modelling (PBM), which intends to solve the population balance equation (PBE) in terms of the particulate number concentration. Typical examples of approaches to solve the population balance equation are the Method of Moments and the Sectional Method, whose advantages and disadvantages have been reviewed in [142, 63].

In this section, it will be explained why a solution through a Monte-Carlo method is not feasible for problems at laboratory scales. Furthermore, generally applied solution methods for the PBE together with common models for the description of particulate nucleation, surface growth and agglomeration are presented. This is followed by a description of the integration of aerosol modelling into the MMC framework.

### 3.3.1 Direct Monte-Carlo methods

The direct Monte Carlo method aims to describe the entire polydispersed aerosol phase so that the evolution of each (primary) particulate is resolved in space and time by a stochastic process such as Brownian movement. A common assumption in direct Monte Carlo methods is that a primary particulate adheres rigidly to the solid target agglomerate at the first point of contact. Since the positions of the individual primary particulates within an agglomerate are thus also known, this approach allows a precise insight into the instantaneous morphological structure of all particulates as well as into the particulate history. With this knowledge, important parameters such as the fractal dimension, the collision diameter or even the chemical composition of each individual agglomerate can be determined. This enables a very simple description of surface reactions or particulate dispersion, which in the case of larger particulates is mainly determined by inertial effects.

Mitchell & Frenklach [143, 144] developed a direct Monte Carlo method which accounts for agglomeration and surface growth and showed that the fractal dimension is significantly altered when these phenomena occur. A direct Monte Carlo method involving aggregation and sintering is performed by [145], where the primary particulates rigidly stick at first contact to the target agglomerate and the sintering is rendered by a change in the surface-to-volume ratio. Gutsch [146] investigated the collision frequencies of agglomerates, since this information is very helpful in aerosol simulations based on statistical approaches in which the particulate number density is a key quantity of consideration.

Solving the dynamic equation of motion for each particulate for a laboratory-sized problem implies that an enormous number of differential equations must be solved simultaneously to adequately describe the particulate size distribution. This is not practical even with modern computing capacities. Therefore, the direct Monte Carlo method is mostly limited to generic or academic problems, which are investigated in order to deepen the understanding of the underlying particulate-related phenomena. This information can then be used in statistical approaches whose range of applications is much broader.

### 3.3.2 Population balance equation modelling

Various methods have been developed for solving the population balance equation, the most established being the method of moments and the sectional method, which has been reviewed in the publications of Rigopoulos [16, 17, 18] on which the relevant sections are based.

### 3.3.2.1 Moment methods

The Method of Moments is one of the earliest and the most widespread approaches to solve the PBE and its mathematical development was largely driven by Hulbert & Katz [8]. Due to its relatively simple mathematical methodology and its excellent performance in terms of the computational resources required, the method of moments is one of the most commonly used techniques in connection with CFD applications aiming at solving the PBE. The key feature of the Method of Moments is the transformation of the PBE into a set of ODEs for the dynamic evolution of the moments. The knowledge of all moments is equivalent to the knowledge of the entire particulate size distribution. However, for most applications it is sufficient to consider only a few moments to solve the problem under consideration. The numerical efficiency of the Method of Moments originates from replacing the infinite number of differential equations to be solved by a small number of equations for the corresponding moments. Such an approach implies an inherent loss of information, since it is not the distribution itself that is represented, rather only some of its integral properties, which are nevertheless often sufficient to describe the problem with adequate accuracy. Usually the first four moments are of interest in synthesis investigations. The zeroth moment corresponds to the particulate number density, the first moment is proportional to the particulate size, the second moment is proportional to the particulate surface area and the third moment is proportional to the total particulate volume per unit gas volume.

In the general case where the growth and agglomeration is an arbitrary function of particulate size, a suitable particulate size distribution must be assumed since the growth and agglomeration terms include the unknown distribution  $n(v, x, t)$ . This is one of the major drawbacks of the Method of Moments. Size-independent surface growth is only present under very contrived conditions and the assumption of linear-dependent surface growth unnecessarily limits the application range of the method. The same applies to the agglomeration modelling which similarly involves the unknown particulate size distribution. This disadvantage can be overcome by assuming a constant collision kernel [147], but this is not an acceptable assumption for most cases.

The characteristics of the moment method are that not the particulate size distribution itself but specific moments are preserved and for a general treatment of surface growth and agglomeration the system is not closed and can only be inferred via an assumed particulate size distribution. A large variety of approaches has been developed to close the moment equations, which includes (i) presuming the particulate size distribution [148, 147] (ii) Taylor series expansion of the particulate number density [8] (iii) deriving the fractional moments by interpolation [149] and (iv) approximating the moment integrals with numerical quadrature [150].

### 3.3.2.2 Sectional methods

Sectional methods, which are often also referred to as discretisation methods, are based on a discrete representation of the continuous particulate size distribution, which can be divided into a finite number of intervals along the particulates internal size space. The individual discretisation intervals may be of different widths, so that a very large scale range in the particulate size space can be covered with relatively few sections, possibly covering several orders of magnitude. There are several challenges associated with developing a reliable discretisation method for the PBE, as it is an integro-differential and non-linear function. The advantage of a wide scale coverage also brings some difficulties that need to be addressed. On the one hand, particulate formation appears as a local source term at the lower end of the size scale space, while coagulation is a source term operating over the entire scale space [18]. The coagulation source term contains integral operators, which consequently leads to a non-local discretisation that requires many operations on the entire size spectrum. Furthermore, in selecting the discretisation method of the coagulation terms, it is important to ensure that it is conservative with respect to the moments on a non-uniform grid. Due to its first-order hyperbolic nature, some numerical challenges must also be overcome with respect to the size growth term, as it can produce sharp fronts in the solution of the particulate size distribution. A vast plethora of discretisation methods has been developed to solve aerosol related problems within the chemical engineering and combustion research community.

Gelbard *et al.* [151] proposed a numerical solution of the PBE where the particulate size distribution is approximated by a piecewise constant function. The representation of the particulate size distribution via a stepwise constant function allows the integration term to be converted into a product of particulate concentrations and pre-integrated coagulation kernels. The method was originally developed to model pure coagulation, but was later extended to growth processes by Gelbard & Seinfeld [151]. Due to the relatively straightforward procedure and conservative characteristics, this model has been successfully used to predict soot size distributions in laminar premixed flames [152] and laminar diffusion flames [153, 154, 155].

An even simpler approach is to consider the particulate size distribution as a finite set of delta functions at fixed nodes. This method is often referred to as nodal form of the sectional approach. The major advantage of this method is the high efficiency, as integrations of the coagulation kernel function now effectively reduce to a simple summation of the components at the respective nodes. This peculiarity can be illustrated more clearly by examining the coagulation source

term for the size scale range  $(v_i - \delta v_i/2, v_i + \delta v_i/2)$ , which becomes

$$\int_{v_i - \delta v_i/2}^{v_i + \delta v_i/2} \beta(v - v', v') N(v - v', t) N(v', t) dv' \approx \sum_j \chi_{ijk} \beta_{ij} N_i N_j, \quad (3.48)$$

with  $v_k + v_j = v_i$  and the function  $\chi_{ijk}$  being a size dependent splitting operation correction factor required for this specific approximation scheme. This correction factor is necessary because in general the sum of the volumes  $v_k + v_j$  does not coincide exactly with one of the other volumes, unless a uniform grid is selected. Accordingly, the imaginary formed particulate needs to be weight-distributed to the two adjacent volumes which is illustrated in Fig.3.1. The size dependent

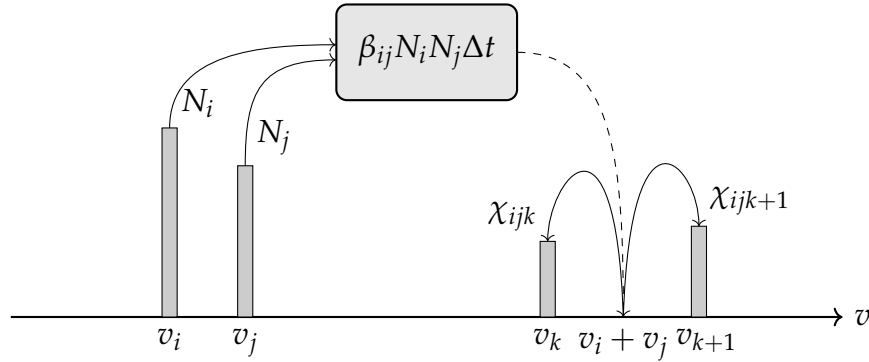


Figure 3.1: Illustration of the distribution of coagulated particulates to the two adjacent sections. (Sketch following Prakash *et al.* [156])

splitting operator correction factor  $\chi_{ijk}$  takes the form

$$\chi_{ijk} = \begin{cases} \frac{v_{k+1} - (v_i + v_j)}{v_{k+1} - v_k} & : \text{if } v_k \leq v_i + v_j \leq v_{k+1}, \\ \frac{(v_i + v_j) - v_{k-1}}{v_k - v_{k+1}} & : \text{if } v_{k-1} \leq v_i + v_j \leq v_k, \\ 0 & : \text{otherwise.} \end{cases} \quad (3.49)$$

for a two-point method, for example described by Prakash *et al.* [156], but may be of different appearance for other approaches.

Thus, the purpose of the correction factor is it to preserve the moments of the particulate size distribution and an comprehensive formulation will be given further below. The model has difficulties in the correct reproduction of surface processes in which there is an increase or decrease in particulate size. For example, provided pure surface growth is considered, a uni-modal particulate distribution should be conserved under homogeneous conditions. However, the distribution of the particulates to the two adjacent nodes results in a purely numerically-induced broadening of the PSD. This effect can be counteracted by increasing the grid points used, but this negates the high efficiency as a major advantage of the method. Thus, when choosing the number of grid points, efficiency considera-

tions must be weighed against losses of accuracy. The nodal form of the sectional approach was first proposed by [157] and applied to aerosol problems including particulate formation, surface growth and coagulation by [158, 159, 160].

A more sophisticated discretisation method was proposed by Kumar & Ramkrishna [161, 162] in which a finite set of algebraic equations is solved in order to conserve any two moments on an arbitrary grid. Park & Rogak [163] advanced the model so that even three moments can be obtained and applied their method to a problem on aerosol modelling of coagulation and volumetric surface growth. The model was then successfully validated on laminar premixed [164] and diffusion flames [165, 166, 167, 168] to predict soot particulate distributions.

Another method to approximate the particulate size distribution is based on the finite element method, where higher order trial functions are adopted to represent the distribution within each element. Gelberd & Seinfeld [169] applied cubic splines as trial functions, but also linear trial functions [170] or methods based on the Galerkin framework [171, 172] are possible. A methodology based on the finite volume method for the approximation of the piecewise constant particulate size distribution on an arbitrary grid was proposed by Liu & Rigopoulos [173].

As mentioned above, modelling the surface growth term features some difficulties, since the first-order derivative in particulate size space introduces the hyperbolic characteristic of the population balance equation. To overcome these difficulties related to numerical diffusion in particulate size space, several concepts have been developed in the literature, including the use of (i) high-resolution fixed grids [174, 175], (ii) the moving grid methods [176, 177] and (iii) the adaptive grid methods [178], where that latter has been successfully applied to a turbulent sooting diffusion flame [179, 180].

If not only spherical particulates are to be considered, but also the change in the morphological structure is to be simulated, further challenges arise for the discretisation method. The simplest and most efficient way of considering the morphological structure is to discretise the particulate size space by applying the power law for agglomerates, cf. Eq. (2.23). There are some non-trivial modifications to the structure of the collision kernel, which will be discussed in more detail below. Furthermore, the prediction of the particulate surface needs particular attention. For example, surface growth must be considered as integral growth, so that surface reactions or deposits lead to an overall increase in particulate volume and the other parameters describing the morphology, such as the fractal prefactor and the fractal dimension, remain unchanged. This approach can only be justified if the change in particulate size space due to surface growth is much smaller than other processes, such as coagulation. If measurement data about the morphological structure of the particulates as a function of size are available [181], better estimates of the particulate surface can be obtained via correction functions [51].

A more sophisticated approach is to employ two one-dimensional discretisa-

tions for the particulates, one for the particulate volume and one for the particulate surface area as proposed by Jeong & Choi [182]. There, a comparison with the a two-dimensional discretisation of the PBE showed good results for the prediction of silica and titania particulate size distributions. While this approach is much more efficient than a two-dimensional discretisation the computational effort is still relatively high.

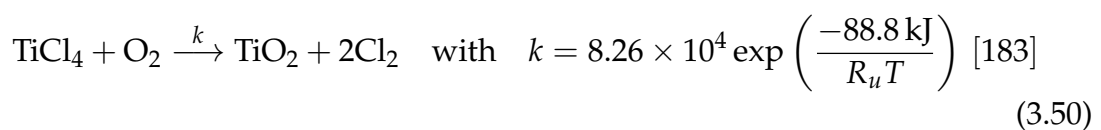
A more recent methodology to approximate the particulate size distribution was proposed by Yang & Mueller [52], where a so called Multi-Moment Sectional Method (MMSM) is used to combine the advantages of both, the moment methods and sectional methods, respectively. Here, statistical moments are solved within a finite number of section and a polynomial profile is adopted to reconstruct the particulate size distribution within them. In two extreme cases the MMSM can be reduced to a conventional moment method if only one section is used and can be converted to a conventional sectional method when the number of solved moments per section is one. The MMSM was applied to a laminar sooting diffusion flame for modelling spherical soot particulates [52] and it was shown that the MMSM can increase the accuracy in contrast to conventional sectional methods by equal computational costs and that the quality of results increase by increasing the number of sections although some difficulties arise by interpreting the PSD due to their discontinuous shape.

### 3.3.3 Aerosol dynamic modelling

Now that the numerical techniques for modelling the evolution of the PBE have been presented, there only remains the modelling of the individual aerosol-related processes, such as particulate formation, surface growth and coagulation. The remaining processes, such as fragmentation and sintering, are outside the scope of this thesis and will not be discussed here. Since flame synthesis of solid particulates with fractal morphology is the main feature of this work, the modelling aspects are therefore limited to solid particulates and the aerosol processes of liquid particulates are presented in the relevant passages.

#### 3.3.3.1 Particulate Formation

Particulate formation, which in the context of solid particulates is often referred to as particulate inception, usually occurs at the lower end of the particulate size spectrum and can either be described by a global one-step chemical reaction, e.g.



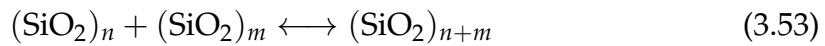
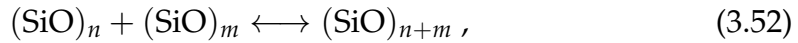
for the inception of titania particulates, or the particulate inception is determined by a detailed finite-rate chemistry reaction mechanism, where the production rate of incipient particulates is usually given by an irreversible reaction involving the precursor species at the end of the reaction chain [34, 45, 184, 179, 42].

The newly formed particulates are primary particulates and therefore added to one of the first sections of the discretised particulate size distribution. The volumetric size of this section is determined by the size of the solid species molecule, which is assumed to be spherical:

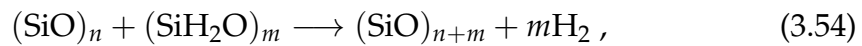
$$v_0 = \frac{M_s}{\rho_s N_A} . \quad (3.51)$$

It is important to note, that particulate inception only increases the total number of particulates.

This particulate inception shall be illustrated by the flame synthesis of silica particulates, where the formation is purely determined by the underlying chemical reactions. Here, the finite rate chemical reaction mechanism proposed by Suh *et al.* [45, 184] with 67 chemical species and 264 reactions, presented in Appendix A, was used for the prediction of silica particulates<sup>2</sup>. The core of the reaction mechanism is based on preceding studies [185, 186, 187] and Suh *et al.* [184] identified SiO, SiO<sub>2</sub>, SiH<sub>2</sub>O and HSiOOH as the four silicon-containing species that contribute most to the clustering process for the formation of particulates. Subsequently, there is a first set of reversible self-clustering reactions of SiO and SiO<sub>2</sub> given by



with  $1 \leq n \leq 9$ ,  $1 \leq m \leq 9$  and  $n + m \leq 10$ . This is followed by a second set of irreversible reactions which include the contribution of the species SiH<sub>2</sub>O and HSiOOH



Suh *et al.* [184] assumed that the formation reactions of species with more than ten silicon atoms are irreversible and counted them as particulates. Thus, their inception rate is given by the sum of their production rates and solid particulates were no longer considered as gas molecules. Suh *et al.* [184] further discussed that the truncation point of ten silicon atoms is arbitrary and pointed out that for

<sup>2</sup>I would like to thank Dr. Michael R. Zachariah (University of Maryland, USA) for providing the original chemical reaction mechanism for silica oxidation.

the pressure range considered, the monomers of SiO and SiO<sub>2</sub> are already above the critical nuclei size, but a significant amount of chemical information would be lost as the chemical mechanism is more accurate than the aerosol dynamics. As uncertainties in the enthalpies of formation increase for species containing more than ten silicon atoms, the truncation point of ten represents a compromise between chemical uncertainties and aerosol dynamic shortcomings [184].

The applied particulate inception method is compared against *perfectly stirred reactor* simulations published by Suh *et al.* [45] using the same reaction mechanism which is used in this study. In Fig. 3.2 the particulate nucleation rate and the particulate number density are shown, respectively. One can see that the onset of particulate nucleation is reasonably predicted, although the maximum is somewhat overestimated. Larger differences appear for the region of decaying

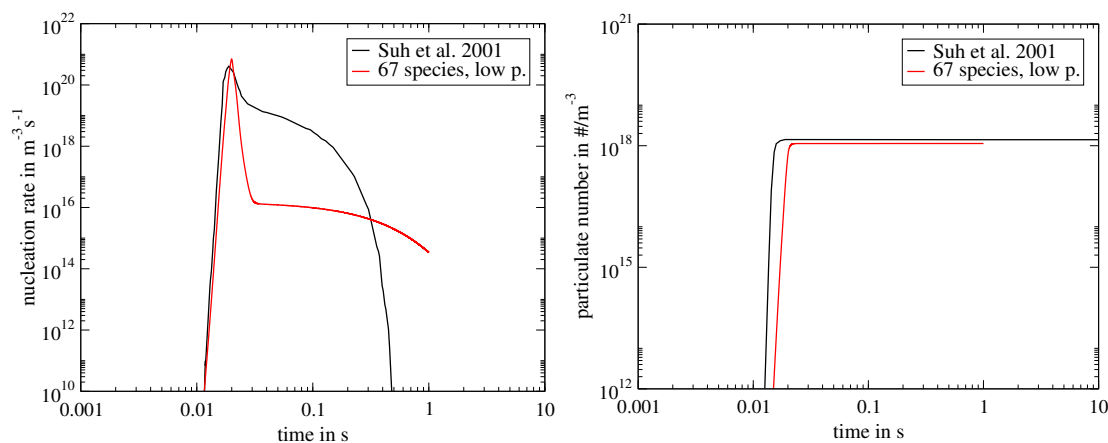


Figure 3.2: (left) Particulate inception rate and (right) particulate number density for perfectly stirred reactor simulations at  $T = 773 \text{ K}$ ,  $p = 107 \text{ Pa}$  and a  $\text{O}_2$  to  $\text{SiH}_4$  ratio of 15.

inception, where the largest fraction of the precursor species has already been converted. This can mainly be attributed to the unknown thermodynamic data of the species, which were not published in Suh's study, as sensitivity studies confirm. Here, only the chemical reaction mechanism is available without the JANAF polynomial parameters and a custom set of JANAF polynomials taken from the NIST database has been used, see Appendix A. The general time dependence of the particulate number density is consistent with the nucleation rate observations. Here, the particulate number density calculated by Suh *et al.* [45] increases faster, which is due to the steeper increase in the nucleation rate, and a corresponding particulate number density is achieved with the chemical reaction mechanism used here. Overall, in the complex Si-O-H system, a reasonable agreement of the inception rate is observed, which is considered to be sufficiently captured to calculate reactive particulate synthesis processes in diffusion flame simulations.

### 3.3.3.2 Surface growth

Surface growth occurs when a molecule from the gas phase collides with a particulate and sticks to it, thus increasing its mass. The volume of the particulate formed is the sum of the volume of the depositing molecule and that of the particulate. For high Knudsen numbers, the rate of the process is based on the free molecular collision kernel and, following Shekar et al. [46], the size dependent growth rate of the particulate takes the form

$$G_{v,i}^{fm} = 2.2\alpha C \frac{M_{\text{dep}}}{\rho_{\text{dep}}} \sqrt{\frac{\pi k_B T}{2m}} (d + d_{c,i})^2, \quad (3.56)$$

where  $C$ ,  $M_{\text{dep}}$ ,  $\rho_{\text{dep}}$ ,  $m$  and  $d$  are the gas phase concentration, molecular weight, density, monomer mass and collision diameter of the depositing species, respectively. Furthermore,  $d_c$  is the collision diameter of the particulate and  $\alpha$  is the collision efficiency, which is a parameter set in the range from zero to one. The collision diameter of the depositing species,  $d$ , is assumed to be the diameter of a spherical molecule (fractal dimension  $D_f = 3$ ). Following the power law of agglomerates, the collision diameter of the particulate in section  $i$ ,  $d_{c,i}$ , is calculated as

$$d_{c,i} = d_{p,0} N_i^{1/D_f}, \quad (3.57)$$

with  $N_i$  being the number of primary particulates within the agglomerate, calculated by  $N_i = v_i/v_0$ .

For molecules depositing on large particulates whose Knudsen numbers are smaller than 1, Eq. (3.56) does not apply, since particulate growth is diffusion-limited, i.e. determined by the rate at which the surface-growth-relevant species diffuse towards the particulate's surface, which can be modelled by

$$G_{v,i}^{dl} = D_{\text{dep}} Y_{\text{dep}} \frac{a_{p,i}}{d_{p,i}/2}, \quad (3.58)$$

where  $D_{\text{dep}}$  is the diffusion of the surface-growth-relevant species calculated by the Chapman-Enskog theory,  $Y_{\text{dep}}$  is the mass fraction of the depositing species in the close vicinity of the particulate and  $a_{p,i}$  is the surface area of the particulate. In order to use both approaches in the respective valid regime, a harmonic mean formulation is used

$$G_{v,i} = \frac{G_{v,i}^{fm} G_{v,i}^{dl}}{G_{v,i}^{fm} + G_{v,i}^{dl}}. \quad (3.59)$$

In Fig. 3.3, the surface growth rate versus particulate diameter is shown and different slopes for the free-molecular and diffusion-limited growth formulations can be observed. For both very small and very large particulates, the volumetric growth rates differ by more than three orders of magnitude, showing that the application of a singular growth formulation is insufficient. The harmonic mean formulation provides a good prediction for the whole particulate size range, albeit with a slight underestimation of size growth in the transition area, which is typical for harmonic means [188].

Particulate growth conserves the number of particulates and only results in increased surface and volume fractions. Due to the surface growth, the particulates are shifted in sections towards the upper end of the discretisation. For fixed grid resolutions, the grown particulates usually have to be distributed between the two adjacent sections, which can be modelled by a two-point or three-point [163, 160] formulation.

### 3.3.3.3 Coagulation

Coagulation, also often referred to as agglomeration, is a process where two particulates collide and form a larger particulate. The particulate number density thus decreases due to coagulation. The coagulated particulate has the same volume and primary particulate number as the sum of the two colliding particulates, therefore conservation of mass applies. Although the fractal dimension of the particulates may indeed change under the coagulation process, it is a common as-

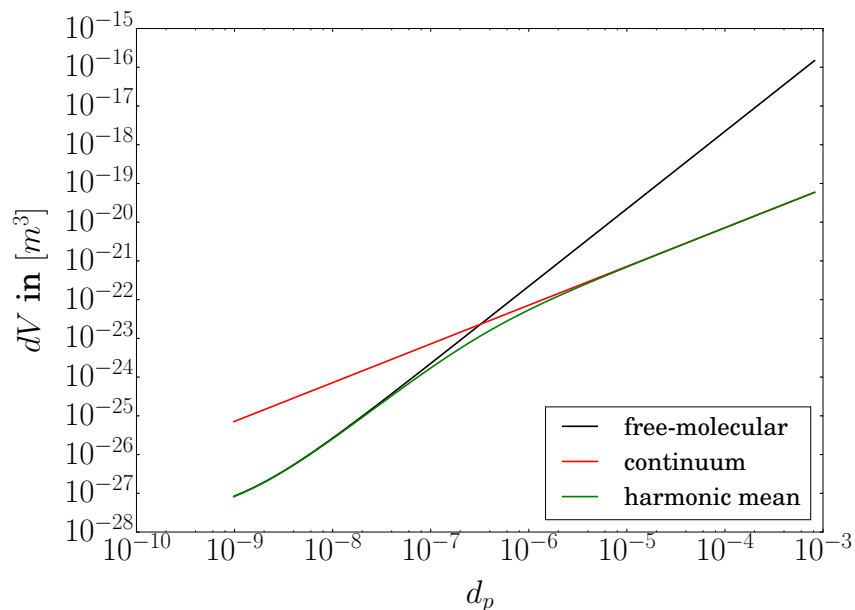


Figure 3.3: Volumetric surface growth rate for particulates of size  $d_p$  using different growth rate formulations at  $T = 800$  K in a  $\text{SiO}_2\text{-N}_2$  mixture for a depositing species mass fraction of  $Y_{\text{SiO}_2} = 2 \cdot 10^{-5}$ .

sumption that it remains constant [12]. The rate at which the particulates collide is described by the coagulation kernel and a plethora of different formulations are available in the literature [189, 190, 191, 65, 192], which has been reviewed in [193]. The agglomeration is a highly non-linear process as it is strongly dependent on particulate size, particulates fractal dimension and particulate number density. As with surface growth, there is a different formulation for the coagulation kernel for the free-molecular and continuum regime. Depending on the Knudsen number, the following formulas for spherical particulates are available [12]

$$\beta_{ij} = \begin{cases} \left( \frac{3}{4\pi} \right)^{\frac{1}{6}} \left( \frac{6kT}{\rho_s} \right)^{\frac{1}{2}} \left( \frac{1}{v_i} + \frac{1}{v_j} \right)^{\frac{1}{2}} \left( v_i^{\frac{1}{3}} + v_j^{\frac{1}{3}} \right)^2 & : \text{Kn} > 1, \\ \frac{2kT}{\mu} \left( \frac{1}{v_i^{\frac{1}{3}}} + \frac{1}{v_j^{\frac{1}{3}}} \right) \left( v_i^{\frac{1}{3}} + v_j^{\frac{1}{3}} \right) & : \text{Kn} \leq 1, \end{cases} \quad (3.60)$$

with  $k$  being the Boltzmann constant. Since Eq. (3.60) is valid for spherical particulates only, some modifications have been proposed to model the coagulation of fractals [30, 12]. The coagulation kernel of particulates with fractal dimension  $D_f$  then reads

$$\beta_{ij} = \begin{cases} \left( \frac{3}{4\pi} \right)^{\lambda} a_0^{2-\frac{1}{D_f}} \left( \frac{6kT}{\rho_s} \right)^{\frac{1}{2}} \left( \frac{1}{v_i} + \frac{1}{v_j} \right)^{\frac{1}{2}} \left( v_i^{\frac{1}{D_f}} + v_j^{\frac{1}{D_f}} \right)^2 & : \text{Kn} > 1, \\ \frac{2kT}{\mu} \left( \frac{1}{v_i^{\frac{1}{D_f}}} + \frac{1}{v_j^{\frac{1}{D_f}}} \right) \left( v_i^{\frac{1}{D_f}} + v_j^{\frac{1}{D_f}} \right) & : \text{Kn} \leq 1, \end{cases} \quad (3.61)$$

with  $\lambda = \frac{2}{D_f} - \frac{1}{2}$  and valid for fractal dimensions larger than  $D_f = 2.0$  [194]. Equation (3.61) is a general formulation as it reduces again to Eq. (3.60) for  $D_f = 3$ . For modelling coagulation for the entire size space, Fuchs [192] proposed a superior formulation than a simple harmonic mean blending which takes the form

$$\beta_{ij} = 2\pi(D_i + D_j)(d_{c,i} + d_{c,j}) \left[ \frac{d_{c,i} + d_{c,j}}{d_{c,i} + d_{c,j} + 2\sqrt{g_i^2 + g_j^2}} + \frac{8(D_i + D_j)}{(d_{c,i} + d_{c,j})\sqrt{c_i^2 + c_j^2}} \right]^{-1}, \quad (3.62)$$

with the transition parameter

$$g_k = \frac{(d_{c,k} + L_k)^3 - (d_{c,k}^2 + L_k^2)^{\frac{3}{2}}}{3L_k d_{c,k}} - d_{c,k}, \quad (3.63)$$

where  $L_k$  is the mean free path given by

$$L_k = \frac{8D_k}{\pi c_k} \quad (3.64)$$

and  $c_k$  being the particulate velocity

$$c_k = \sqrt{\frac{8k_B T}{\pi m_s}}. \quad (3.65)$$

In the above equations  $D_k$  is the particulate diffusivity, whose calculation is given by the theory of Einstein-Smoluchowski [195]

$$D_k = \frac{k_B T}{3\pi\mu d_{c,k}} C_S \quad (3.66)$$

with the Cunningham correction factor [196]

$$C_S = \frac{5 + 4\text{Kn}_k + 6\text{Kn}_k^2 + 18\text{Kn}_k^3}{5 - \text{Kn}_k + (8 + \pi)\text{Kn}_k^2} \quad (3.67)$$

which accounts for the inaccuracy of the Einstein-Smoluchowski theory for particulate scales in the order of the mean free path of the gas phase molecules.

Figure 3.4 illustrates the dependences of the collision rates of the different collision kernels on the particulate diameter and highlights the excellent blending of the collision kernel proposed by Fuchs *et al.* [192] between the free-molecular and the continuum regimes.

The validation of the current implementation of the coagulation process can be done by comparing results with numerical data published by Wu & Friedlander [194]. There Direct Monte Carlo simulations of particulates with different fractal dimensions have been conducted for the prediction of the self-preserving size distribution which was discretised with 40 sections and coagulation kernels for the free-molecular and continuum regimes have been applied. Figure 3.5 presents normalised particulate number densities for calculations of coagulation of particulates with two different fractal dimensions.

The sectional method can reproduce the decay of the particulate number with almost perfect agreement. Assuming a self-preserving size distribution, the slope of the decay can be calculated analytically to -2 and -6/5 for  $D_f = 2$  and  $D_f = 3$  [194], respectively, and these slopes were precisely reproduced.

Figure 3.6 shows the time evolution of the mass mean diameter for pure coagulation of particulates with different fractal dimensions ranging from  $D_f = 2$  to  $D_f = 3$ . Although some odd artefacts of the shape of the mass mean diameter evolution are presets for very small times the data enables the validation of coagulation differently shaped particulates.

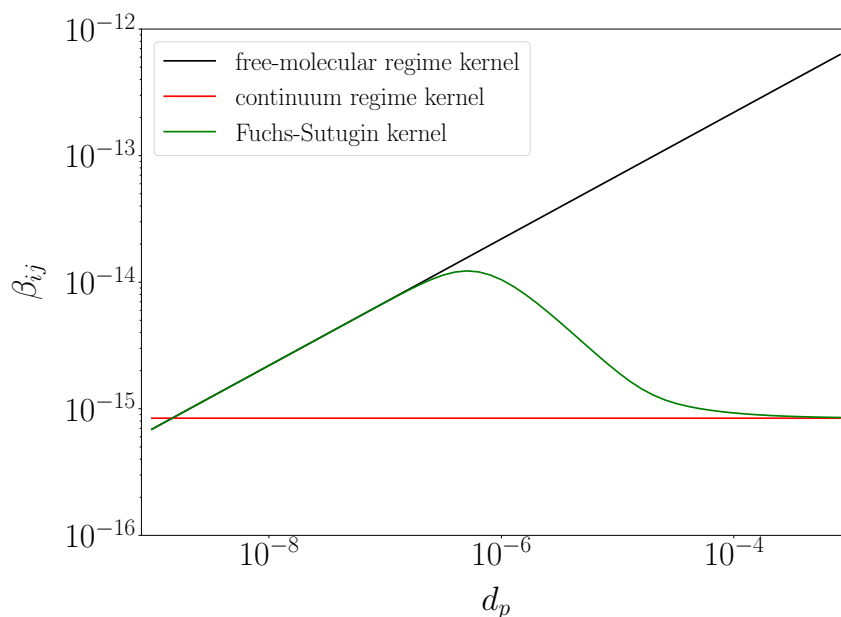


Figure 3.4: Dependence of the collision kernel on particulate size  $d_p = d_{c,i}$  and fixed size  $d_{c,j}$  for the different kernel formulations at  $T = 800$  K and a gas phase of pure nitrogen.

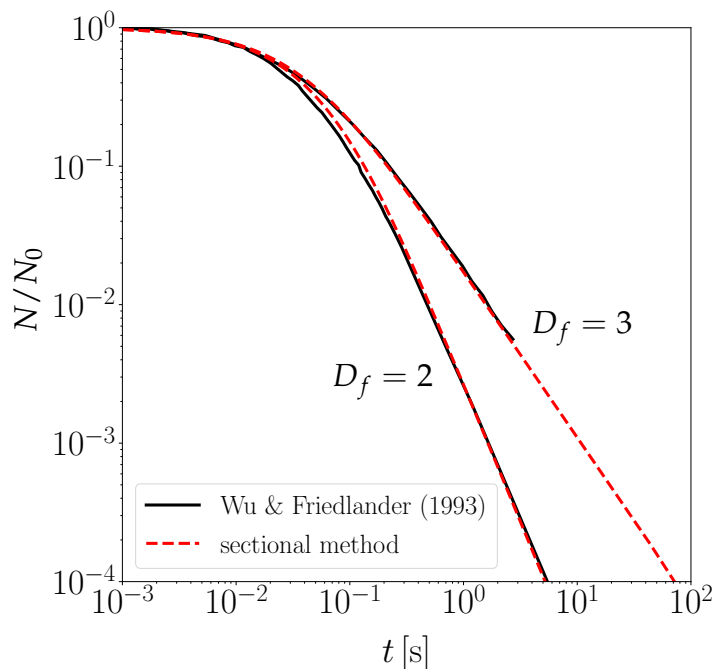


Figure 3.5: Decay of normalised particulate number density assuming different fractal dimensions for conditions of  $d_0 = 10$  nm,  $N_0 = 1 \cdot 10^8$  m<sup>-3</sup>,  $T = 1500$  K and  $\rho_s = 2000$  kg/m<sup>3</sup> [194].

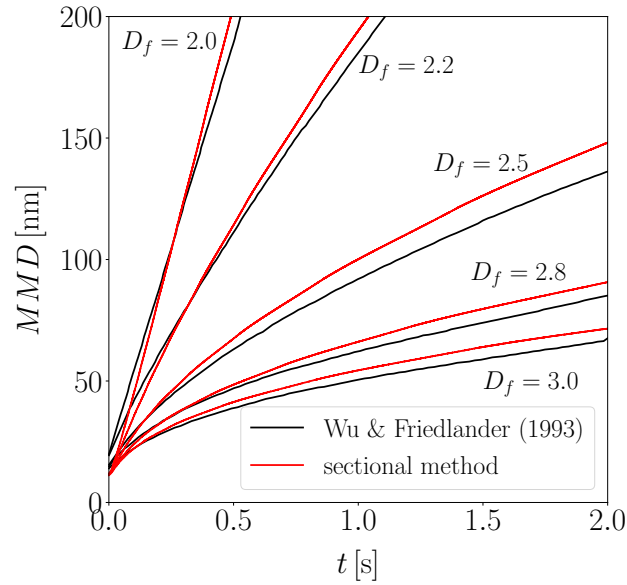


Figure 3.6: Time evolution of mass mean diameter for particulates with different fractal dimensions for conditions of  $d_0 = 10 \text{ nm}$ ,  $N_0 = 1 \cdot 10^8 \text{ m}^{-3}$ ,  $T = 1500 \text{ K}$  and  $\rho_s = 2000 \text{ kg/m}^3$  [194].

Comparing numerical results with data obtained using the sectional method, it can be seen that although the results do not perfectly match the original data, the correct trend may indeed be correctly reproduced. Mass mean diameter may slightly be over-predicted but more consistent data have been obtained with the sectional method at the beginning of the coagulation process for times lower than  $t = 0.2 \text{ s}$ .

A validation setup involving both inception and coagulation has been presented in Suh *et al.* [45] for data obtained with a moment method for spherically shaped particulates assuming a log-normal size distribution. Here, Fig. 3.7 compares the evolution of particulate number densities for numerical data obtained by Suh *et al.* [45] with a sectional method. The results presented in Fig. 3.7 are in line with observations for the inception rate, which have been discussed above. The particulate number density increases somewhat later, as inception is also predicted at a later stage. Since the peak of the inception rate for the sectional method is slightly higher compared to Suh *et al.* [45], the maximum of the particulate number density becomes also higher.

Once a certain threshold of particulate number density is reached, gradually increasing coagulation leads to a decrease of the particulate number density. The bulge in the numerical reference data stems from the persistent inception process, which cannot be reproduced with the applied reaction mechanism and thus does not occur within the method presented here. More interesting is the slope at which the particulate number density is decreasing: For times larger than one second, the graphs show the same slope, indicating that coagulation is correctly

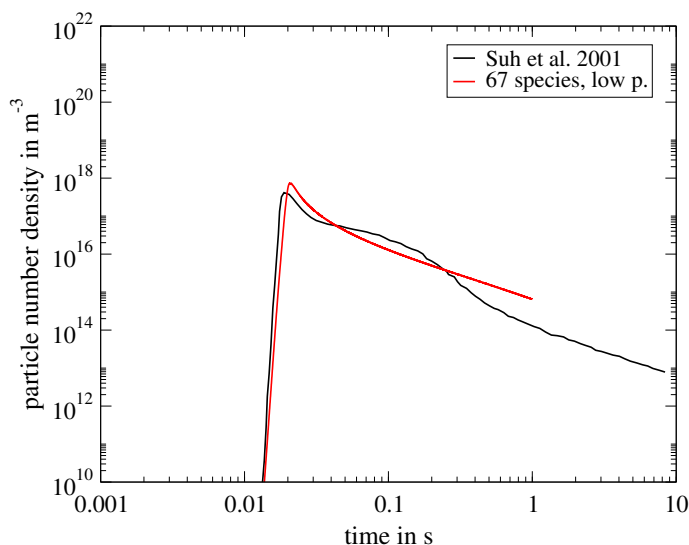


Figure 3.7: Time evolution of particulate number density for perfectly stirred reactor simulations at  $T = 773\text{ K}$ ,  $p = 107\text{ Pa}$  and a  $\text{O}_2$  to  $\text{SiH}_4$  ratio of 15.

predicted, as inception is no longer the predominant factor.

The comparison with different numerical reference results allows the implemented coagulation process to be considered reliable even under the influence of varying fractal dimensions and to be used for further analyses.

### 3.3.4 Incorporation into the sparse-Lagrangian MMC framework

This section aims to show how the population balance transport equation for turbulent flows can be coupled to a flow solver. The aerosol dynamic processes significantly depend on the precursor chemistry and thus also on the quality of their prediction. For this reason, it is important to use a comprehensive framework that can capture turbulence-chemistry interactions as well as turbulence-aerosol interactions in an accurate way. Modelling turbulence-aerosol interactions is challenging since, as with chemistry-turbulence interactions, highly non-linear terms describing the inception, growth and coagulation processes occur, which are unclosed under averaging approaches for RANS and filtering operations for LES. As outlined in the study of Rigopoulos [16] the correlations which arise by the coupling to a turbulent flow solver can be categorised into three types as follows:

- (i) correlation between reactive scalars, e.g. inception term,
- (ii) correlation between reactive scalars and number density, e.g. growth term,
- (iii) correlation between number densities, e.g. coagulation term.

The correlation of type (i) is of the same character as the chemical reaction source terms for the species transport equations. Correlations of type (ii) and (iii) are

unique to turbulent flows involving aerosol dynamics and closure models are required for the correct treatment of growth and coagulation processes.

Attempts to describe the aerosol processes in turbulent flows were based on the eddy dissipation model [197, 198] and on the flamelet method [199, 200, 201, 202]. There, it was pointed out that the prediction accuracy of these approaches is limited, despite the good comparison with experimental data, and that higher quality techniques are required for a correct simulation of aerosol processes.

This has led to the development of transported PDF models including the mixture fraction, enthalpy and soot volume fraction [203]. In the context of a discretised PBE method the transported PDF model was applied to the prediction of particulate matter within a turbulent jet flow without chemical reactions [204]. While RANS approaches [201, 205, 206] had been in the focus in the past decades due to the limited computing capacities, the currently available computing resources also permit simulations based on LES [207, 43, 42, 179, 51, 208, 180, 41]. Kronenburg *et al.* [92] coupled the soot model of Leung *et al.* [209] to a CMC approach and showed that considering differential diffusion effects leads to a significant improvement with respect to the soot predictions. Some LES studies omit the correlations between turbulent scales and aerosol processes [36, 210], despite there is being clear evidence [38] that these correlations are of key importance for aerosol predictions.

Transported PDF models in combination with a stochastic Lagrangian particle method allow aerosol processes to be made accessible for turbulent simulations in a very straightforward manner, since the source terms, just like the reaction source term for the chemical species, are then available in closed form and can be calculated directly without further assumptions. Even for a traditional Lagrangian PDF method, the computational requirements are enormous if the discretised particulate size distribution is to be represented with a sufficiently high resolution in size space. As discussed in Sec.3.2.4.3, the sparse-Lagrangian stochastic particle method is an excellent way to reduce the computational burden to an acceptable level without compromising accuracy. The coupling is achieved by adding the sections of the discretised size distribution to the transported scalar vector

$$\phi_\alpha^p = (Y_1, \dots, Y_{n_s}, h, Z, N_1, \dots, N_{n_k}), \quad (3.68)$$

such that it now comprises the transported reactive species, the enthalpy and the discretised size sections for the approximation of the PSD. The temporal change of the scalar vector then becomes

$$d\phi_\alpha^p = [S_\alpha^p + M_\alpha^p + A_\alpha] dt, \quad (3.69)$$

where  $A_\alpha$  represent the aerosol dynamics, like particulate formation, volumetric

surface growth, coagulation and others if required. Aerosol dynamics such as particulate formation and surface growth are dependent on species composition and temperature, and this information is readily available on the stochastic particles, whose displacement can still be described by Eq. (3.26). This equation shows that a unified diffusivity ( $\mathcal{D} + \mathcal{D}_t$ ) is assumed for all elements of the scalar vector including the size sections. In the context of describing the diffusion of particulates, this is a major shortcoming, as particulate diffusion may differ by orders of magnitude compared to the gas phase diffusivity [12]. Consequently, the diffusivity of the particulates is overestimated, which can lead to a smoothing of local particulate accumulations, which in turn underestimates coagulation effects. If diffusion effects are negligible compared to convection, this assumption should not have a major impact and this aspect is discussed further below.

## Chapter 4

# Incorporation of polydispersed particulates simulation into a variable density flow solver

For the calculation of aerosol dynamics, e.g. nucleation processes or particulate flame synthesis, in turbulent reactive flames, the MMC model and the governing equations for the aerosol dynamic processes have been incorporated into the OpenFOAM solver collection. The purpose of this chapter is to describe the characteristics of the entire framework. Therefore, the OpenFOAM framework is first presented as a starting point for the further implementations followed by a description of the MMC-based solvers. Secondly, the numerical methods for density coupling and for generating suitable boundary conditions for turbulent jet investigations are presented.

### 4.1 OpenFOAM

OpenFOAM (Open Field Operation And Manipulation) is an open-source framework mainly used for the computation of CFD related problems and its initial version has been developed at Imperial College London [211, 212]. The governing equations are usually solved via the finite volume approach on unstructured grids, but in general OpenFOAM provides a powerful code basis for the numerical solution of partial differential equations. As the entry barrier for an efficient usage of OpenFOAM is very low, OpenFOAM enjoys a broad user community in both research and industry, which have intensively extended the applied solution methods and libraries over the past years. Especially in the turbulent flow and combustion modelling community, this has prompted many profound developments of methods, tools and solvers [213, 214, 215, 216, 217]. OpenFOAM

provides second-order numerical schemes for the finite volume-based terms for convection, diffusion and time derivatives and allows the deployment of complex boundary conditions.

## 4.2 Incorporation of the MMC method into the OpenFOAM framework

The favourable extension properties of OpenFOAM led to the incorporation of the generalised MMC method into a comprehensive RANS and LES solver framework of turbulent, reactive flows which was validated against numerous experimental investigations and DNS studies as presented in Galindo-López *et al.* [124]. The standard solver for the calculation of LES flows with variable density was extended to meet the requirements of the MMC method. Therefore the standard `particle` and `cloud` classes provided by the native OpenFOAM version form the starting point to add the desired functionalities. The `particle` class contains the basic variables and functionalities to perform a regular Lagrangian simulation that, through a particle tracking algorithm, allows stochastic particles to be deleted, pushed back or passed on when they encounter boundary or parallel processor patches.

The standard `cloud` is a container class that provides tools to delete and add the stochastic particles. Additionally, the numerical and physical features of the stochastic MMC model are added by nesting four template class layers, where each layer is derived from the previous layer inheriting its properties.

The four layers are denoted as `Advection`, `Thermo`, `Mixing` and `Reacting` and the line of inheritance is as follows:

$$\text{Reacting} \leftarrow \text{Mixing} \leftarrow \text{Thermo} \leftarrow \text{Advection} \leftarrow \text{particle} .$$

The `Advection` layer implements Eq. (3.26) and thus provides the transport of the stochastic particles in physical space. The remaining layers implement Eq.(3.69) and describe the evolution of the transported scalar space, where `Thermo` accounts for the allocation of the species and enthalpy, `Mixing` realises the mixing algorithm and `Reacting` processes the execution of the chemistry. For each class layer, so-called sub-models are available, which are abstract classes to include runtime selectable processes, so that for example the mixing operator can be optionally realised by a standard Curl or MMC-Curl model.

The MMC framework in the OpenFOAM library environment was tested against experimental data of the Sydney burner with inhomogeneous inlets [218] showing very good LES results for conditional and unconditional quantities [219]. The implementation of a RANS-based MMC method was validated by Varna *et al.* [220] against experimental measurements of the turbulent Sandia D flame configuration [221]. An assessment of mixing time scale models for the MMC method

was performed by Vo *et al.* [138] for a turbulent shear layer configuration, with validation data obtained using DNS. More recently, the MMC method has been extended to predict premixed combustion using a double-conditioned approach [222, 223] and its excellent performance has been validated against experimental data for the Darmstadt stratified flame configuration. The performance of the MMC method for the prediction of spray combustion has been tested by Sonthaimer *et al.* [224] and that for coal particulates by Zhao *et al.* [225].

The numerical sub-models employed for the density coupling and the mixing process as well as the provision of well-defined boundary conditions for turbulent jet flames warrant further attention and are therefore discussed below.

## 4.2.1 Density Coupling

Since the heat release due to the chemical reaction process resides on the side of the Lagrangian scheme, whereas the Favre-filtered governing equations are computed on the Euler fields, a density feedback from the stochastic particles to the Eulerian grid cells is required. Especially in a sparsely distributed particle method, a stable and reliable density feedback is not easy to achieve and two methods for the calculation of the conditional equivalent species  $\langle \tilde{\phi}_\alpha^E | \tilde{\phi}_c \rangle$  occurring in the source term of Eq. (3.47) will be described in the following.

### 4.2.1.1 FlameletCurves

The `FlameletCurves` approach implements the method presented in Cleary & Klimenko [96] which is based on the ideas of the equivalent enthalpy method proposed by Muradoglu *et al.* [141] and Raman *et al.* [226, 227]. There, the species mass fractions and sensible enthalpy as a function of a coupling variable, e.g. the mixture fraction, are obtained by a pre-computed set of flamelet curves calculated by solving Eq.(3.18). During the reactive simulation, a least squares analysis is performed to find the flamelet solution that best resembles the selected stochastic particle ensemble, see Fig. 4.1. Once the flamelet curve is selected, the values of the conditional equivalent species,  $\langle \tilde{\phi}_\alpha^E | \tilde{\phi}_c \rangle$ , on the LES mesh cell is approximated from the consistent flamelet solution using the Eulerian value of the coupling variable as the input parameter.

### 4.2.1.2 KernelEstimation

The `KernelEstimation` model is based on the methods developed for the field of smoothed particle hydrodynamics [228] and have been implemented by Galindo-López *et al.* [124]. The model estimates the values of the conditional equivalent

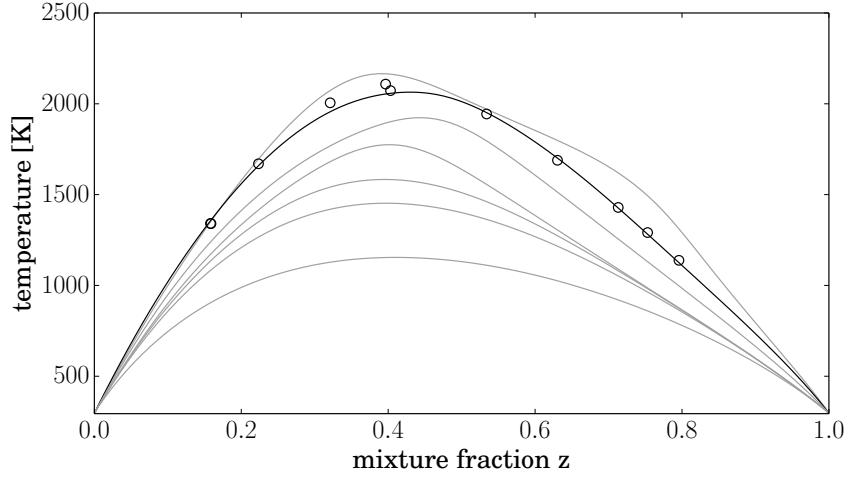


Figure 4.1: Temperature profiles of flamelet equation solutions for different scalar dissipation rates together with instantaneous Lagrangian particle temperatures. Courtesy to Jonas Kirchmann.

species  $\langle \tilde{\phi}_\alpha^E | \tilde{\phi}_c \rangle$  by the computation of a radial basis function

$$\langle \tilde{\phi}_\alpha^E | \tilde{\phi}_c \rangle = \int_{-\infty}^{\infty} \phi_\alpha^E(\mathbf{r}') \Omega(\mathbf{r} - \mathbf{r}', \Delta) d\mathbf{r}', \quad (4.1)$$

with  $\mathbf{r} = \{\phi_c^E, \mathbf{x}\}$ . To obtain an exact value of  $\phi_\alpha^E$ , the kernel would have to be a delta function, implying that the resolution length scale  $\Delta$  is zero. Since the stochastic particle number is finite the composition is only known at discrete locations and thus the integral is approximated by a sum over the entire particle ensemble

$$\langle \tilde{\phi}_\alpha^E | \tilde{\phi}_c \rangle = \sum_p m^p \frac{\phi_\alpha^p}{\rho^p} \Omega(\mathbf{r} - \mathbf{r}^p, \Delta). \quad (4.2)$$

In this study, only mixture fraction based coupling approaches are used ( $\tilde{\phi}_c = \tilde{f}$ ), where  $\mathbf{r}$  and  $\mathbf{r}^p$  are set to  $\mathbf{r} = \{\mathbf{x}, \tilde{f}\}$  and  $\mathbf{r}^p = \{\mathbf{x}^p, Z^p\}$ , respectively.

## 4.2.2 Mixing operation

The mixing process is executed by calling a submodel at the layer level of the `Mixing` class and is the only inter-particle operation that redistributes the transported scalar vector among the stochastic particles. To date, two mixing submodels are available in `mmcFoam`: the standard Curl mixing model for dense stochastic particle simulations and the MMC variant of the Curl mixing model, which can be applied to both dense and sparse Lagrangian approaches, respectively.

The MMC Curl mixing model implements the approach outlined in Sec. 3.2.4.3 such that the stochastic particles are selected in pairs such that the effective

squared distance is minimised, see Eq. (3.37). The particle pair selection is realised by sorting the particles in a space comprised of  $\Gamma = \{x, \zeta_c\}$ , where the sorting algorithm is realised by a k-dimensional binary tree, whose concept is described in Bentley [229]. For three-dimensional simulations with mixture fraction as conditioning variable the sorting space becomes  $\Gamma = \{x, \tilde{f}\}$ . In a k-d tree, at each leaf, the given space is recursively split into two parts along a hyperplane perpendicular to that space, resulting in two so-called half-spaces, one containing values larger and the other smaller than the splitting value. Following Friedmann [230], the splitting dimension is selected according to in which the data points have the largest spread and can be calculated by

$$d_s = \left\langle s \left| \max \left( \frac{\max(\Gamma_s) - \min(\Gamma_s)}{\Gamma_{m,s}} \right) \right. \right\rangle \quad (4.3)$$

with  $\Gamma_{m,s}$  being a normalisation vector comprised of  $\Gamma_{m,s} = \{\mathbf{r}_m, \zeta_{m,s}\}$ . This procedure is depicted in Fig. 4.2, where data points are sorted in a two-dimensional space.

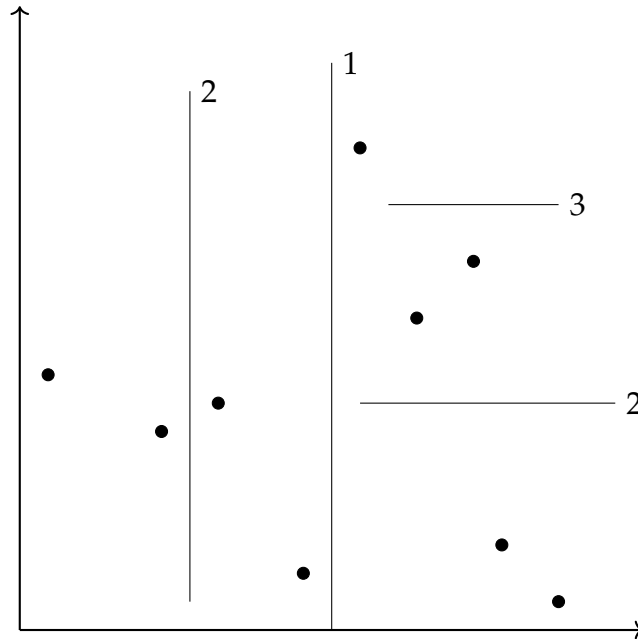


Figure 4.2: Representation of the k-d tree here with  $k = 2$ . The circles represent the data points in a two-dimensional space and the thin lines represent the respective splitting plane of the subset.

### 4.2.3 Boundary conditions

Well-defined boundary conditions are of utmost importance in order to calculate reliable simulations with high predictive validity. In general, constant time Dirichlet or Neumann boundary conditions are sufficient to reflect the physical

characteristics of the boundary conditions. In simulations of turbulent jet diffusion flames, one challenge is to specify excellent time-varying boundary conditions for the jet nozzle velocity field to ensure that the decay of the jet and the acting shear forces can be reproduced correctly. For this purpose, turbulent inflow boundary conditions are generated in a non-reactive simulation of a pipe flow prior to the reactive simulation. The turbulent velocity field of the pipe flow is stored and later retrieved for the reactive simulation as boundary data of the jet velocity field. Here, the specification of nozzle diameter and bulk velocity sufficiently defines the flow pattern of the pipe flow due to the Reynolds similarity. Periodic boundary conditions are applied for a pipe flow of finite length. Due to the occurrence of coherent structures whose scale dimension increases with lower Reynolds number, it is important to properly select the length of the pipe flow domain, as otherwise a correlation bias could arise. Wu & Moin [231] conducted an excellent DNS study on correlations of flow structures in turbulent pipe flows. For pipe flows with Reynolds numbers higher than  $Re_D = 10\,000$ , six longitudinal diameters are usually sufficient to avoid unwanted correlation bias. The grid resolution of the pipe domain should be chosen based on the best practice recommendations given in [26, 232]. Since fully resolved LES of pipe flows are prohibitively expensive due to the excessive computational requirements, some of which would even exceed the requirements of reactive simulation, an ID-DES (cf. 3.1.2) can be performed as a much more efficient approach. The instantaneous velocity field and the formed flow structures highlighted by the  $q$ -criterion are depicted in Fig. 4.3 showing that even small flow structures can be resolved.

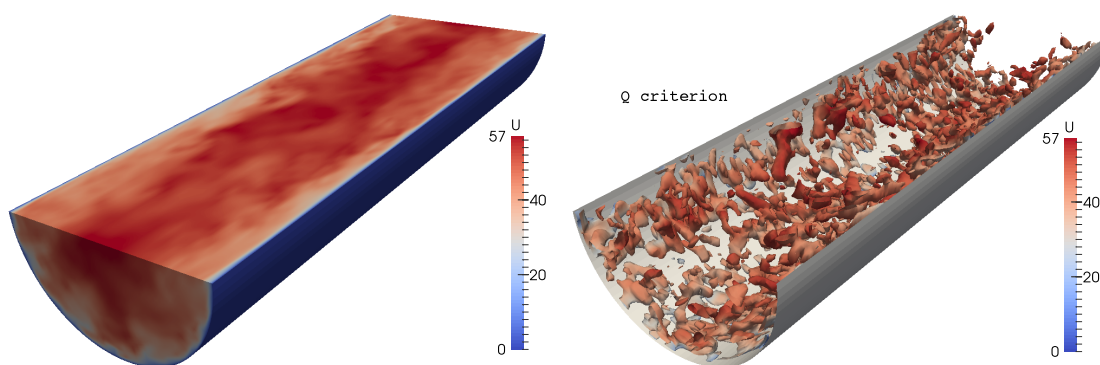


Figure 4.3: Half of the flow domain at Reynolds number of  $Re_D = 28\,300$  showing (a) instantaneous velocity field (b)  $q$ -criterion shaded by instantaneous velocity

Figure 4.4 compares numerical results against experimental measurements [233, 234] of axial velocity and its RMS directly at the jet exit plane of the turbulent Sandia DME D jet flame. From the plot it is easily seen that both the mean velocity and the mean velocity fluctuations can be modelled excellently so that

well-defined boundary conditions can be provided for the reactive simulation.

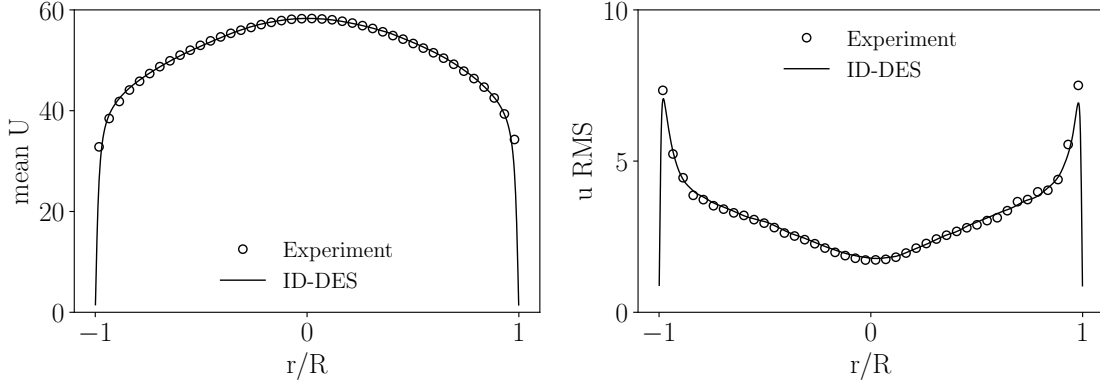


Figure 4.4: Mean and RMS of axial velocity of the Sandia DME D flame configuration operating at a Reynolds number of  $Re_D = 29\,300$  with a diameter of  $D = 7.45$  mm ( $\circ$ ) Experimental data [235] measured 1 mm downstream of the nozzle exit plane and (—) simulation data obtained with an ID-DES of a pipe flow.

### 4.3 Incorporation of the aerosol dynamics into the MMC framework

To account for flame synthesis of solid particulates in turbulent flames the concepts of aerosol dynamics presented in Sec. 3.3.3 have to be incorporated into the existing `mmcFoam` code environment. Therefore, the four class layer implementation has been extended by a fifth layer, called `Aerosol`

Reacting  $\leftarrow$  Mixing  $\leftarrow$  Aerosol  $\leftarrow$  Thermo  $\leftarrow$  Advection  $\leftarrow$  particle ,

where sub-models of this layer implement different particulate aerosol dynamic approaches, e.g. the nucleation and surface growth of liquid droplets or the flame synthesis of solid fractals. The newly implemented solver is called `mmcPbeFoam` and a flow diagram shown in Fig. 4.5 depicts the sequence of the individual computational steps of the solver. At first the Eulerian and Lagrangian schemes are initialised. Then, the turbulent Favre-filtered transport equations of mass, velocity, reference mixture fraction, equivalent species mass fraction and sensible enthalpy are solved. Discretisation schemes are second order central difference scheme (CDS) for the momentum and a total variation diminishing (TVD) scheme is applied to all other differential transport equations. A second order backward scheme is used for time integration. The PISO algorithm [236] ensures a consistent coupling of velocity and pressure. Gas phase diffusivity is calculated based of the Sutherland law [237] and the turbulent diffusivity is determined by the LES turbulence model. The variables and properties required by

the Lagrangian scheme are interpolated to the stochastic particle position. The evolution of the Lagrangian scheme is performed according to the fractional step procedure, where the stochastic particle position is updated first, followed by calculation of the aerosol dynamics, the mixing and reaction. The just updated transported scalar vector is used to find conditional equivalent species and sensible enthalpy required for the density feedback.

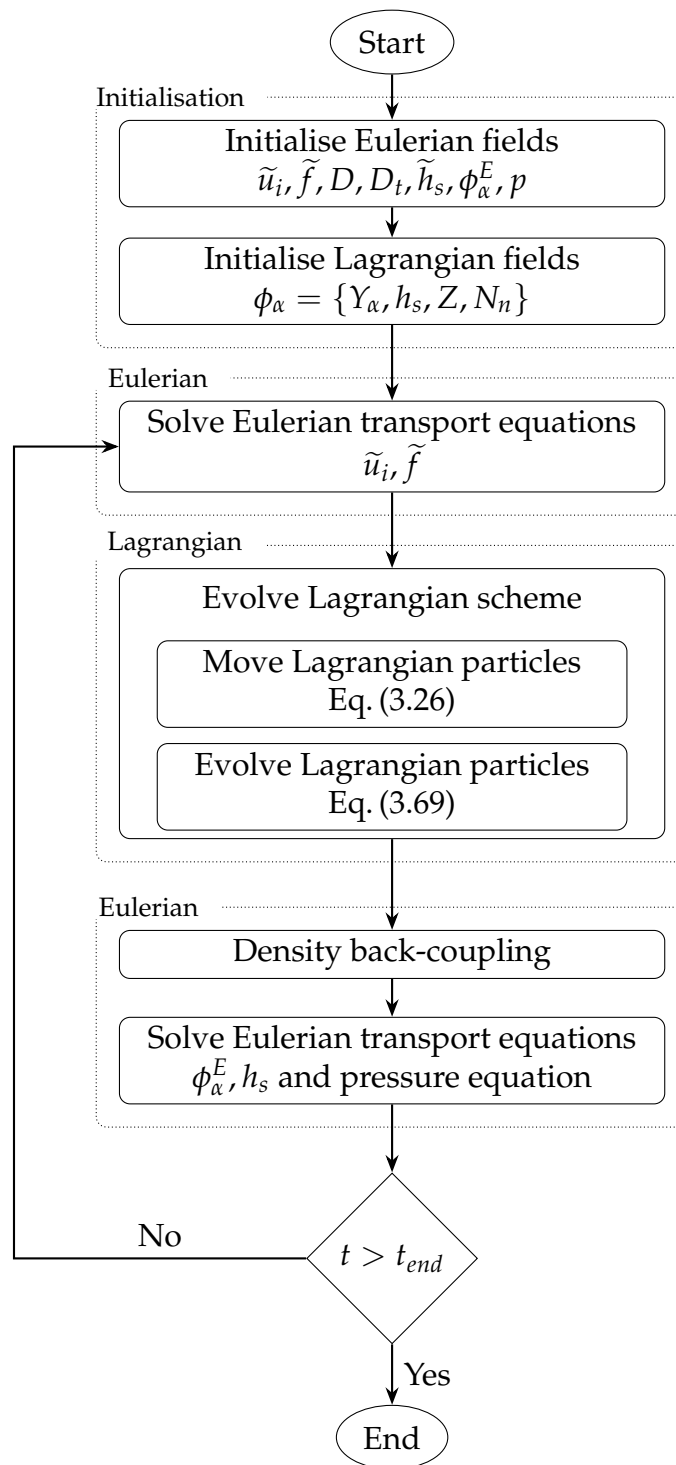


Figure 4.5: Flow chart of the mmcPbeFoam solver.



## Chapter 5

# Application of the Multiple Mapping Conditioning model to particulate laden flows

With the numerical methods and techniques presented in Chapters 3 and 4, all necessary tools for simulating particulate flame synthesis within turbulent, reactive flows are now available. Section 3.2.4.3 presented a scheme for a stochastic particle mixing procedure in the context of MMC-LES, aimed at modelling the turbulence-scalar interactions in an appropriate way. Similarly, standard methods for predicting particulate size distributions were outlined in Sec. 3.3.3. These standard methods have been combined into a comprehensive PBE-MMC-LES framework, cf. Sec. 4.2, the generality of which is now to be validated on the basis of various flow problems. The combined PBE-MMC-LES model can be considered as validated if it is able to provide the

- correct modelling of turbulence-scalar interactions at challenging conditions,
- modelling of two-phase flows with high accuracy that is comparable to common PDF methods,
- correct correlations between reactive scalars, turbulence and particulate synthesis models (e.g. inception, growth and coagulation), and
- correct prediction of trends for a broad range of boundary conditions.

In the context of this study, four consecutive journal papers [1, 2, 3, 4] were published to assess the listed requirements and thus to prove the generality of the comprehensive PBE-MMC-LES model. These publications are presented below, highlighting the main features and results.

### **Paper 1:**

The first issue has been addressed in the publication Neuber *et al.* [1]. This paper presents results for a complete turbulent, reactive flame series ranging from

moderate to relatively high Reynolds numbers obtained within the MMC-LES framework. This configuration does not include particulates; however, it poses a challenging test case for a combustion model, as local extinction events become more prominent with increasing Reynolds number. As a consequence, the conditional variances of the (reactive) scalars increase significantly or, in other words, the correlation between the scalar fluctuations and the filtered mixture fraction as a conditioning variable declines.

The main aspect of this paper is the demonstration of the MMC-LES method's ability to predict the correct degree of conditional scalar fluctuations with a single set of model parameters for a complete flame series. This was necessary due to two circumstances: First, the MMC-LES model had not been fully validated at the time of the publication; second, the newly developed a-ISO model for predicting the mixing time, cf. Eq. (3.45), had only been validated against a generic flow configuration (cf. Vo *et al.* [138]) and its application to a real flame configuration was still pending.

In previous MMC-LES investigations of a turbulent jet configuration [136, 137], which also exhibited pronounced local extinction events due to an increase in Reynolds number, satisfactory results could only be obtained by adjusting the parameters of the mixing model. This was a major shortcoming of the MMC-LES model, as it is of predominant importance to show that a model provides excellent simulation results with a single set of model parameters under various boundary conditions. Moreover, in the preliminary studies by Neuber *et al.* [238, 239, 240], the previously used mixing time scale model C&K, cf. (3.44), proved to be unable to yield satisfactory conditional variances of the temperature for the Sandia DME flame configurations with higher Reynolds numbers.

These aspects have been addressed in Neuber *et al.* [1], where an efficient modelling framework was presented and it was shown that results in terms of conditional and unconditional means could be significantly enhanced by application of the a-ISO model for a sophisticated calculation of the mixing time scale. This is exemplified by scatterplots of the temperature conditioned on particle mixture fraction for the flame configuration with the highest Reynolds number, see Fig. 5.1. The experimental data shows significant deviations from a simple flamelet-like structure and an almost bimodal distribution is observed. It is obvious that the C&K model is unable to accurately account for the effect of turbulence on chemistry. On the contrary, the a-ISO model performs far better and the numerical calculation even captures the bimodal distribution of the experiment appropriately.

A more quantitative assessment of the performance of the a-ISO model is provided by Fig. 5.2, where the conditionally averaged standard deviations of CO mole fraction for the different flames are shown.

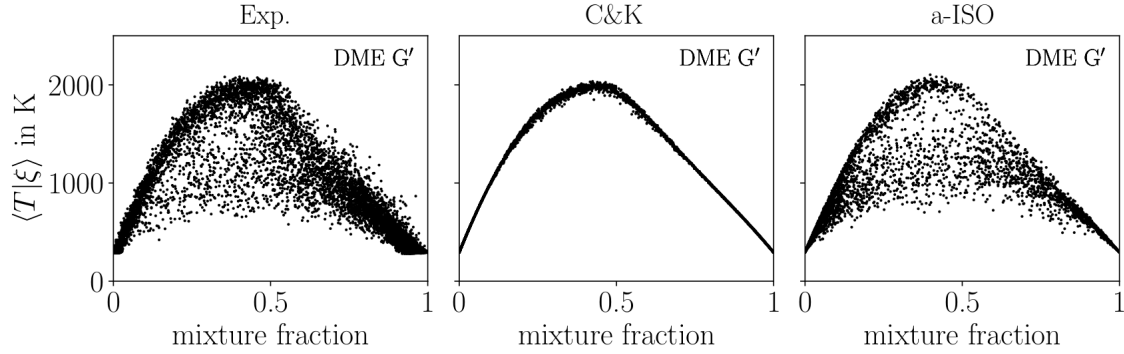


Figure 5.1: Stochastic particle temperature conditioned on mixture fraction  $\xi$  at location  $z/D = 7.5$  for the Sandia DME G' configuration. A total number of 10 000 samples is shown in each plot. Figure taken from Neuber *et al.* [1].

It is clearly illustrated that MMC-LES with a-ISO captures the progression of local extinction and its effect on the flame structure very well and is therefore suitable as a new standard approach.

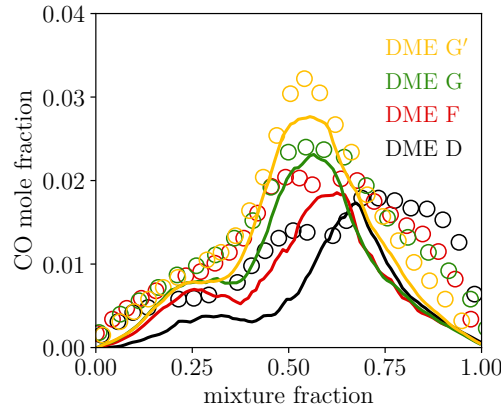


Figure 5.2: Profiles of experimental (symbols) and numerical (solid lines) standard deviation of stochastic particle CO mole fraction conditioned on mixture fraction  $\xi$  at  $z/D = 7.5$  for the different Reynolds number flames. Figure taken from Neuber *et al.* [1].

These excellent results could only be obtained through the application of a sophisticated density coupling model, since the flamelet curves approach, see Sec. 4.2.1.1, has proven to be a source of significant numerical bias. The partial extinction leads to locally strongly varying particle compositions and the FlameletCurves approach induces numerical density fluctuations in the entire flow field when the least squares evaluation selects a new flamelet curve. For this reason, this density coupling is not suitable for flame configurations with local extinction events. Here, the application of the KernelEstimation density coupling model, see Sec. 4.2.1.2, provides much better results, although numerically induced density fluctuations are not entirely eliminated.

A further important feature to be mentioned is that for Neuber *et al.* [1] the turbulent inlet flow data were generated with an *a priori* ID-DES of a pipe flow, cf. Sec. 4.2.3. This approach for generating turbulent flow data was validated using experimental measurements near the nozzle outlet. Due to the excellent numerical results, the approach now provides a reliable model for subsequent investigations in cases where no velocity measurements are available or possible.

Based on the presented results, it was demonstrated that the implemented MMC-LES model provides a

- ✓ correct modelling of turbulence-scalar interactions at challenging conditions

and can now be considered as a validated starting point for developments in two-phase flow simulations.

## Paper 2:

The publication Neuber *et al.* [2] constitutes the first study to present a combined PBE-PDF approach, including nucleation and growth, within the MMC-LES framework for a laboratory-scale flow configuration. The full PBE-MMC-LES model is validated by comparison with experimental data from nucleation studies in a turbulent, hot nitrogen jet loaded with dibutyl phthalate (DBP), which condenses during mixing with a cold air stream.

Previously, only a few synthesis studies have combined LES with the sectional method [36, 37]. As outlined in Neuber *et al.* [2], all of them neglected the interactions of turbulence with aerosol nucleation and growth, although studies using direct numerical simulation (DNS) [38] demonstrated clearly that such contributions are typically not small and must not be neglected.

The synthesis of aerosols in turbulent flames involves coupled, three-way interactions between turbulence, chemistry and aerosol dynamics. In fundamental studies, it is reasonable to eliminate one of these aspects in order to analyse the other interactions in isolation. Since the present work focuses on model closures for turbulence-aerosol interactions, the investigation of a non-reacting system with a condensing species represents an ideal test case. New thermodynamic data have been presented for DBP in Neuber *et al.* [2] and served as an additional source for subsequent studies [241, 242].

Acceptable agreement is found between the MMC-LES predictions and experimental data as well as other numerical investigations, as shown in Fig. 5.3. The average DBP droplet sizes are well predicted, and predictions of the total droplet number and the dependencies of droplet statistics on precursor concentrations are satisfactory.

A remarkable outcome is that the comparison of the sparse particle method with results from conventional (dense) Monte Carlo LES simulations demonstrates the capabilities of the MMC-LES framework to predict aerosol nucleation

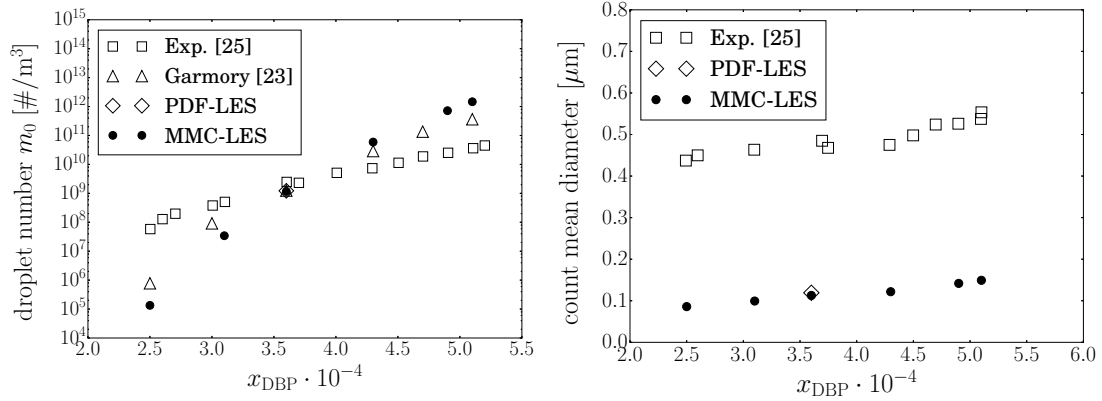


Figure 5.3: Droplet number density (left) and count mean droplet diameter (CMD) (right) as function of the DBP mole fraction in the hot jet issuing into the domain at  $z/D = 20$ . Figures taken from Neuber *et al.* [2].

and growth at relatively low computational costs while providing comparable prediction quality, cf. Fig.5.3. Thus, on the basis of the results presented in Neuber *et al.* [2] it can be concluded that sparse MMC-LES simulations produce results that are nearly identical with the much more expensive dense PDF-LES simulations and that sub-grid interactions related to the particulate matter modelling must not be neglected. Neuber *et al.* [2] assess the effects and importance of turbulence interactions with the gas-phase composition and aerosol evolution. The effects of sub-grid interactions are analysed by comparison of the averaged nucleation and growth rates predicted by MMC-LES with the averaged quantities from the filtered LES fields and the Reynolds-averaged quantities produced from RANS-type closures. Moreover, errors introduced when omitting any LES sub-grid modelling are quantified.

In general, reasonable agreement of predicted droplet concentrations with measurements has been achieved and the quality of the results compares favourably with other simulations presented in the archival literature. The study demonstrates that the effect of turbulence on nucleation must not be neglected but may be small for fine LES resolutions and/or low turbulence levels. Thus, the study presented in Neuber *et al.* [2] is a first successful step towards a comprehensive PBE-MMC-LES framework which is capable of

- ✓ modelling two-phase flows with high accuracy that is comparable to common PDF methods,

which makes it a very promising tool for simulating aerosol dynamics in turbulent reacting environments.

### Paper 3:

The publication Neuber *et al.* [3] constitutes the first LES-coupled sparse PDF study modelling particulate formation, surface growth and coagulation in a laboratory-scale turbulent reactive flow configuration involving finite rate chemistry. Additionally, it is one of the very few joint computational and experimental studies that address the issue of particulate synthesis under the influence of turbulence. The full PBE-MMC-LES model is validated by comparison with experimental data obtained on a flow configuration developed specifically for this project. Laser induced fluorescence (LIF) and elastic light scattering (ELS) signals have been measured to get insight into the particulate formation process, where the calculation of the signals are described in Neuber *et al.* [3]. Thus, model validation follows the paradigm shift approach [243, 244, 245], which is based on the calculation of "predicted signals" that are directly compared against the experimentally obtained signals. This avoids considerable uncertainties that would arise when the measured values are converted into physically meaningful quantities, such as e.g. particulate number densities.

The turbulent flow configuration considers a cold, silane-doped nitrogen jet issuing into a hot, vitiated co-flow. Oxidation of silane leads to particulate formation, followed by surface growth and agglomeration, and the individual aerosol dynamic processes are simulated by the models presented in Sec. 3.3.3. The particulate inception rate is determined by the chemical reaction mechanism proposed by Suh *et al.* [45], which is listed in Appendix A. The key feature of Neuber *et al.* [3] is that particulates with fractal morphology are now considered here, rather than spherical droplets as assumed in the previous study, and the corresponding models used for describing the aerosol dynamics had to be modified accordingly.

The publication Neuber *et al.* [3] aims at a thorough validation of the combined PBE-MMC-LES model against reference test cases with and without silane doping, and therefore without particulate formation. The corresponding contour plots of the ELS signals are shown in Fig. 5.4. The calculation and normalisation procedure of the ELS signal is given in Neuber *et al.* [3]. In the absence of particulate matter the ELS signal is a function of species composition and temperature only. This allows an assessment of the correct prediction of the flow field, which is only obtained if the boundary conditions are well defined, the turbulent flow content is accurately captured and the MMC mixing model is accurately calibrated.

In Figs. 5.4(a) and 5.4(b) experimental and numerical results are presented for the reference case without silane. The decay of the jet stream appears to be slightly overestimated. This could be due to an over-prediction of the turbulent velocity fluctuations within the (pre-calculated) pipe flow simulation used for the jet inlet condition. In the experiments, the jet inlet tube is surrounded by a hot,

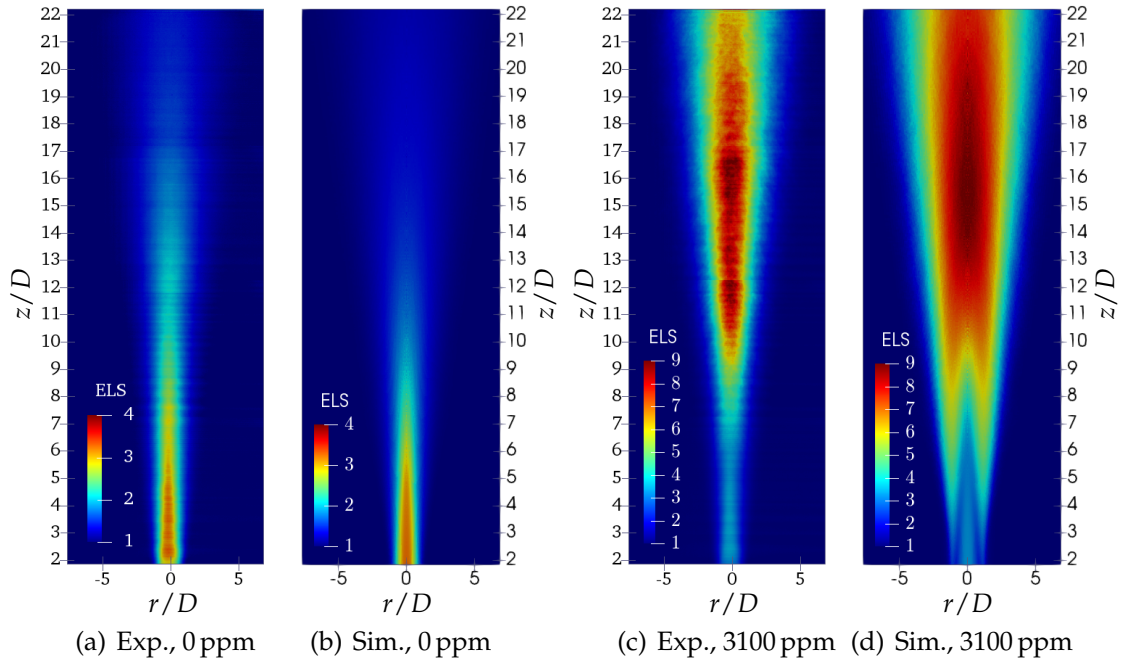


Figure 5.4: Contour plots of the normalised elastic light scattering signal for cases with and without silane loading in the central turbulent jet. Figures taken from Neuber *et al.* [3].

vitiated co-flow, and the heat flow towards the central jet stream increases the temperature of the jet. This leads to an increase in molecular viscosity, which dampens the internal velocity fluctuations. In the simulations of the pipe flow, no heat flow was accounted for, such that the velocity fluctuations at the inlet boundary are slightly overestimated.

Figures 5.4(c) and 5.4(d) allow for a comparison of the ELS signal for the reference case with a silane doping of 3100 ppm. The comparison shows that the numerical signal agrees relatively well with the experimentally measured one; for example, the peak value is predicted at approximately the same downstream position. However, there seem to be larger deviations in terms of the lateral dispersion of the particulates, as well as for the early shear layer. Here, the numerical model predicts more or larger particulates, whereas these were measured rather on centerline positions.

Attempts to improve the predictive quality of the PBE-MMC-LES model include varying the underlying chemical reaction mechanism, the assumed fractal morphology of the particulates and the boundary conditions. Concerning the last, a heat transfer from the hot, vitiated co-flow to the cold jet stream was simulated and the velocity field was later superimposed on the reactive simulation, see Sec. 4.2.3. Similarly, velocity and temperature variations were forced onto the co-flow flow stream. None of these efforts lead to any improvements for the comparison against the experiment, but to insights regarding the dependencies

on particulate formation.

The numerical results show that the combined PBE-MMC-LES method is able to correctly predict both the turbulent flow field and the particulate dynamics for cases with two different silane dopings, implying the ability of calculating

- ✓ correct correlations between reactive scalars, turbulence and particulate synthesis models (e.g. inception, growth and coagulation).

In the present stage the PBE-MMC-LES model – together with the well-defined computational setup – may now serve as a starting point for more complex variations with respect to boundary conditions and model-related parameters.

#### **Paper 4:**

Starting from the validated reference cases, in Neuber *et al.* [4] the combined PBE-MMC-LES model was applied to a set of test cases with varying boundary conditions. This is the final step in the process of model validation, because it is the best proof that the developed model has not only been adjusted to a specific test case but rather has a reasonable degree of generality. By conducting this final step, a single set of parameters was defined on the basis of the simulations carried out prior to the main investigation and fixed for the subsequent simulations. Thus, parameters were adjusted with respect to the discretisation of the particulate size distribution, the morphological structure of the particulates, and the underlying chemical reaction kinetics, as shown in Neuber *et al.* [4].

The model was challenged in its predictive capability across a wide range of silane concentrations of the turbulent jet, co-flow temperatures and Reynolds numbers of the jet stream, and results are presented in Fig. 5.5. Results for the variation of silane doping, cf. 5.5(a), reveal that for the reference case with 3100 ppm the predicted ELS signal increases with the same rate as the signal from the measurements, indicating that particulate number and size are well predicted. It can be concluded that particulate inception, volumetric surface growth and agglomeration are likely to be modelled well, too. The simulations predict the correct trends, i.e. for lower silane loadings, lower ELS signals are calculated. However, the numerical data show a much lower sensitivity of the signal strength to changes in silane doping, which is moderate compared to the experimental data.

The discussion in Neuber *et al.* [4] identifies the omission of differential diffusion, limitations of the precursor chemistry and the rigorous assumptions about the fractal morphology of the particulates as the most likely influencing factors, as all of these processes entail a non-linearity that is clearly present in the experimental trends. In Fig. 5.5(b) it is observable that, again, although the general trend can be correctly reproduced, the sensitivity of the model to the different co-flow temperatures is underestimated compared to the experiment. The sensitivities towards the jet Reynolds number is shown in Fig. 5.5(c). Here, the experiment

shows a strong non-linearity that is not reflected by the computational model, which can most likely be attributed to a missing model to account for differential diffusion, cf. Sec. 3.3.4.

The publication Neuber *et al.* [4] shows that the combined PBE-MMC-LES model is able to provide

- ✓ correct predictions of trends for a broad range of boundary conditions,

although sensitivities are considerably underestimated.

### Summary

The four publications [1, 2, 3, 4] represent a thorough validation of the combined PBE-MMC-LES framework through a step-by-step analysis of several aspects and model features. They prove that the framework provides the correct modelling of turbulence-scalar interactions at challenging conditions, modelling of two-phase flows with high accuracy that is comparable to common PDF methods, correlations between reactive scalars, turbulence and particulate synthesis models (e.g. inception, growth and coagulation), and prediction of trends for a broad range of boundary conditions. This demonstrates that the presented PBE-MMC-LES framework represents a comprehensive computational model for simulating the aerosol dynamics of particulates with fractal morphology and meets the requirements mentioned above. Model shortcomings were identified and may form the starting point for possible further developments, as discussed in Chap. 6.

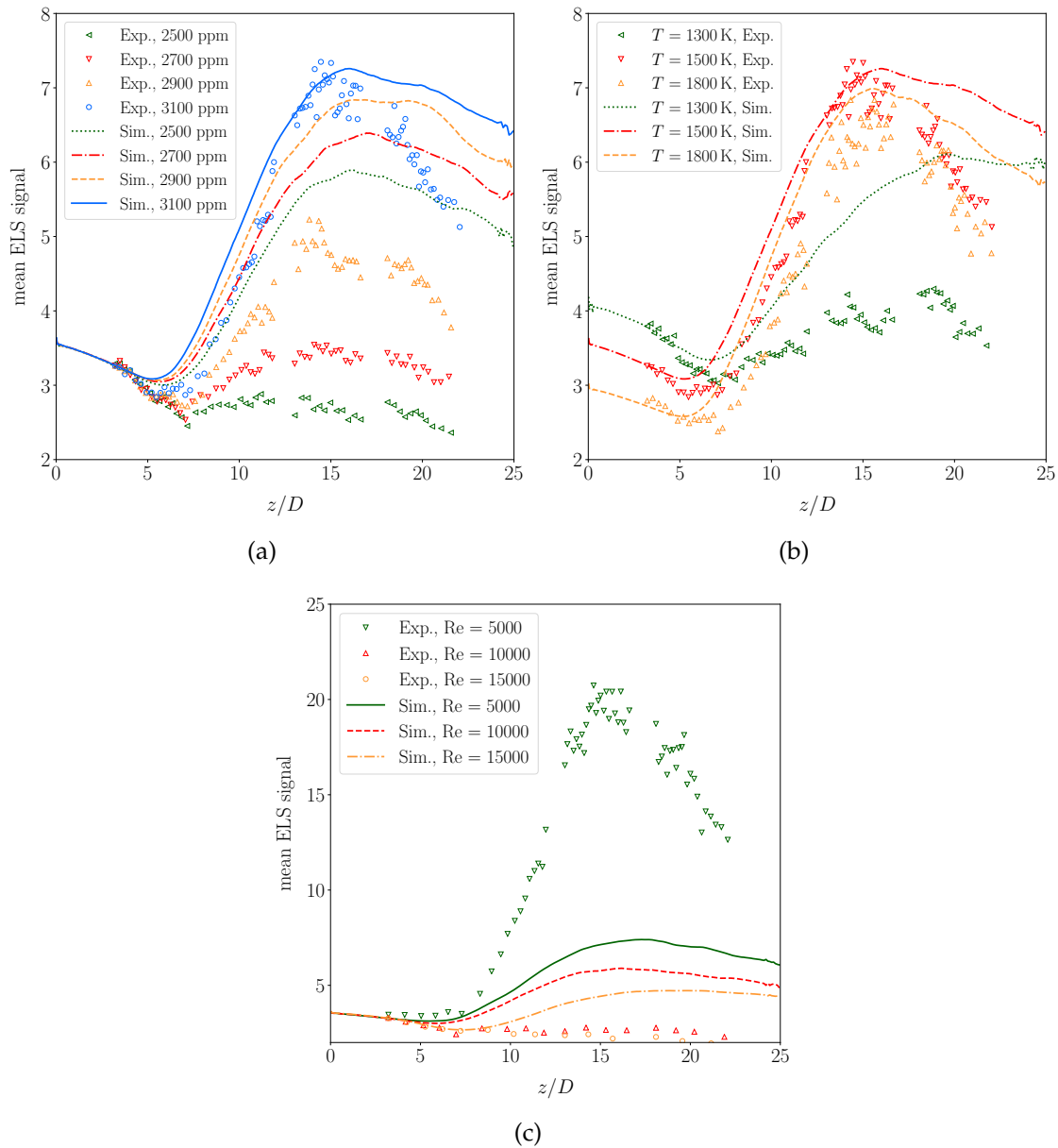


Figure 5.5: Mean elastic light scattering signal along the centerline for cases with (a) a co-flow temperature of  $T = 1500$  K and different silane loadings in the central jet stream, (b) a silane loading of 3100 ppm and different co-flow temperatures and (c) a silane loading of 2500 ppm and different jet Reynolds numbers. Experiment (symbols) and PBE-MMC-LES (lines). Figures taken from Neuber *et al.* [4].

## Paper 1:

**Title:** Sparse-Lagrangian MMC modelling of the Sandia DME flame series

**Authors:** Gregor Neuber

Institut für Technische Verbrennung,  
University of Stuttgart, 70174 Stuttgart, Germany

Frederik Fuest

Combustion Research Facility,  
Sandia National Laboratories, Livermore, CA 94551, USA

Jonas Kirchmann

Institut für Technische Verbrennung,  
University of Stuttgart, 70174 Stuttgart, Germany

Andreas Kronenburg

Institut für Technische Verbrennung,  
University of Stuttgart, 70174 Stuttgart, Germany

Oliver T. Stein

Institut für Technische Verbrennung,  
University of Stuttgart, 70174 Stuttgart, Germany

Sebastian Galindo-Lopez

School of Aerospace, Mechanical and Mechatronic Engineering,  
The University of Sydney, NSW 2006, Australia

M. J. Cleary

School of Aerospace, Mechanical and Mechatronic Engineering,  
The University of Sydney, NSW 2006, Australia

Robert S. Barlow

Combustion Research Facility,  
Sandia National Laboratories, Livermore, CA 94551, USA

Bruno Coriton

Combustion Research Facility,  
Sandia National Laboratories, Livermore, CA 94551, USA

Jonathan H. Frank

Combustion Research Facility,  
Sandia National Laboratories, Livermore, CA 94551, USA

Jeffrey A. Sutton

Department of Mechanical and Aerospace Engineering,  
The Ohio State University, OH 43210, USA

**Journal:** Combustion and Flame

**Volume:** 208

**Pages:** 110 – 121





Contents lists available at ScienceDirect

Combustion and Flame

journal homepage: [www.elsevier.com/locate/combustflame](http://www.elsevier.com/locate/combustflame)

## Sparse-Lagrangian MMC modelling of the Sandia DME flame series

Gregor Neuber<sup>a</sup>, Frederik Fuest<sup>b</sup>, Jonas Kirchmann<sup>a</sup>, Andreas Kronenburg<sup>a,\*</sup>,  
Oliver T. Stein<sup>a</sup>, Sebastian Galindo-Lopez<sup>c</sup>, Matthew J. Cleary<sup>c</sup>, Robert S. Barlow<sup>b</sup>,  
Bruno Coriton<sup>b</sup>, Jonathan H. Frank<sup>b</sup>, Jeffrey A. Sutton<sup>d</sup>

<sup>a</sup> Institute for Combustion Technology, University of Stuttgart, Stuttgart 70174, Germany

<sup>b</sup> Combustion Research Facility, Sandia National Laboratories, Livermore, CA 94551, USA

<sup>c</sup> School of Aerospace, Mechanical and Mechatronic Engineering, The University of Sydney, New South Wales 2006, Australia

<sup>d</sup> Department of Mechanical and Aerospace Engineering, The Ohio State University, OH 43210, USA



### ARTICLE INFO

#### Article history:

Received 22 March 2019

Revised 6 May 2019

Accepted 26 June 2019

#### Keywords:

Dimethyl ether

Turbulent combustion modelling

MMC

LES

### ABSTRACT

A series of turbulent, piloted dimethyl ether (DME)/air jet flames (Sandia DME flames D–G<sup>\*</sup>), with Reynolds numbers ranging from 29,300 to 73,250, has been simulated using a sparse-Lagrangian multiple mapping conditioning (MMC) approach coupled to a large eddy simulation (LES) flow field solver. Mixing between the Monte-Carlo particles is modelled by a generalised form of MMC combined with a sparse distribution of particles leading to significant computational savings compared to what is required for conventional mixing models. This is achieved by pairwise mixing of particles that are selected dependent on their distance in an extended space comprised of a reference variable, given by the LES mixture fraction, and spatial location. The MMC-LES method successfully predicts the flame structure and composition field for the full flame series. Numerical results are compared against conditional statistics and spatially resolved experimental data acquired with Raman/Rayleigh scattering and laser-induced fluorescence measurements. They show good agreement even for flame DME-G<sup>\*</sup> where large turbulence-chemistry interactions lead to significant local extinction and large deviations from a flamelet structure. The influence of the mixing time on the predicted flame structure is investigated, and the systematic validation of the time scale models with the aid of measurements of the entire flame series has corroborated the findings of earlier DNS and single flame studies: a modified time scale model is needed to provide accurate predictions of conditional fluctuations and thus of possible deviations from a flamelet-like combustion regime.

© 2019 The Combustion Institute. Published by Elsevier Inc. All rights reserved.

### 1. Introduction

In the past decade, Large Eddy Simulation (LES) has become a very efficient computational tool to predict combustion processes ranging from lab scale experiments to applications of engineering interest. Many models have been developed to close the reaction source terms that appear in unclosed form in the filtered reactive species conservation equations. Amongst these methods are the flamelet-progress variable approach [1], Conditional Moment Closure (CMC) [2] and the transported probability-density function (PDF) methods [3]. In more recent years, the Multiple Mapping Conditioning (MMC) model has been developed [4] as a computationally efficient variant of the transported PDF method and has been validated against many flame configurations [5].

For validation purposes, the International Workshop on Measurement and Computation of Turbulent Nonpremixed Flames (TNF) [6] defined the well-known Sandia jet flames series (Sandia flames A–F) as benchmark cases. This original flame series consisted of a pilot-supported, diluted methane jet of varying Reynolds numbers issuing into a coflow of air. The Sandia flames D–F have been quite popular for turbulent combustion modellers as they exhibit turbulence–chemistry interactions increasing from relatively low levels in flame D through to strong interactions and near blow-off conditions in flame F. The same burner configuration has been used to combust dimethyl ether (DME) [7–9]. DME has sparked some interest as it exhibits attractive properties as an alternative fuel. It can be burned in diesel engines with only modest design changes [10] and being an oxygenated fuel with no direct carbon-carbon bonds, it tends to emit less NO<sub>x</sub>, CO and soot. However, there are challenges. One of these challenges is associated with the increase in complexity of the DME combustion chemistry relative to that for methane, particularly in reactions involving fuel

\* Corresponding author.

E-mail address: [kronenburg@itv.uni-stuttgart.de](mailto:kronenburg@itv.uni-stuttgart.de) (A. Kronenburg).

decomposition of rich mixtures. Coriton et al. [7] published hydroxyl (OH) and formaldehyde (CH<sub>2</sub>O) laser-induced fluorescence (LIF) and velocity data for Sandia DME flame D. For Sandia DME flames D and F, 1D Raman/Rayleigh multispecies data were obtained by Fuest et al. [9,11]. Numerical investigations performing conditional moment closure (CMC) [7] and flamelet [1] simulations of DME flame D provided good agreement with experiments. The Sandia DME-D and F flames were modelled using a PDF approach with specific focus on the effects of differential diffusion [12]. However, as DME oxidation is fast the intensity of turbulence-chemistry interactions is lower than in the Sandia methane flames for the same Reynolds number and fewer extinction events are observed. Higher Reynolds numbers are needed for DME flames when compared to methane flames to observe significant effects of turbulence on the flame structure. The present work presents selected data of additional flame configurations with much larger jet Reynolds numbers posing additional challenges, and – for the first time – the full series of Sandia DME flames D–G is modelled and extinction levels are analysed in more detail. An extended set of comparisons between simulations and experiments can be found in the supplementary information available with the online version of this paper, and the data has been made available online on [tnfworkshop.org](http://tnfworkshop.org).

Simulations are performed with a sparse-Lagrangian MMC model coupled with a large eddy simulation (LES) flow solver [5]. MMC, originally derived by Klimenko and Pope [4], is a probability density function (PDF) method [3] and in the context of LES it models the sub-filter PDF of the composition, known as the filtered density function (FDF). A Monte Carlo Lagrangian particle scheme is used to solve the FDF, and MMC plays the role of a mixing model to close the conditional sub-filter scalar dissipation. The high quality of MMC mixing, specifically its localness, independence and linearity, allow for a low-cost, sparse-Lagrangian method involving far fewer stochastic particles for the FDF simulation than LES grid cells [13]. Here, we use the MMC version of Curl's [14,15] mixing model where particles mix in pairs which are selected dependent on their proximity to each other in an extended space comprised of physical location and a reference mixture fraction, the latter being the filtered mixture fraction obtained from the Eulerian LES. In non-premixed flames, localness in mixture fraction space implies a strong degree of localness in composition space.

The Lagrangian mixing time scale is a crucial property as it controls the amount of conditional scalar dissipation in the transported PDF methods. The original version of the Lagrangian mixing time scale model, which we call the C&K model [16], was used to validate the MMC-LES method against the original Sandia D, E and F methane flames [17]. More recently, Vo et al. [18] and Huo et al. [19] demonstrated that conditional variances are significantly underpredicted by the C&K model and hence that local extinction events are hardly captured. Based on a direct numerical simulation (DNS) analysis, Vo et al. [20] proposed a new anisotropic formulation of the Lagrangian mixing time scale, which was found to produce significantly more accurate conditional variance than the C&K model and to be much less sensitive to the model localness parameter,  $f_m$ . This new approach has also been used to successfully simulate a syngas shear layer configuration [21] and the Sydney swirling flame [19]. It is noted that in both publications only a single flame condition was investigated, but thorough validation and calibration needs more than this. To this end, a flame series provides an ideal test suite for model calibration, and successful prediction of the entire series strongly confirms the model's predictive capability especially if one set of parameters can be used for all flames. In the present work, this is attempted for the full Sandia DME flame series.

The MMC-LES model is presented in Section 2. The experimental and numerical setups are described in Sections 3 and 4,

respectively. Predictions are compared against experimental data in Section 5 and conclusions are drawn in Section 6.

## 2. Methodology

### 2.1. Multiple mapping conditioning implementation

A hybrid Euler/Lagrange approach is used. It consists of an Eulerian LES for the computation of the continuity, velocity, pressure and mixture fraction fields, where the filtered mixture fraction  $\bar{f}$  is used as a reference variable for conditioning the mixing of the stochastic particles. Following Pope [3], we employ a Lagrangian Monte-Carlo formulation for the solution of the FDF of the transported reactive scalar vector  $\phi_\alpha = (h, Y_1, \dots, Y_i, \dots, Y_{n_s}, Z)$ , where  $h$  is the total enthalpy,  $Y_i$  are the species mass fractions and  $Z$  is the mixture fraction, which is consistent with the species composition on the particles. The reactive scalar vector is transported on notional particles and a set of stochastic differential equations is solved by a fractional step approach to describe the particle dispersion due to the spatial displacement

$$d\mathbf{x}_i^p = \mathbf{A}_i^p dt + b_{ij}^p d\omega_j \quad (1)$$

and the scalar time evolution

$$d\phi_\alpha^p = (W_\alpha^p + S_\alpha^p) dt. \quad (2)$$

The drift and diffusion in Eq. (1) are given by [22]

$$\mathbf{A}_i = \tilde{u}_i + \frac{1}{\bar{\rho}} \frac{\partial}{\partial x_i} (\bar{\rho} (\mathcal{D} + \mathcal{D}_t)) \quad (3)$$

and

$$b_{ij} = \delta_{ij} \sqrt{2(\mathcal{D} + \mathcal{D}_t)}, \quad (4)$$

where  $\tilde{u}_i$  is the filtered instantaneous velocity,  $\bar{\rho}$  is the density,  $\mathcal{D}$  and  $\mathcal{D}_t$  are the molecular and turbulent diffusivities, respectively, and  $d\omega_j$  is the increment of the stochastic Wiener process. The time evolution in Eq. (2) is given by the reaction source term  $W_\alpha$  and the mixing operator  $S_\alpha$ , which emulates the sub-filter scalar dissipation. To model the mixing process, we adopt a modified version of the Curl's mixing model where two particles ( $p$  and  $q$ ) are mixed linearly towards their weighted mean  $\bar{\phi}_\alpha^{p,q}(t)$  with the mixing extent  $\gamma$ ,

$$\phi_\alpha^p(t + \Delta t) = \phi_\alpha^p(t) + \gamma (\bar{\phi}_\alpha^{p,q}(t) - \phi_\alpha^p(t)), \quad (5)$$

$$\phi_\alpha^q(t + \Delta t) = \phi_\alpha^q(t) + \gamma (\bar{\phi}_\alpha^{p,q}(t) - \phi_\alpha^q(t)). \quad (6)$$

The mixing extent is given by  $\gamma = 1 - \exp(-\Delta t/\tau_L)$  and the Lagrangian mixing time scale,  $\tau_L$ , is calculated based on local turbulence length scales. More details about the employed mixing time scale model will be given in Section 2.2. The pairs are selected by minimising the mean square distance in an extended space comprised of particle location and the reference mixture fraction (interpolated from the LES mixture fraction field) [16]

$$\hat{d}_{p,q}^2 = \sum_{i=1}^3 \left( \frac{d_{x_i}^{p,q}}{r_m/\sqrt{3}} \right)^2 + \left( \frac{d_f^{p,q}}{f_m} \right)^2. \quad (7)$$

Here,  $d_{x_i}^{p,q}$  and  $d_f^{p,q}$  are the actual distances between particle pairs in physical and reference mixture fraction spaces and the model input parameters  $r_m$  and  $f_m$  are characteristic distances. These two parameters specify the target distance between mixing particles in physical and reference space. A smaller value of one of these quantities increases localness in this respective space, a larger value relaxes the requirement of localness. The independent reference mixture fraction  $\bar{f}$  differs stochastically from the Lagrangian solution  $Z$

but they have a topological similarity [23]. The constant  $\sqrt{3}$  is a geometric factor relating the diagonal of a cubic spatial domain to its side length. Based on a fractal perspective of turbulent scalar contours,  $r_m$  is related to  $f_m$  by [16]

$$r_m = C_m \left( \frac{d\tilde{f}}{dn} \frac{\Delta_L^3}{\Delta_E^{2-D_f}} \frac{1}{f_m} \right)^{1/D_f}, \quad (8)$$

where  $C_m = 0.5$  is a model constant,  $d\tilde{f}/dn$  is the reference mixture fraction gradient normal to the flame,  $\Delta_E$  is the LES filter width,  $\Delta_L$  is the nominal interparticle distance based on the stochastic particle number density and  $D_f = 2.36$  is the fractal dimension of an iso-slicer of mixture fraction [16]. This leaves  $f_m$  as the only input parameter requiring explicit specification. A default value of  $f_m = 0.03$  has been established in the literature [17,19,24,25] and was also applied in our study. As in all past MMC-LES simulations, both  $f_m$  and  $r_m$  are global parameters, where the latter has a value of  $r_m = 0.0033$  m as given by Eq. (8). The relevant quantities such as filtered mixture fraction gradient are calculated one diameter downstream of the jet exit plane in the shear layer region between jet and the pilot where scalar gradients are large.

Two-way coupling ensures consistency between the Eulerian LES and Lagrangian particle schemes. The LES filtered velocity, turbulent diffusivity and mixture fraction are interpolated at particle locations and used in the integration of the stochastic differential equations and mixing model. The particle scheme in-turn provides density feedback to the LES field. Here, the coupling is realised by the solution of additional LES filtered equivalent species and enthalpy transport equation with source terms dynamically matched to the kernel estimation of the exact stochastic particle composition. A detailed explanation can be found in Galindo-Lopez et al. [5].

## 2.2. Lagrangian mixing time scale model

The Lagrangian mixing time scale determines the degree of sub-filter conditional scalar dissipation. In intensive stochastic FDF simulations where there are possibly 10 or more stochastic particles in each LES cell, mixing is constrained to the particle ensemble within each cell. Thus, the particle filter time and length scales are determined from the local filter scales of the Eulerian scheme. The Eulerian mixing time scale has the form

$$\tau_E = \tilde{f}_E^2 / \tilde{\chi}_E, \quad (9)$$

where  $\tilde{f}_E$  is the sub-grid reference mixture fraction variance and  $\tilde{\chi}_E$  is the scalar dissipation, respectively. For these quantities, standard models are commonly used in combustion LES investigations that lead to

$$\tilde{f}_E^2 = C_f \Delta_E^2 \nabla \tilde{f} \cdot \nabla \tilde{f} \quad (10)$$

for the sub-grid variance. Here, the scaling parameter  $C_f$  is usually set to  $C_f = 0.1$  [26], and

$$\tilde{\chi}_E = 2(D + D_t) \nabla \tilde{f} \cdot \nabla \tilde{f}. \quad (11)$$

Substitution of Eqs. (10) and (11) into Eq. (9) results in

$$\tau_E = \frac{C_f \Delta_E^2}{2(D + D_t)}. \quad (12)$$

Corresponding expressions for the Lagrangian time scale have been discussed in Vo et al. [20] and two models are briefly described here.

### 2.2.1. Model 1: Cleary and Klimenko model (C&K)

The C&K model was developed in [16] and has been used in most of the MMC-LES related publications to date. It was derived

on the basis of simple geometrical reasoning that led to the time scale expression

$$\tau_{L,C\&K} = \frac{\beta C_f d_f^2}{2(D + D_t) \nabla \tilde{f} \cdot \nabla \tilde{f}}. \quad (13)$$

### 2.2.2. Model 2: anisotropic model (a-ISO)

As it was shown in Vo et al. [20], the C&K mixing time scale model underpredicts conditional variances and a new mixing time scale model was proposed therein. The new model attempts to account for the anisotropy of the turbulent structures at the Lagrangian filter size and has the form

$$\tau_{L,a-ISO} = \frac{C_f d_x^2}{2(D + D_{t,L})}, \quad (14)$$

where  $D_{t,L}$  is a turbulent sub-grid scale diffusivity which scales to the respective Lagrangian length scales  $D_{t,L} = d_x / \Delta_E D_t$ . It should be noted that the a-ISO model has a similar form to the Eulerian mixing time given by Eq. (12).

## 3. Experimental configuration

The Sandia DME series consists of a piloted, partially premixed turbulent DME/air jet flame with a jet diameter of  $D = 7.45$  mm. The jet exit bulk velocities are  $U_b = 45.9$  m/s, 68.85 m/s, 91.8 m/s, 114.75 m/s for the corresponding flame series Reynolds numbers (29,300–73,250), respectively, while the hot pilot gas inlet velocities are 6.4 m/s, 9.3 m/s, 12.2 m/s and 15.1 m/s. The pilot velocity of flame DME-G is reduced to 80% of that for flame G, resulting in a pilot bulk velocity of 12.08 m/s.

An extensive set of experimental data is available for model validation. The measurements include stereo particle image velocimetry (SPIV) of the three-dimensional velocity field, simultaneous laser-induced fluorescence (LIF) imaging of OH and CH<sub>2</sub>O and 1D Raman/Rayleigh measurements of seven major species (CO<sub>2</sub>, O<sub>2</sub>, CO, N<sub>2</sub>, DME, H<sub>2</sub>O, H<sub>2</sub>).

OH-LIF was excited by the frequency-doubled output of a Nd:YAG-pumped dye laser tuned to the Q<sub>1</sub>(6) line ( $\lambda = 283.01$  nm, 1.2 mJ/pulse) of the  $A^2\Sigma^+ \leftarrow X^2\Pi^+$  ( $v' = 1, v'' = 0$ ) band of OH. CH<sub>2</sub>O-LIF was excited by the third harmonic of an injection seeded Nd:YAG laser (42 mJ/pulse) tuned to  $\lambda = 354.83$  nm to excite overlapping transitions in the 4<sub>1</sub><sup>0</sup> band of the  $\tilde{A}^1A_2 \leftarrow \tilde{X}^1A_1$  system. The projected pixel size is 53  $\mu$ m for OH and 19  $\mu$ m for CH<sub>2</sub>O-LIF imaging. Statistics of the LIF measurements were compiled from 700 to 1000 single-shot images, and the resulting mean and RMS profiles were filtered using the DCT-PLS method of Garcia [27].

Mole fractions of CO<sub>2</sub>, O<sub>2</sub>, CO, N<sub>2</sub>, H<sub>2</sub>O, H<sub>2</sub>, and accumulated hydrocarbons including DME, CH<sub>4</sub>, C<sub>2</sub>H<sub>4</sub>, C<sub>2</sub>H<sub>6</sub>, CH<sub>3</sub> and temperature were measured using simultaneous 1D Raman/Rayleigh scattering and CO laser induced fluorescence (CO-LIF) at the Combustion Research Facility of the Sandia National Laboratories. Previously published data of the turbulent DME flame series and the additional data reported in this work were taken during the same measurement campaign. The most relevant information about the experimental setup is outlined below. For further details the reader is referred to [9]. The Raman/Rayleigh setup consisted of four sequentially-fired frequency-doubled Nd:YAG lasers operating at 532 nm. In addition, a Nd:YAG-pumped tunable dye laser was used for the simultaneous CO-LIF measurement. The redundant measurement by LIF and Raman scattering of CO provided two important benefits in the DME flames. While CO-LIF is more accurate in regions of the flame with large fluorescence interferences from C<sub>2</sub> and polycyclic aromatic hydrocarbons, CO-Raman provided a more reliable calibration stability. Therefore, the interference-free region of the CO-Raman was used to correct for drift in the CO-LIF calibration factor. For the Raman/Rayleigh

measurements a combined energy of 1 J/pulse at 532 nm was focused to a projected beam waist of 200  $\mu\text{m}$ . The Raman, Rayleigh and CO-LIF light along a 6 mm line segment is separated and acquired on three cameras in a custom spectrometer as described in [28]. The data was processed using the hybrid matrix inversion method [29] using laminar flame calculations of different strain rates to derive Raman response and crosstalk curves and temperature-dependent Rayleigh scattering cross section models to account for DME decomposition into smaller hydrocarbons as outlined in [8]. The processed species and temperature data is matched to the Raman pixel resolution of 102.6  $\mu\text{m}/\text{pixel}$ .

Earlier studies on the DME flame series comprised flames D–F only with Reynolds numbers ranging from  $Re_D = 29, 300$  to 58, 600. As DME requires higher strain rates for local extinction than methane and DME flame F showed little deviations from a fully burning flame, the flame series was extended to flames G ( $Re_D = 73, 250$ ) and DME-G'. Flame DME-G' has the same Reynolds number as flame G but the pilot velocity was reduced to 80% of the original value to promote increased levels of extinction. Major species composition, temperature and mixture fraction are available for the full flame series (D–DME-G'), but the stereo particle image velocimetry (PIV) and simultaneous laser-induced fluorescence imaging (LIF) of OH and CH<sub>2</sub>O are available for flames D to G only. This is due to the fact that flame DME-G' was introduced at a later stage to include a flame at the brink of global extinction. Flame DME-G' is indeed quite sensitive to any change of condition and poses a significant challenge to combustion models.

## 4. Numerical configuration

### 4.1. Solver setup and boundary conditions

The MMC-LES model has been implemented into a code called *mmcFoam* which is compatible with OpenFOAM open source C++ libraries. The sparse-Lagrangian MMC classes are coupled with OpenFOAM's existing compressible LES solver. The LES solves equations for spatially filtered quantities where the turbulent sub-grid viscosity is modelled by the  $\sigma$ -model [30] and a model constant of  $C_\sigma = 1.5$  is used.

The cylindrical computational domain extends  $45D$  in the axial direction and  $15D$  in the radial direction. There are 145 cells distributed along the domain diameter, where the jet diameter is resolved by 53 cells which results in a characteristic cell size of 140  $\mu\text{m}$  within the jet at the jet exit plane. The circumferential and the axial directions of the domain are resolved by 60 and 480 cells, respectively, resulting in approximately 2 million LES grid cells overall. Gradual mesh stretching yields the largest characteristic cell sizes of around 1.15 mm at the outflow boundary. Over 80 % of the kinetic energy is resolved everywhere with the exception of regions in the immediate vicinity of the burner lip that are, as usual, under-resolved. Separate pipe flow simulations were conducted inside the fuel nozzle to provide realistic inflow turbulent velocity boundary conditions for the flame calculations along with zero-gradient velocity outflows. The hot pilot velocities have been set to match the experimental bulk exit velocities. Pressure boundaries are zero-gradient at the inlets and fixed total pressure at the outlets. To minimise numerical diffusion a second-order central difference scheme is used for the filtered momentum equation, while all other transport equations are discretised by the total variation diminishing (TVD) scheme reverting to first order in regions of large gradients. On the particle side, nominally one particle for every 4.5 LES cells is used corresponding to 450,000 particles overall. This sparse distribution of particles is at least two orders of magnitude lower than commonly employed in intensive FDF simulations with conventional mixing models with at least 10 particles per LES grid cell. However, compared to earlier MMC-LES

investigation with as few as one particle for every 10 or even 30 grid cells this number is increased, and this is done to achieve a stable density coupling between the Eulerian and Lagrangian schemes for the high Reynolds number cases where local extinction events are predominant and density variations in space and time are large. To enable a comparison among all Reynolds number configurations the particle resolution is kept constant for all the simulations presented below. It was demonstrated previously that by keeping the model parameter  $f_m$  constant while particle number is varied the model remains unchanged and predictions are insensitive to the particle number [16,19]. We use the detailed DME reaction mechanism of Zhao et al. [31] containing 55 species and 290 reactions. The computational cost for the particle solution is about 3.65 times that of the LES solution. After each simulation reached a statistically stationary state, statistics were collected for a minimum of 15 flow-through times to achieve statistical convergence. The total computational time for each simulation is about 2900 CPU hours on a Intel Xeon processor (E5-2680 v3) architecture.

### 4.2. Computation of LIF signals

In Section 5 we compare measured with computed LIF signals of OH and CH<sub>2</sub>O. As in our earlier paper [7], the experimental LIF signals are not converted into species concentrations due to the absence of simultaneous temperature and major species measurements. Instead, comparison is made against a modelled LIF signal that is computed in a post-processing step from sampled stochastic particles information, e.g. temperature and composition fields. A minimum of 500,000 particles were sampled per cross-section over a certain sampling time exploiting the statistically stationary nature of the flames. The instantaneous temperature and mole fractions were used to compute the Boltzmann fraction population of the OH-LIF transition and the total collisional quenching rate using quenching cross sections from Tamura et al. [32]. The simulation of the formaldehyde LIF signal is less certain due to the lack of available quenching cross sections over a wide range of temperatures. More details on the experimental procedure and on the computation of the simulated LIF signals can be found in [1] and [7].

### 4.3. Comparison of simulations with Raman/Rayleigh experiment data

The mixture fraction is an essential property to quantify the mixing process in non-premixed combustion. To enable the comparison between the model predictions and the experimental data, we calculate a modified version of the numerical mixture fraction defined by Bilger [8,9,33],

$$\xi = \frac{2(Z_C - Z_{C,2})/M_C + (Z_H - Z_{H,2})/2M_H}{2(Z_{C,1} - Z_{C,2})/M_C + (Z_{H,1} - Z_{H,2})/2M_H}, \quad (15)$$

where  $Z_C$  and  $Z_H$  are the elemental mass fractions of carbon and hydrogen and based on the measured subset of species. In Eq. (15),  $M_C$  and  $M_H$  are the elemental molar masses and the subscripts 1 and 2 refer to the jet and coflow conditions, respectively. Experimental and numerical data are consistently reported based on the adapted mixture fraction as outlined in Fuest et al. [8].

## 5. Results

In this section, selected results of the entire flame series are presented and these are complemented by the complete set of data that is provided in the Supplementary Material online. First, we analyse computed spatial profiles against experimental data. Then, conditionally averaged quantities such as temperature and species

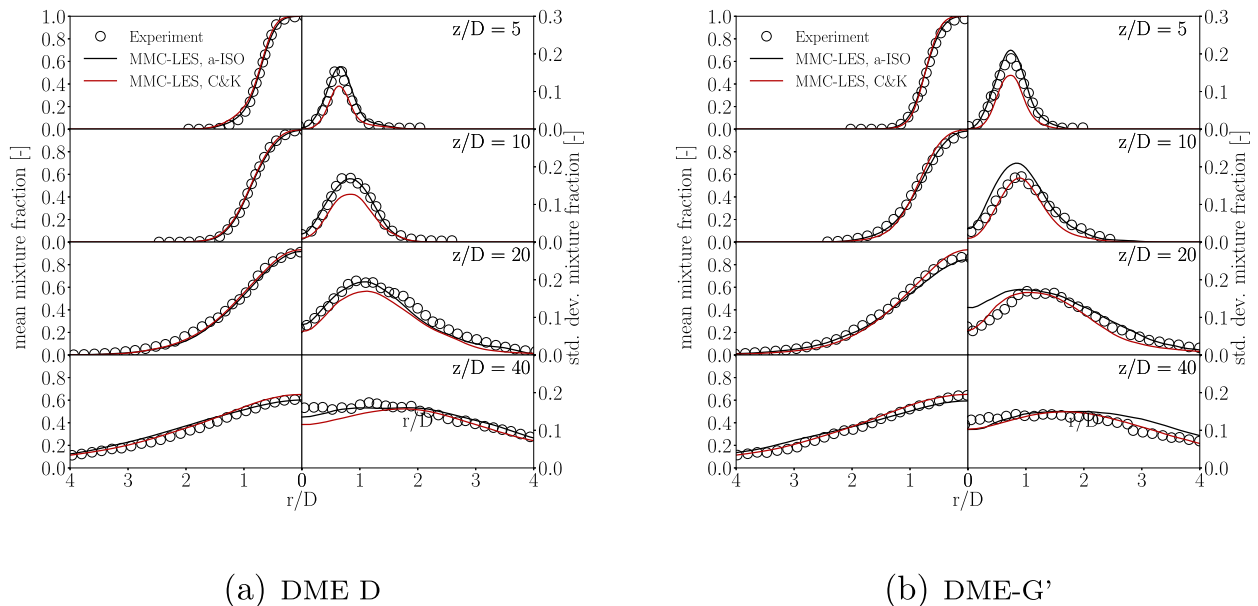


Fig. 1. Mean and standard deviation profiles of mixture fraction  $\xi$  at different heights above the burner.

concentrations will be discussed. This is the first publication presenting both experimental and numerical data from flames DME-G and DME-G', where local extinction events significantly affect the flame. Flame DME-G' is quite sensitive to the pilot velocity and by setting the simulation's pilot velocity to 80% of that of flame G, the flame experienced global blow-off. A rather stable solution was obtained in the modelling by increasing the pilot velocity to 85% instead. Even then, the model occasionally produces global extinction due to rare turbulent events. This high sensitivity of the flame at near-blowoff conditions is consistent with the observed behaviour in the laboratory. To circumvent the problem numerical sampling for DME-G' is conducted until a rare global extinction event occurs. In the present case, sampling times for DME-G' are 5 domain flow through times based on the jet bulk velocity.

### 5.1. Spatial mean profiles

We first compare computed radial profiles of mixture fraction and temperature against experimental data at four axial positions. In Fig. 1 mean and standard deviation of mixture fraction are shown for the flames DME-D and DME-G' and the performance of the two mixing time scale models C&K and a-ISO are compared. For flame DME-D very good agreement with the measured mean values is achieved using both models. However, the results are slightly different for the standard deviation. The C&K model notably underpredicts the peak RMS values in the shear layer at upstream positions with somewhat better predictions further downstream, while the a-ISO model predictions are generally good everywhere in the domain. Further downstream, where mixture fraction gradients and mixing rates are lower, results from both mixing time scale models are in very good agreement with the experimental data. For flame DME-G' the mean mixture fraction predicted by the a-ISO model is in good agreement with the measurements but an underprediction of mixing at the centreline yields relatively high values for the RMS at  $z/D = 10$  and 20. Here, the C&K model seems to capture the centreline behaviour more accurately. Similar results are obtained for flames DME-F and DME-G (cf. supplementary information).

Mean temperatures and standard deviations are shown in Fig. 2. For flame DME-D the predicted mean values do not differ significantly from the measured data with the C&K model giving slightly higher peak temperature values throughout the flame. The radial dependence of the standard deviation and its magnitude are matched very well by computations using the a-ISO model while the C&K time scale closure seems to overpredict mixing leading to a notable underprediction at  $z/D = 5$  and 10. Again, comparable results have been obtained for flames DME-F and DME-G and are shown in the supplementary information. The trends are somewhat different for flame DME-G'. The a-ISO model captures local extinction events better, and the peak temperature reduction by 580 K between flames DME-D and DME-G' is predicted accurately at  $z/D = 5$ . However, for the a-ISO model re-ignition is delayed; the a-ISO predictions are too low at  $z/D = 10$ . Re-ignition occurs further downstream leading to a good match with experimental data for  $z/D > 20$ . In contrast, the C&K model underpredicts the level of local extinction with averaged peak temperatures always above 1680 K. This effect is most noticeable at  $z/D = 5$ , where the predicted peak mean value exceeds that of the measurements by 326 K. Due to the lack of local extinction it is not surprising that fully burning solutions are predicted at  $z/D = 10$  providing an apparently better match with experimental mean values than the a-ISO model. For the C&K model radial profiles of temperature standard deviation are generally well predicted, but are more narrow at  $z/D = 10$  and 20.

A comparison of computations with LIF measurements of the radical species OH and  $\text{CH}_2\text{O}$  confirms the observed sensitivities towards increases in strain rates when moving from flame D to G'. For flame DME-G', no LIF measurements are available, but numerical results are provided for completeness. The experimental values are normalised by the maximum mean value at  $z/D = 5$  of the DME-D flame. Similarly, computational results are normalised by their corresponding maximum values leading to a signal strength of 1 at this position.

Figure 3 depicts the OH-LIF signals at all axial positions where measurements exist. The overall agreement is good for both models. It seems that the a-ISO model captures the variation of the

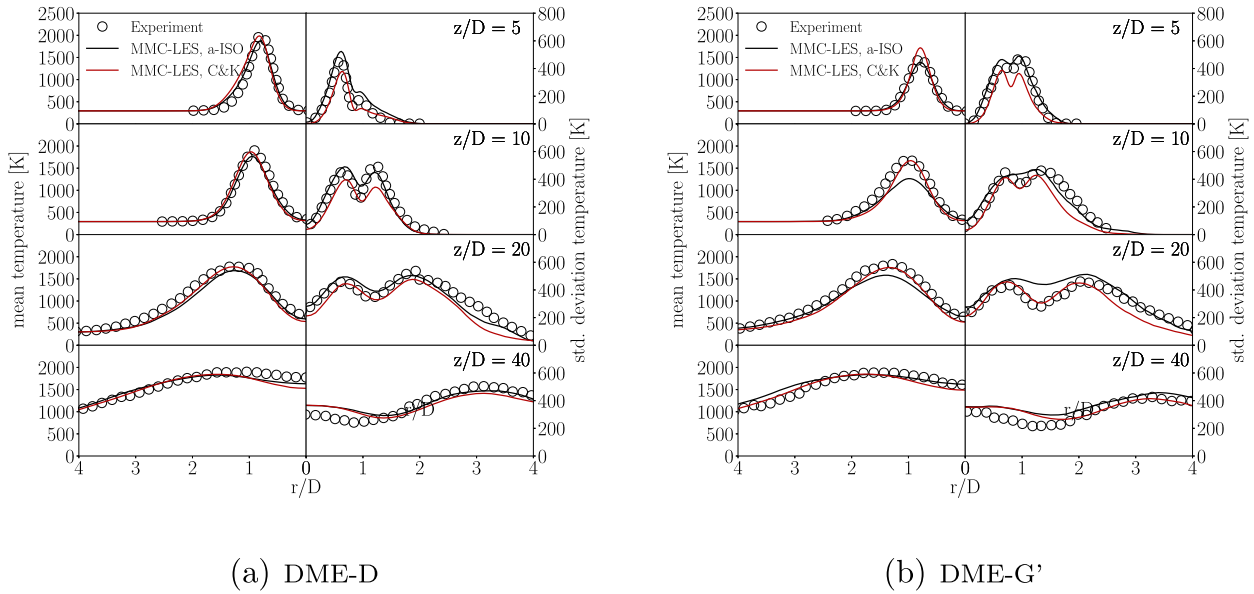


Fig. 2. Mean and standard deviation profiles of temperature at different heights above the burner.

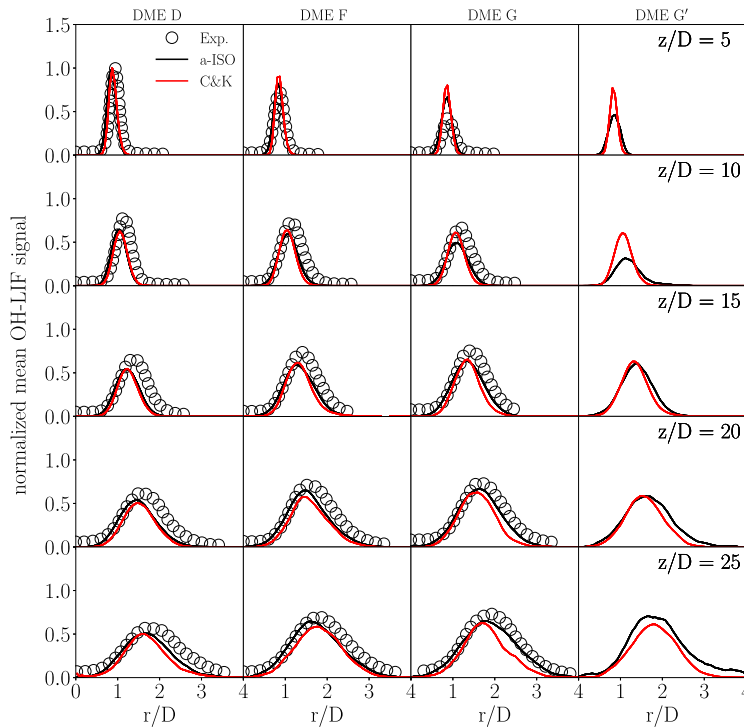


Fig. 3. Mean profiles of OH-LIF signal at different heights above the burner.

peak normalised OH signal with Reynolds number slightly better than the C&K model but differences are only significant for flame DME-G' where a-ISO is expected to capture the extinction events (and therefore also the intermediate species concentrations) better as was observed in Fig. 2. For downstream positions of flame DME-G, the a-ISO model is generally in much better agreement with the experimental data than the C&K model. Similar observations can be made for the RMS of the OH-LIF signal (cf. supplementary

material); predictions by the models do not differ significantly and are comparable in quality to the RMS predictions of temperature. They capture the radial dependence very well, but indicate some overprediction of up to 30% at downstream positions. Despite all these similarities between the computations it should not be forgotten that the comparison of computations with experiments requires normalised LIF signals. The normalisation factors of the C&K and a-ISO calculations differ by 30%. Thus, the maximum OH

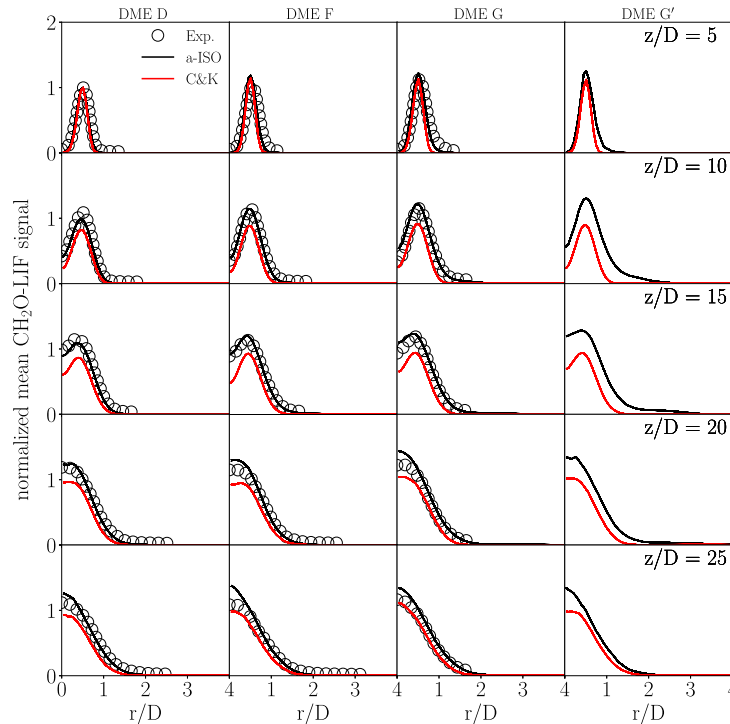


Fig. 4. Mean profiles of  $\text{CH}_2\text{O}$ -LIF signal at different heights above the burner.

concentration at  $z/D = 5$  predicted by the C&K model is higher by the same percentage than that predicted by the a-ISO model, but the measured LIF signals do not allow conclusions to be reached about the accurate absolute values of OH.

Slightly different trends are observed in the mean radial profiles of the  $\text{CH}_2\text{O}$ -LIF signal shown in Fig. 4. Results for a-ISO are overall better than for C&K, although the increase of formaldehyde with increasing Reynolds number is slightly overpredicted by the a-ISO model while the C&K model shows hardly any sensitivity to variations in Reynolds number. While we observe an overprediction of the normalised formaldehyde concentration with the a-ISO model for more downstream positions, the C&K model constantly underpredicts the signal. The predicted profiles of the RMS of the  $\text{CH}_2\text{O}$ -LIF signal (supplementary information) capture the measured radial dependencies very well but a-ISO tends to overpredict the normalised fluctuations by up to 30% for  $z/D > 20$ . The better match of the C&K model may be misleading as (again) normalisation leads to comparable LIF-signals, but absolute  $\text{CH}_2\text{O}$  concentrations differ notably with the C&K model giving a normalisation factor 50% higher than that of the a-ISO model. Using the same normalisation factor leads to differences in the predicted means but very similar results for the RMS.

## 5.2. Conditional statistics

Differences in predictions due to time scale closure are apparent but difficult to quantify on the basis of unconditional means and RMS alone. In particular the normalisation needed for the comparison with OH- and  $\text{CH}_2\text{O}$ -LIF signals may lead to erroneous conclusions. We therefore compare now conditional quantities that are typically used, firstly, to separate the influence of the flow field modelling from modelling of the turbulence-chemistry interactions and, secondly, to better analyse the flame structure and possible deviations from a flamelet-like behaviour due to turbulence.

Figure 5 shows scatter plots of temperature versus mixture fraction,  $\xi$ , for flames DME-D to DME-G' at  $z/D = 7.5$  where extinction levels are expected to be highest, and therefore deviations from a simple flamelet structure should be most notable if they exist. For flame DME-D (top row), it is apparent that the flame has a flamelet-like structure due to the relatively low level of turbulence-chemistry interactions and hardly any fluctuations around the conditional mean exist. This is correctly reproduced by both mixing time scale models, although departures from a flamelet solution are slightly higher for the a-ISO model. An increase in Reynolds number from flame DME-D to DME-F leads to a small increase in local extinction events as indicated by the data points that lie below the main temperature profile. This is captured well by the a-ISO model, but the C&K model fails to predict any local extinction at all. For flames DME-G and DME-G', the experimental data reveal moderate to significant local extinction and an almost bimodal distribution is observed for flame DME-G'. The a-ISO mixing time scale model approximates the correct level of extinction for both flames and even predicts the bimodal distribution for flame DME-G'. A fully burning branch and an extinguished branch can easily be identified. In contrast, the C&K mixing time scale model predicts conditional means similar to the DME-D flame for all Reynolds number cases and, as in earlier publications [19,21], scatter around the mean is always strongly underpredicted. It is thus apparent that the mixing time scales predicted by the C&K model do not correctly (or not at all) account for the effect of turbulence on the chemistry, and the reasons for the Reynolds number dependence of the unconditional means by C&K are therefore most due to differences in large scale fluctuations of the underlying mixing field as the Reynolds number is varied.

The reason for the differences in conditional fluctuations for the C&K and a-ISO models warrants some further discussion and the time scales are quantitatively investigated. Figure 6 shows  $\tau_L$  from both Eqs. (13) and (14) conditioned on mixture fraction. We

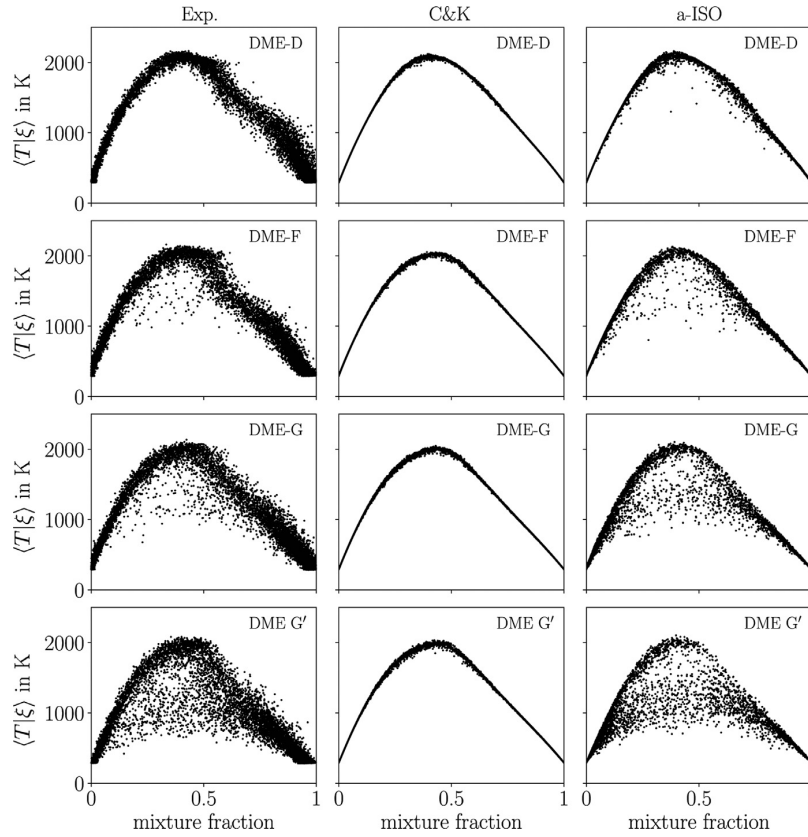
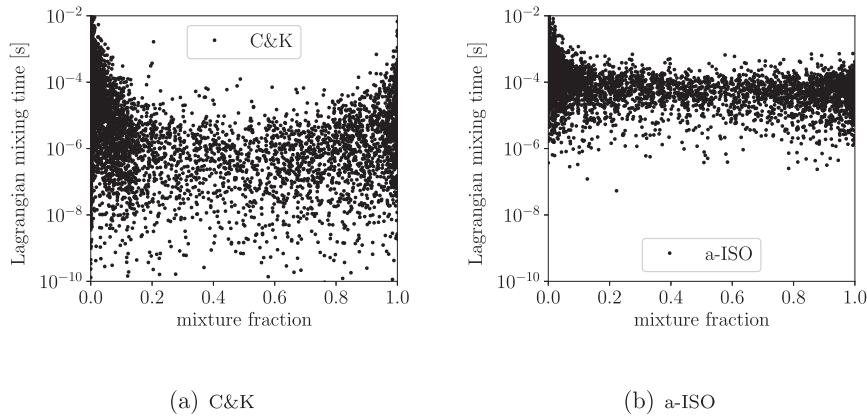


Fig. 5. Stochastic particle temperature conditioned on mixture fraction  $\xi$  at location  $z/D = 7.5$ . A total number of 10,000 samples are shown in each plot.



(a) C&K

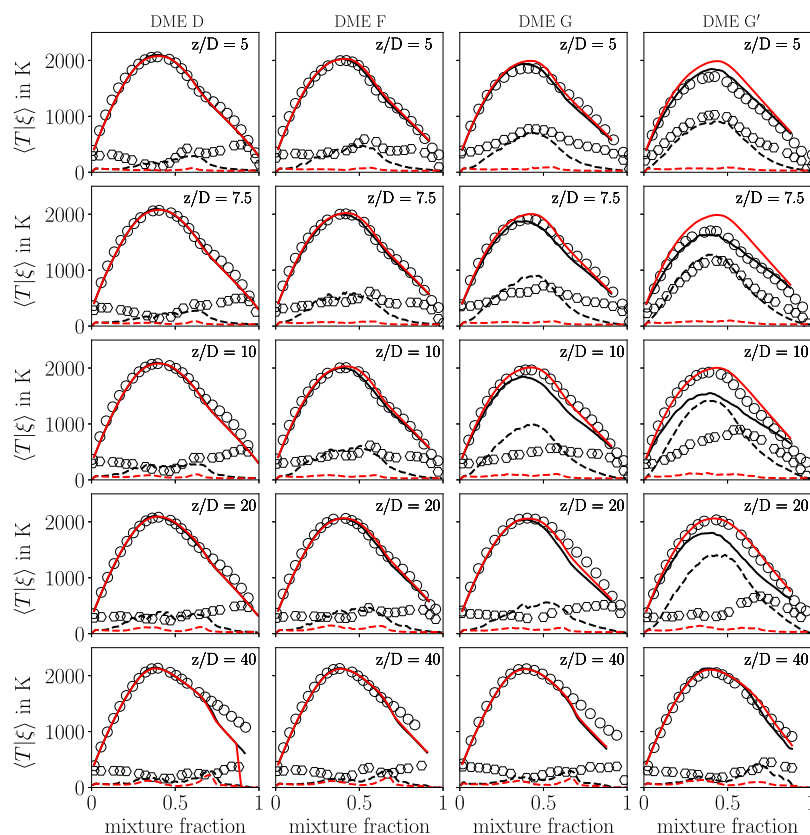
(b) a-ISO

Fig. 6. Scatter plots of the Lagrangian mixing time of (a) the C&K and (b) the a-ISO models conditioned on mixture fraction at  $z/D = 7.5$ . 10,000 samples are shown for each model.

observe that the two models predict very different values over the entire mixture fraction space with the C&K model giving, on average, a time scale about 4.5 times lower than the values obtained with the a-ISO model. This result is similar to results from DNS of a turbulent shear layer as reported in Vo et al. [20]. In regions close to stoichiometric ( $\xi = 0.35$ ) where mixing is expected to influence the flame structure most, differences can be up to two orders of magnitude leading to significantly higher mixing rates for the C&K model. Hence, the C&K model mixes very quickly towards

the burning solution preventing any local extinction. The much longer mixing times of the a-ISO model reduce mixing and allow for local extinction events to occur and therefore better approximate the effects of turbulence on chemistry in this flame.

A more quantitative comparison is given in Fig. 7, where conditionally averaged means and standard deviations of temperature are shown. For the a-ISO model, conditionally averaged mean profiles are in very good agreement with experimental data and a shortcoming of the model can be identified only for flame DME-G' at  $z/D = 10$  and



**Fig. 7.** Profiles of temperature conditioned on mixture fraction  $\xi$  at different downstream locations. Experiment (symbols), a-ISO (black), C&K (red). The conditional standard deviation is multiplied by a factor of 3. (For interpretation of the references to colour in this figure caption, the reader is referred to the web version of this article).

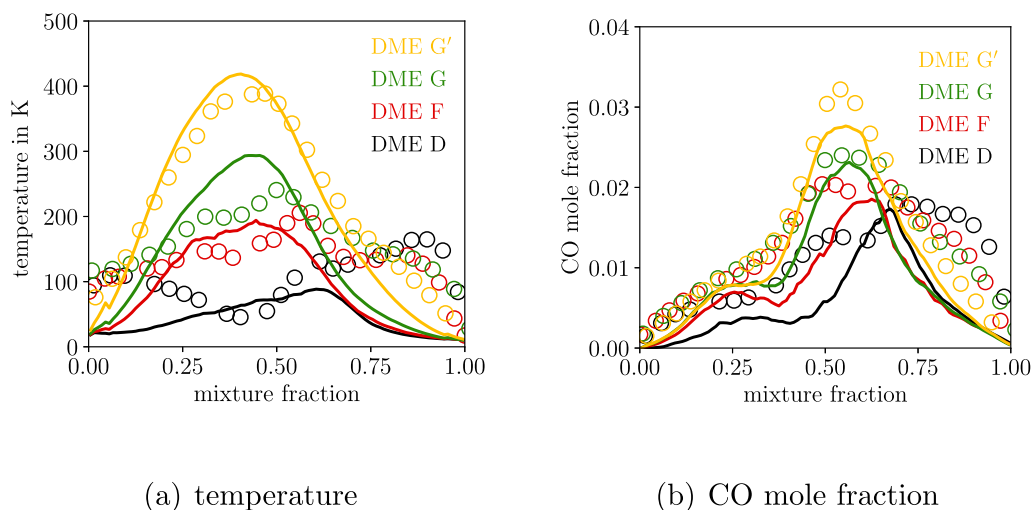


**Fig. 8.** Profiles of standard deviation of (a) temperature and (b) CO mole fraction conditioned on mixture fraction  $\xi$  at  $z/D = 7.5$  for the different Reynolds number flames. Only results obtained with the a-ISO model are shown here: experiment (symbols) and MMC-LES (solid line).

20, where the model predicts a delayed re-ignition of the flame and a notable underprediction of temperature. The plots once more reveal that predictions by the C&K model do not reflect any change in turbulence levels at axial locations where moderate to significant extinction occurs ( $z/D = 5$  and  $z/D = 7.5$ ) but tend to

provide relatively constant levels of conditionally averaged temperatures at all downstream locations for all Reynolds numbers.

The differences in predicted conditional temperature standard deviation by the two models are significant. While the C&K model does not yield any conditional fluctuations and wrongly predicts

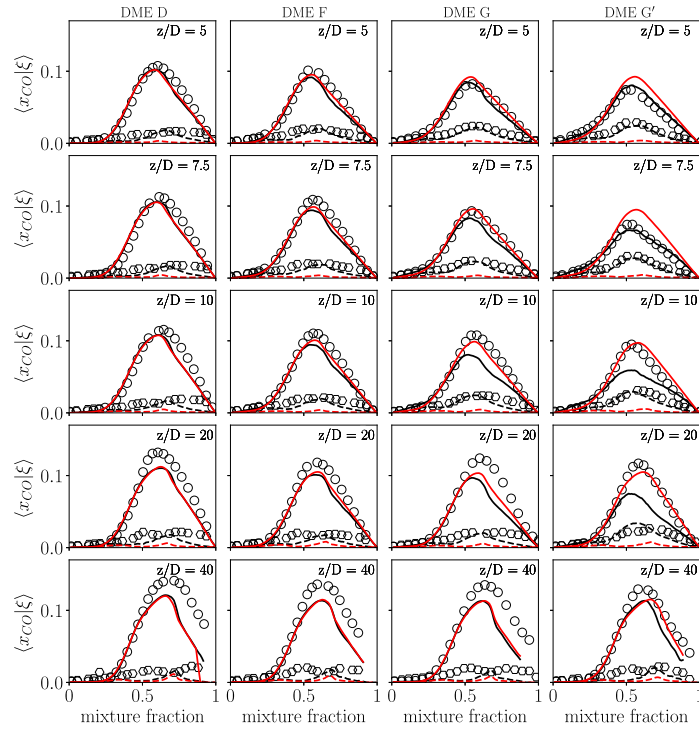


**Fig. 9.** Profiles of CO mole fraction conditioned on mixture fraction  $\xi$  at different downstream locations. Experiment (symbols), a-ISO (black), C&K (red). (For interpretation of the references to colour in this figure caption, the reader is referred to the web version of this article.)

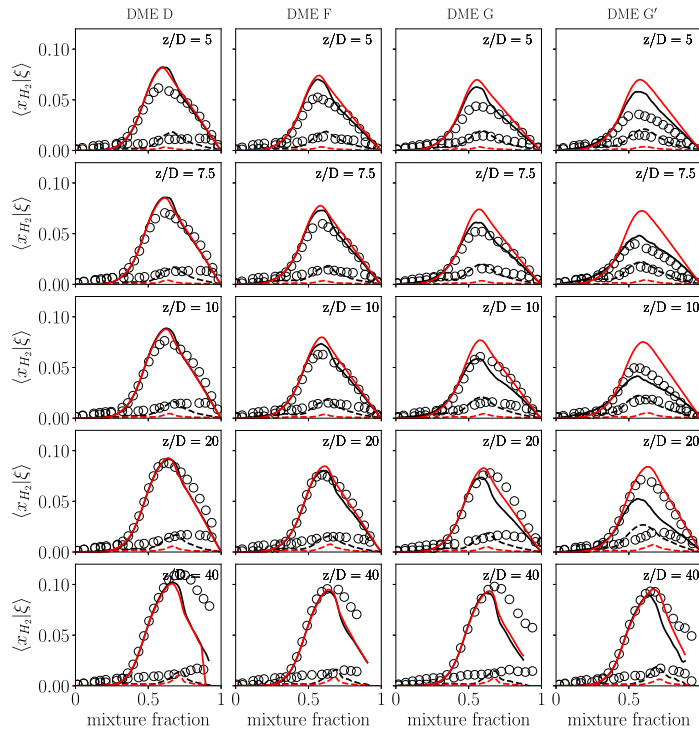


**Fig. 10.** Profiles of H<sub>2</sub> mole fraction conditioned on mixture fraction  $\xi$  at different downstream locations. Experiment (symbols), a-ISO (black), C&K (red). (For interpretation of the references to colour in this figure caption, the reader is referred to the web version of this article.)

a flamelet-like structure throughout the entire computational domain and for all flames in the series, a-ISO gives very good agreement between predictions and measurements except in flame G' at  $z/D = 10$  and  $20$  where the re-ignition is delayed and conditional variance is overpredicted. The elevated level of experimental conditional fluctuations of temperature near  $\xi = 0$  and  $\xi = 1$  is due mainly to uncertainty in mixture fraction, which, in regions of high gradients in the conditional mean temperature, causes a broadening of the temperature distribution within a given conditioning interval. The low levels of fluctuations at the bounds predicted by MMC-LES are thus reasonable.

For better illustration, the important observations are summarised in Fig. 8. Here, the conditionally averaged standard deviation of temperature for the different flames are plotted in one figure showing results from the a-ISO model only. Figure 8 illustrates clearly that MMC with a-ISO captures the progression of local extinction and its effect on flame structure very well. These observations are further corroborated by analysing the conditional profiles of the intermediate species CO and H<sub>2</sub> in Figs. 9 and 10, respectively. The mean profiles obtained by both models are very similar for flame DME-D and differ only for the two highest Reynolds number cases. The peak conditional mean profiles tend to be overpredicted by the C&K model and are better matched by the a-ISO model and this is particularly evident at  $z/D = 5$  and  $7.5$ . Corresponding to the observations made above with respect to conditional temperature, re-ignition of the locally extinguished fluid elements tends to be delayed for the a-ISO model leading to deviations particularly at  $z/D = 10$  and here, the relatively constant conditional CO and H<sub>2</sub> profiles predicted by C&K provide an apparently better match. Similar to the results shown above, the most obvious differences between the two models are in the predicted conditional standard deviations which are grossly underestimated by the C&K model but are captured well by the a-ISO model with the exception of the overprediction of conditional RMS at  $z/D = 10$  due to the delayed reignition (see also Fig. 8(b)).

## 6. Conclusions

Sparse-Lagrangian MMC-LES with a single set of turbulent model constants has been applied to the Sandia DME flame series which consists of four partially premixed DME/air flames with Reynolds numbers ranging from 29,300 for flame D to 73,250 for flames G and G'. Experimental data for flames G and G' are presented here for the first time and this paper is also the first attempt to simulate them with any model. As the Reynolds number increases so do local extinctions and turbulence-chemistry interactions. Flame D has negligible local extinctions and Flame G', which has the same Reynolds number as flame G but with 20% lower pilot flame power, exhibits very strong local extinction approaching global blow-off. MMC-LES is a filtered density function model. Here, a sparse stochastic particle distribution (nominally 1 particle for every 4.5 LES cells) is used to predict the reactive turbulent composition field and this represents a significant reduction in particle number and associated computational cost relative to conventional intensive FDF methods which have many more particles than LES cells. This computational saving is very attractive for flames with complex chemical kinetics and its application for DME represents a step along the path to applying the model to practical fuels that may be used in real engines.

The ability to accurately predict the full DME flame series using one model and one set of model constants constitutes a very thorough validation. The key turbulence submodels that have been used here are the  $\sigma$ -model for the subgrid turbulent viscosity and the MMC mixing model for dissipation of subgrid conditional variance of the reactive composition. For the turbulent viscosity model the model constant  $C_\sigma = 1.5$  is set for all cases. In the MMC mixing

model localness is enforced in a reference space given by the LES filtered mixture fraction field and a localness constant of  $f_m = 0.03$  is used in all simulations. Two mixing time scale models have been tested; the original MMC time scale model (called C&K) and a recently proposed model which applies a consistent anisotropic treatment of the subgrid scalar fields (called a-ISO). The a-ISO model has been applied to individual DNS and experimental flames in the past, and this is the first time it has been tested against a full flame series.

Statistical results from the simulations are compared to experimental data in both unconditional and conditional form. Overall the unconditional statistics are very well predicted and both the C&K and a-ISO models are of comparable accuracy. Bigger differences are revealed however in the conditional statistics. In agreement with the earlier work, it is revealed that a-ISO does a good job of capturing the correct level of conditional fluctuations and their dependence on Reynolds number. On the other hand the C&K model grossly underpredicts the conditional variances and fails to predict the trend of increasing conditional variances with increasing Reynolds number. This difference between the two models was analysed and found to be due to the much smaller mixing time scale values that are obtained by the C&K model which lead to a very rapid dissipation of fluctuations towards the burning (flamelet) structure. The a-ISO model produces very good results for flames D to F at all locations and for all quantities. For flames G and G' the a-ISO model very accurately predicts the extent of local extinction in the upstream regions of the flame but also yields a delayed reignition and, as a result, the peak conditional temperatures are underpredicted and conditional variances are overpredicted at  $z/D = 10$  and  $20$ . Further downstream the predictions are, once again, in excellent agreement with the data.

## Acknowledgments

We would like to acknowledge the financial support by the Deutsche Forschungsgemeinschaft (DFG) (SPP 1980-KR 3684/12) and by the 2016 Universities Australia – Germany Joint Research Co-operation Scheme. The experimental data was obtained through partial support from the Combustion Energy Frontier Research Center funded by the US Department of Energy, Office of Science, BES under Award DE-SC0001198. R. S. Barlow, B. Coritton, and J. H. Frank gratefully acknowledge support of the U.S. Department of Energy, Office of Basic Energy Sciences, Division of Chemical Sciences, Geosciences, and Biosciences. Sandia National Laboratories is a multimission laboratory managed and operated by National Technology and Engineering Solutions of Sandia, LLC., a wholly owned subsidiary of Honeywell International, Inc., for the U.S. Department of Energy's National Nuclear Security Administration under contract DE-NA-0003525. The views expressed in the article do not necessarily represent the views of the U.S. Department of Energy or the United States Government.

## Supplementary material

Supplementary material associated with this article can be found, in the online version, at doi:10.1016/j.combustflame.2019.06.026.

## References

- [1] S. Popp, F. Hunger, S. Hartl, D. Messig, B. Coritton, J.H. Frank, F. Fuest, C. Hasse, LES flamelet-progress variable modelling and measurements of a partially-premixed turbulent dimethyl ether jet diffusion flame, *Combust. Flame* 162 (2015) 3016–3029.
- [2] M.R. Roomina, R.W. Bilger, Conditional Moment Closure (CMC) predictions of a turbulent methane-air jet flame, *Combust. Flame* 125 (2001) 1176–1195, doi:10.1016/S0010-2180(01)00237-1.

- [3] S.B. Pope, PDF methods for turbulent reacting flows, *Prog. Energy Combust. Sci.* 11 (1985) 119–192, doi:10.1016/0360-1285(85)90002-4.
- [4] A.Y. Klimenko, S.B. Pope, The modelling of turbulent reacting flows based on multiple mapping conditioning, *Phys. Fluids* 15 (7) (2003) 1907–1925, doi:10.1063/1.1575754.
- [5] S. Galindo-Lopez, F. Salehi, M.J. Cleary, A.R. Masri, G. Neuber, O.T. Stein, A. Kronenburg, A. Varna, E.R. Hawkes, B. Sundaram, A.Y. Klimenko, Y. Ge, A stochastic multiple mapping conditioning computational model in OpenFOAM for turbulent combustion, *Comput. Fluids* 172 (2018) 410–425, doi:10.1016/j.compfluid.2018.03.083.
- [6] R.S. Barlow, International Workshop on Measurement and Computation of Turbulent Nonpremixed Flames (TNF), Sandia, available at <http://www.tnfworkshop.org> (2015).
- [7] B. Coriton, M. Zendeledel, S. Ukai, A. Kronenburg, O.T. Stein, S.-K. Im, M. Gamba, J.H. Frank, Imaging measurements and LES-CMC modeling of a partially-premixed turbulent dimethyl ether/air jet flame, *Proc. Combust. Inst.* 35 (2015) 1251–1258, doi:10.1016/j.proci.2014.06.042.
- [8] F. Fuest, R.S. Barlow, J.-Y. Chen, A. Dreizler, Raman/Rayleigh scattering and CO-LIF measurements in laminar and turbulent jet flames of dimethyl ether, *Combust. Flame* 159 (8) (2012) 2533–2562, doi:10.1016/j.combustflame.2011.11.001.
- [9] F. Fuest, G. Magnotti, R.S. Barlow, J.A. Sutton, Scalar structure of turbulent partially-premixed dimethyl ether/air jet flames, *Proc. Combust. Inst.* 35 (2) (2015) 1235–1242, doi:10.1016/j.proci.2014.07.062.
- [10] G. Thomas, B. Feng, A. Veeraragavan, M.J. Cleary, N. Drinnan, Emissions from DME combustion in diesel engines and their implications, *Fuel Process. Technol.* 119 (2014) 286–304, doi:10.1016/j.fuproc.2013.10.018.
- [11] F. Fuest, R.S. Barlow, G. Magnotti, J.A. Sutton, Scalar dissipation rates in a turbulent partially-premixed dimethyl ether/air jet flame, *Combust. Flame* 188 (2018) 41–65, doi:10.1016/j.combustflame.2017.09.020.
- [12] J. You, Y. Yang, S.B. Pope, Effects of molecular transport in LES/PDF of piloted turbulent dimethyl ether/air jet flames, *Combust. Flame* 176 (2017) 451–461.
- [13] S. Subramaniam, S.B. Pope, A mixing model for turbulent reactive flows based on Euclidean minimum spanning trees, *Combust. Flame* 115 (1998) 487–514.
- [14] R.L. Curl, Dispersed phase mixing: I. Theory and effects of simple reactors, *AIChE J.* 9 (47) (1963) 175–181, doi:10.1002/aic.690090207.
- [15] J. Janicka, W. Kolbe, W. Kollmann, Closure of the transport-equation for the probability density-function of turbulent scalar fields, *J. Non-Equilib. Thermodyn.* 4 (1979) 47–66, doi:10.1515/jnet.1979.4.1.47.
- [16] M.J. Cleary, A.Y. Klimenko, A detailed quantitative analysis of sparse-Lagrangian filtered density function simulations in constant and variable density reacting jet flows, *Phys. Fluids* 23 (11) (2011), doi:10.1063/1.3657085.
- [17] Y. Ge, M.J. Cleary, A.Y. Klimenko, A comparative study of Sandia flame series (D-F) using sparse-Lagrangian MMC modelling, *Proc. Combust. Inst.* 34 (2013) 1325–1332, doi:10.1016/j.proci.2012.06.059.
- [18] S. Vo, A. Kronenburg, O.T. Stein, M.J. Cleary, MMC-LES of a syngas mixing layer using a new mixing time scale model, *Combust. Flame* 189 (2018) 311–314, doi:10.1016/j.combustflame.2017.11.004.
- [19] Z. Huo, F. Salehi, S. Galindo-Lopez, M.J. Cleary, A.R. Masri, Sparse MMC-LES of a Sydney swirl flame, *Proc. Combust. Inst.* 27 (2) (2019) 2191–2198, doi:10.1016/j.proci.2018.06.193.
- [20] S. Vo, O.T. Stein, A. Kronenburg, M.J. Cleary, Assessment of mixing time scales for a sparse particle method, *Combust. Flame* 179 (2017) 280–299, doi:10.1016/j.combustflame.2017.02.017.
- [21] S. Vo, A. Kronenburg, O.T. Stein, M.J. Cleary, MMC-LES of a syngas mixing layer using an anisotropic mixing time scale model, *Combust. Flame* 189 (2018) 1339–1351, doi:10.1016/j.combustflame.2017.11.004.
- [22] P.J. Colucci, F.A. Jaber, P. Givi, S.B. Pope, Filtered density function for large eddy simulation of turbulent reacting flows, *Physics of Fluids* 10 (1998) 499–515, doi:10.1063/1.869537.
- [23] M.J. Cleary, A.Y. Klimenko, A generalised multiple mapping conditioning approach for turbulent combustion, *Flow. Turbul. Combust.* 82 (2009) 477–491, doi:10.1007/s10494-008-9161-3.
- [24] C. Straub, S. De, A. Kronenburg, K. Vogiatzaki, The effect of timescale variation in multiple mapping conditioning mixing of PDF calculations for Sandia flame series D-F, *Combust. Theor. Model.* 20 (5) (2016) 894–912, doi:10.1080/13647830.2016.1191677.
- [25] G. Neuber, C.E. Garcia, A. Kronenburg, B.A.O. Williams, F. Beyrau, O.T. Stein, M.J. Cleary, Joint experimental and numerical study of silica particulate synthesis in a turbulent reacting jet, *Proc. Combust. Inst.* 37 (2019) 1213–1220, doi:10.1016/j.proci.2018.06.074.
- [26] N. Branley, W.P. Jones, Large eddy simulation of a turbulent non-premixed flame, *Combust. Flame* 127 (2001) 1914–1934, doi:10.1016/s0010-2180(01)00298-x.
- [27] D. Garcia, Robust smoothing of gridded data in one and higher dimensions with missing values, *Comp. Stat. Data Anal.* 54 (2010) 1167–1178, doi:10.1016/j.csda.2009.09.020.
- [28] R.S. Barlow, G.-H. Wang, P. Anselmo-Filho, M.S. Sweeney, S. Hochgreb, Application of Raman/Rayleigh/LIF diagnostics in turbulent stratified flames, *Proc. Combust. Inst.* 32 (2009) 945–953, doi:10.1016/j.proci.2008.06.070.
- [29] F. Fuest, R.S. Barlow, D. Geyer, F. Seffrin, A. Dreizler, A hybrid method for data evaluation in 1-D Raman spectroscopy, *Proc. Combust. Inst.* 33 (1) (2011) 815–822, doi:10.1016/j.proci.2010.06.064.
- [30] F. Nicoud, H.B. Toda, O. Cabrit, S. Bose, J. Lee, Using singular values to build a subgrid-scale model for large eddy simulations, *Phys. Fluids* 23 (2011) 085106, doi:10.1063/1.3623274.
- [31] Z. Zhao, M. Chaos, A. Kazakov, F.L. Dryer, Thermal decomposition reaction and a comprehensive kinetic model of dimethyl ether, *Int. J. Chem. Kinet.* 40 (2008) 1–18, doi:10.1002/kin.20285.
- [32] M. Tamura, P.A. Berg, J.E. Harrington, J. Luque, J.B. Jefferies, G.P. Smith, D.R. Crosley, Collisional quenching of CH(A), OH(A), and NO(A) in low pressure hydrocarbon flames, *Combust. Flame* 114 (1998) 501–514, doi:10.1016/s0010-2180(97)00324-6.
- [33] R.W. Bilger, The structure of turbulent nonpremixed flames, in *Twenty-Second Symposium (Int'l) on Combustion*, p. 475–488, Pittsburgh, Pa, 1988, The Combustion Institute.

**Paper 2:**

**Title:** MMC-LES modelling of droplet nucleation and growth  
in turbulent jets

**Authors:** Gregor Neuber  
Institut für Technische Verbrennung,  
University of Stuttgart, 70174 Stuttgart, Germany

Andreas Kronenburg  
Institut für Technische Verbrennung,  
University of Stuttgart, 70174 Stuttgart, Germany

Oliver T. Stein  
Institut für Technische Verbrennung,  
University of Stuttgart, 70174 Stuttgart, Germany

M. J. Cleary  
School of Aerospace, Mechanical and Mechatronic Engineering,  
The University of Sydney, NSW 2006, Australia

**Journal:** Chemical Engineering Science

**Volume:** 167

**Pages:** 204 – 218





## MMC-LES modelling of droplet nucleation and growth in turbulent jets

G. Neuber<sup>a</sup>, A. Kronenburg<sup>a,\*</sup>, O.T. Stein<sup>a</sup>, M.J. Cleary<sup>b</sup><sup>a</sup>Institut für Technische Verbrennung, University of Stuttgart, 70174 Stuttgart, Germany<sup>b</sup>School of Aerospace, Mechanical and Mechatronic Engineering, The University of Sydney, NSW 2006, Australia

## HIGHLIGHTS

- Sparse-Lagrangian particle method for particle nucleation and growth.
- Sparse particle and standard (dense) particle methods yield near to identical results.
- New particle method captures the correct trends when varying the precursor concentration.
- The interactions between turbulence and nucleation can modify the averaged nucleation rates by up to 250%.

## ARTICLE INFO

## Article history:

Received 29 November 2016

Received in revised form 28 March 2017

Accepted 6 April 2017

Available online 08 April 2017

## Keywords:

Aerosol

Nucleation

Condensation

PBE

MMC

LES

PDF method

## ABSTRACT

An Eulerian large-eddy simulation (LES) is coupled with a sparse-Lagrangian particle method to solve the population balance equation for aerosol nucleation and growth in turbulent flows. We use the LES for the solution of the filtered velocity and mixing fields while the particle method provides one-point statistics of the gaseous species and the condensed phase such that the non-linear aerosol nucleation and growth terms appear naturally in closed form. A sparse particle implementation requires additional localisation in a reference space, and this localisation is realised here by employing the generalised multiple mapping conditioning (MMC) mixing model. The complete model, called MMC-LES, is validated by comparison with experimental data from nucleation studies in a turbulent, hot, nitrogen jet laden with dibutylphthalate (DBP) that condenses during mixing with a coflow of cold air. Acceptable agreement is found between the MMC-LES predictions and the experimental data. The average DBP droplet sizes are well predicted, and predictions of the total droplet number and the dependencies of droplet statistics on precursor concentrations are satisfactory. A comparison of the sparse particle method with results from conventional (dense) Monte Carlo-LES simulations demonstrates the capabilities of MMC-LES to predict aerosol nucleation and growth at relatively low computational cost. An additional quantitative analysis of the interactions between the turbulence and the non-linear nucleation source and growth terms shows that sub-grid effects must not be neglected and interactions between turbulence and nucleation can modify averaged nucleation rates by more than 250%.

© 2017 Elsevier Ltd. All rights reserved.

## 1. Introduction

The formation of aerosols or particulate matter from the gas phase is widespread in both nature and industry. Examples include condensation leading to the formation of raindrops, the formation of soot and flame synthesis of industrial commodities such as carbon black, titania, silica and specialised metals and metal oxides. Existing experimental databases provide some understanding of the physics of aerosol dynamics and their resulting characteristics (Hu et al., 2003; Echavarría et al., 2011; Gupta et al., 2011), but do

not usually provide all necessary correlations between hydrodynamic and thermodynamic quantities needed for model development. This is particularly true for small scale turbulence effects on precursor chemistry, droplet nucleation and growth. As a consequence, although there has been some success in modelling the evolution of aerosol particle size distributions (PSD) in laminar flame reactors (Echavarría et al., 2011; Tsantilis et al., 2002; Dang and Swihart, 2009), turbulent flame synthesis modelling efforts have been less successful.

The spatio-temporal evolution of the PSD is governed by the population balance equation (PBE). In devising methods to solve the PBE, we distinguish between sectional methods (Friedlander, 2000), moment methods (Pratsinis, 1988) and direct Monte Carlo

\* Corresponding author.

E-mail address: [kronenburg@itv.uni-stuttgart.de](mailto:kronenburg@itv.uni-stuttgart.de) (A. Kronenburg).

methods (Kruis et al., 2000, 2012). Moment methods, of which there are many varieties, mathematically reduce the PSD to its moments. Typically only the first two or three moments are required leading to a method with low computational cost. In sectional methods the PSD is discretized into sections representing discrete particulate sizes. Implementation may be conceptually quite simple as the governing equations for gaseous species and particulates are solved in the same way and the transition between the phases is uncomplicated. Direct Monte Carlo methods use a large number of stochastic particles to reconstruct the statistics of the aerosol interactions including direct modelling of collisions and agglomeration. The reader is referred to Rigopoulos (2010) for a comprehensive review of the different flavours of PBE methods in reactive flows.

Independent of the PBE solution method, some specific closure problems arise in turbulent environments and convincing (and universal) modelling strategies for accurate predictions are not yet well established. Temporally and/or spatially averaged conservation equations can be derived, but the key challenge for turbulent flows is the closure of the averaged nucleation and growth terms due to their highly non-linear dependence on instantaneous and local thermodynamic properties such as supersaturation and surface tension. It is acknowledged that simplified approaches which neglect turbulence-chemistry-aerosol interactions (e.g. the *perfectly stirred reactor* model) may suffice for some flow conditions (Bhatt and Lindstedt, 2009; Xiong and Pratsinis, 1991). However, most applications of practical interest feature distinctly inhomogeneous conditions, such as turbulent jets, and modelling of the large and small (i.e. subgrid) scale inhomogeneities is of paramount importance for accurate predictions.

In the context of large eddy simulations (LES) of the turbulent flow field, the most common methods for the solution of the PSD are the different flavours of the method of moments (Marchisio and Fox, 2013). When the moment method for the PSD is combined with flamelet models for the gaseous reactive species, predictions of soot formation are good (Mueller and Pitsch, 2013; Chittipotula et al., 2011), albeit uncertainties with respect to the parameterisation of the flamelets for both kinetically fast gaseous species and kinetically slow aerosol species remain. So far, only a few flame synthesis studies have combined LES (Loeffler et al., 2011; Garrick and Wang, 2011) with the sectional method. These have all neglected turbulence interactions with aerosol nucleation and growth despite clear evidence from direct numerical simulation (DNS) studies (Das and Garrick, 2010) that such contributions are typically not small. The synthesis of aerosols in turbulent flames involves coupled, three-way interactions between turbulence, chemistry and aerosol dynamics. It is convenient in fundamental studies to eliminate one of these aspects allowing for the other interactions to be analysed in isolation. As the present paper focuses on model closures for turbulence-aerosol interactions non-reacting systems with a condensating species present themselves as ideal test cases. Droplet nucleation and growth of dibutylphthalate (DBP) in a turbulent mixing layer constitutes such a case, and the recent DNS by Zhou et al. (2014) confirms the value of investigating turbulence-aerosol interactions in isolation. Two key observations were made: (1) instantaneous droplet number density strongly correlates with the instantaneous gaseous DBP mass fraction; and (2) number density does not show a unique dependence on the mixture fraction due to aerosol transport in mixture fraction space. From the first observation we conclude that turbulent correlations between nucleation and gaseous species concentrations cannot be neglected when modelling the nucleation rate. From the second observation we conclude that particulate evolution cannot be solely based on the state of the mean mixing field.

From the above discussion, it is apparent that additional fundamental research into the model closures for averaged or filtered nucleation and growth terms is needed. To address this issue, the modelling community is putting considerable effort into modelling the Lesniewski and Friedlander (1998) and Lesniewski (1997) experimental cases of DBP at varying concentrations issuing from turbulent round jets, which are also studied in this paper. Most relevant for the current work are the studies by Veroli and Rigopoulos (2011), Garmory and Mastorakos (2008) and more recent studies that primarily focused on the modelling of the nucleation rates (Zhou and Chan, 2011, 2014; Pasmazoglou et al., 2014). Veroli and Rigopoulos (2011) employed the Monte Carlo PDF form of the PBE method combined with a RANS solution of the turbulent flow field. They highlighted the importance of the averaging effects on supersaturation and thus liquid droplet inception. The shapes of the droplet size distributions (DSD's) were predicted reasonably well but nucleation rates were noticeably under-predicted. Garmory and Mastorakos (2008) used a stochastic fields PDF-PBE approach to solve the first three moments of the DSD. They investigated the effect of different surface tension models on nucleation rates and achieved much improved agreement of the predicted zeroth moment with measurements reported in Lesniewski (1997). Zhou and Chan (2011, 2014) and Pasmazoglou et al. (2014) investigated the accurate implementation and closure of nucleation in an LES context. Although nucleation rates were predicted with satisfactory accuracy, the approaches neglected surface growth and the back-coupling of condensation rates on gaseous DBP concentrations, which can become important for cases with higher DBP concentrations.

The present work on DPB nucleation and growth complements the modelling reviewed above with extension to a highly computationally efficient formulation of the PDF-PBE approach in an LES framework. A hybrid scheme is used, involving an Eulerian solver for the LES of the turbulent velocity field and a Monte Carlo stochastic particle method for the joint PDF of the mass fractions of gaseous species and the size-dependent number density of the liquid DBP droplets. While Monte Carlo PDF methods traditionally require stochastic particle resolutions of  $\mathcal{O}(10)$  to  $\mathcal{O}(100)$  per RANS or LES grid cell (the so called dense, or intensive, particle method), here the simulation is performed by a sparse particle method requiring far fewer stochastic particles than LES grid cells. This sparse particle method, called MMC-LES, is well established for turbulent combustion modelling (Cleary et al., 2009) and was recently applied to the synthesis of silica nanoparticles in a direct numerical simulated mixing layer (Vo et al., 2017a). The objective here is to apply MMC-LES for the first time to droplet nucleation and growth in a turbulent lab-scale flow. Additionally, analysis is performed to identify the influence of turbulence on aerosol inception and growth and to quantify potential errors associated with inaccurate modelling of the interactions of turbulence with the instantaneous thermo-physical state. We also test the sensitivity of the predicted droplet characteristics toward different formulations of the growth rate.

This paper is structured as follows: the governing equations for droplet dynamics, nucleation and growth are presented in Section 2. Section 3 introduces the MMC-LES concept for the solution of these governing equations plus the equations for the conservation of the gas phase species, mass and momentum. The experimental configuration and the numerical setup are introduced in Sections 4 and 5, respectively. Section 6 presents results on droplet statistics for a reference case and cases with varying DBP loadings. The interactions of turbulence and nucleation and growth at the LES subgrid scales are analysed in Section 7, before conclusions are drawn in Section 8.

## 2. Droplet dynamics, nucleation and growth

The droplet size distribution is governed by the instantaneous population balance equation (Hulburt and Katz, 1964; Rigopoulos, 2010)

$$\frac{\partial N}{\partial t} + \nabla(\vec{u} \cdot N) + \frac{\partial}{\partial d_p} (G(d_p, \vec{Y}) \cdot N) = D_p \nabla^2 N + \dot{W}_N(\vec{Y}, N), \quad (1)$$

where  $N$  is the droplet number density. Eq. (1) is applicable to laminar and turbulent flows, but if turbulence occurs either all scales must be resolved or a modelling of the unresolved contributions is required. The number density,  $N$ , is function of  $d_p$ ,  $\vec{x}$  and  $t$  that denote the droplet diameter, droplet position and time, respectively. In the real flow  $d_p$  can take any positive value but here we use a sectional approach so that the number density is solved for a static number of discrete droplet sizes or sections. The vectors  $\vec{Y}$  and  $\vec{u}$  are the gaseous species mass fractions and velocity, respectively. The droplets are small and assumed to move with the same speed as the gas. Both  $\vec{Y}$  and  $\vec{u}$  are turbulent quantities; the former is solved stochastically along with  $N$ , while the latter is solved using an Eulerian LES. The details appear in Section 3.3. The rate of droplet growth due to surface condensation is denoted as  $G$ . The source term,  $\dot{W}_N$ , accounts for droplet births and deaths. In general this may be due to nucleation, aggregation/coagulation and break up, but in the present work, the estimated characteristic droplet collision time is of the order of  $\tau_{coll} = \mathcal{O}(100 \text{ s})$  (Veroli and Rigopoulos, 2011). Thus, droplet collisions and subsequent agglomeration are rare events, and only nucleation leading to droplet births is considered,  $\dot{W}_N = B_{nucl}$ . Using classical nucleation theory the nucleation rate  $B$  and the growth rate  $G$  are given by (Sutugin and Fuchs, 1968; Girshick and Chiu, 1990)

$$B_N(T) = N_v^2 v_m \left( \frac{2\sigma}{\pi m} \right)^{\frac{1}{2}} \exp \left( - \frac{16\pi\sigma^3 m^2}{3(k_B T)^3 \rho_l^2 \ln^2(S)} \right) \exp \left( \frac{S_{mon}\sigma}{k_B T} \right), \quad (2)$$

$$G_{d_p}(T) = \alpha(Kn) \frac{4D v_m p_{sat}}{k_B T d_p} (S - 1), \quad (3)$$

with  $N_v$  being the vapour concentration in [molecules/m<sup>3</sup>]. Super-saturation,  $S$ , is the ratio of the condensing species partial pressure,  $p_{v,con}$ , and its saturation pressure,  $p_{sat}$ ,  $k_B$  is the Boltzmann constant,  $v_m = m/\rho_l$  the molecular volume,  $\sigma$  the surface tension and  $S_{mon}$  is the surface area of the monomer. The quantities  $m$  and  $\rho_l$  are the weight of the monomer and density of the liquid phase, respectively. The growth rate has been extended by the correction coefficient  $\alpha(Kn) = (1 + Kn)/(1 + 1.71Kn + 1.333Kn^2)$  as suggested in Jacobson (1999). Here, the Knudsen number is defined as  $Kn = 2\lambda/d_p$  with  $\lambda$  being the mean free path of the gas molecules. Eq. (3) can then be applied to the full range of Knudsen numbers (from the free molecular to the continuum regime) that are observed during the droplet growth process.

## 3. Methodology

A hybrid Euler/Lagrange approach is used to solve the governing equations for mass, momentum, species and droplet size distribution. More specifically, conservation of mass and momentum is computed using an Eulerian LES approach with standard closures. An additional LES-filtered conservation equation is solved for a conserved scalar called mixture fraction. This conserved scalar is used as a reference field for the PDF mixing model and this is further explained in Section 3.3. The joint probability density function of the gas phase composition field, temperature and of the droplet size distribution is computed by a Lagrangian particle approach as

detailed in the next two sections. Note that the joint PDF should rather be termed “joint filtered density function” in the LES context but here, we use the abbreviation PDF throughout to facilitate reading of the paper.

### 3.1. Stochastic Monte Carlo method

In turbulent flows, the solution of the LES-filtered form of Eq. (1) is not straightforward (Rigopoulos, 2010). The key challenges are the closures of the filtered nucleation and growth rates due to their strong non-linear dependencies on the local, instantaneous thermodynamic state (cf. Eqs. (2) and (3)). In general,  $B_N(\tilde{S}, \tilde{\sigma}, T) \neq B_N(\tilde{S}, \tilde{\sigma}, \tilde{T})$  where tilde denotes filtered values. An accurate closure for the filtered value of a general function  $f$  is obtained by

$$\tilde{f}(\vec{x}, t) = \int f(Y_i, N_i, T; \vec{x}; t) P(Y_i, N_i, T; \vec{x}, t) dY_i dN_i dT \quad (4)$$

if the joint-PDF,  $P$ , of species, temperature and the discretized DSD is known. The solution of the Eulerian transport equation for the joint-PDF is, however, computationally prohibitive due to the PDF's high dimensionality. Instead, an equivalent system of stochastic differential equations can be solved for an ensemble of stochastic Monte Carlo particles which represent a discrete form of the PDF (Gardiner, 1985; Pope, 1985). Thus, a Lagrangian Monte Carlo formulation of the PDF is used in our simulations for the transported scalars. The notional Monte Carlo particles carry information on the gas phase species mass fractions and temperature and the size dependent number density of DBP droplets. The particles are transported according to stochastic differential equations with fractional steps for spatial transport, scalar source term  $W_x$  and mixing operator  $S_x$ . In general,  $W_x$  is the source term of gas phase species, temperature and nucleation. The focus of this work are the turbulence-aerosol dynamics and therefore only the latter is considered. The particle evolution is governed by

$$dx_i^p = A_i^p dt + b_{ij}^p d\omega_j, \quad (5)$$

$$d\phi_x^p = (W_x^p + S_x^p) dt, \quad (6)$$

where  $d\omega_j$  is the increment of a Wiener process with zero mean and variance  $\sqrt{\Delta t}$ , with the time step width  $\Delta t$ . The shorthand notation  $(\cdot)^p = (\cdot)(\vec{x}^p, t)$  indicates that properties are determined at the location  $\vec{x}^p$  of particle  $p$ . Models for the convection term,  $A_i$ , and diffusion term,  $b_{ij}$ , are given by (Cleary and Klimenko, 2011)

$$A_i = \tilde{u}_i + \frac{1}{\bar{\rho}} \frac{\partial}{\partial x_i} (\bar{\rho}(\mathcal{D} + \mathcal{D}_t)), \quad (7)$$

$$b_{ij} = \delta_{ij} \sqrt{2(\mathcal{D} + \mathcal{D}_t)}, \quad (8)$$

where  $\tilde{u}_i$  is the filtered velocity,  $\bar{\rho}$  is the filtered density and  $\mathcal{D}$  and  $\mathcal{D}_t$  are the molecular and turbulent diffusivities, respectively. Eq. (6) describes the rate of change of the transported scalar  $\phi_x$ , where  $\phi_x = (T, Y_1, \dots, Y_i, Z, N_1, \dots, N_n)$  includes temperature,  $T$ , the species mass fractions,  $Y_i$ , the particle mixture fraction,  $Z$ , and all  $n$  sections necessary to represent the discrete DSD. In contrast to Eulerian solution approaches for the PBE, where the sub-grid contributions are unknown, the information carried by the Monte Carlo particles represents an instantaneous, local solution, and hence, all one point correlations such as the source terms do not require closure.  $S_x$  is a mixing term which emulates the effects of molecular diffusion on the dissipation of the conditional sub-filter variance of  $\phi$ . It is applied to all quantities in  $\phi$  regardless of the phase. The mixing term is unclosed and its modelling is discussed next.

### 3.2. Generalised multiple mapping conditioning mixing model

The conventional mixing models most commonly used in the literature are interaction by exchange with the mean (IEM) (Villermaux and Devillion, 1972), Curl's model (Curl, 1963), modified Curl's model (Janicka et al., 1979) and the Euclidean minimum spanning tree (EMST) model (Subramaniam and Pope, 1998). Characteristics of these are reviewed by Celis and da Silva (2015). Subramaniam and Pope (1998) nominated the key properties required of mixing models and one of the most important is that the mixing operation should be local in composition space; here  $\phi$ -space. Of the models listed above only EMST is a local mixing model but, in enforcing localness by direct comparison of  $\phi$  values solved on the notional particles, it violates linearity and independence which are two other important mixing model properties (Subramaniam and Pope, 1998). This has been shown to lead to so-called stranding and non-physical suppression of conditional fluctuations. MMC (Klimenko and Pope, 2003) is also a local mixing model but, since the localness is enforced indirectly with the use of independent reference variables, linearity and independence are not violated and the quality of the predictions has the potential to be much higher. In the present work we use a generalised form of MMC which has emerged mostly in the context of combustion LES (Cleary and Klimenko, 2009). In the present context the key distinguishing feature of generalised MMC is that LES based quantities may be used as the reference variables. Through the development of generalised MMC the concept of sparse particle methods has evolved. Since localness of mixing in composition space has been found to be much more important to modelling accuracy than is localness of mixing in physical space (Klimenko, 2009a,b; Vo et al., 2017b) it is possible to increase the spatial distance between mixing particles without loss of accuracy provided that localness in the composition space is maintained. This increase in the spatial mixing distance allows for a much reduced number of particles used in the simulations and an up to three order of magnitude reduction in computational cost. Whereas the conventional mixing models require  $\mathcal{O}(10)$  -  $\mathcal{O}(100)$  particles per LES cell, MMC-LES simulations have been performed with as few as 1 particle per 27 LES cells (Cleary and Klimenko, 2011). It is noted that generalised MMC can be used in either sparse or dense methods, but in either case the mixing is not confined to within a single LES cell and instead particles mix with a partner particle at a controllable distance in the reference space as described next.

MMC does not stipulate the exact form of the mixing operation, rather it imposes localness onto one of the existing conventional mixing models. The present work uses the MMC version of the modified Curl's model to close the stochastic differential equations at the mixing operator level. Particle pairs ( $p$  and  $q$ ) are selected and then mix linearly towards their mean,

$$\phi_x^p(t + \Delta t) = \phi_x^p(t) + \gamma(\bar{\phi}_x^{p,q}(t) - \phi_x^p(t)), \quad (9)$$

$$\phi_x^q(t + \Delta t) = \phi_x^q(t) + \gamma(\bar{\phi}_x^{p,q}(t) - \phi_x^q(t)). \quad (10)$$

Here,  $\bar{\phi}_x^{p,q}(t)$  is the weighted mean of the two particles and  $\gamma = 1 - \exp(-\Delta t/\tau)$  controls the extent of mixing with a timescale,  $\tau$ , which is related to local turbulence quantities. Details on the modelling of  $\tau$  can be found in Cleary and Klimenko (2011) and Vo et al. (2017b). The particle pairs are selected such that the average square distance

$$\hat{d}_{p,q}^2 = \sum_{i=1}^3 \left( \frac{d_{x_i}^{p,q}}{r_m/\sqrt{3}} \right)^2 + \left( \frac{d_f^{p,q}}{f_m} \right)^2. \quad (11)$$

is minimised. Here  $d_{x_i}^{p,q} = |x_i^p - x_i^q|$  is the inter-particle distance in physical space while  $d_f^{p,q} = |\tilde{f}^p - \tilde{f}^q|$  denotes the particle distance

in reference space,  $\tilde{f}$ . Here the reference space is given by the LES filtered mixture fraction as discussed in Section 3.3. Its value at the particle position is obtained by interpolation. The parameter  $f_m$  is a model parameter, and  $r_m$  is related to  $f_m$  by (Cleary and Klimenko, 2011)

$$r_m = C_m \left( \frac{d\tilde{f}}{dn} \frac{\Delta_L^3}{\Delta_E^{2-D_f}} \frac{1}{f_m} \right)^{1/D_f}, \quad (12)$$

with  $\Delta_L$  and  $\Delta_E$  being the nominal interparticle distance and the LES filter width and  $D_f = 2.36$  denotes the fractal dimension of the scalar surface where mixing occurs. The parameter  $C_m$  is set to  $C_m = 0.5$ . Small values of  $f_m$  enforce localness in reference space while larger values of  $f_m$  favours the selection of particles that are closer in physical space. The results are relatively independent of  $f_m$  and as in previous MMC-LES we use  $f_m = 0.03$  (Vo et al., 2017a,b; Ge et al., 2013; Galindo et al., 2017).

### 3.3. The reference scalar: mixture fraction

The model enforces localness in  $\phi$ -space indirectly through the particle mixing pair selection according to Eq. (11). With the model input parameters  $r_m$  and  $f_m$  this selection produces a controlled degree of mixing localness in an extended space given by the reference variable,  $\tilde{f}$ , and particle physical location,  $\vec{x}$ . In this way the reference variable is said to condition the mixing operation and it is sometimes referred to as a conditioning variable. The reference variable needs to be selected with care so that localness in that space also implies localness in  $\phi$ -space. For mixing controlled flows the mixture fraction is a good marker of compositional localness and to date MMC-LES has been applied to a number of turbulent non-premixed flames by using a reference variable that is given by the LES filtered mixture fraction field (Cleary and Klimenko, 2011, 2009; Vo et al., 2017b). In combustion applications the mixture fraction is usually defined as the fraction of the mass (at a location) originating from the fuel stream, having values of zero and unity in the pure air and pure fuel streams, respectively. As such it quantifies the mixing of fuel and oxidizer. Observations confirm that turbulent fluctuations of the reactive scalars correlate with fluctuations of the mixture fraction in non-premixed flames due to the chemical reaction being located the mixture is close to stoichiometric. For the Friedlander jet that will be investigated here, we also use mixture fraction as a reference field,

$$\tilde{f} \equiv (\tilde{T} - T_{\text{co-flow}})/(T_{\text{jet}} - T_{\text{co-flow}}) \quad (13)$$

where  $T_{\text{jet}}$  and  $T_{\text{co-flow}}$  refer to the jet and co-flow temperature. Eq. (13) holds since heat release due to condensation is very small (less than 0.5% at locations of maximum condensation) and normalised temperature is equivalent to mixture fraction,  $\tilde{f}$ , due to an equivalent conservation equation and the same types of boundary conditions. Nucleation and growth as given in Eqs. (2) and (3) are strong functions of temperature and a good correlation between these source terms and the reference scalar can be expected. We also define mixture fraction on the particles,

$$Z \approx (T - T_{\text{co-flow}})/(T_{\text{jet}} - T_{\text{co-flow}}) \approx Y_{\text{con}}/Y_{\text{con}}^0 \quad (14)$$

and denote this mixture fraction  $Z$  to distinguish it from the LES-filtered value  $\tilde{f}$ . The functional dependence is not unique due to a reduction of the mass fraction of the condensing species  $Y_{\text{con}}$  (and therefore changes in the level of supersaturation independent of  $T$ ), but depletion of the condensing species is small for all the cases investigated here (not shown). The last approximation in Eq. (14) holds, and a sufficiently high correlation between the thermophysical state

of the gas phase, the droplets and mixture fraction (or normalised temperature) is ensured throughout the jet. The strong dependence of supersaturation, nucleation and growth is not a necessity for the validity of MMC but can be further exploited for our analysis in Section 7.

### 3.4. Coupling between the Eulerian and Lagrangian fields

The hybrid Euler/Lagrange method requires coupling between the Eulerian LES field and the Lagrangian stochastic particles. Forward coupling is achieved by interpolation of the LES quantities to the particle location. This includes the filtered velocities, diffusion coefficients and densities as required for particle transport (cf. Eqs. (5), (7) and (8)), and filtered mixture fraction for localisation of the particle mixing model (cf. Eq. (11)) and for computation of the local mixing time scale (cf. Cleary and Klimenko, 2011). An adapted equivalent enthalpy method is usually used for backward coupling of the thermodynamic density from the Lagrangian to the Eulerian field (Cleary and Klimenko, 2011; Vo et al., 2017b). However, backward coupling can be omitted here due to the very low DBP loadings of the jet. In addition, the vast majority of droplets will be of the order or smaller than  $1\ \mu\text{m}$  (cf. Fig. 6) and thus momentum coupling between the gaseous and droplet fields can be neglected.

## 4. Experimental configuration

Lesniewski and Friedlander (1998) used a hot ( $T_{\text{jet}} = 413\ \text{K}$ ) nitrogen jet laden with dibutyl-phthalate (DBP) for the investigation of homogeneous nucleation and condensation in turbulent environments. The turbulent mixing of the heated jet with the co-flow of air at ambient temperature leads to rapid cooling of the central jet region, which triggers supersaturation and consequently droplet nucleation and growth. It is thus apparent that mixture fraction,  $Z$ , introduced in Section 3, is one key quantity characterising the nucleation and growth processes. The coflow conditions were kept constant during the experimental campaign ( $u_{\text{co}} = 0.18\ \text{m/s}$ ,  $T_{\text{co}} = 299\ \text{K}$ ), while the effect of various different jet conditions was investigated. The seeding (mole fraction) of DBP was varied and different jet Reynolds numbers were examined. The experimental campaign comprised measurements of the total number density of the droplets ( $m_0$ ) and the mean droplet diameter for various locations along the jet centreline. The droplet size distribution is measured at  $z/D = 20$  only. As a reference case, we use the experimental configuration where  $D_{\text{jet}} = 2.35\ \text{mm}$ ,  $u_{\text{jet}} = 51.55\ \text{m/s}$  ( $Re_D = 4700$ ),  $T_{\text{jet}} = 413\ \text{K}$  and the DBP mole fraction was set to  $x_{\text{jet,DBP}} = 3.6 \cdot 10^{-4}$ . This configuration is labelled *trial 824* in Lesniewski (1997). To examine the effect of DBP loading we use the conditions given by *trial 819*, which is identical in its setup to *trial 824*, with the exception of a variation of the gaseous DBP mole fractions at the jet inlet within the bounds of  $x_{\text{jet,DBP}} \in [2.5 \cdot 10^{-4}, 5.1 \cdot 10^{-4}]$ .

## 5. Numerical configuration

### 5.1. Description of the numerical implementation

The MMC-LES model has been implemented into a code called *mmcFoam* which is compatible with OpenFOAM opensource C++ libraries. The sparse-Lagrangian MMC classes are coupled with OpenFOAM's existing low Mach, compressible LES solver and the existing OpenFOAM particle classes have been adapted for the solution of Eqs. (5) and (6). The code has been validated for the computation of turbulent reacting flows (Vo et al., 2017b;

Galindo et al., 2017; Salehi et al., 2017), including aerosol nucleation (Vo et al., 2017a).

At first, the Eulerian scheme is presented while the Monte Carlo scheme is discussed afterwards. The discretisation scheme for the transport equations is second order in time and space, and the standard Smagorinsky model, with a model constant of  $C_s = 0.17$ , has been used for the closure of the sub-grid stresses. Ambient pressure is specified as an outlet condition for the pressure and a zero-gradient condition is used as the standard boundary condition for all other quantities at the outlet. Dirichlet boundary conditions are set for velocity, temperature, species mass fractions and mixture fraction at the jet and coflow inlet. The simulation domain measures 70 jet diameters in length and 31 diameters in radial direction. Results appeared to be quite insensitive to resolutions above 1.5 million LES cells, which is consistent with typical grid sizes for the LES computation of turbulent reacting single – (Kronenburg and Stein, 2016) and multi-phase (Ukai et al., 2015) jets. The mesh is locally refined towards the nozzle, where the jet diameter is resolved with 39 cells resulting in a grid size of around  $90\ \mu\text{m}$ . For the nozzle region, this is a much higher resolution than in one of the reference LES (Pesmazoglou et al., 2014), where ten points were used to resolve the nozzle diameter. In reference Garmory and Mastorakos (2008) the computational domain was extended upstream by  $8D$  to enable the establishment of a fully developed boundary layer and Veroli and Rigopoulos (2011) made use of a predefined fixed turbulence intensity and a viscosity ratio of 5% and 10, respectively. In the present study the inflow conditions are generated by a separate pipe flow simulation using a hybrid RANS-LES turbulence model.

The Monte Carlo method is first order in time and space and a total number of 480,000 Monte Carlo particles has been used in the sparse simulations, which results in an average of 3 Monte Carlo particles per 10 LES cells. On every Monte Carlo particle, we solve Eq. (6) for mixture fraction, temperature, the mass fractions of DBP,  $\text{N}_2$ ,  $\text{O}_2$  and all  $n$  sections of the droplet size distribution. Mixture fraction is thus computed twice, by the LES on the Eulerian grid (named  $\tilde{f}$ ) and on the particles (named  $Z$ ) as illustrated in Fig. 1, but coupling between the Eulerian and Lagrangian solutions as described in Section 3.4 ensures correlation between the two fields.

### 5.2. Properties of dibutyl-phthalate

Modelling particle nucleation and growth requires accurate models for DBP properties. The dependencies of surface tension, liquid density and saturation pressure on temperature are depicted in Fig. 2. In earlier publications (Veroli and Rigopoulos, 2011; Garmory and Mastorakos, 2008; Zhou and Chan, 2011, 2014; Pesmazoglou et al., 2014) the models of Bedanov et al. (1990), Okuyama et al. (1987), Riddick and Bunger (1971) and Potin-Gautier et al. (1982) were used to model the properties of DBP. Some uncertainty regarding the appropriate expressions exist, prompting Garmory and Mastorakos (2008) to arbitrarily modify the expression for surface tension to achieve a better agreement between their simulations and the corresponding experiments by Lesniewski and Friedlander (1998). We apply the Perturbed-Chain Statistical Associating Fluid Theory (PC-SAFT) (Gross and Sadowski, 2001), as a physically-based equation of state to correlate and predict the properties of DBP. The pure component parameters of PC-SAFT were adjusted to vapour pressure data from 22 and to liquid density data from 15 experimental data sources (Data Bank Software & Separation Technology Dortmund). The surface tension can be predicted using the PC-SAFT model without adjustable parameters using a Density Functional Theory formalism proposed by Gross (2009). The such obtained prediction is in

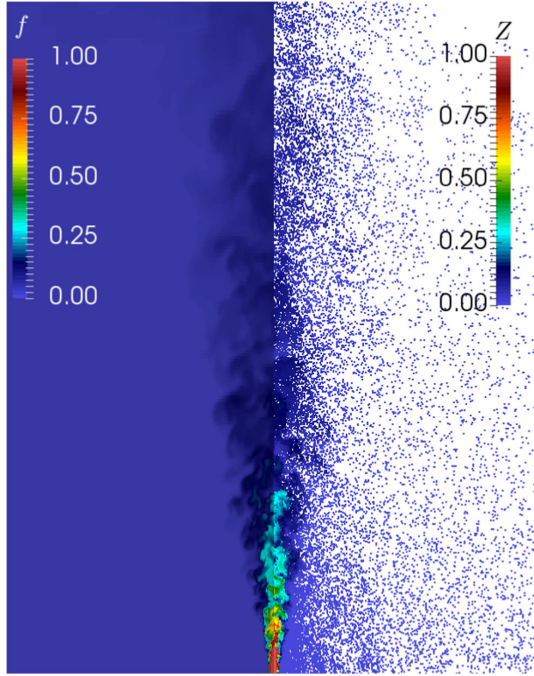


Fig. 1. Instantaneous mixture fraction profiles from the filtered LES solution,  $\hat{f}$  (left) and on the Monte Carlo particles,  $Z$  (right).

very good agreement to experimental data of surface tension, as Fig. 2 confirms.

All relevant properties of DBP and the corresponding mathematical expressions are summarised in Table 1.

### 5.3. Numerical implementation of particle growth

The droplet size distribution is characterised here by the droplet's diameter,  $d_p$ . The DSD is discretized by  $n$  sections with  $d_0 \approx 2.32$  nm and  $d_k = c^k d_0$ . The parameter  $c$  is chosen to cover the entire size distribution of droplets up to diameters of  $d_{max} \approx 10$   $\mu$ m. Droplet growth occurs due to condensation of DBP on the droplet surface and is modelled by the third LHS-term in Eq. (1). The implementation of this term warrants some further attention: it is treated here as a source/sink term of the respective section. We use the nodal form of the sectional method and the distribution of particles to their respective nodes is adapted from Prakash et al. (2003). This approach conserves mass but leads to an artificial broadening of the size distribution. The effect can be best quantified by the growth of an originally monodisperse distribution as shown in Fig. 3. Here, the conditions of the gas phase correspond to conditions for a mixture fraction value of  $Z = 0.6$  of the reference case. The conditions are kept constant and represent conditions where the growth is largest in the DBP jet. The results from two distinct times are shown with  $t = 200$   $\mu$ s yielding roughly the same geometric mean droplet diameter as measured at  $z/D = 20$ . The vertical lines represent the analytical solution. It is apparent that the discretization error leads to a broadening of the DSD, with three to five sections representing the majority of droplets while sections further away contribute less than 10% to the total number

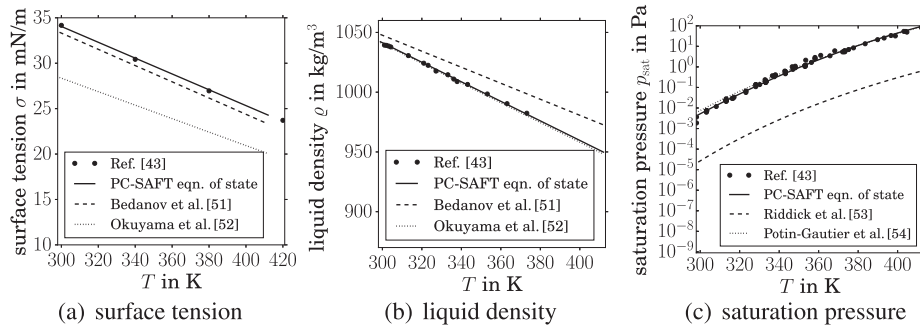


Fig. 2. Dependence of surface tension, liquid density and saturation pressure on temperature.

Table 1  
Thermodynamic properties of DBP.

Quantity	Formula	Ref.
Surface tension	$\sigma = [33.93 - 0.0894(T/K - 293.15)]$ (mN/m)	Bedanov et al. (1990)
	$\sigma = [35.3 - 0.0863(T/K - 273)]$ (mN/m)	Okuyama et al. (1987)
	$\sigma = [36.399 - 0.087134(T/K - 273)]$ (mN/m)	this paper
Liquid density	$\rho_l = 1049.2 - 0.67(T - 293.15)$ (kg/m <sup>3</sup> )	Bedanov et al. (1990)
	$\rho_l = 1063.0 - 0.826(T - 273)$ (kg/m <sup>3</sup> )	Okuyama et al. (1987)
	$\rho_l = 1047.0 - 0.81758(T - 293.15)$ (kg/m <sup>3</sup> )	this paper
Saturation pressure	$\log_{10}(p_{sat}/\text{mmHg}) = 7.065 - \frac{1666}{T/K} - \frac{547700}{(T/K)^2}$	Riddick and Bunger (1971)
	$\log_{10}(p_{sat}/\text{Pa}) = -\frac{4501}{T/K} + 12.88$	Potin-Gautier et al. (1982)
	$\log_{10}(p_{sat}/\text{Pa}) = -27.567 + 0.1187/T/K - 0.000112(T/K)^2$	this paper
Crit. droplet diameter	$d_{p,cr} = 4\sigma v_m/k_B T \ln(S)$	Girshick and Chiu (1990)
Diffusion coefficient	$D = 0.25(T^{1.75}/p)$ (cm <sup>2</sup> /s)	Ensley et al. (1969)

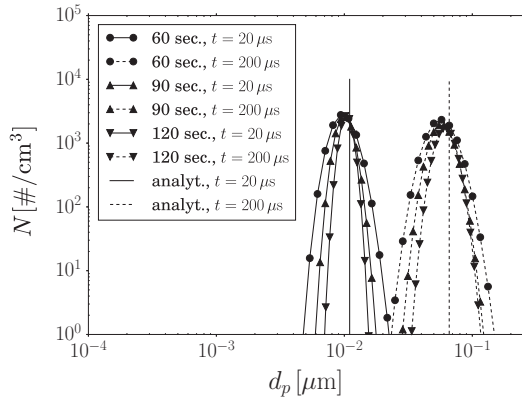


Fig. 3. Comparison of droplet size distributions by condensation in a homogeneous environment at different times.

of droplets. This is rather independent of the total number of sections used for the discretization. For all discretizations shown here, the geometric mean deviates less than 14% from the analytical solution. The artificial broadening can be quantified by the logarithm of the geometric standard deviation,  $\ln \sigma$ . It is zero for the analytical solution and approximates  $\ln \sigma \approx 0.19$  and  $\ln \sigma \approx 0.16$  for 90 and 120 nodes, respectively.

The total number of sections influences the results of the DBP jet simulations. Fig. 4 shows predicted droplet size distributions from MMC-LES of the DBP jet at  $z/D = 20$  (left) and droplet numbers along the centerline (right). Here, the number of sections does have a small influence on the shape of the DSD only. The predicted geometric means deviate by less than 17% and their standard deviations range from  $\ln \sigma = 0.84$  to  $\ln \sigma = 0.92$ . We make two observations: (1) The absolute values of these standard deviations are around 6 times larger than standard deviations due to discretization error; (2) the difference of 10% between  $\ln \sigma = 0.84$  and  $\ln \sigma = 0.92$  is rather small when compared to the uncertainties associated with the general modelling of the nucleation and growth terms. In addition, the different discretizations do not have a large effect on the condensed mass and thus on the nucleation rate. This is evidenced by the very low dependency of  $m_0$  on DSD discretization (see Fig. 4 (right)). The reduction of sections to 90 seems therefore justified, it reduces the computational cost for

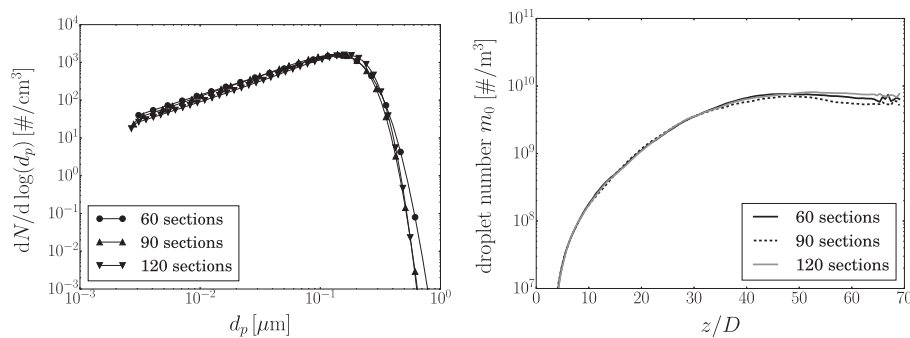


Fig. 4. Comparison of droplet size distribution at  $z/D = 20$  (left) and number of droplets (zereth moment) along the centerline (right) for simulations with different DSD discretisations.

the stochastic particles by 25%, and is used for the remainder of the paper. We may conclude that a reduction of the total number of sections does not unduly influence the droplet size distribution. However, a discretization error exists and may contribute up to 18% to the broadening of the DSD. Since a clear separation of the discretization error is difficult to achieve, we base the latter estimate on  $\ln \sigma \approx 0.86$  for the DBP jet and  $\ln \sigma \approx 0.16$  for monodisperse growth under constant gas phase conditions.

One last issue refers to the coupling of the condensing gas phase species,  $Y_{DBP}$  with the liquid phase. The nucleated and condensed droplet mass is deducted from the gas phase and the related energy transfer is also considered on the particles. The effects for lower DBP concentrations are not significant with less than 5% DBP depletion along the centreline for the cases with  $x_{jet,DBP} \leq 3.6 \cdot 10^{-4}$  and only very small effects on the DSD can be observed (not shown). Also for higher DBP loadings, depletion effects are negligible at  $z/D = 20$ , i.e. at the position where comparison with experimental data is made. Note that condensation effects on temperature are always less than 0.5% even for the highest DBP loading, and the approximations introduced in Eq. (13) seem justified – certainly for positions  $z/D < 20$  – and can be used for further analysis as presented in Section 7.

#### 5.4. Standard PDF implementation

For validation of the sparse method and to check its capability to approximate droplet nucleation and growth in turbulent flow, an additional computation using a dense particle method with 30 million Monte Carlo particles has been realised. In this simulation the conventional modified Curl's mixing model (Janicka et al., 1979) is used without MMC localisation in mixture fraction space. The ratio of the number of particles between the dense and the sparse method is about 60 while the ratio of the computational time is about 50 due to additional overheads in the MMC mixing model due to localisation and particle pair selection. The overall computational time can be reduced by a factor of 9, but gains in computational efficiency are expected to be even larger in case of reacting flows due to the increased computational demand on the Lagrangian solution of the composition field and the nearly constant requirements for the Eulerian LES solution of the flow and mixing fields.

Statistics reported in the following sections have been collected from the Monte Carlo particle simulations over 16 characteristic flow through times (based on the jet bulk velocity and the domain length) after the initial transient period. The computational cost is around 720 and 6600 CPU-hours for the sparse and dense simula-

tions, respectively, using two AMD Opteron processors 6172 (16 cores each).

## 6. Validation with experiments

### 6.1. Comparison with the base case

The first comparison with measurements by Lesniewski and Friedlander (1998) is conducted for the reference case with the jet's DBP loading of  $x_{DBP} = 3.6 \cdot 10^{-4}$ . It includes both sparse PDF simulations with an MMC mixing model closure and dense PDF simulations with a modified Curl's mixing model closure, where the sparse simulations are denoted as MMC-LES and the dense PDF data is referred to as PDF-LES in the following. The predictions of the normalised mean axial velocity along the centreline are satisfactory as shown in Fig. 5. It is seen that the present simulations with either MMC or PDF produce nearly identical results for the mean velocity. The present predictions also have a similar agreement to the experimental data as do past published results reported in Veroli and Rigopoulos (2011) and Garmory and Mastorakos (2008). Pasmazoglou et al. (2014) noted that the flow configuration should not be approximated by a fully turbulent jet due to the relatively small Reynolds numbers in the experiment. They used the inflow generator by Klein et al. (1998) specifying 10% turbulence intensity. We avoid the rather arbitrary specification of inflow turbulence and use a pipe flow simulation as intro-

duced in Section 4. This procedure gives a good match with the experiment. It provides an overall similar agreement with data when compared to reference Pasmazoglou et al. (2014) and explains the much better predictions in comparison to the results of Garmory and Mastorakos (2008) and Veroli and Rigopoulos (2011).

The evolution of the droplet number density is somewhat more difficult to predict, primarily due to the uncertainties in modelling the droplet nucleation and growth terms. Fig. 6 shows a reasonable agreement of predicted droplet number density with experiments along the centreline. The differences between the sparse MMC-LES and the dense PDF-LES approach are small. For comparison, we also plot the results from references (Veroli and Rigopoulos, 2011; Garmory and Mastorakos, 2008). Differences to the work by Garmory and Mastorakos (2008) are minor, the large differences to Veroli and Rigopoulos (2011) may primarily stem from Girshick and Chiu's (1990) correction of the nucleation rate that was omitted in Veroli and Rigopoulos (2011). Di Veroli and Rigopoulos advocated the presence of continued droplet nucleation in the sampling tube. Postprocessing of their results using plug flow computations with a residence time similar to the residence time in the sampling tube yields much better approximations of the experimental values. Garmory and Mastorakos (2008) modified the temperature dependence of the surface tension to shift the maximum droplet number upstream and to match the centreline evolution of  $m_0$  better for regions with  $z/D > 20$ . MMC-LES with modified expressions for surface tension leads to very similar improvements of the results (not shown), however, our analysis using the PC-SAFT model as presented in Section 2 does not justify any of the modifications suggested in Garmory and Mastorakos (2008), and only results using the expression by Okuyama et al. (1987) denoted as  $\sigma_1$  are included in Fig. 6 (left). The agreement of the computed DSD with measurements (cf. Fig. 6 (right)) is acceptable. The growth rate is underpredicted resulting in an abundance of small droplets and too few droplets with much larger sizes. It needs to be noted, though, that the measurements are also associated with some uncertainty. The increase in droplet numbers for droplets larger than  $1 \mu\text{m}$  cannot be explained and the reported number density  $m_0$  does not match the integrated (measured) DSD at  $z/D = 20$ . They differ by a factor of 12 and uncertainties in the reported data – especially for the smaller droplets – may be significant. Furthermore it should be pointed out that no other published numerical dataset shows a bi-modal shape of the DSD at centreline positions. For our model development it is most noteworthy that the results from the sparse particle method do not markedly deviate from results obtained by the dense PDF-LES method.

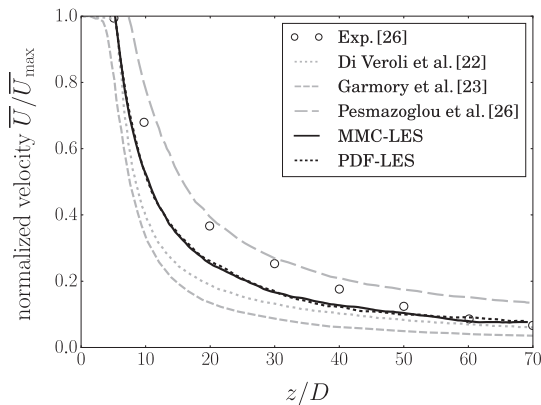


Fig. 5. Comparison of the mean axial velocity along the centreline.

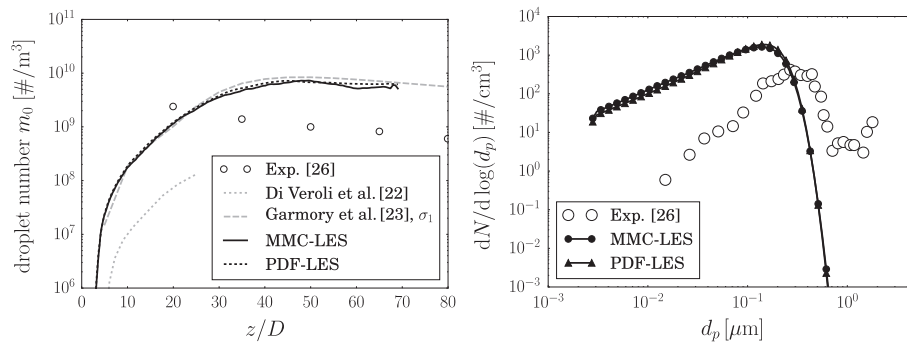


Fig. 6. Comparison of the evolution of the droplet number density along the centreline between simulations and experiments (left) and of the droplet size distribution at  $z/D = 20$  and  $r/D = 0$  (right).

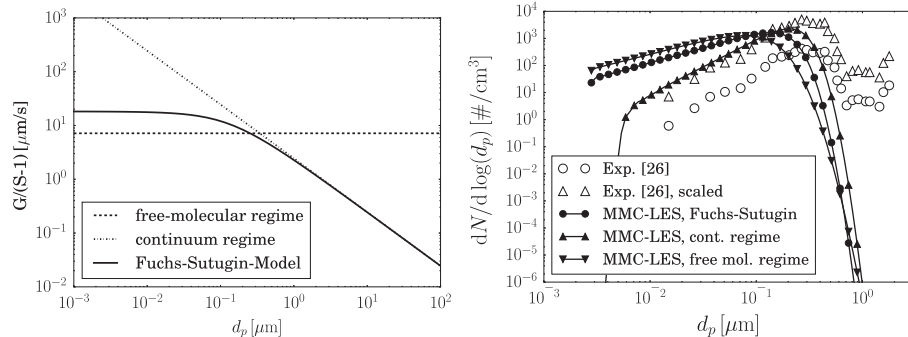


Fig. 7. Comparison of different growth models as a function of droplet diameter for conditions given at a mixture fraction of  $Z = 0.45$  (left) and the respective droplet size distribution at  $z/D = 20$  and  $r/D = 0$  of the jet simulation with a seeding of  $x_{\text{jet,DBP}} = 3.6 \cdot 10^{-4}$  (right).

Now we analyse the impact of the droplet growth model. As already discussed in Section 2 we use the Fuchs-Sutugin model, which continuously blends between the free molecular (large Kn, small  $d_p$ ) and continuum (small Kn, large  $d_p$ ) regimes of aerosol dynamics. This is illustrated in Fig. 7 (left) for supersaturation values prevalent at mixture fraction  $Z = 0.45$ , where growth rates are large. Consistent with standard aerosol dynamics literature (Friedlander, 2000) growth rates are independent of droplet diameter  $d_p$  in the free molecular regime, but linearly decrease with  $d_p$  in the continuum regime. Fig. 7 (right) shows the effect of different variants of the droplet growth model on the DSD in the present simulations. It can be observed that the results obtained from the assumption of continuum across the full DSD reproduce the experimental trend, at least for small droplets. Furthermore, when scaling the experimental DSD by a factor of 12 (justified as it renders a consistency between the experimentally observed DSD and zeroth moment in Fig. 6) then there is a good agreement between the MMC-LES results with the continuum growth model and the data. Literature suggests (Chen and Pfender, 1983) that the centre of the transition between the free molecular and continuum regimes could occur for a Knudsen number of  $\text{Kn} = 10$ . This is in contrast to considering the transition to be centred around  $\text{Kn} = 1$  as presumed in the Fuchs-Sutugin model (Sutugin and Fuchs, 1968). Assuming  $\text{Kn} = 10$  would shift the regime transition to droplets of order  $d_p = 10^{-2} \mu\text{m}$  and thus justify the use of the continuum model (which gives better results, Fig. 6 (right)) for the majority of the droplet sizes in the present simulations. However, for the purpose of making direct comparisons between the present work and the model results reported in the literature, the Fuchs-Sutugin growth model is used for the remainder of this paper.

## 6.2. Comparison to DBP mole fraction variation

As discussed in Section 2, high sensitivities of the nucleation rate on the exact expression of  $p_{\text{sat}}$ ,  $\rho_l$  and  $\sigma$  have been observed (Veroli and Rigopoulos, 2011; Garmory and Mastorakos, 2008), and an exact match of the experimental data shall not be the primary objective under these conditions. Instead, it has become common practice to analyse measurement series and to validate models by their capability to predict the respective trends (Barlow; Kempf et al., 2008).

It seems apparent that a good match with experimental data can be reached when selecting appropriate fits for key thermo-physical data. This, of course, does not constitute a satisfactory model validation, and a better practice is to focus on predicted trends for a range of operating conditions rather than matching the absolute values of one specific experiment. The droplet number density and the count mean droplet diameter at  $z/D = 20$  are shown in Fig. 8 for different DBP loadings. Note that the PDF-LES data in Fig. 8 is only available for the single reference DBP loading of  $x_{\text{DBP}} = 3.6 \cdot 10^{-4}$ , whereas a range of  $x_{\text{DBP}}$  values was studied with (the much cheaper) MMC-LES. The latter simulations capture the measured trends but the dependence of the droplet number on DBP doping is overpredicted, albeit of similar quality to the predictions reported in Garmory and Mastorakos (2008). This also holds for the (count) mean droplet diameter, Fig. 8 (right). The averaged droplet sizes are too low. It is apparent that growth rates predicted by Eq. (3) are distinctly too low, but trends are correct and all results are consistent with the DSDs shown in Figs. 6 and 7.

Fig. 9 shows the variation of the DSD with increased DBP concentration at  $z/D = 20$ . Simulations with larger DBP concentrations tend to better approximate the shape of the measured DSD while

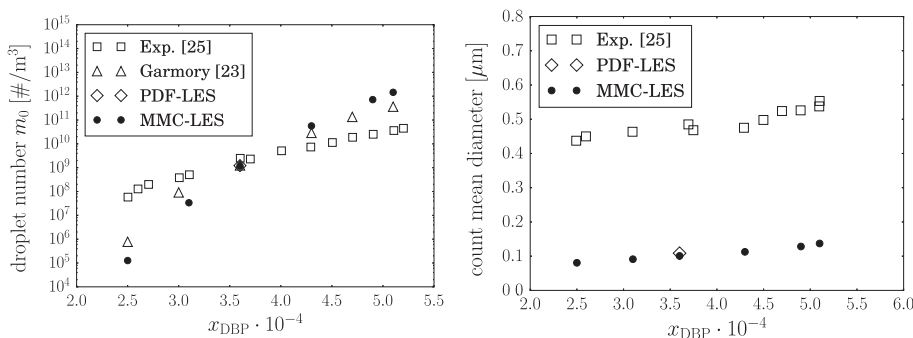
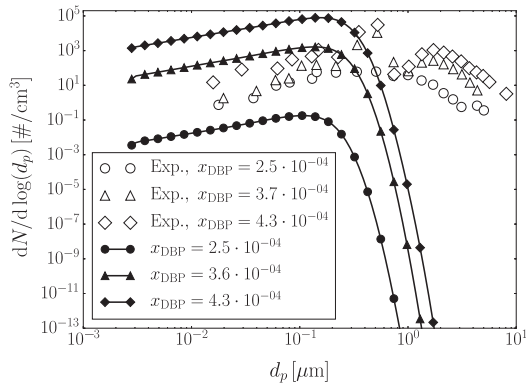


Fig. 8. Droplet number density (left) and count mean droplet diameter (CMD) (right) as function of the DBP mole fraction in the hot jet issuing into the domain at  $z/D = 20$ .



**Fig. 9.** Droplet size distributions for different jet DBP concentrations at  $z/D = 20$ . Experimental data are taken from Lesniewski (1997).

Fig. 8 indicates that  $m_0$  for the cases with intermediate DBP loadings are predicted best by MMC-LES. The computed droplet size distributions widen and predict larger maximum droplet sizes with increasing  $x_{DBP}$ . This trend is not so clear in the experiments where an increase in DBP concentration seems to increase the number of droplets rather evenly and independent of the droplet size. Garmory and Mastorakos (2008) scaled the measured DSDs by 18.5, 100.4 and 15 for the three DBP loadings, respectively, to reach consistency between measured DSDs and  $m_0$ . This would improve the current simulations' quantitative agreement with the experiment, however, additional measurements would certainly be desirable for further, reliable model validation.

In summary, from the above results we may conclude that (a) sparse MMC-LES simulations produce results that are nearly identical to the much more expensive dense PDF-LES simulations, (b) the present set of simulations produces the correct trends with increasing DBP loading and is in good qualitative agreement with the experimental data, (c) the quantitative agreement of the present simulations with the experimental data is good and similar to results reported in the literature, and (d) additional measurements and improved thermo-physical, nucleation and growth models are needed in order to better judge the predictive capabilities of the present and similar modelling efforts. MMC-LES is now used to assess the effects (and importance) of turbulence interactions with the gas-phase composition and aerosol evolution.

## 7. Turbulence interactions with nucleation and growth

The major purpose of PDF modelling is the accurate closure of all one point statistics, namely the modelling of all sub-grid interactions between turbulence and the gaseous scalar field that determine the average nucleation and growth rates of the droplets. The same applies in MMC-LES, albeit at a much reduced computational cost compared to conventional PDF models. The effects of sub-grid interactions can best be analysed by comparison of the averaged nucleation and growth rates predicted by MMC-LES (model M1)

with the averaged quantities from the filtered LES fields (model M2) and the Reynolds averaged quantities produced from RANS-type closures (model M3). Thus, M2 evaluates the droplet evolution based on the filtered thermo-physical state and then averages over time, whereas M3 is based on the evaluation on the time-averaged (filtered) state, respectively. The latter two do not incorporate any subgrid effects thus neglect turbulence-droplet interactions at the unresolved scales. Therefore, differences between models M1 and M2 can be attributed to LES sub-grid effects and quantify errors introduced when omitting any LES sub-grid modelling. Differences between M1 and M3 can be attributed to scalar fluctuations relative to the temporal mean (the RANS average for statistically stationary flows) and quantify errors that the omission of any turbulence closure for  $B$  and  $G_N$  would induce. Note that no separate RANS computations are conducted here because a RANS-type solution for the temperature and gas phase composition can be obtained from temporal averages of the LES data. The three models are listed in Table 2. The tilde operator denotes LES-filtered values, whereas the overbar indicates time averages accumulated during the steady state of the large eddy simulation.

### 7.1. Saturation

Fig. 10 illustrates the effect of the three averaging procedures on supersaturation for the reference case with  $x_{DBP} = 3.6 \cdot 10^{-4}$ . The difference between M1 and M2 is relatively small while the RANS averaged data (M3, Fig. 10 (right)) wrongly predicts very high supersaturation values in the entire shear layer including the regions upstream near the jet exit. A more quantitative comparison is provided by Fig. 11 where the mean (super-) saturation predicted by the three models is plotted along the centreline and as

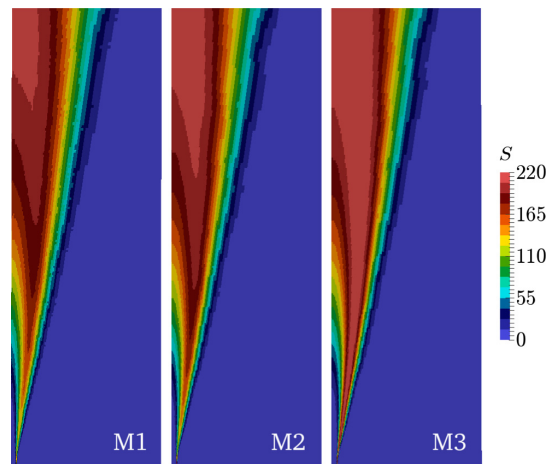


**Fig. 10.** Contour plots of the time-averaged supersaturation computed by the MMC-LES approach (M1), by the 1st order LES approximation (M2) and by the 1st order RANS approximation (M3) for  $x_{DBP} = 3.6 \cdot 10^{-4}$ .

**Table 2**  
Models for the analysis of the sub-grid effects on nucleation and growth.

	Nucleation	Growth	Interpretation
M1	$B(S(\bar{T}, \bar{Y}_{DBP}), \sigma(\bar{T}), \bar{T})$	$\bar{G}_N(D(\bar{T})S(\bar{T}, \bar{Y}_{DBP}), p_{sat}(\bar{T}), \bar{T})$	MMC model, exact closure
M2	$B(\bar{S}(\bar{T}, \bar{Y}_{DBP}), \sigma(\bar{T}), \bar{T})$	$\bar{G}_N(D(\bar{T})\bar{S}(\bar{T}, \bar{Y}_{DBP}), p_{sat}(\bar{T}), \bar{T})$	1st order LES-type closure
M3	$B(\bar{S}(\bar{T}), \sigma(\bar{T}, \bar{Y}_{DBP}), \bar{T})$	$\bar{G}_N(D(\bar{T})\bar{S}(\bar{T}, \bar{Y}_{DBP}), p_{sat}(\bar{T}), \bar{T})$	1st order RANS-type closure

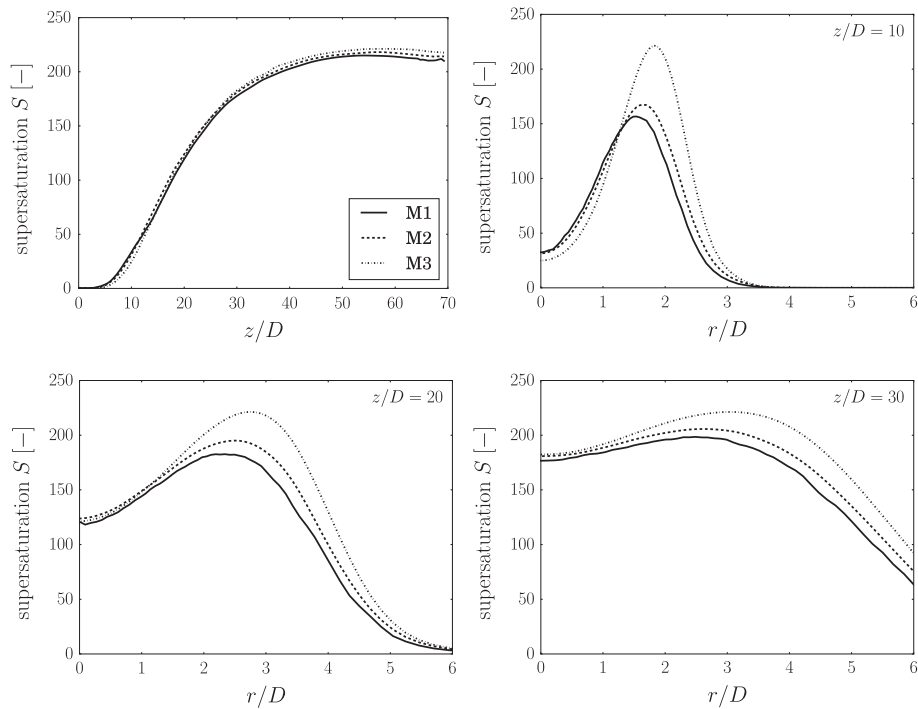


Fig. 11. Comparison of the saturation  $S$  computed by the different models along the centreline (top, left) and as function of radial position at  $z/D = 10, 20, 30$ .

a function of radius for different downstream positions. It is apparent that the maximum of the averaged supersaturation is reached in the centre of the jet at about  $z/D \approx 55$  and that the evolution of supersaturation along the centreline is largely unaffected by sub-grid turbulence (cf. Fig. 11(a)). The radial profiles demonstrate that LES sub-grid effects do account for a decrease in maximum mean supersaturation by approximately 10%, however, RANS predictions without sub-grid model would overpredict supersaturation by up to 40% at  $z/D = 10$ .

## 7.2. Nucleation

More pronounced effects of subgrid interactions can be observed for the nucleation rate,  $B$ . A qualitative comparison of the three averaged nucleation rates is given in Fig. 12 and a quantitative comparison for the centreline and selected downstream positions is presented in Fig. 13. The contour plot indicates clear qualitative differences between M1 and M3, while LES without subgrid model captures the mean nucleation rate qualitatively right, and only quantitative differences persist with respect to the maximum values in the shear layer and on the centreline. M3 shifts droplet nucleation on the centreline downstream, however, it overpredicts maximum mean nucleation rates by up to a factor of 4 and clearly underpredicts the width of the zone with significant droplet nucleation rates. The overprediction by M2, i.e. neglecting LES sub-grid scale effects, reaches 25% throughout most of the domain. This percentage seems rather low and the small differences between M1 and M2 warrant some further analysis. As indicated above, supersaturation, nucleation and growth are functions of temperature and DBP mass fraction. Overall, depletion of gaseous DBP is small for positions upstream of  $z/D = 20$  (cf. Section 3), the approximation indicated in Eq. (13) holds and both, temperature and DBP mass fractions can be represented by the mixture fraction  $Z$ . Supersaturation, nucleation and growth are then unique functions of mixture fraction as shown in Fig. 14 for the expression derived from the PC-SAFT model. It is apparent that all three quantities,  $S$ ,  $B$ , and  $G$ , are non-linear functions of the mixing process. The nucleation rate  $B$  is important across a very narrow band in mixture fraction space only and peaks at  $Z \approx 0.13$ . In contrast, growth by condensation is high across a relatively wide range of mixture fraction with its peak at  $Z \approx 0.6$ . Hence, nucleation and condensation rates act in different regions of the turbulent mixing field. Fig. 14 also indi-

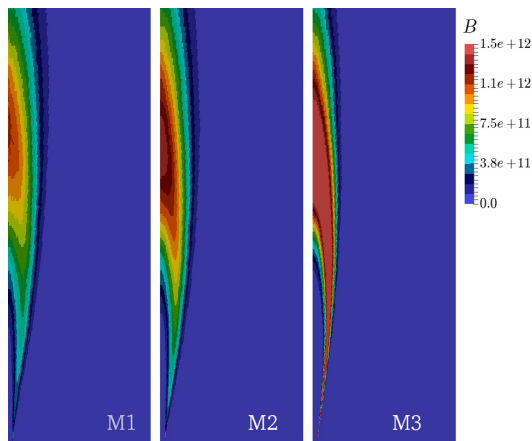


Fig. 12. Contour plots of the time-averaged nucleation rates computed by the MMC-LES approach (M1), by the 1st order LES approximation (M2) and by the 1st order RANS approximation (M3) for  $x_{DBP} = 3.6 \cdot 10^{-4}$ .

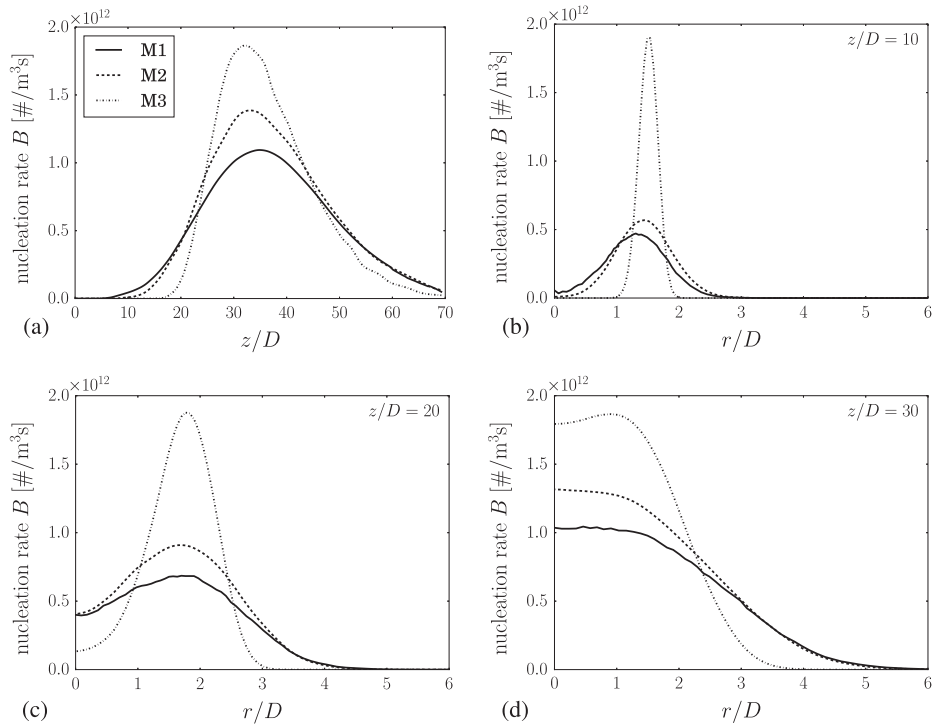


Fig. 13. Comparison of the nucleation rate  $B$  computed by the different models (a) along the centreline and as function of radial position at (b)  $z/D = 10$ , (c)  $z/D = 20$  and (d)  $z/D = 30$ .

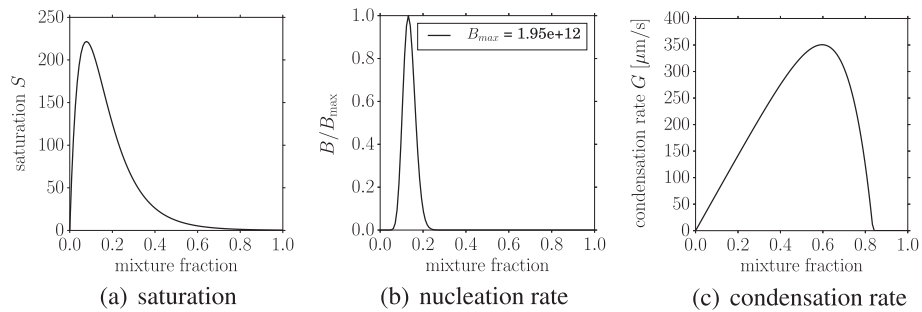


Fig. 14. Dependence of saturation, nucleation rate and condensation rate on mixture fraction.

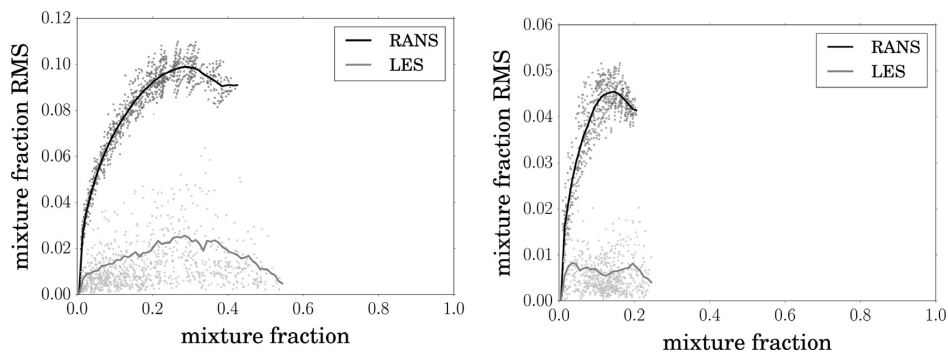


Fig. 15. Conditional root mean square of mixture fraction  $Z$  for  $z/D = 10$  (left) and  $z/D = 20$  (right) from LES (grey) and RANS (black).

icates that the maximum nucleation rate amounts to  $B_{max} = 1.95 \cdot 10^{12} \#/(m^3s)$  as can also be observed for M3 in Figs. 12 and 13. There, nucleation peaks at locations where the RANS-averaged mixture fraction equals  $\bar{Z} = 0.13$ . The mean of the nucleation rate is computed by

$$\bar{B}(\bar{x}) = \int B(Z, \bar{x}) P(Z, \bar{x}) dZ \quad (15)$$

with M3 neglecting turbulence-nucleation rate interactions and assuming a  $\delta$ -PDF for  $Z$  at every position  $\bar{x}$ . Turbulence, however,

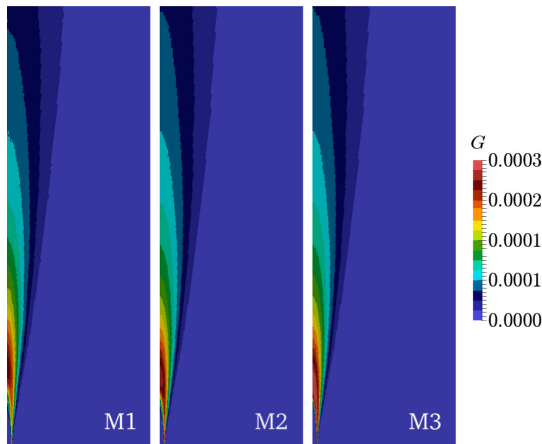


Fig. 16. Contour plots of the time-averaged growth rates for the 10th size section computed by the MMC-LES approach (M1), by the 1st order LES approximation (M2) and by the 1st order RANS approximation (M3) for  $\chi_{DEP} = 3.6 \cdot 10^{-4}$ .

reduces the averaged nucleation rate due to finite probabilities for values of  $Z \neq 0.13$ . Fig. 14 should not be seen in isolation but in the context of other properties of the flow such as the conditional RMS of the mixture fraction shown in Fig. 15. The black symbols

represent  $Z_{RMS,RANS} = \sqrt{\bar{Z}^2}$ , i.e. the time averaged RMS of mixture fraction, while the red symbols represent the instantaneous LES sub-grid RMS,  $Z_{RMS,LES} = \sqrt{\tilde{Z}^2} \equiv \sqrt{C_f \Delta_E^2 \nabla \tilde{Z} \cdot \nabla \tilde{Z}}$ , where a standard LES sub-grid variance model was employed (Cleary and Klimenko, 2011). Thus, the lines represent the RMS of each model conditionally averaged on  $\bar{Z}$  and  $\tilde{Z}$ , respectively. At  $Z = 0.13$  (where  $B(Z)$  peaks, cf. Fig. 14(b)) and  $z/D = 10$ , the time-averaged RMS amounts to  $Z_{RMS,RANS} \approx 0.075$ , indicating a relatively wide distribution of mixture fraction and thus, a relatively large error can be expected when approximating the PDF by a  $\delta$ -PDF as for M3. The error will be very pronounced at  $Z = 0.13$  due to the strong non-linearity of  $B$  around this mixture fraction value, cf. Fig. 14b.

A Taylor series expansion around  $B(Z)$  shows that second order effects are of the same order of magnitude as the leading term if sub-grid fluctuations are around  $Z_{RMS,LES} \approx \mathcal{O}(0.1)$ . Typical LES sub-grid fluctuations can reach these values in the shear layer, however, the relatively fine mesh used here leads to conditionally averaged mixture fraction RMS values below  $Z_{RMS,LES} \approx \mathcal{O}(0.02)$  in most regions of the flow. The RMS is below  $Z_{RMS,LES} \approx \mathcal{O}(0.015)$  at  $z/D = 10$  for values of  $\bar{Z} \approx 0.13$ , i.e. where nucleation rates are highest and the effects of turbulence on the nucleation should be most pronounced. Thus, LES sub-grid effects are small for the current setup and the sub-grid variance represents only 5% of the corresponding RANS value. This in line with the work by Pesmazoglou et al. (2014) where hardly any LES sub-grid effects were observed. This seemed counterintuitive at the time since combustion research suggests that turbulence interactions with non-linear sub-grid terms, such as chemical reaction, require modelling. Sim-

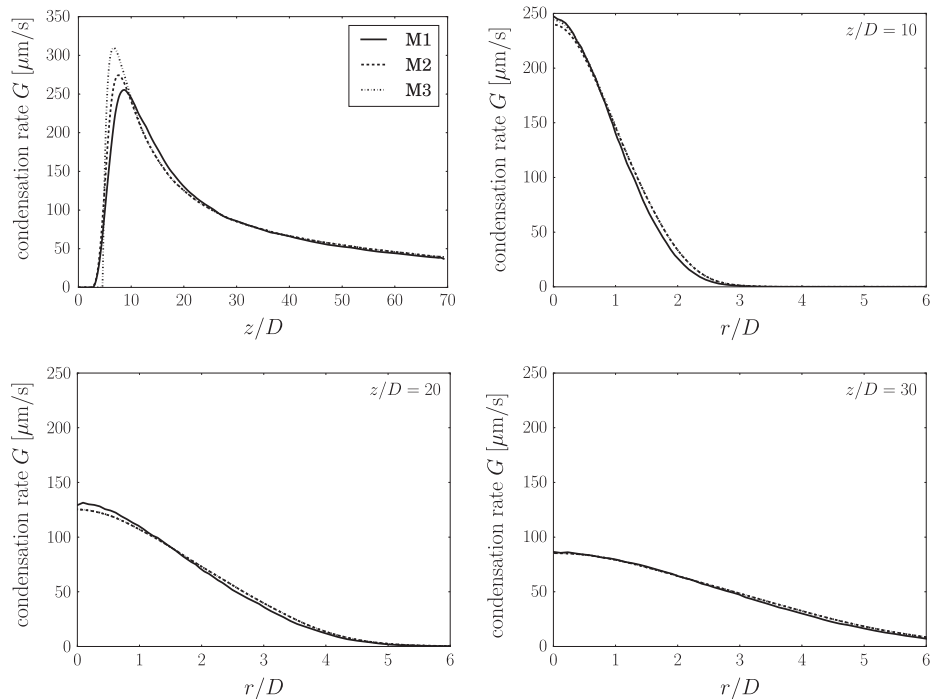


Fig. 17. Comparison of the condensation rate  $G$  computed by the different models along the centreline (top, left) and as function of radial position at  $z/D = 10, 20, 30$ .

ilarly, nucleation will certainly be affected by turbulence and require sub-grid closure, however, very fine LES cells, low turbulence levels and thus small (instantaneous) sub-grid variances will render the errors small if sub-grid effects are omitted. It shall be emphasised that the present Reynolds number is relatively low ( $Re_D = 4700$ ), so the flow is only moderately turbulent. Therefore, the differences in nucleation between the exact closure (M1) and the 1st order LES-type closure (M2) are not as pronounced as in comparison to the 1st order RANS-type closure (M3) and can be quantified to be around 35%. This will certainly change for higher turbulence levels in typical turbulent jets with – say – Reynolds numbers of around 30,000 and more. There, conditionally averaged RMSs can easily exceed  $Z_{RMS,RANS} \approx \mathcal{O}(0.2)$  and  $Z_{RMS,LES} \approx \mathcal{O}(0.05)$  (Kronenburg and Stein, 2016), and LES sub-grid scale effects must not be neglected.

### 7.3. Condensation

For completeness, Fig. 16 compares the averaged growth rates for the different models. Here, the growth rates of the 10th section are shown, but very similar trends can be observed for all droplet sizes. Differences in structure and magnitude are noticeable in the upstream shear layer but become insignificant for  $z/D > 20$ . Taking the MMC-LES result M1 as a base case, Model M3 overpredicts growth rates by up to 25% while overpredictions by model M2 are very moderate and do not exceed 10%. The radial profiles in Fig. 17 show that sub-grid contributions are not significant for predicting the condensation rate and models M1–M3 give nearly identical results. This can be attributed to the linear dependency on mixture fraction for a wide range of mixture fractions, see Fig. 14, and a moderate change of absolute values in the region  $Z \approx 0.6$ , where the condensation rates are largest.

## 8. Conclusions

In this paper we have employed an MMC-LES method for the modelling of droplet nucleation and growth in a turbulent jet laden with dibutyl-phthalate. The transport equations for discrete sections of the droplet size distribution are solved on the notional Monte Carlo particles such that all interactions between turbulence and nucleation/growth appear in closed form and it is not necessary to model the mean or filtered rates of these non-linear terms. In general, reasonable agreement of predicted droplet concentrations with measurements have been achieved and the quality of the results compares favourably with other simulations presented in the archival literature. The study demonstrates that

1. an MMC-LES method using a sectional method for the representation of the droplet size distribution is computationally feasible and can reduce the overall computational cost compared with a dense PDF method by a factor of 9,
2. differences between sparse and dense PDF methods are negligible and MMC therefore offers a computationally economic variant of standard PDF methods, and
3. the effect of turbulence on nucleation must not be neglected but may be small for fine LES resolutions and/or low turbulence levels. If the mixture fraction RMS spans a sufficiently large region in mixture fraction space where nucleation (and/or growth) exhibit non-linear dependencies on mixture fraction, sub-grid effects cannot be neglected.

Parameter studies demonstrate the robustness of the implemented method, and the dependence of the droplet number density on changes in DBP concentration are captured satisfactorily. Less satisfactory is the predicted shape of the droplet size distribu-

tion, but some reservations towards the consistency of the experimental data persist and future validation studies shall aim at a more complete experimental characterisation of the nucleation and growth processes at various locations in the shear layer.

## Acknowledgements

The authors would like to thank Prof. J. Gross (Stuttgart) for the DFT analysis of the DBP properties reported in Section 5.2. We also thank Mr. N. Seubert for one of the early versions of the PBE implementations in OpenFOAM and acknowledge the computational resources provided by HLRs (Stuttgart) and the financial support by ARC (MJC – Grant No. DP160105023).

## References

- Barlow, R.S. International Workshop on Measurement and Computation of Turbulent Nonpremixed Flames (TNF). Available at <<http://www.sandia.gov/TNF>>.
- Bedanov, V.M., Vaganov, V.S., Gadiyak, G.V., Kodenev, G.G., Rubakhin, A., 1990. Experimental determination of the number of molecules in a critical nucleus. Test of homogeneous nucleation theory. *Sov. J. Chem. Phys.* 7 (4), 933.
- Bhatt, J., Lindstedt, R., 2009. Analysis of the impact of agglomeration and surface chemistry models on soot formation and oxidation. *Proc. Comb. Inst.* 32 (1), 713–720. <http://dx.doi.org/10.1016/j.proci.2008.06.201>.
- Celis, C., da Silva, L.F.F., 2015. Lagrangian mixing models for turbulent combustion: review and prospects. *Flow Turbul. Combust.* 94, 643–689.
- Chen, X., Pfender, E., 1983. Effect of the Knudsen number on heat transfer to particle immersed into a thermal plasma. *Plasma Chem. Plasma Process.* 3 (1), 97–113.
- Chittipotula, T., Janiga, G., Thévenin, D., 2011. Improved soot prediction models for turbulent non-premixed ethylene/air flames. *Proc. Combust. Inst.* 33 (1), 559–567.
- Cleary, M., Klimenko, A., 2009. A generalised multiple mapping conditioning approach for turbulent combustion. *Flow Turbul. Combust.* 82, 477–491.
- Cleary, M.J., Klimenko, A.Y., 2011. A detailed quantitative analysis of sparse-Lagrangian filtered density function simulations in constant and variable density reacting jet flows. *Phys. Fluids* 23 (11).
- Cleary, M., Klimenko, A., Janicka, J., Pfitzner, M., 2009. A sparse-lagrangian multiple mapping conditioning model for turbulent diffusion flames. *Proc. Combust. Inst.* 32, 1499–1507.
- Curl, R.L., 1963. Dispersed phase mixing: I. Theory and effects of simple reactors. *AIChE J.* 9 (47), 175–181.
- Dang, H., Swihart, M.T., 2009. Computational modeling of silicon nanoparticle synthesis: I. A general two-dimensional model. *Aerosol Sci. Technol.* 43, 250–263.
- Das, S., Garrick, S., 2010. The effects of turbulence on nanoparticle growth in turbulent reacting jets. *Phys. Fluids* 22, 103303-1–103303-10.
- DBBST Dortmund Data Bank Software & Separation Technology GmbH, Oldenburg Germany. Available at <<http://www.dbbst.com>>.
- Echavarría, C.A., Sarofim, A.F., Lighty, J.S., D'Anna, A., 2011. Evolution of soot size distribution in premixed ethylene/air and ethylene/benzene/air flames: experimental and modeling study. *Combust. Flame* 158 (1), 98–104. <http://dx.doi.org/10.1016/j.combustflame.2010.07.021>.
- Ensley, K., Fuller, E.N., Giddings, J.C., 1969. Diffusion of halogenated hydrocarbons in helium. The effect of structure on collision cross section. *J. Phys. Chem.* 73, 3679–3685.
- Friedlander, S.K., 2000. *Smoke, Dust and Haze*. Oxford University Press, Oxford, New York.
- Galindo, S., Salehi, F., Cleary, M.J., Masri, A.R., 2017. MMC-LES simulations of turbulent piloted flames with varying levels of inlet inhomogeneities. *Proc. Combust. Inst.* 36, 1759–1766.
- Gardiner, C., 1985. *Handbook of Stochastic Methods*. Springer-Verlag, New York.
- Garmory, A., Mastorakos, E., 2008. Aerosol nucleation and growth in a turbulent jet using the stochastic fields method. *Chem. Eng. Sci.* 63 (16), 4078–4089. <http://dx.doi.org/10.1016/j.ces.2008.05.012>.
- Garrick, S.C., Wang, G., 2011. Modeling and simulation of titanium dioxide nanoparticle synthesis with finite-rate sintering in planar jets. *J. Nanopart. Res.* 13, 973–984.
- Ge, Y., Cleary, M.J., Klimenko, A.Y., 2013. A comparative study of Sandia flame series (D-F) using sparse-Lagrangian MMC modelling. *Proc. Combust. Inst.* 34, 1325–1332.
- Girshick, S., Chiu, C., 1990. Kinetic nucleation theory: a new expression for the rate of homogeneous nucleation from an ideal supersaturated vapor. *L. Chem. Phys.* 93, 1273–1277.
- Gross, J., 2009. A density functional theory for vapor–liquid interfaces using the PCP-SAFT equation of state. *J. Chem. Phys.* 131 (20), 1244–1260.
- Gross, J., Sadowski, G., 2001. Perturbed-chain SAFT: an equation of state based on a perturbation theory for chain molecules. *Ind. Eng. Chem. Res.* 40, 1244–1260.
- Gupta, A., Ifeacho, P., Schulz, C., Wiggers, H., 2011. Synthesis of tailored  $WO_3$  and  $WO_3$  ( $2.9 < x < 3$ ) nanoparticles by adjusting the combustion conditions in a

- H<sub>2</sub>/O<sub>2</sub>/Ar premixed flame reactor. *Proc. Combust. Inst.* 33 (2), 1883–1890. <http://dx.doi.org/10.1016/j.proci.2010.06.162>.
- Hu, B., Yang, B., Koylu, U.O., 2003. Soot measurements at the axis of an ethylene/air non-premixed turbulent jet flame. *Combust. Flame* 134 (1/2), 93–106. [http://dx.doi.org/10.1016/S0010-2180\(03\)00085-3](http://dx.doi.org/10.1016/S0010-2180(03)00085-3).
- Hulburt, H.M., Katz, S., 1964. Some problems in particle technology. *Chem. Eng. Sci.* 19, 555–579.
- Jacobson, M., 1999. *Fundamentals of Atmospheric Modeling*. Cambridge University Press.
- Janicka, J., Kolbe, W., Kollmann, W., 1979. Closure of the transport-equation for the probability density-function of turbulent scalar fields. *J. Non-Equilib. Thermodyn.* 4, 47–66.
- Kempf, A., Malalasekera, W., Ranga-Dinesh, K.K.J., Stein, O.T., 2008. Large eddy simulations of swirling non-premixed flames with flamelet models: a comparison of numerical methods. *Flow Turb. Comb.* 81 (4), 523–561. <http://dx.doi.org/10.1007/s10494-008-9147-1>.
- Klein, M., Sadiki, A., Janicka, J., 1998. A digital filter based generation of inflow data for spatially developing direct numerical or large eddy simulations. *J. Comput. Phys.* 10, 1246–1248.
- Klimenko, A.Y., 2009a. Lagrangian particles with mixing. I. Simulating scalar transport. *Phys. Fluids* 21 (6), 065101.
- Klimenko, A.Y., 2009b. Lagrangian particles with mixing. II. Sparse-Lagrangian methods in application for turbulent reacting flows. *Phys. Fluids* 21 (6), 065102.
- Klimenko, A.Y., Pope, S., 2003. The modelling of turbulent reacting flows based on multiple mapping conditioning. *Phys. Fluids* 15 (7), 1907–1925.
- Kronenburg, A., Stein, O.T., 2016. LES-CMC of a partially premixed, turbulent dimethyl ether jet diffusion flame. *Flow Turb. Combust.*, 1–14 <http://dx.doi.org/10.1007/s10494-016-9788-4>.
- Kruis, F., Maisels, A., Fissan, H., 2000. Direct simulation Monte Carlo method for particle coagulation and aggregation. *AIChE J.* 46 (9), 1735–1742.
- Kruis, F.E., Wei, J., van der Zwaag, T., Haep, S., 2012. Computational fluid dynamics based stochastic aerosol modeling: combination of a cell-based weighted random walk method and a constant-number Monte-Carlo method for aerosol dynamics. *Chem. Eng. Sci.* 70, 109–120.
- Lesniewski, T., 1997. *Particle Nucleation and Growth in Turbulent Jets*, Ph.D. thesis, University of California, Los Angeles.
- Lesniewski, T., Friedlander, S., 1998. Particle nucleation and growth in a free turbulent jet. *Proc. Roy. Soc. A* 454, 2477–2504.
- Loeffler, J., Das, S., Garrick, S.C., 2011. Large eddy simulation of titanium dioxide nanoparticle formation and growth in turbulent jets. *Aerosol Sci. Technol.* 45 (5), 616–628. <http://dx.doi.org/10.1080/02786826.2010.551147>.
- Marchisio, D., Fox, R., 2013. *Computational Models for Polydisperse Particulate and Multiphase Systems*. Cambridge University Press.
- Mueller, M.E., Pitsch, H., 2013. Large eddy simulation of soot evolution in an aircraft combustor. *Phys. Fluids* 25 (11), 110812.
- Okuyama, K., Kousaka, Y., Warren, D.R., Flagan, R.C., Seinfeld, J.H., 1987. Homogeneous nucleation by continuous mixing of high temperature vapor with room temperature gas. *Aerosol Sci. Technol.* 6 (15), 15–27.
- Pesmazoglou, I., Kempf, A., Navarro-Martinez, S., 2014. Aerosol nucleation in a turbulent jet using large eddy simulations. *Chem. Eng. Sci.* 116 (0), 383–397.
- Pope, S.B., 1985. PDF methods for turbulent reacting flows. *Prog. Energy Combust. Sci.* 11, 119–192.
- Potin-Gautier, M., Grenier, P., Bonastre, J., 1982. Nouvelle application analytique de la methode de determination des pressions de vapeur par saturation d'un gaz inerte. *Anal. Lett.* 15, 1431–1448.
- Prakash, A., Bapat, A., Zachariah, M., 2003. A simple numerical algorithm and software for solution of nucleation, surface growth, and coagulation problems. *Aerosol Sci. Technol.* 37 (11), 892–898.
- Pratsinis, S.E., 1988. Simultaneous nucleation, condensation, and coagulation in aerosol reactors. *J. Colloid Interf. Sci.* 124 (2), 416–427.
- Riddick, J., Bunger, W., 1971. *Organic Solvents*. John Wiley & Sons, Inc., Hoboken, USA.
- Rigopoulos, S., 2010. Population balance modelling of polydispersed particles in reactive flows. *Prog. Energy Combust. Sci.* 36 (4), 412–443.
- Salehi, F., Cleary, M., Masri, A., Ge, Y., Klimenko, A., 2017. Sparse-Lagrangian MMC simulations of an n-dodecane jet at engine-relevant conditions. *Proc. Comb. Inst.* 36, 3577–3585. <http://dx.doi.org/10.1016/j.proci.2016.07.074>.
- Subramaniam, S., Pope, S.B., 1998. A mixing model for turbulent reactive flows based on Euclidean minimum spanning trees. *Combust. Flame* 115, 487.
- Sutugin, A., Fuchs, N., 1968. Formation of condensation aerosols at high vapor supersaturation. *J. Colloid Interf. Sci.* 27 (2), 216–228.
- Tsantilis, S., Kammler, H.K., Pratsinis, S.E., 2002. Population balance modeling of flame synthesis of titania nanoparticles. *Chem. Eng. Sci.* 57, 2139–2156.
- Ukai, S., Kronenburg, A., Stein, O.T., 2015. Large eddy simulation of a dilute acetone spray flame using CMC coupled with tabulated chemistry. *Proc. Combust. Inst.* 35, 1667–1674. <http://dx.doi.org/10.1016/j.proci.2014.06.013>.
- Veroli, G.Y.D., Rigopoulos, S., 2011. Modeling of aerosol formation in a turbulent jet with the transported population balance equation-probability density function approach. *Phys. Fluids* 23, 043305.
- Villiermaux, J., Devillion, J., 1972. Representation de la coalescence et de la redispersion des domaines de segregation dans un fluide par un modele d'interaction phenomenologique. *Proc. Sec. Int. Symp. Chem. React. Eng.*, 1–13.
- Vo, S., Kronenburg, A., Stein, O., Cleary, M., 2017a. Multiple mapping conditioning for silica nanoparticle nucleation in turbulent flows. *Proc. Combust. Inst.* 36, 1089–1097. <http://dx.doi.org/10.1016/j.proci.2016.08.088>.
- Vo, S., Stein, O., Kronenburg, A., Cleary, M.J., 2017b. Cleary, assessment of mixing time scales for a sparse particle method. *Combust. Flame* 179, 280–299. <http://dx.doi.org/10.1016/j.combustflame.2017.02.017>.
- Xiong, Y., Pratsinis, S.E., 1991. Gas phase production of particles in turbulent reactive flows. *J. Aerosol Sci.* 22 (5), 637–655.
- Zhou, K., Chan, T.L., 2011. Simulation of homogeneous particle nucleation in a free turbulent jet. *Aerosol Sci. Technol.* 45 (8), 973–987. <http://dx.doi.org/10.1080/02786826.2011.572935>.
- Zhou, K., Chan, T.L., 2014. Analytical approximation schemes for mean nucleation rate in turbulent flows. *Aerosol Sci. Technol.* 48 (5), 459–466. <http://dx.doi.org/10.1080/02786826.2014.890279>.
- Zhou, K., Attili, A., Alshaarawi, A., Bisetti, F., 2014. Simulation of aerosol nucleation and growth in a turbulent mixing layer. *Phys. Fluids* 26, 065106.



**Paper 3:**

**Title:** Joint experimental and numerical study of silica particulate synthesis in a turbulent reacting jet

**Authors:** Gregor Neuber  
Institut für Technische Verbrennung,  
University of Stuttgart, 70174 Stuttgart, Germany

Carlos E. Garcia  
Department of Mechanical Engineering,  
Imperial College London, London SW7 2AZ, United Kingdom

Andreas Kronenburg  
Institut für Technische Verbrennung,  
University of Stuttgart, 70174 Stuttgart, Germany

Benjamin A. O. Williams  
Department of Engineering Science,  
University of Oxford, Oxford OX1 3PU, United Kingdom

Frank Beyrau  
Institute of Fluid Dynamics and Thermodynamics,  
University of Magdeburg, Magdeburg 39106, Germany

Oliver T. Stein  
Institut für Technische Verbrennung,  
University of Stuttgart, 70174 Stuttgart, Germany

M. J. Cleary  
School of Aerospace, Mechanical and Mechatronic Engineering,  
The University of Sydney, NSW 2006, Australia

**Journal:** Proceedings of the Combustion Institute

**Volume:** 37

**Pages:** 1213 – 1220





ELSEVIER



CrossMark

Available online at [www.sciencedirect.com](http://www.sciencedirect.com)

ScienceDirect

Proceedings of the Combustion Institute 37 (2019) 1213–1220

Proceedings  
of the  
Combustion  
Institute

[www.elsevier.com/locate/proci](http://www.elsevier.com/locate/proci)

# Joint experimental and numerical study of silica particulate synthesis in a turbulent reacting jet

Gregor Neuber<sup>a</sup>, Carlos E. Garcia<sup>b</sup>, Andreas Kronenburg<sup>a,b,\*</sup>,  
Benjamin A.O. Williams<sup>b,c</sup>, Frank Beyrau<sup>b,d</sup>, Oliver T. Stein<sup>a</sup>,  
Matthew J. Cleary<sup>e</sup>

<sup>a</sup> *Institute for Combustion Technology, University of Stuttgart, Stuttgart 70174, Germany*

<sup>b</sup> *Department of Mechanical Engineering, Imperial College London, London SW7 2AZ, United Kingdom*

<sup>c</sup> *Department of Engineering Science, University of Oxford, Oxford OX1 3PU, United Kingdom*

<sup>d</sup> *Institute of Fluid Dynamics and Thermodynamics, University of Magdeburg, Magdeburg 39106, Germany*

<sup>e</sup> *School of Aerospace, Mechanical and Mechatronic Engineering, The University of Sydney, 2006, New South Wales, Australia*

Received 29 November 2017; accepted 11 June 2018

Available online 8 September 2018

## Abstract

This paper presents results from a joint experimental and numerical study of silica particulate synthesis for a turbulent reacting jet configuration where a cold jet doped with silane issues into a hot vitiated coflow. The experimental investigation involves simultaneous measurements of elastic light scattering and planar laser-induced fluorescence signals and these are used for validation of a novel computational approach, called PBE-MMC-LES, for the solution of the joint scalar probability density function of the gas phase species and the discretised particulate size distribution. Model validation follows the “paradigm shift” approach which is based on the computation of “predicted signals” which are compared directly with the experimentally-acquired signals. The results demonstrate that PBE-MMC-LES can model particulate inception, surface growth and agglomeration at reasonable computational cost. The agreement between the measured and computed signals is good in the light of the modelling complexities associated with particle flame synthesis, but predictions are rather sensitive to the uncertainties in precursor chemistry leading to nucleation and growth.

© 2018 The Combustion Institute. Published by Elsevier Inc. All rights reserved.

**Keywords:** Silica particulates; Particulate flame synthesis; Turbulent combustion modelling; Multiple mapping conditioning; PBE-MMC-LES

## 1. Introduction

Silica particulates have widespread applications (see e.g. [1]), and it has been shown that the gas phase reactions leading to particulate formation [2] as well as interparticulate interactions [3] are

\* Corresponding author at: Institute for Combustion Technology, University of Stuttgart, 70174 Stuttgart, Germany.

E-mail address: [kronenburg@itv.uni-stuttgart.de](mailto:kronenburg@itv.uni-stuttgart.de) (A. Kronenburg).

<https://doi.org/10.1016/j.proci.2018.06.074>

1540-7489 © 2018 The Combustion Institute. Published by Elsevier Inc. All rights reserved.

crucial for the final product properties. The prediction of these interactions is challenging - in particular in turbulent flows that are needed for high product throughput - and the current work presents a novel modelling strategy for the prediction of particulate size distributions in turbulent particulate synthesis processes.

The spatio-temporal aerosol evolution can be described by the population-balance equation (PBE). Typical implementations include the direct Monte-Carlo methods [4], moment methods [5] and discretised sectional methods [6] with a comprehensive summary given in [7]. Loeffler et al. [8] and Wang and Garrick [9] investigated the formation and growth of titanium dioxide nanoparticles in the context of large eddy simulation (LES). They all neglected aerosol-turbulence interactions, although recently Neuber et al. [10] showed that the introduced error can be large and sub-grid scale contributions should not be neglected. Agglomeration in turbulent jet flows was examined in planar [11] and round turbulent jets [12] using the sectional model. More recently, Sewerin and Rigopoulos [13] presented an explicit adaptive grid approach for the numerical solution of the population balance equation and applied this method to soot formation and growth in a turbulent diffusion flame.

Most of the common approaches couple an Eulerian solution of the PBE with an Eulerian solver for the flow field and the gas phase composition. Here, we pursue a different approach: we apply a hybrid Euler/Lagrange method where the Eulerian scheme solves the turbulent LES-filtered flow field only, and a stochastic Monte-Carlo method is used for the prediction of the spatial and temporal evolution of the joint scalar filtered density function (FDF) of the reactive scalars and the particulate size distribution of the silica particulates. To avoid any ambiguity we strictly distinguish between “stochastic particles” which are computational elements for solving the FDF equation in a Lagrangian sense, and “particulates” which are the physical nanoparticles that are formed in the flame synthesis process. While traditional stochastic FDF methods require particle numbers of 20–50 per LES cell, we employ a so-called sparse-Lagrangian approach where far fewer stochastic particles are required (as low as 1 stochastic particle per 27 Eulerian cells [14]). The key ingredient in sparse modelling of the FDF is the use of a novel mixing model called multiple mapping conditioning (MMC) [15] to emulate the effects of molecular diffusion. It has been applied and validated for a range of turbulent reacting flows [14,16]. More recent publications demonstrate the method’s applicability to particulate nucleation and growth processes [10,16] where interactions with turbulence are of importance. The objective of this work is to demonstrate the capability of a combined PBE-MMC-LES method to model particulate inception,

surface growth and agglomeration of non-spherical agglomerates in a turbulent, reactive jet. The model is validated by comparison with measured signals of OH and silica particulates obtained by planar laser-induced fluorescence (PLIF) and elastic light scattering (ELS).

This paper is structured as follows: The modelling of the particulate matter and the PBE-MMC-LES model are described in Section 2. The experimental and numerical setups are presented in Sections 3 and 4. Predictions are compared with experimental ELS and OH-PLIF signals in Section 5. Conclusions follow in Section 6.

## 2. Methodology

### 2.1. Particulate flame synthesis modelling

The evolution of the particulate size distribution (PSD) is modelled by the solution of the population balance equation. We use the nodal form of the sectional approach [17] which discretises the particulate volume space into a finite number of sections. The PBE then reads

$$\begin{aligned} \frac{\partial n_k}{\partial t} + \frac{\partial}{\partial x_j} \left( u_j n_k - D_k \frac{\partial n_k}{\partial x_j} \right) \\ = - \frac{\partial (G(v, \mathbf{Y}) n_k)}{\partial v} + \dot{s}_k, \end{aligned} \quad (1)$$

where  $n_k$  is the number density of particulates in section  $k$ ,  $G(v, \mathbf{Y})$  is the volumetric growth term that can be modelled as a function of particulate volume,  $v$ , and the gas phase composition characterised by the gaseous species mass fractions  $\mathbf{Y}$ ,  $u_i$  and  $D_k$  denote the velocity in direction  $i$  and the diffusion coefficient of section  $k$ , respectively, and the source term  $\dot{s}_k$  accounts for inception and agglomeration. The inception rate is given by the production rate of the precursor species and is described by the underlying chemical reaction mechanism for the gaseous species. Upon inception these primary particulates are added to the first section of the discretised particulate size distribution.

For small particulates the surface growth is described as a collision process where the growth rate is based on the free-molecular collision kernel and the collision diameter of the depositing species is assumed to be the diameter of the molecule [3]. In our sectional approach we assume that the agglomerates are fractal-like and their morphology follows the power law of agglomerates [6]. The collision diameter of the agglomerate is then given by  $d_{c,k} = d_{p,0} N_k^{1/D_f}$ , with  $N_k$  being the number of primary particulates in the agglomerate,  $d_{p,0}$  being the primary particulate diameter and with  $D_f$  being the fractal dimension which is set to  $D_f = 1.8$  as suggested in e.g. Ref. [3]. The volumetric surface growth of larger particulates is determined by the diffusion rate of the depositing species towards

the agglomerates' surface and therefore a diffusion-limited growth method [18] is used. The harmonic mean of the two formulations serves as a blending function for the growth of intermediate-sized particulates.

The agglomeration process is treated as outlined in Loeffler et al. [8]. Due to the discretised form of the PSD the agglomeration needs a size-splitting operator to ensure mass conservation by distributing formed particulates into two adjacent sections. This method introduces a slight broadening of the PSD but this effect is small compared to growth and agglomeration [10]. As agglomerate sizes cover a wide Knudsen number range, we use a modified Fuchs interpolation - proposed by Kruis et al. [19] - between the free molecular and continuum regimes to model the collision frequencies.

## 2.2. Implementation using multiple mapping conditioning

The hybrid Eulerian/Lagrangian scheme consists of an Eulerian LES solver for the conservation equations for mass, momentum, and mixture fraction. We do not, however, solve Eq. (1) directly in an Eulerian framework, but aim at the solution of the joint filtered density function of the composition field  $\phi = (Y_1, \dots, Y_s, h, Z, n_1, \dots, n_e)$ . The scalar vector  $\phi$  includes the gas phase composition  $Y$ , the enthalpy,  $h$ , mixture fraction,  $Z$  (which is different to but should be correlated with the Eulerian LES-filtered mixture fraction field labelled  $\tilde{f}$ ), and the discretised particulate number density  $n$ .

The major advantage of an FDF method is that the chemical source terms in the gas phase and the rates of particulate nucleation and growth appear in closed form. Unknown sub-grid effects due to turbulence do not require any closure. As the direct solution of the joint FDF transport equation is intractable for a system of high dimensionality, it is standard procedure to solve an equivalent system for an ensemble of stochastic (notional) particles instead [20]. The evolution of the stochastic particles is described by stochastic differential equations with fractional steps for spatial transport, gas phase reaction, mixing and aerosol dynamics. The particle transport and the change of the composition field in time are governed by Cleary and Klimenko [14]

$$dx_j^p = \left[ \tilde{u}_j + \frac{1}{\rho} \frac{\partial}{\partial x_j} (\bar{\rho} D_{\text{eff}}^p) \right]^p dt + \sqrt{2D_{\text{eff}}^p} d\omega, \quad (2)$$

$$d\phi_\alpha^p = (W_\alpha^p + S_\alpha^p) dt, \quad (3)$$

where  $\omega$  is a Wiener process and standard notation is used for diffusion, density, velocity, space and time, and unity Lewis number assumptions have been employed. In Eq. (3),  $S_\alpha$  is the mixing operator and  $W_\alpha$  accounts for source terms including



Fig. 1. Modified version of the Cabra burner.

chemical reactions, particulate inception, surface growth and agglomeration. The chemical reaction rates and particulate nucleation are given by a suitable reaction mechanism and models for surface growth and agglomeration have been introduced in Section 2.1. The mixing term, however, appears in unclosed form. It requires modelling, and here we use multiple mapping condition (MMC) in its generalised form [15] for closure. MMC requires the additional solution of a reference field. This reference field is the (Eulerian) LES solution of mixture fraction,  $\tilde{f}$ , and the mixing of the stochastic particles is then conditioned on  $\tilde{f}$ , which is interpolated to the particle position. The correlation between mixture fraction and reactive scalars (as expected in diffusion-limited flames) enforces localisation in composition space and allows for a significant reduction of the number of notional particles needed for the accurate prediction of the joint FDF. More details on the implementation can be found in [14,21].

## 3. Experimental configuration

The modelled configuration is a modified version of the Cabra burner [22]. The setup is depicted in Fig. 1 and consists of a turbulent nitrogen jet doped with different concentrations (0, 300, 1000 and 3100 ppm) of silane as a precursor for the silica particulates. The jet is centred in a hot vitiated coflow with an outer diameter of 210 mm. The Reynolds number is  $Re_D = 10\,000$  based on a jet diameter of  $D = 4.57$  mm and the cold jet bulk velocity of  $U_j = 33.2$  m/s. The coflow consists of a hot lean premixed hydrogen-air mixture with an equivalence ratio of  $\phi = 0.4$  at a temperature of  $T_c = 1447$  K. The coflow velocity is  $U_c = 1$  m/s based on cold conditions. The nozzle exit plane extends 70 mm above the perforated plate of the coflow that leads to heating of the central jet by the co-flow. Radial temperature profiles were measured with a radiation-corrected bare-wire R-type thermocouple and used to adjust the temperature inflow conditions for the LES.

Measurements include two laser diagnostic techniques; planar laser-induced fluorescence (PLIF) and elastic light scattering (ELS). The

investigation is supplemented with extractive particulate sampling. OH-PLIF is used to validate the chemical kinetic model whereas ELS is used to validate both the particulate formation model and the temperature field. Hence, our model validation follows the “paradigm shift” approach used for a variety of analyses in turbulent combustion [23,24] including particulate nucleation and growth [25]. This strategy avoids incurring assumptions needed to convert experimental signals into a physical quantity such as particulate number density.

In the ELS experiment, a Q-switched frequency-doubled Nd:YAG laser with four independent heads is used in conjunction with sheet-forming optics to illuminate a 23 mm × 400 μm region across the burner centreline. The ELS signal is collected using a CCD camera with an f/2 105 mm lens perpendicular to the laser beam. Using three of the four available heads, the shot energy is approximately 3 × 450 mJ with a repetition rate of 10 Hz. Data from different heights is obtained by vertical translation of the burner. Post-processing steps include background subtraction, shot energy correction, beam profile correction, spatial calibration and image de-warping. The ELS signal is a combination of contributions from molecular and particulate scattering. The ELS signal  $S$  originating from gas molecules is calculated according to

$$S^{\text{molec}} \propto \frac{\sum_{i=1}^{Y_i} \chi_i \sigma_i}{T} \quad (4)$$

where  $T$  is the temperature,  $\chi_i$  is the species mole fraction and  $\sigma_i$  is the ELS cross section of species  $i$  at 532 nm. Normalised ELS cross sections have been determined by Fuest et al. [26]. Since both chemical composition and temperature are fully defined in the simulation, the ELS signal is predicted within the model. Additionally, the ELS signal originating from agglomerates is calculated according to the Rayleigh–Debye–Gans theory of light scattering by fractal agglomerates (RDG-FA) [27]. The contribution of each agglomerate is given by

$$S^{\text{agg}} \propto \sum_k^{N_s} C_{\text{sca}}^{\text{agg}} N_k, \quad (5)$$

where the  $C_{\text{sca}}^{\text{agg}}$  is the scattering cross section of the fractal agglomerate. The latter is a function of the agglomerate size [27] and needs to be weighted with the computed PSD to be comparable to the measured signal.

The fourth head of the Nd:YAG laser is used to pump a frequency-doubled Rhodamine 6G dye laser, tuned to a wavelength of 283.6 nm to excite the  $Q_1(8)$  transition ( $v = 1 \leftarrow 0$ ) of the  $A^2\Sigma \leftarrow X^2\Pi$  electronic system of the OH radical. This transition has been chosen such that the LIF signal is weakly sensitive to temperature. A CCD camera with intensifier (multi-alkali, P43) and f/2.8

UV lens is placed at 90° to collect the fluorescence signals from the ( $v = 0 \leftarrow 0$ ) and ( $v = 1 \leftarrow 1$ ) branches of OH around 309–315 nm. Laser energy and sheet thickness have been adjusted to ensure operation within the linear LIF regime [28]. The volume probed is 23 mm × 700 μm and the shot energy 1.15 mJ. Background subtraction, shot energy correction, beam profile correction and beam extinction along the direction of travel of the beam are applied to the experimental signal. The predicted OH-LIF signal is calculated as detailed in Coriton et al. [29].

The ELS and OH-LIF signals are calculated on each stochastic particle where the instantaneous and local species composition and particulate size distribution are known. The signals from the particulates are then collected to obtain mean and variances that are compared with the experimental data in Section 5.

#### 4. Numerical configuration

The MMC-LES model has been implemented into a code called *mmcFoam* [30] which is compatible with the OpenFOAM open source C++ libraries. The computational domain extends 25D in the axial direction and 11D in the radial direction. The jet diameter is resolved by 63 cells. The circumferential and the axial directions of the domain are resolved by 84 and 576 cells, respectively, resulting in more than 4 million LES grid cells overall with 95% of the total turbulent kinetic energy being resolved everywhere except at the nozzle lip.

The turbulent sub-grid viscosity is modelled by the  $\sigma$ -Model [31] and a model constant of  $C_\sigma = 1.5$  is applied. Pipe flow simulations were conducted inside the nozzle to provide realistic turbulent inflow velocity boundary conditions and zero-gradient outflow conditions were used at all other boundaries. Second-order central difference and TVD schemes are used for discretization of momentum and species transport, respectively. For the Lagrangian scheme, one particle for every 17.5 LES cells is used corresponding to 230,000 stochastic particles overall. As in earlier publications [10,14] we use standard MMC modelling parameters ( $f_m = 0.03$ ) and the time scale model introduced in [21].

Silica nanoparticles can be obtained from thermal decomposition methods or from nucleation of hydrogenated silicon particulates during silane pyrolysis [2,32], and the latter variant is used here. We use the mechanism provided by Suh et al. [2] including 63 species and 264 reactions at their reported rates for atmospheric pressure. For the solid silica particulates, the primary particulate diameter is given as  $d_{p,0} = 0.98$  nm with a density of  $\rho_p = 2196$  kg/m<sup>3</sup>. We use 50 sections to discretise the volume-based PSD of the silica particulates with  $v_k = 2^k v_0$ . Thus the stochastic

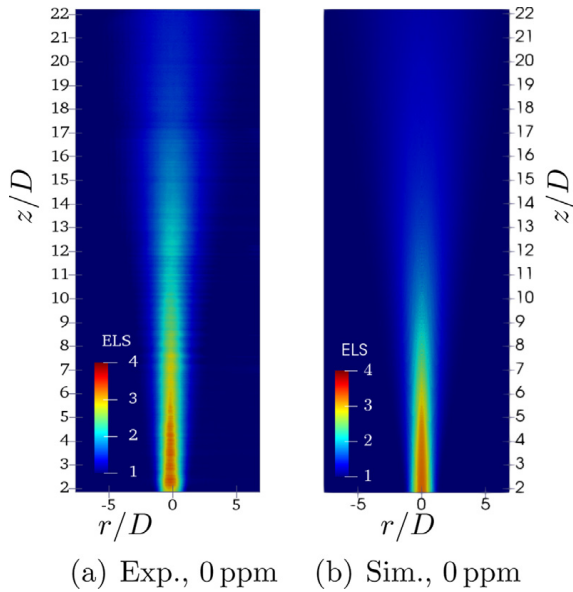


Fig. 2. Contour plots of the normalised elastic light scattering signal for the reference case without silane loading.

particles carry the information of 63 species, the enthalpy, the mixture fraction and the 50 size sections of the PSD. The simulations have been run for 6300 CPUh, where the stochastic particle costs are about 3 times the costs of the LES.

## 5. Results

First, the general computational setup needs to be validated before the capabilities of PBE-MMC-LES to model particulate synthesis can be assessed. A first comparison between experiments and simulations is therefore conducted for a reference case without any silane doping and therefore without particulate formation. The corresponding contour plots of the predicted and measured ELS signals are shown in Fig. 2. In the absence of particulate matter the ELS signal is a function of species composition and temperature only. Thus, for the silane-free case predicted and measured signals are normalised with their respective value in the coflow. We considered all major species' cross sections ( $N_2$ ,  $O_2$ ,  $H_2$ ,  $H_2O$ ,  $OH$ ,  $O$ ,  $H$ ) with the remaining species contributing less than 0.1% to the total signal. The ELS cross section for nitrogen is set to unity, leaving the temperature as the only free variable in the unmixed jet stream (cf. Eq. (4)) with an inverse proportionality between signal and temperature. The decay of the jet seems somewhat over-predicted. This may be due to an over-prediction of turbulent velocity fluctuations in the (precomputed) pipe flow simulation that are used as inlet conditions. In the experiments, the jet inlet pipe is surrounded by a hot coflow and the heat flux towards the central jet will

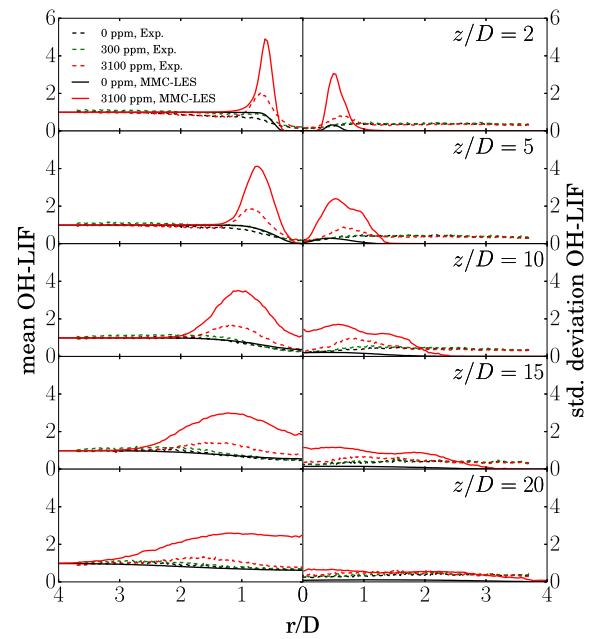


Fig. 3. Radial profiles of the OH-LIF signal at different downstream positions. The signals are normalised with the respective value in the coflow at  $z/D = 5$ .

increase the jet's temperature. This will increase the molecular viscosity and dampen the initial velocity fluctuations. No heat flux is considered in the pipe flow simulations, and the fluctuations of the velocity at the inlet boundary are therefore slightly over-predicted. We now turn our attention to the prediction of the normalised OH-LIF signal as it is an indication for the position of the shear layer, and it allows for conclusions about gas phase chemistry, i.e. whether the kinetics of the silane decomposition process are modelled accurately. Radial profiles of the mean and standard deviation are shown in Fig. 3 where experimental and predicted signals are normalised with their respective values in the coflow at  $z/D = 5$ . Results are shown for two cases with 0 ppm of silane loading (the reference case) and with 3100 ppm of silane. Predictions for the reference case are excellent. It is also apparent in the 3100 ppm case that OH radical concentrations are increased due to the decomposition of silane. The positions of the silane decomposition and OH production are well captured, however, the peak in the computed mean OH-LIF signal is more than two times stronger than the measured value. Some uncertainties in the kinetics of silane oxidation certainly persist and this is now reflected in the quantitative predictions by MMC. Following the trends of the means, standard deviations are also overpredicted in the shear layer by a similar margin. It is noted that experimental standard deviations do not drop to zero in the coflow. This is believed to be mostly due to shot noise and, to a lesser extent, readout noise and

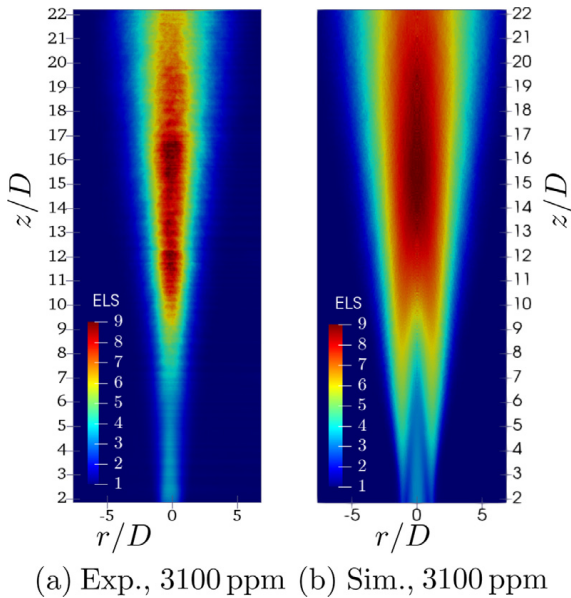


Fig. 4. Contour plots of the normalised elastic light scattering signal for case with 3100 ppm silane loading.

temperature fluctuations in the coflow. Overall, we achieve satisfactory agreement between measured and predicted reaction zone position and silane decomposition considering the uncertainty in the detailed chemical mechanisms for silane oxidation.

Figure 4 compares the measured and predicted ELS signals for the case with 3100 ppm silane doping. For the cases with silane doping the predicted ELS signal is the sum of the signal of the gas and the particulate phases. The gaseous signal is normalised as for the reference case. The signal associated with scatter from the particulate matter is normalised to match the maximum signals in the domain. The agreement is good and the position of the peak value is well matched. As the radical concentration is overpredicted, particulate precursors and hence, particulates are formed somewhat too quickly as the clear increase in the predicted ELS signal within the shear layer demonstrates. In contrast, experimental data does not show significant formation and growth of particulates so far upstream and larger particulates that lead to significant scattering are formed predominantly along the centreline. The ELS signal starts to decrease at around  $z/D = 20$  for both, the experiment and simulation. It is noted, however, that the predicted ELS signal is broader than the measured signal and tends to decrease more slowly. This may be attributed to an overprediction of the agglomeration process. The larger agglomerates lead to stronger signals and a slower signal decay with downstream distance. As several quantities affect the ELS signal (in particular particulate number, size and agglomerate morphology), it is difficult to identify the error source that leads to the differences between measurement and computation. We have

therefore conducted a number of parameter studies that help to assess the relative influence of our modelling uncertainties. We tested two additional reaction mechanisms: one proposed by Lewis and Chang [33] and one by Miller et al. [34]. Lewis and Chang [33] failed to produce a sufficiently large number of particulates, as key species of the irreversible particulate clustering mechanism are not present in the base mechanism. The mechanism proposed by Miller et al. [34] yielded a comparable spatial distribution of the ELS signal, but excessive particulate formation in the early shear layer increased the ELS signal therein and led to much larger qualitative differences to the LES signal than the reaction mechanism of Suh et al. [2].

The effect of particulate morphology on the ELS signal can be assessed by variation of the fractal dimension,  $D_f$ . Here, we have used  $D_f = 1.8$  as commonly reported in the literature for silica agglomerates, and this predicts the correct position of the peak ELS signal. We have also conducted simulations with different - but still constant - fractal dimensions ( $D_f = 2.0$  and  $2.2$ ) which reduced the impact of agglomeration and shifted the ELS signal peak downstream by around 10 to 15 jet diameters, respectively. We have also tested the effect of coalescence up to primary particulate diameters of  $d_{p,0} = 10$  nm. This also shifted the peak of the ELS signal by slightly more than 15 jet diameters. These modifications are rather “ad hoc” but useful to assess the model’s sensitivity to these parameters. More complex models that can characterize particulates by e.g. particulate size and a distribution of fractal dimensions, are not easy to implement and beyond the scope of the present paper but will be investigated in future work.

Figure 5 allows for a more quantitative analysis. The overall trend is captured well, but the overprediction of particulate formation in the shear layer is confirmed by the predicted ELS peak at  $z/D = 5$  and  $r/D = 0.6$ . It is also apparent that particulate dynamics seem to be more intermittent than the model predicts and the measured standard deviations are much higher along the centreline for axial positions between  $10 < z/D < 20$ .

The experimental ELS signals from the cases with 300 ppm and 1000 ppm silane loading do not provide any additional information for model validation as particulate formation seems to be low and signals do not differ from the reference case with 0 ppm silane. This is firstly due to reduced particulate formation and secondly, due to the lack of agglomeration. Figure 6 shows transmission electron microscope (TEM) images of particulates extracted from the exhaust. These images do certainly not represent the particulates’ PSD, however, they clearly demonstrate the reduced particulate nucleation and lack of agglomeration in the case with 300 ppm. The computed PSDs indicate that the computations capture the growth and agglomeration processes and provide results that are

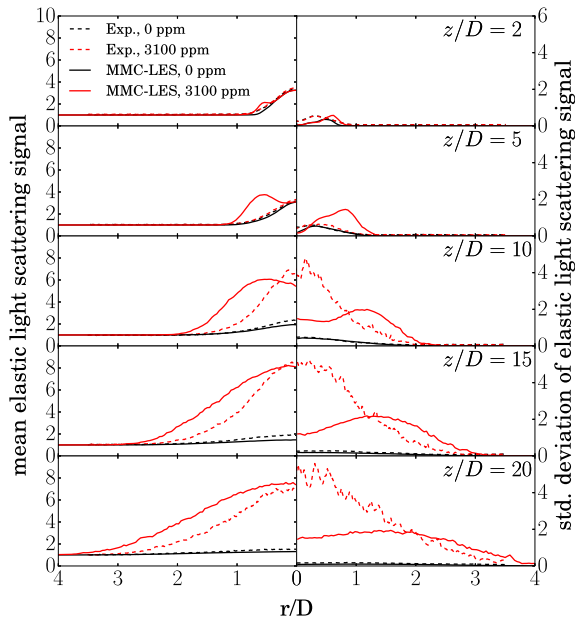
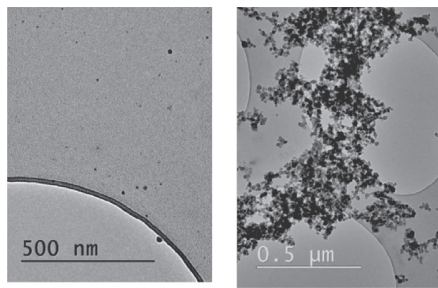
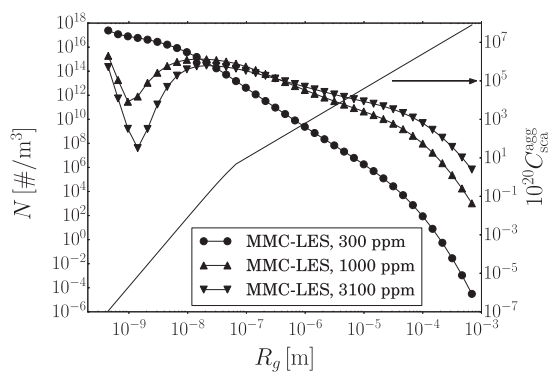


Fig. 5. Radial profiles of the ELS signal at different downstream positions.



(a) TEM, 300 ppm (b) TEM, 3100 ppm



(c) PSD at  $z/D = 20$  on centreline position

Fig. 6. (a), (b) transmission electron microscope (TEM) image of particulates extracted in the exhaust using a filter for different silane loadings; (c) predicted PSDs of particulates at  $z/D = 20$  and scattering cross section of fractal agglomerates.

in the range of the measured agglomerate sizes. Figure 6(c) also shows the scattering cross section,  $C_{sca}^{agg}$  (cf. Eq. (5)), as function of the agglomerate size. It is apparent why the very small particulates for the low silane loading do not yield a significant signal despite a particulate number density that is not small. The low scattering cross section for small particulates leads to a maximum signal that is about more than three orders of magnitude lower than the maximum signal observed for 3100 ppm, and it is also low when compared to the ELS signal originating from the cold jet center. We note that the size distribution is rather broad. We see that large agglomerates ( $> 1 \mu\text{m}$ ) are 8 orders of magnitude less likely than the incipient particulates for the 300 ppm case, however, large particulates have a notable probability for higher silane loadings. The TEM analysis does not allow for the extraction of a PSD, but Fig. 6(b) demonstrates that very large aggregates co-exist with very small clusters consisting of only few primary particulates.

It is apparent that uncertainties with respect to the modelling of silane chemistry and - potentially - the assumption of a constant fractal dimension persist, and a combination of these may lead to discrepancies between measurements and computations. Despite these uncertainties, however, a first important step has been taken towards a validated prediction of particulate synthesis in turbulent flows. Most recent LES studies of nanoparticulate formation do not provide a quantitative validation by direct comparison with signals acquired by concomitant measurements (see e.g. [8,35]), and LES studies of the similarly difficult to model soot formation are known to feature much larger discrepancies between predictions and measurements [36].

## 6. Conclusions

We have presented a joint experimental and numerical investigation of silica particulate synthesis in a turbulent environment. Measurements include simultaneous planar OH-LIF and ELS measurements that have been used to characterise particulate formation in the turbulent jet and to validate a novel PBE-MMC-LES implementation for the prediction of such process. The stochastic solution of the joint scalar FDF provides a sub-grid model for the unresolved interactions between turbulence, chemistry and particulate dynamics such as nucleation and growth, and the specific MMC mixing model allows for a significant reduction of notional particles when compared to standard FDF approaches. Measurements and computations agree fairly well, but uncertainties persist and can - to a large extent - be associated with uncertainties in the precursor chemistry leading to nucleation of the first particulates. Despite these discrepancies, this study is a major step towards the development of validated computational tools for the prediction

of nanoparticulate flame synthesis as it is one of the very few joint computational and experimental studies that address the issue of nanoparticle synthesis under the influence of turbulence. The predictive capability of PBE-MMC-LES is good when compared to results from existing studies of similar complexity such as soot formation in turbulent flames.

### Acknowledgments

We would like to thank R.P. Lindstedt (Imperial), M.R. Zachariah (Maryland) and M. Fuchs (CFD Software GmbH Berlin) for provision of the burner, the chemical mechanism and the  $\sigma$ -model source code. We acknowledge the partial financial support by Deutsche Forschungsgemeinschaft (KR 3684/12-1), ARC (DP180104190) and by the 2016 Universities Australia Germany Joint Research Co-operation Scheme.

### References

- [1] R.K. Iler, *The Chemistry of Silica*, Wiley, 1979.
- [2] S.-M. Suh, M. Zachariah, S. Girshik, *J. Vac. Sci. Technol. A* 19 (2001) 940–951.
- [3] S. Shekar, M. Sander, R. Riehl, A. Smith, A. Braumann, M. Kraft, *Chem. Eng. Sci.* 70 (2012) 54–66.
- [4] F. Kruis, A. Maisels, H. Fissan, *AIChE J.* 46 (2000) 1735–1742.
- [5] S.E. Pratsinis, *J. Colloid Interface Sci.* 124 (1988) 416–427.
- [6] S.K. Friedlander, *Smoke, Dust and Haze*, second, Oxford University Press, Oxford, New York, 2000.
- [7] D. Marchisio, R. Fox, *Computational Models for Polydisperse Particulate and Multiphase Systems*, Cambridge University Press, 2013.
- [8] J. Loeffler, S. Das, S.C. Garrick, *Aerosol Sci. Technol.* 45 (2011) 616–628.
- [9] G. Wang, S. Garrick, *J. Aerosol Sci.* 37 (2006) 431–451.
- [10] G. Neuber, A. Kronenburg, O.T. Stein, M.J. Cleary, *Chem. Eng. Sci.* 167 (2017) 204–218.
- [11] S. Miller, S. Garrick, *Aerosol Sci. Technol.* 38 (2004) 79–89.
- [12] I. Pasmazoglou, A. Kempf, S. Navarro-Martinez, *J. Aerosol Sci.* 111 (2017) 1–17.
- [13] F. Sewerin, S. Rigopoulos, *Combust. Flame* 189 (2018) 62–76.
- [14] M.J. Cleary, A.Y. Klimenko, *Phys. Fluids* 23 (2011) 115102-1–115102-19.
- [15] A.Y. Klimenko, S. Pope, *Phys. Fluids* 15 (2003) 1907–1925.
- [16] S. Vo, A. Kronenburg, O.T. Stein, M. Cleary, *Proc. Combust. Inst.* 36 (2017) 1089–1097.
- [17] A. Prakash, A. Bapat, M. Zachariah, *Aerosol Sci. Technol.* 37 (2003) 892–898.
- [18] J. T. A. Witten, L.M. Sander, *Phys. Rev. Lett.* 47 (1981) 1400–1403.
- [19] F.E. Kruis, K.A. Kusters, B. Scarlett, S.E. Pratsinis, *Aerosol Sci. Technol.* 19 (1993) 514–526.
- [20] S.B. Pope, *Prog. Energy Combust. Sci.* 11 (1985) 119–192.
- [21] S. Vo, O.T. Stein, A. Kronenburg, M. Cleary, *Combust. Flame* 179 (2017) 280–299.
- [22] R. Cabra, T. Myrvold, J.Y. Chen, R.W. Dibble, A.N. Karpetis, R.S. Barlow, *Proc. Combust. Inst.* 29 (2002) 1881–1888.
- [23] E.D. Tornaiainen, A.K. Hinz, F.C. Gouldin, *AIAA J.* 36 (1998) 1270–1278, doi:10.2514/2.509.
- [24] J. Floyd, A. Kempf, *Proc. Combust. Inst.* 33 (2011) 751–758, doi:10.1016/j.proci.2010.06.015.
- [25] B.C. Connelly, B.A.V. Bennett, M.D. Smooke, M. Long, *Proc. Combust. Inst.* 32 (2009) 879–886, doi:10.1016/j.proci.2008.05.066.
- [26] F. Fuest, R. Barlow, J.-Y. Chen, A. Dreizler, *Combust. Flame* 159 (2012) 2533–2562.
- [27] C.M. Sorensen, *Aerosol Sci. Technol.* 35 (2001) 648–687.
- [28] J.M. Seitzman, R.K. Hanson, *AIAA J.* 31 (1993) 513–519, doi:10.2514/3.11359.
- [29] B. Coriton, M. Zendejdel, S. Ukai, et al., *Proc. Combust. Inst.* 35 (2015) 1251–1258, doi:10.1016/j.proci.2014.06.042.
- [30] S. Galindo-Lopez, F. Salehi, M.J. Cleary, et al., *Comput. Fluids* 172 (2018) 410–425, doi:10.1016/j.compfluid.2018.03.083.
- [31] F. Nicoud, H.B. Toda, O. Cabrit, S. Bose, J. Lee, *Phys. Fluids* 23 (2011) 085106.
- [32] S.-M. Suh, M. Zachariah, S. Girshik, *J. Aerosol Sci.* 33 (2002) 943–959.
- [33] M. Lewis, J. Chang, *J. Propul. Power* 16 (2000) 365–367.
- [34] T. Miller, M. Wooldridge, J. Bozzelli, *Combust. Flame* 137 (2004) 73–92.
- [35] A. Rittler, L. Deng, I. Wlokas, A. Kempf, *Proc. Combust. Inst.* 36 (2017) 1077–1087.
- [36] M.E. Mueller, H. Pitsch, *Combust. Flame* 159 (2012) 2166–2180.

**Paper 4:**

**Title:** Sparse-Lagrangian PDF Modelling of Silica Synthesis  
from Silane Jets in Vitiated Co-flows with  
Varying Inflow Conditions

**Authors:** Gregor Neuber  
Institut für Technische Verbrennung,  
University of Stuttgart, 70174 Stuttgart, Germany

Andreas Kronenburg  
Institut für Technische Verbrennung,  
University of Stuttgart, 70174 Stuttgart, Germany

Oliver T. Stein  
Institut für Technische Verbrennung,  
University of Stuttgart, 70174 Stuttgart, Germany

Carlos E. Garcia  
Department of Mechanical Engineering,  
Imperial College London, London SW7 2AZ, United Kingdom

Benjamin A. O. Williams  
Department of Engineering Science,  
University of Oxford, Oxford OX1 3PU, United Kingdom

Frank Beyrau  
Institute of Fluid Dynamics and Thermodynamics,  
University of Magdeburg, Magdeburg 39106, Germany

M. J. Cleary  
School of Aerospace, Mechanical and Mechatronic Engineering,  
The University of Sydney, NSW 2006, Australia

**Journal:** Flow, Turbulence and Combustion

**Volume:** 106

**Pages:** 1167 – 1194





# Sparse-Lagrangian PDF Modelling of Silica Synthesis from Silane Jets in Vitiated Co-flows with Varying Inflow Conditions

Gregor Neuber<sup>1</sup> · Andreas Kronenburg<sup>1</sup> · Oliver T. Stein<sup>1</sup> · Carlos E. Garcia<sup>2</sup> · Benjamin A. O. Williams<sup>3</sup> · Frank Beyrau<sup>4</sup> · Matthew J. Cleary<sup>5</sup>

Received: 4 December 2019 / Accepted: 13 April 2020  
© The Author(s) 2020

## Abstract

This paper presents a comparison of experimental and numerical results for a series of turbulent reacting jets where silica nanoparticles are formed and grow due to surface growth and agglomeration. We use large-eddy simulation coupled with a multiple mapping conditioning approach for the solution of the transport equation for the joint probability density function of scalar composition and particulate size distribution. The model considers inception based on finite-rate chemistry, volumetric surface growth and agglomeration. The sub-models adopted for these particulate processes are the standard ones used by the community. Validation follows the “paradigm shift” approach where elastic light scattering signals (that depend on particulate number and size), OH- and SiO-LIF signals are computed from the simulation results and compared with “raw signals” from laser diagnostics. The sensitivity towards variable boundary conditions such as co-flow temperature, Reynolds number and precursor doping of the jet is investigated. Agreement between simulation and experiments is very good for a reference case which is used to calibrate the signals. While keeping the model parameters constant, the sensitivity of the particulate size distribution on co-flow temperature is predicted satisfactorily upstream although quantitative differences with the data exist downstream for the lowest coflow temperature case that is considered. When the precursor concentration is varied, the model predicts the correct direction of the change in signal but notable qualitative and quantitative differences with the data are observed. In particular, the measured signals show a highly non-linear variation while the predictions exhibit a square dependence on precursor doping at best. So, while the results for the reference case appear to be very good, shortcomings in the standard submodels are revealed through variation of the boundary conditions. This demonstrates the importance of testing complex nanoparticle synthesis models on a flame series to ensure that the physical trends are correctly accounted for.

**Keywords** Multiple mapping conditioning · Nanoparticle flame synthesis · Elastic light scattering · LES

---

✉ Andreas Kronenburg  
kronenburg@itv.uni-stuttgart.de

Extended author information available on the last page of the article

## 1 Introduction

A large variety of nano-sized particulates are produced by combustion processes, some as unwanted by-products in the energy sector such as soot, others as commodities such as catalysts or stabilising agents (Iler 1979). In all cases, the final product characteristics are significantly influenced by precursor reactions, interparticulate interactions and the gas-phase conditions (composition, temperature, fluid dynamics) under which they are formed. The numerical simulation of all these processes and the accurate prediction of the particulate size distribution (PSD) are vital if we are to understand and control flame synthesis. The evolution of the PSD is usually described by the population balance equation (PBE) that can be solved by Direct Monte Carlo methods (Kruis et al. 2000), moment methods (Pratsinis 1988) or discretised sectional methods (Friedlander 2000; Marchisio and Fox 2013). When the PBE is coupled with the Navier-Stokes equation, modelling is required for the multiscale, non-linear interactions of the particulate dynamics and the turbulent flow. In the context of large eddy simulations (LES), Loeffler et al. (2011) and Wang and Garrick (2006) investigated the formation and growth of titanium dioxide nanoparticles, but neglected particulate-turbulence interactions. Neuber et al. (2017) used the sectional method and showed that the error associated with omission of sub-grid turbulence interactions can be large for the highly non-linear nucleation and surface growth processes. Similar conclusions were drawn by Pasmazoglou et al. (2017) and Sewerin and Rigopoulos (2018) who modelled particulate aggregation and soot formation and growth, respectively.

In Neuber et al. (2017, 2019a) we presented the implementation of a stochastic Monte-Carlo method for the spatial and temporal evolution of the joint filtered density function (FDF) of the gaseous composition and number density of the particulates. The number density is discretised into sections representing particulates of different sizes. To avoid ambiguities, we strictly distinguish in this paper between “stochastic particles”, which are computational elements for solving the FDF equation in the Lagrangian sense, and “particulates”, which are the physical nanoparticles produced during the flame synthesis process. Conventional stochastic FDF methods require stochastic particle numbers up to 20–50 per LES cell (You et al. 2017), and even though optimised methods—such as in-situ adaptive tabulation (Pope 1997)—exist for the calculation of reaction kinetics, the simulation of flame synthesis processes remains computationally expensive. When using a sectional method, the computing time for the particulate synthesis may even exceed the computing time for the chemical kinetics of the gas phase. For such problems it is therefore beneficial to use a so-called sparse-Lagrangian FDF approach, which requires far fewer stochastic particles than traditional intensive methods (Cleary and Klimenko 2011). The key enabler of the sparse FDF approach is the use of a novel mixing model called multiple mapping conditioning (MMC) (Klimenko and Pope 2003) which helps to correctly emulate molecular and turbulent diffusion despite the relatively large physical distances between the particles to be mixed. The MMC model has been validated widely for different turbulent flames, e.g. see (Cleary and Klimenko 2011; Vo et al. 2017a; Galindo-Lopez et al. 2018; Neuber et al. 2019b). Recent publications have shown that the method can also be applied to particulate nucleation and growth processes (Neuber et al. 2017; Vo et al. 2017a) where interactions with turbulence are important. We demonstrated the capability of the combined PBE-MMC-LES method to model particulate inception, surface growth and agglomeration of non-spherical agglomerates in a turbulent, reactive jet flow (Neuber et al.

2019a). That study included, however, only one specific setup. MMC could capture some features of the flame synthesis process but notable differences between computations and experiments were observed.

Complete model evaluation demands the computation of a series of cases with varying boundary conditions to establish the sensitivity of the model and its input parameters. The comparison with a series will also ensure the model's capacity to capture trends and thus to have incorporated all the important physics of the particulate synthesis process. Here, we apply the model to the flame synthesis of silica nanoparticles from a silane doped nitrogen jet issuing into a vitiated hot co-flow and investigate the sensitivity towards variations in precursor loading and gas phase temperatures and assess the model's performance against experimental OH-LIF, SiO-LIF and elastic light scattering (ELS) signals.

## 2 Methodology

PBE-MMC-LES is a hybrid Euler/Lagrange approach where the mass and momentum transport equations are solved by an Eulerian LES solver, here employing standard closures for the sub-grid terms. The gas-phase composition and particulate size distribution are solved using a Lagrangian Monte Carlo approach whose details are provided now. For the solution of the particulate size distribution we use the nodal form of the sectional approach (Prakash et al. 2003) which discretises the particulate volume space into a finite number of sections. If the particulate matter is transported by a fluid of gas-phase composition  $\mathbf{Y}$ , temperature  $T$  and velocity field  $u_j(x_i, t)$ , the nodal form of the population balance equation takes the form

$$\frac{\partial n_k}{\partial t} + \frac{\partial}{\partial x_j} \left( u_j n_k - D_k \frac{\partial n_k}{\partial x_j} \right) = - \frac{\partial(G(v, \mathbf{Y}, T)n_k)}{\partial v} + \dot{s}_k(\mathbf{Y}, T), \quad (1)$$

where  $n_k$  is the number density of particulates in section  $k$ ,  $D_k$  is the diffusion coefficient of section  $k$ , and  $G(v, \mathbf{Y}, T)$  is the volumetric growth term that can be modelled as a function of particulate volume,  $v$ , and  $\mathbf{Y}$ . Changes of the PSD due to inception and agglomeration are included via the source term  $\dot{s}_k$ . The rate at which primary particulates are formed is determined by the production rate of the precursor species, which in turn is given by the gas phase chemistry described by the underlying reaction mechanism. Incipient particulates that are newly formed by chemical reaction are added to the first section of the discretised particulate size distribution.

The volumetric surface growth is determined by two processes, each dominating in different size ranges. For small particulates the surface growth is determined by a collision process whereas for large agglomerates the surface growth is driven by diffusion processes. For the former, the growth rate is based on the free-molecular collision kernel. The collision diameter of the species which is depositing on the agglomerates surface is assumed to be the diameter of the molecule (Shekar et al. 2012). In our sectional approach we consider fractal-like structures with their morphology given by a power law (Friedlander 2000). The collision diameter of the agglomerate is given by  $d_{c,k} = d_{p,0} N_k^{1/D_f}$ , with  $N_k$  being the number of primary particulates in the agglomerate,  $d_{p,0}$  being the diameter of the primary particulate and  $D_f$  being the fractal dimension which is set to  $D_f = 1.8$  as suggested in Refs. Shekar et al. (2012); Schaefer and Hurd (1990). Hence, the volumetric growth rate is given by the collision rate of the depositing species with the agglomerate. For the larger particulates we apply a diffusion-limited growth method (Witten and Sander 1981)

because there the volumetric surface growth is mainly determined by the diffusion rate of the depositing species towards the agglomerates' surface. We use the harmonic mean of the two formulations which serves as a blending function between the two regimes.

For agglomeration the Fuchs interpolation expression between the free molecular and continuum regimes was proposed by Seinfeld (1986). For arbitrarily shaped agglomerates (Kruis et al. 1993) proposed to replace the spherical particulate diameter in the Fuchs interpolation expression by the collision diameter of the agglomerate and this was also done here. The implemented discretised representation of the PSD requires a size-splitting operator for the agglomeration term which ensures particulate number and mass conservation by distributing the formed particulates into two adjacent sections (Loeffler et al. 2011). This procedure introduces a slight broadening of the PSD but this effect is small compared to the broadening due to growth and agglomeration. Due to the relatively low temperatures in regions where particulates are formed we assume that the agglomerates are not subject to any sintering processes. This assumption is justified as agglomerate samples in the exhaust do not show significant signs of neck formation between the primary particulates (see also Fig. 2 and discussion in Sect. 3).

We apply a Lagrangian scheme to approximate the evolution of Eq. (1) as part of the joint FDF,  $F_\phi$ , of the composition field  $\phi = (Y_1, \dots, Y_s, h, Z, n_1, \dots, n_e)$  which includes the gas phase composition vector  $\mathbf{Y}$ , the total enthalpy,  $h$ , the mixture fraction,  $Z$ , and the discretised particulate number density field  $\mathbf{n}$ . The FDF method has the major advantage that the chemical source terms as well as the rates for nucleation, volumetric surface growth and agglomeration appear in closed form in its governing equations. Thus, no closures are required for these terms to incorporate unknown sub-grid effects due to turbulence. As we use a Monte-Carlo technique a fractional step approach is applied to describe the spatial dispersion, gas phase reaction, mixing and aerosol dynamics (Pope 1985). The time evolution is then given by the equivalent stochastic differential equations (Cleary and Klimenko 2011) for particle transport

$$dx_j^p = \left[ \tilde{u}_j + \frac{1}{\bar{\rho}} \frac{\partial}{\partial x_j} (\bar{\rho}(D + D_t)) \right]^p dt + \sqrt{2(D + D_t)^p} d\omega, \quad (2)$$

and the change of the composition field in time is governed by Cleary and Klimenko (2011)

$$d\phi_\alpha^p = (S_\alpha^p + M_\alpha^p) dt, \quad (3)$$

where  $\omega$  is a Wiener process and standard notation is used for diffusion, density, velocity, space and time. The molecular diffusion coefficient,  $D$ , is set equal for all species and particulate sizes except in our discussion conducted in Appendix 3 and  $D_t$  denotes the turbulent diffusivity.  $S_\alpha$  accounts for source terms including chemical reactions, particulate inception, surface growth and agglomeration and  $M_\alpha$  is a mixing operator which emulates the sub-filter scalar dissipation. A suitable reaction mechanism provides chemical reaction rates and thus determines the particulate inception (cf. Sect. 4). Models for volumetric surface growth and agglomeration have been discussed above.

The mixing operator appears in unclosed form and requires modelling. A mixing model like the interaction by exchange with the mean (IEM) (Villermaux and Devillion 1972), Curl's mixing model (Curl 1963), the modified Curl mixing model (Janicka et al. 1979) or the Euclidean minimum spanning tree (EMST) model (Subramaniam and Pope 1998) can be used to close the equation on mixing operator level. Subramaniam and Pope (1998) specified requirements for mixing models, such as linearity, independence and localness

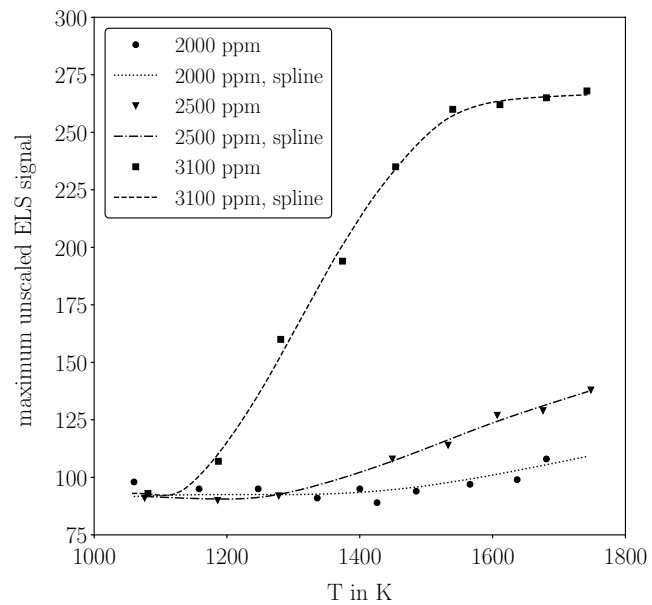
in composition space. A mixing model which provides such requirements is the multiple mapping conditioning (MMC) model (Klimenko and Pope 2003) as it enforces localisation in composition space indirectly by localisation in an independent reference space. MMC requires the additional solution of such a reference field. This reference field is the (Eulerian) LES solution of mixture fraction,  $\tilde{f}$ , and the mixing of the stochastic particles is then conditioned on  $\tilde{f}$ . The localisation in reference space allows to increase the spatial distance of the stochastic particles as long as localness in composition space is maintained. This has led to the development of the so-called sparse-Lagrangian MMC method, where there are fewer stochastic particles than LES grid cells. In contrast to conventional mixing models sparse particle methods use up to three orders of magnitude fewer particles resulting in significant computational savings. Here, we use Curl's mixing model where particles are pairwise mixed in combination with the MMC conditioning. The particle pairs are selected such that they are local in reference mixture fraction space and the mixing extent is controlled by a mixing time scale,  $\tau_L$ . For a detailed discussion on the modelling of the mixing time scale the reader is referred to Vo et al. (2017a, b) and Neuber et al. (2019b).

### 3 Experimental Configuration

The general experimental configuration is based on the Cabra burner (Cabra et al. (2002)) where a central turbulent jet (here nitrogen) issues into a hot vitiated co-flow of premixed hydrogen-air combustion products. The central jet has a diameter of  $D = 4.57$  mm and the outer diameter of the vitiated co-flow is 210 mm. The cold jet bulk velocity is  $U_j = 33.2$  m/s resulting in a jet Reynolds number of  $Re_D = 10,000$ . The co-flow velocity is  $U_c = 1$  m/s based on cold conditions (i.e. no combustion of co-flow mixture). The nozzle exit plane extends 70 mm above the perforated plate of the co-flow. The experimental campaign consists of measured signals from parameter variations where the central jet is doped with different concentrations of silane (0, 300, 1000, 2500, 2700, 2900 and 3100 ppm). Also, the co-flow temperatures (1300, 1500 and 1800K) and the jet Reynolds numbers (5000, 10,000 and 15,000) were varied. The case with no silane doping (0 ppm) is used as baseline for the OH-LIF signal and served for the validation of the flow and mixing field predictions (Neuber et al. 2019a). Preliminary measurements demonstrated that dopings below 2000 ppm do not lead to any detectable light scattering signal from the particulate matter while for a range between 2500 and 3100 ppm a large variation of the signal is observed (cf. Fig. 1). There is a clear temperature dependence of the signal over the temperature range between 1300 to 1800 K and the dependence is less pronounced for lower loadings such that here, the analysis with respect to silane loading considers cases with silane doping larger or equal 2500 ppm only. The temperature sensitivity studies focus on the case with 3100 ppm and the Reynolds number dependence is based on 2500 ppm doping due to restrictions of the mass flow rate controller in the high Reynolds number case.

Silica particulate synthesis is investigated experimentally by two laser diagnostic techniques, planar laser-induced fluorescence (PLIF) and elastic light scattering (ELS). The investigation is supplemented with extractive particulate sampling. OH-PLIF and SiO-LIF are used to validate the chemical kinetic model whereas ELS is used to validate both the particulate formation model and the temperature field. Model validation follows the "paradigm shift" approach described by Connelly et al. (2009), which involves computing 'synthetic signals' that are compared with experimentally-acquired signals as a strategy to

**Fig. 1** Influence of co-flow temperature on the ELS signal in the  $Re = 10,000$  case



avoid incurring assumptions needed by the experimentalist for conversion of the signal to physically meaningful quantities.

For ELS, a four-head Q-switched frequency-doubled Nd:YAG laser is used in conjunction with sheet-forming optics to illuminate a  $23 \text{ mm} \times 400 \mu\text{m}$  region across the burner centerline. The ELS signal is collected using a CCD camera with a  $105 \text{ mm f}/16$  lens perpendicular to the laser beam. Using three of the four available heads, the shot energy is approximately  $3 \times 450 \text{ mJ}$ . Measurements of different regions of the jet are performed by vertical translation of the burner. Data post-processing includes background subtraction, shot energy correction, beam profile correction, spatial calibration and image de-warping. Besides corrections that stem from the particulars of the experimental setup such as background subtraction and laser profile and energy corrections, no physical interpretation of the signal is attempted, as the measurement process is already simulated within the numerical model.

The fourth head of the Nd:YAG laser is used to pump a frequency-doubled Rhodamine 6G dye laser, tuned to a wavelength of  $283.6 \text{ nm}$  to excite the  $Q_1(8)$  transition ( $v = 1 \leftarrow 0$ ) of the  $A^2\Sigma \leftarrow X^2\Pi$  electronic system of the OH radical. This transition has been chosen so that the LIF signal is only weakly sensitive to temperature. A CCD camera with intensifier (multi-alkali, P43) and  $f/2.8$  UV lens is placed at  $90^\circ$  to collect the fluorescence signals from the ( $v = 0 \leftarrow 0$ ) and ( $v = 1 \leftarrow 1$ ) branches of OH around  $309\text{--}315 \text{ nm}$ . Laser energy and sheet thickness have been adjusted to ensure operation within the linear LIF regime (Seitzman and Hanson 1993). The area probed is  $23 \text{ mm} \times 700 \mu\text{m}$  and the shot energy  $1.15 \text{ mJ}$ . Again, background subtraction, shot energy correction, beam profile correction and beam extinction along the direction of travel of the beam are applied to the experimental signal.

For the SiO-LIF experiments, the fourth head from the Nd:YAG laser was converted to third harmonic emission ( $355 \text{ nm}$ ) and the dye laser converted to run on a Coumarin dye mixture.  $100 \text{ mJ}$  of  $355 \text{ nm}$  radiation was used to pump the dye laser, generating around  $15 \text{ mJ}$  pulse energy, tuneable around  $460\text{--}470 \text{ nm}$ . The beam was then frequency doubled in a BBO crystal, producing up to  $1.5 \text{ mJ}$  of narrowband radiation which could be varied in the range  $230\text{--}235 \text{ nm}$ . The laser was tuned to the  $Q_{11}$  ( $J = 32$ )  $A^1\Pi \leftarrow X^1\Sigma^+(0, 0)$

absorption line in SiO (235.087 nm) and the fluorescence signal was detected and corrected in the same way as the OH experiments (extinction corrections were not made, since SiO was not found in the co-flow).

Additionally, particulate samples were obtained in two ways, using a thermophoretic sampling device (TPS) similar to that described in Dobbins and Megaridis (1987) and using a Dekati PM10 impactor. The TPS samples were collected at specific locations in the jet, whilst the impactor samples were collected far downstream ( $\sim 2$  m), in the extraction hood positioned over the burner. The TPS device uses a double-action pneumatic cylinder to rapidly push a 3 mm perforated carbon TEM grid into the jet and remove it after a pre-set residence time of 50 ms. The grid is held vertically during sampling in order to minimize disruption to the flow. Both types of samples are analysed using a Jeol 2100+ transmission electron microscope (TEM) at an acceleration potential of 200 kV without additional preparation and images are exported to *Image-J* for analysis.

Figure 2 shows typical TEM images of particulates extracted from within the flame and from the exhaust. TPS samples at  $z = 70$  mm had a dwell time in the jet of 250 and 50 ms in the 1000 ppm and 3100 ppm cases, respectively. The downstream samples, collected at  $z = 2$  m, resulted from drawing the sampled gas through the finest impactor filter for 5 min at 3100 ppm and 20 min at 1000 ppm. Only few and small particulates can be seen on the samples for a silane loading of 1000 ppm indicating the presence of nucleation and surface growth but only moderate rates of agglomeration at this silane doping concentration. The

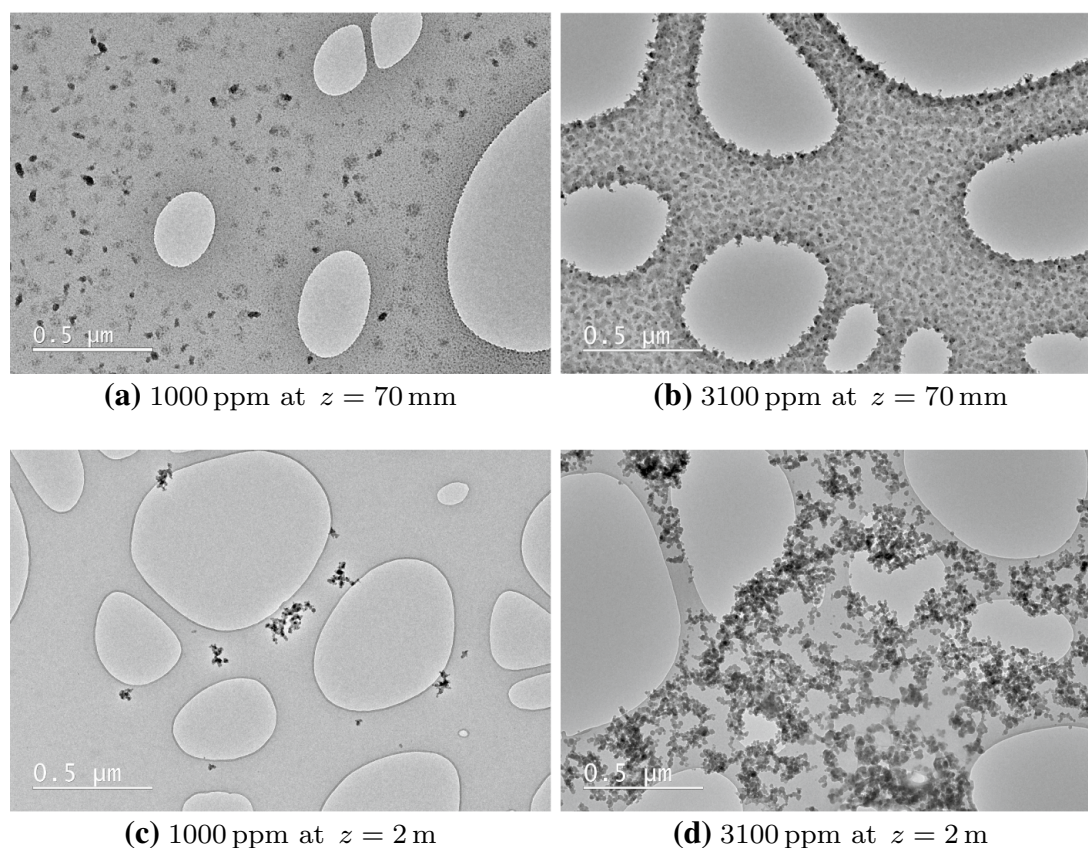


**Fig. 2** Transmission electron microscope (TEM) image of silica particulates: **a, b** extracted from within the flame by thermophoretic sampling; **c, d** captured by suction two metres above the burner using a filter. The large empty areas correspond to holes in the carbon film of the TEM grid, used for mechanical support during imaging

picture for the case with 3100 ppm is not that clear. Much larger silica structures can be observed for samples taken within the flame, but clear agglomerate structures are absent. This “coating” of the sample probe may be due to condensation of the silica on the surface of the sample probe forming a surface film. When sampling within the exhaust two meters above the burner, large particulates of fractal shape have deposited on the sample probe indicating that the agglomeration process is the predominant growth mechanism and that sintering effects are irrelevant at conditions investigated here, see Fig. 2d. These images do certainly not represent the agglomerates’ PSD, however, they clearly demonstrate the moderate particulate nucleation in the case with 1000 ppm and significant agglomeration yielding very large cluster for loadings with 3100 ppm.

## 4 Numerical Configuration

The hybrid Euler/Lagrange approach has been implemented into a code package called *mmcFoam* (Galindo-Lopez et al. 2018) which is based on OpenFOAM-5.0. The computational domain extends  $25D$  in the axial direction and  $11D$  in the radial direction. A priori investigations of three different grids with 0.5, 1.5 and 4 million cells revealed that results for the latter two cases are similar. The 1.5 million cell grid is used for all results presented in this paper. The mesh is refined near the nozzle, which is resolved by 45 cells along the jet diameter giving smallest cell sizes of  $50\ \mu\text{m}$  in the center and the shear layer of the jet. The turbulent sub-grid viscosity is modelled by the  $\sigma$ -model (Nicoud et al. 2011) and a model constant of  $C_\sigma = 1.5$  is applied. Pipe flow simulations were conducted inside the nozzle to provide realistic turbulent inflow velocity boundary conditions and zero-gradient outflow conditions are used at all other boundaries. Second-order central difference and TVD schemes are used for discretization of momentum and species transport, respectively. For the Lagrangian scheme, 230 000 stochastic particles have been used to compute the subgrid distribution of composition and particulate number density, which corresponds to one particle for every 6.5 LES cells. All MMC modelling parameters are standard as defined in earlier publications (Neuber et al. 2017; Cleary and Klimenko 2011; Vo et al. 2017b; Neuber et al. 2019b).

A finite rate chemistry model for the precursor chemistry is applied to model silane combustion (Suh et al. 2001; Suh et al. 2002). We use the mechanism provided by Suh et al. (2001) including 63 species and 264 reactions at their reported rates for atmospheric pressure. The mechanism includes clustering of silicon oxides in the gas phase that leads to nucleation of the first incipient particulates once the molecules are large enough. Suh et al. (2001) selected  $(\text{SiO}_n)_{11}$  to represent the first solid particulate but acknowledged this choice to be arbitrary as it depended on a trade-off between increased detail for gas-phase precursors and increasing uncertainties in the reaction kinetics for larger gas-phase molecules. Assuming spherical symmetry of incipient particulates with a solid matter density of  $\rho_p = 2196\ \text{kg/m}^3$  gives a diameter of  $d_{p,0} = 0.98\ \text{nm}$  for all primary particulates. A constant primary particulate size appears restrictive and Fig. 2d indeed demonstrates that particulates of various sizes are present. However, a sectional method including a primary particulate size distribution (i.e. an effectively two-dimensional representation of the particulate characteristics parameterized by the radius of gyration,  $R_g$ , and  $d_{p,0}$ ) is not yet feasible within a PBE-MMC-LES approach and is not attempted here. Therefore, the stochastic particles carry the information of 63 species, enthalpy, mixture fraction and a suitable number of sections of the PSD. This “suitable” number warrants some more

discussion: The number should be as small as possible to avoid unnecessary computational overhead but Neuber et al. (2017) showed that an unsuitably coarse discretisation can lead to excessive numerical diffusion and to an overprediction of the number of larger particulates. Since only nucleation and condensation were considered therein, the sensitivity study should be repeated here to ensure independence of results in the presence of agglomeration. Figure 3 shows the time-averaged PSD on the centerline of the jet with a 3100 ppm silane loading and a co-flow temperature of 1500 K at two different downstream positions. The number of sections has been varied from 30 to 120. It can be seen that all PSDs look similar and have a bimodal character, which indicates that numerical diffusion is small and that agglomeration effects are already dominating the distribution's spread across particulate size space at  $z/D = 10$ . For a higher number of sections the solutions converge. We can clearly observe that for 30 and 60 sections numerical diffusion leads to deviations from the converged solution for the PSD. The results for 90 and 120 sections are very similar. Since calculations with 120 sections increase computational requirements by 25% but differences in predictions are small, we use 90 sections for the approximation of the PSD for all further results presented in this study.

In the next section, we compare measured with computed signals following the “paradigm shift” approach which was used for a variety of analyses in turbulent combustion (Torniainen et al. 1998; Floyd and Kempf 2011) including particulate nucleation and growth (Connelly et al. 2009). This strategy avoids incurring assumptions needed to convert experimental signals to physical meaningful quantities such as particulate number density. The procedures to calculate the ELS and LIF signals are described in Appendices 1 and 2, respectively.

## 5 Results

The PBE-MMC-LES calculations are performed for different silane loadings of the jet stream, different jet Reynolds numbers and different co-flow temperatures. Statistics have been collected for a minimum of 15 flow through times after a statistically

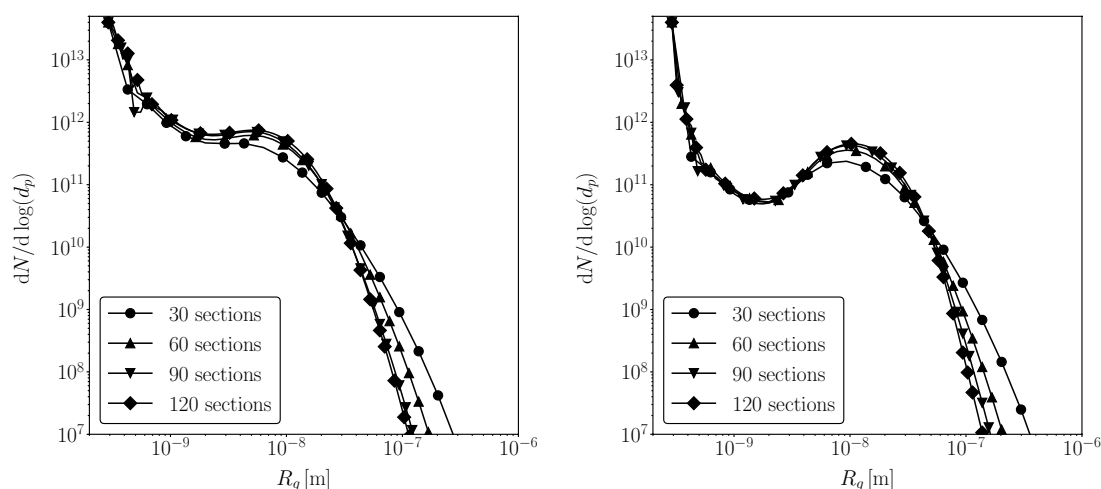


**Fig. 3** Mean particulate size distribution on the centerline at different downstream positions for the case with 3100 ppm:  $z/D = 10$  (left)  $z/D = 20$  (right)

stationary state had been reached. The simulations have been run for 4500 CPUh, where the stochastic particle costs are about 16 times the costs of the LES.

The general numerical setup of this configuration including the predicted flow and mixing fields were validated in Neuber et al. (2019a). There it was shown that good agreement of measured and computed mean and standard deviation of the elastic light scattering (ELS) signal can be achieved. For the case with no silane doping, this indicated good predictions of the temperature (and therefore the mixing) field and that the most important flow phenomena can accurately be reproduced. The agreement for the ELS signal also indicated good predictions for silica nucleation and growth in the case with 3100 ppm silane doping of the jet. However, as measured signals require calibration and calibration has been realized by matching the peak centerline values, a certain degree of agreement is expected to be observed. For a more critical analysis, a series of test cases needs to be assessed and the model's capability to predict trends and to capture the underlying physics needs to be investigated. We now show further validation for the case with the highest silane loading of 3100 ppm (Sect. 5.1) and take this case as reference. Sections 5.2 (variation of silane loading) and 5.3 (variation of co-flow temperature and jet Reynolds number) then provide a critical assessment of the model's capability to predict changes in process and boundary conditions. The variation of model parameters allows the identification of reasons for remaining discrepancies between measurements and computations. We complement our analysis by sensitivity studies towards variation of model parameters. However, these variations are *ad hoc*, they shall serve as indication of sensitivities and identify needs for further model improvements, but do not necessarily provide new suitable modelling constants. Results are therefore deferred to Appendices 3 and 4.

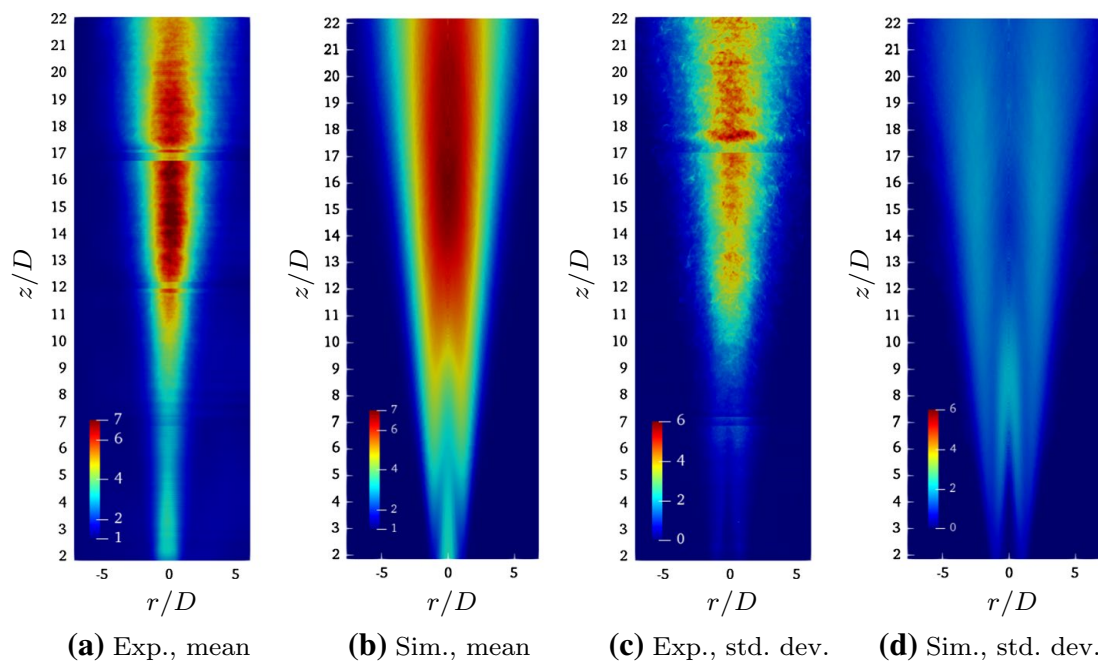


**Fig. 4** Contour plots of the normalised elastic light scattering signal for the reference case with a silane loading of 3100 ppm and a co-flow temperature of 1500 K

## 5.1 Evaluation of the Reference Case

In this section we present results of our reference case with a silane doping of 3100 ppm and a co-flow temperature of 1500 K at a Reynolds number of  $Re_D = 10,000$ . Figure 4 compares the ELS signals from the experiments with those from the simulations. The signals from the LES are calculated as described in Appendix 1. We have calibrated the experimental signal such that it is unity in the co-flow. The predicted signal has two contributions. The signal originating from the gas phase is normalised to match the mean co-flow values, and the signal associated with the particulate matter is normalised such that the peak values of experiment and simulation agree. Note that this procedure is followed for the reference case only. For all other cases reported below the ELS signals are normalised by the same constants and no further adjustments have been applied. Overall, the simulations agree well with the measurements when assessing the mean of the ELS signal. Most notably the positions of the signals' peaks are very similar.

There are, however, a few pronounced differences that warrant some discussion:

1. The spatial extent of high particulate matter concentrations is somewhat too wide. This might be caused by the unity Lewis number assumption used here for the particle composition space including the size sections. The particulates can have very large Schmidt-numbers that are up to several orders of magnitude larger than the gaseous species' Schmidt numbers, and their molecular diffusion will tend to zero. Larger particulates emitting a higher signal tend to follow the streamlines while equal diffusivity assumptions enhance lateral diffusion. Vo et al. (2017a) suggested a modification of the Lagrangian mixing time scale for the particulate matter and this effect is discussed in Appendix 3. In addition, the random walk model (represented by the last RHS term in Eq. 2) induces particle dispersion and thus diffusion independent of the species specific molecular diffusion coefficient. This "enhanced" diffusion of heavy particles is more pronounced in hot regions where molecular diffusion coefficients are large and of the same order of magnitude as the turbulent contribution. In the present setup, the co-flow is hot which contributes to the over-prediction of particulate dispersion. The *mean drift model* developed by McDermott and Pope (2007) may extenuate this artificial diffusion but its implementation in the context of a sparse particle method is unclear to date and beyond the focus of this paper.
2. A comparison of Fig. 4c, d reveals qualitative differences between experiments and computations. The experiments show a clear maximum along the centerline while simulations place the highest fluctuations at the edges of the jet right into the shear layers. Again, neglecting differential diffusion in the model may be the cause of these differences. The heavy particulates would cluster in the inner jet and the larger concentrations there would also lead to larger gradients and thus variances within the jet's center. Indeed, modification of the mixing time scale such that there is differential dissipation of variances of the number densities of small and large particulates enhances variances along the centreline as shown in Appendix 3.
3. The computations predict an early onset of the mean ELS signal and corresponding fluctuations in the shear layers between jet and co-flow (cf. Fig. 4b, d). This is not observed in the experiments. The appearance of the simulated ELS signal within the upstream shear layer can be explained by the (modelled) dynamics within this jet that dominate silica particulate formation and growth. Figure 5 shows the inception rate, volumetric surface growth, primary particulate number density and agglomerate number density

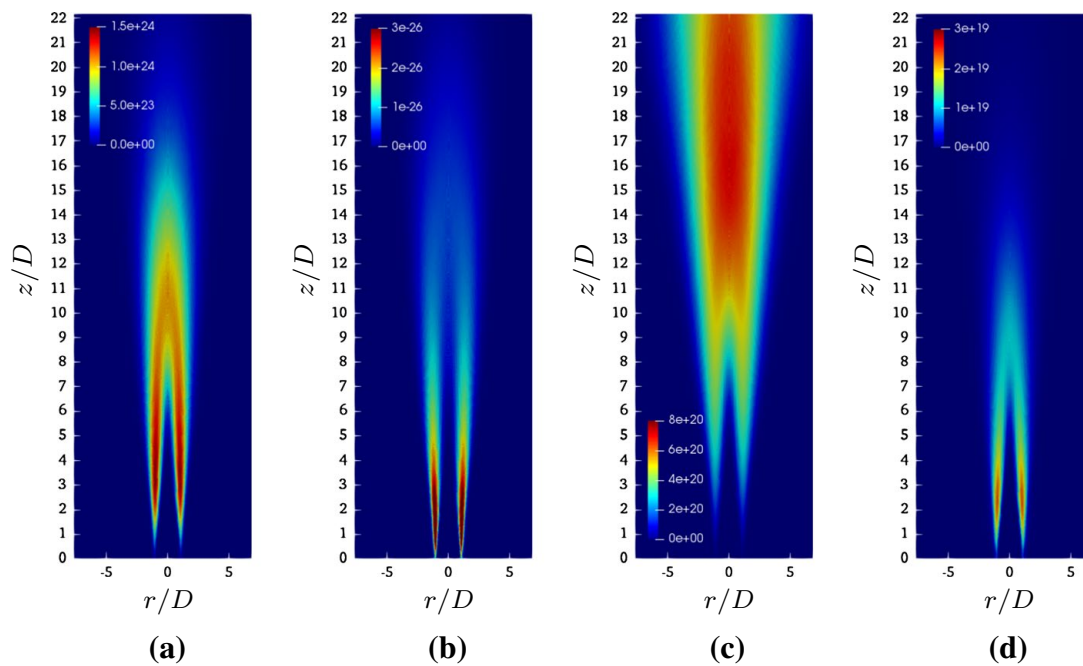


**Fig. 5** Selected aerosol properties of the reference case given by a co-flow temperature of  $T = 1500$  K and a silane loading of 3100 ppm. **a** Inception rate in  $\#/m^3s$ , **b** surface growth rate in  $m^3/s$ , **c** primary particulate number density in  $\#/m^3$  and **d** particulate number density in  $\#/m^3$

on a plane at centerline position. The inception rate is very high in the shear layer close to the jet exit, where the hot surrounding co-flow mixes with the jet and mixing leads to oxidation of silane and particulate inception. Along the centerline the inception rate peaks at  $z/D = 10$  and decreases significantly further downstream, which is in line with the observation that the precursor species is completely consumed at  $z/D = 20$  (not shown). The volumetric surface growth differs qualitatively from the inception rate. It is very large in the shear layer close to the jet exit but rapidly decreases further downstream. This is consistent with the observation that strong surface growth occur in regions where many intermediates are present which then deposit on the particulates' surfaces. Consistent with the inception rate, the number of primary particulates increases first in the turbulent shear layer and reaches its highest value at about  $z/D = 15$  (cf. Fig. 5c). Further downstream, the primary particulate number density decreases again due to ceasing primary particulate inception and due to particulate dispersion. Comparison of agglomerate number density with the number density of primary particulates highlights the influence of agglomeration which is in line with the analysis of the TEM pictures in Sect. 3. In regions where the primary particulate number density is highest, the number density of the agglomerates decreases very quickly due to particulate collision events.

The early inception of particulates in the shear layer is likely to be related to the gas phase chemistry including silane oxidation and formation of gas phase precursors. The validation of the gas phase kinetics includes a comparison of OH and SiO signals. OH can be understood as an indication of the position of the shear layer and it is linked to the kinetics of the silane oxidation process that is typically relatively fast and intimately coupled with the underlying hydrogen-oxygen kinetics. Radial profiles of OH mean values and standard deviation are shown in Fig. 6a, where experimental and predicted signals are normalised

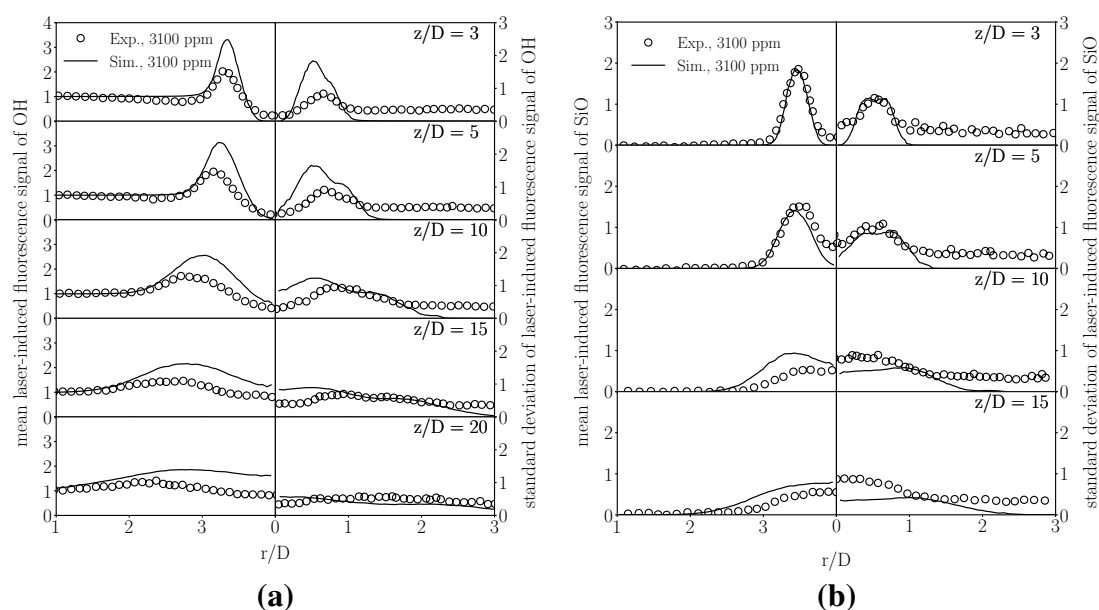


**Fig. 6** Mean and standard deviation of **a** the OH-LIF signal and **b** the SiO-LIF signal at different downstream positions for the reference case with a silane doping of 3100 ppm

with their respective co-flow values at  $z/D = 3$ . It is seen that the positions of silane decomposition and OH production are well detected but peak values of the mean OH-LIF signal is over-predicted by 27%. This is a good agreement given the uncertainties that can be associated with the kinetics of silane oxidation. In line with the trends observed for the mean values the standard deviations are also overestimated. Note that the experimental standard deviations in the co-flow do not tend to zero. This is mainly due to shot noise and to a lesser extent to readout noise and temperature fluctuations in the hot co-flow. Overall, we achieve a satisfactory agreement between the measured and predicted position of the reaction zone and between actual and predicted silane decomposition representing the fast reactions within this process. OH is not, however, a good indicator for the silica formation process. Instead, SiO may serve as a representative species as it is the key intermediate for the formation of gaseous  $\text{SiO}_2$  and one key species for (i) surface growth and (ii) growth of the gas phase precursors leading to the first particulates. Figure 6b shows excellent agreement between measured and predicted SiO-LIF signals. The location of the peak values and the variation with downstream distance for mean and standard deviations agree very well. Deviations at larger radii can be associated with the experimental read noise and shot noise that have a more substantial impact for SiO than for OH due to the relatively small SiO signal intensity.

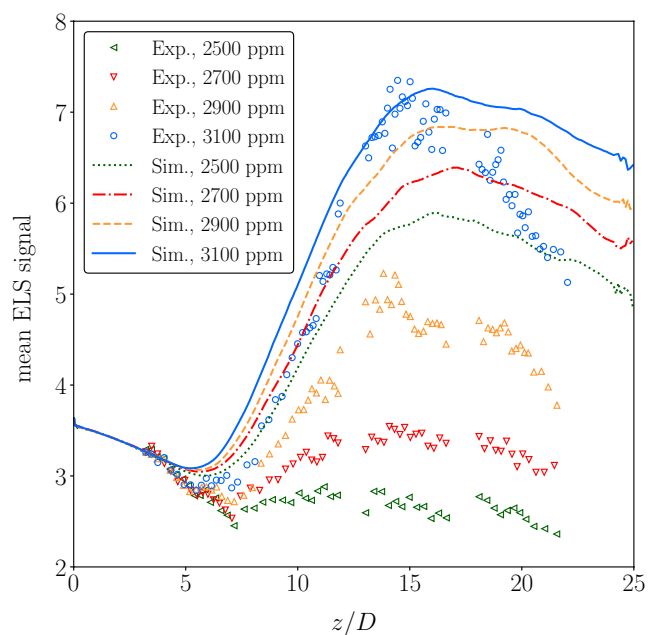
With respect to the chemical kinetics and possible turbulence-chemistry interactions we may conclude that MMC-LES captures silane oxidation and formation of SiO (and possibly of the first silicon dioxide molecules) in the gas phase accurately. High SiO concentrations are correctly predicted in the shear layer close to the jet exit. The apparent agreement of key species in the gas phase and our prediction of the early onset of particulate nucleation (with the latter not being observed in the experiments) suggests some inaccuracies related to the modelling of cluster growth (the formation of  $(\text{SiO}_2)_m$  and  $(\text{SiO})_m$  with  $m \in [2, 10]$ ) in the gas-phase leading to particulate inception. The relevant kinetics were developed for standard pressures at  $T = 773 \text{ K}$  (Suh et al. 2002) and extrapolation of the respective rate constants to the range of temperatures relevant in the present configuration may introduce

some unavoidable inaccuracy. Direct validation of the cluster growth process is difficult as direct measurements of SiO and SiO<sub>2</sub> clusters do not exist and are not easy to perform—in particular for SiO<sub>2</sub> due to its photophysical properties. We can, however, assess the sensitivity of predictions on precursor kinetics and this is discussed in more detail at the end of Sect. 5.2.

## 5.2 Sensitivity Study for Varying Silane Loadings

Figure 7 depicts the means of the ELS signals along the centerline for cases with 2500, 2700, 2900 and 3100 ppm silane loading. For the reference case with 3100 ppm the predicted ELS signal increases with the same rate as the signal from the measurements, indicating that particulate number and size are well predicted. Also growth and agglomeration are likely to be suitably modelled. The measured signal reaches its maximum value at  $z/D = 14$ , while the predicted peak value is very close at  $z/D = 15$ . The simulations predict the correct trends, i.e. lower silane doping leads to lower agglomerate numbers and therefore lower ELS signals. However, the sensitivities towards changes in silane doping are moderate while experiments feature much larger differences in signal strength. Only a small signal is detected for 2500 ppm and the increase in signal strength is strongly non-linear with increasing silane concentrations. The strong dependence is unexpected but consistent with the TEM images shown in Sect. 3: for the low silane loadings only few small agglomerates were captured while higher loadings led to significant increases in particulate production and agglomeration. In contrast, the relatively low sensitivity observed in the simulations is not unexpected and can be explained by the models used for nucleation, growth and agglomeration. Nucleation and growth are linearly dependent on silane loading, and this linear trend is observed in the predictions where the predicted peak ELS signal is (to a good approximation) proportional to the silane loading. Non-linearities that may explain the experimental trends appear in the current models in three expressions only: (1) the agglomeration reveals a square dependence on particulate number, (2) the computed ELS signal increases non-linearly with primary particulate size, agglomerate size and fractal dimension, and (3) chemical kinetics are non-linear. Appendices 1 and 5 give

**Fig. 7** Mean elastic light scattering signal along the centerline for cases with a co-flow temperature of  $T = 1500$  K and with different silane loadings in the central jet stream. Experiment (symbols) and PBE-MMC-LES (lines)



details on the computation of the ELS signal, highlight the signals sensitivity to parameters and demonstrate that neither agglomeration nor ELS signal computation can reasonably explain the large discrepancies. The analysis in App. 5 hints at possible changes in  $D_f$  that might be caused by the different seedings and lead to the different signal strengths. These changes are, however, not clearly identifiable nor quantifiable for seedings between 2500 and 3100 ppm as the TEM images are snapshots and do not provide adequate statistics of the agglomerates' morphologies.

This leaves—next to differential diffusion effects (cf. Sect. 5.1)—chemical kinetics as the primary suspect. Precursor growth in the gas-phase follows the sequence



for  $m \in [1, 9]$  and  $n \in [1, 2]$ . The cluster  $(\text{SiO}_n)_{11}$  represents the first incipient particulates (Suh et al. 2001). An adjustment of the rate constants of these cluster growth mechanisms will lead to non-linear changes in particulate properties. In addition, Fig. 4 indicates particulate nucleation to be predicted too early and a reduction in rate constants seems justifiable. Appendix 4 demonstrates that adjusted rate constants could yield a behaviour similar to the experimental trends observed in Fig. 7. Simple perfectly stirred reactor computations show that the ELS signal depends strongly non-linearly on silane doping at early times. A sufficient delay in particulate nucleation would then yield similar non-linearities at  $z/D = 15$  where the maxima of the measured ELS signals are observed. Appendix 4 also shows additional MMC-LES computations of the Cabra burner with reduced rate parameters. The results demonstrate that (i) nucleation and growth is shifted downstream leading to absence of a particulate signal in the shear layer and continuous growth along the centerline, but (ii) shifts the peak ELS signal significantly further downstream and overall agreement does not improve. It seems that particulate dispersion and lateral species diffusion is not strong enough to suppress a further increase of the ELS signal on the centerline beyond  $z/D = 15$ . We may conclude that this sensitivity study corroborates a strong influence of the kinetics on the predictions but simple scaling will not suffice and key to success will be detailed and validated chemical schemes that ensure the correct growth of precursor species in the gas-phase.

### 5.3 Sensitivity Study for Varying Co-flow Temperature and Reynolds Number

Figure 8a shows the ELS signal's sensitivity towards co-flow temperature. The ELS signals for the upstream positions are in excellent agreement with experiments indicating an accurate numerical treatment of the varying boundary conditions. The ELS signal further downstream is correlated to nucleation and growth of the particulates indicating that the silane conversion is slower for the lowest co-flow temperature leading to lower particulate number densities. Measured and predicted ELS signals have a similar peak value for the two higher co-flow temperature cases and we may conclude that temperatures above 1500 K are high enough for a fast and complete conversion of the precursor. Again, the larger changes observed in the experiments cannot be fully reproduced by the simulations when decreasing the co-flow temperature from 1500 to 1300 K, but we note that the model correctly captures the highest ELS signal for the middle temperature of 1500 K.

In Fig. 8b the sensitivity of the ELS signal towards the jet Reynolds number is shown. Due to restrictions of the mass flow rate controller for the high Reynolds number case, the silane doping of the central jet is set to 2500 ppm for all three cases. Results for the high and medium Reynolds number cases are consistent with the observations made above: no

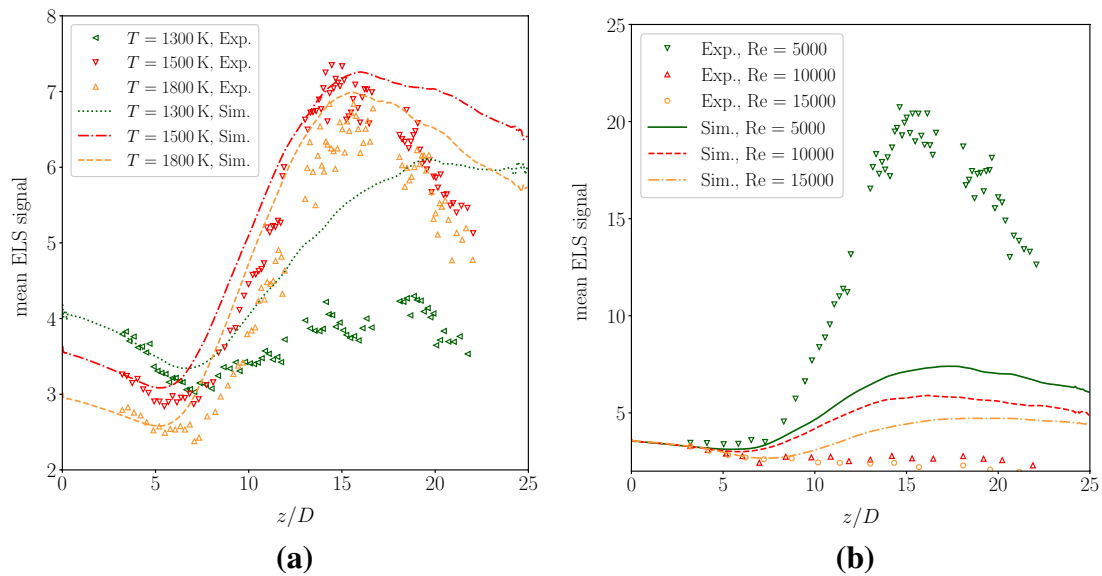


**Fig. 8** Mean elastic light scattering signal along the centerline for cases **a** with a silane loading of 3100 ppm and different co-flow temperatures and **b** with a silane loading of 2500 ppm and different jet Reynolds numbers. Experiment are denoted by symbols and PBE-MMC-LES by lines

significant signal could be measured, but MMC-LES predicts presence of some particulate matter. Notably different is the low Reynolds number case. The much slower convective velocity provides sufficient time for particulate nucleation to set-in. At the same time, (turbulent) dispersion is very low as the flow is quasi-laminar. The reduced dispersion leads to rather high particulate concentrations, fast agglomeration and a strongly non-linear dependence of the ELS signal on Reynolds number variations. MMC-LES cannot capture this re-laminarization of the flow and—similar to above—unity Lewis number assumptions lead to enhanced dispersion and an almost linear dependence of the peak ELS signal is predicted.

## 6 Conclusions

Sparse-Lagrangian PBE-MMC-LES calculations including detailed precursor chemistry, particulate inception, volumetric surface growth and agglomeration have been conducted for a series of silane doped nitrogen jets in a hot co-flow. The reference case with high silane loading is very well predicted and trends for variations in silane loading, jet Reynolds number and co-flow temperature can be captured. However, the measured sensitivities are rather strong and non-linear while the model (based on the assumptions inherent in the submodels) gives an almost linear or at most quadratic dependence on silane concentration. Further comparison with LIF measurements of key gas-phase species representing the fuel conversion process and intermediates for silica formation demonstrates the method's capability to represent gas-phase conversion and its interactions with turbulence. However, sensitivity studies indicate that the gas-phase precursor (cluster formation) chemistry can cause these strong non-linearities, but simple scaling of precursor (cluster) growth does not lead to success. Also, differential diffusion effects are likely to have significant effect on the specific locations in the flame where particulates nucleate and grow. The current work shall be understood as an attempt to identify the specific submodels' sensitivities, to

provide guidelines for the need of future development in the area of modelling particulate flame synthesis and to highlight the need for proper model validation. The validation with one set of measurements only may not identify shortcomings of models or sub-models as the “right” choice of modelling constants may often allow for a good match between simulations and “the” one target experiment. As has been established within the combustion community, a series of measurements with parameter variation is needed to provide an unbiased assessment of modelling approaches. The—at certain conditions—modest agreement between measurements and simulations should not lead to dismissal of some of the sub-models used here, it rather highlights the complexity of the particulate formation process. Nanoparticulate flame synthesis in general and silica particulate formation in particular is similar to soot inception and growth. The quality of predictions presented here is comparable to the quality of predictions of soot in turbulent flames found in the literature. Also, the difficulties with respect to modelling soot formation are commonly associated with the complex kinetics leading to the incipient soot particulates and with differential diffusion. This is consistent with the current paper that identifies the precursor chemistry and differential mixing of heavy species and particulates as key modelling issues that can explain the strongly non-linear dependence of particulate properties on silane doping, and more work is required in these areas if simulations are to be truly predictive for particulate synthesis processes.

**Acknowledgements** Open Access funding provided by Projekt DEAL. We thank R.P. Lindstedt (Imperial College London) for provision of the burner hardware.

**Funding** This research was funded by Deutsche Forschungsgemeinschaft (DFG) (SPP 1980-KR 3684/12 and BE 3773/3 - GN, AK and FB), the Australian Research Council (DP180104190 - MJC) and by the 2016 Universities Australia - Germany Joint Research Co-operation Scheme.

## Compliance with Ethical Standards

**Conflict of interest** The authors declare that they have no conflict of interest.

**Open Access** This article is licensed under a Creative Commons Attribution 4.0 International License, which permits use, sharing, adaptation, distribution and reproduction in any medium or format, as long as you give appropriate credit to the original author(s) and the source, provide a link to the Creative Commons licence, and indicate if changes were made. The images or other third party material in this article are included in the article’s Creative Commons licence, unless indicated otherwise in a credit line to the material. If material is not included in the article’s Creative Commons licence and your intended use is not permitted by statutory regulation or exceeds the permitted use, you will need to obtain permission directly from the copyright holder. To view a copy of this licence, visit <http://creativecommons.org/licenses/by/4.0/>.

## Appendix 1: Calculation of the Elastic Light Scattering (ELS) Signal

The overall ELS signal has contributions from molecular and particulate scattering with two normalisation factors  $a$  and  $b$ :

$$S_{\text{ELS}} = aS_{\text{ELS}}^{\text{molec}} + bS_{\text{ELS}}^{\text{agg}}. \quad (4)$$

The ELS signal  $S_{\text{ELS}}^{\text{molec}}$  originating from gas molecules is calculated according to

$$S_{\text{ELS}}^{\text{molec}} \propto \frac{\sum_{i=1}^{Y_s} x_i \sigma_i}{T} \quad (5)$$

where  $T$  is the temperature,  $x_i$  is the species mole fraction and  $\sigma_i$  is the ELS (Rayleigh scattering) cross section of species  $i$  at 532 nm. Normalised ELS cross sections have been determined by Fuest et al. (2012). Since composition and temperature are fully defined in the simulation the molecular signal can be predicted within the model.

The second contribution of the ELS signal originates from light scattered by agglomerates and is calculated according to the Rayleigh–Debye–Gans theory of light scattering by fractal agglomerates (RDG-FA) (Sorensen 2001). In the case that a sectional method with  $N_s$  sections is used the contribution of each class of agglomerates is added to give the total signal

$$S_{\text{ELS}}^{\text{agg}} \propto \sum_{k=1}^{N_s} C_{\text{sca}}^{\text{agg}} n_k, \quad (6)$$

where the  $C_{\text{sca}}^{\text{agg}}$  is the scattering cross section of the fractal agglomerate and  $n_k$  is the number density within the section  $k$ . The former is a function of the agglomerate size (Sorensen 2001) and needs to be weighted with the computed PSD to be comparable to the measured signal.

For loose, spherical primary particulates several times smaller than the wavelength, the scattering cross section varies with the sixth power of the primary particulate diameter (Rayleigh's approximation). When large fractal aggregates form, the scattering cross section also depends on the radius of gyration. Following the conventions of Link et al. (2011) we can formulate a dependency of the scattering cross section on fractal dimension and size for three different size regimes:

$$C_{\text{sca}}^{\text{agg}} = \begin{cases} N^2 k^4 (d_{p,0}/2)^6 & : \text{Rayleigh regime} \\ & (qR_g < 0.1), \\ & (R_g < 6 \text{ nm}), \\ N^2 k^4 (d_{p,0}/2)^6 \left(1 - (q^2 R_g^2)/3\right) & : \text{Guinier regime} \\ & (0.1 \leq qR_g \leq 1), \\ & (6 \text{ nm} \leq R_g \leq 62 \text{ nm}), \\ N^2 k^4 (d_{p,0}/2)^6 (C(qR_g)^{-D_f}) & : \text{Power-Law regime} \\ & (qR_g > 1), \\ & (R_g > 62 \text{ nm}), \end{cases} \quad (7)$$

where  $N$  is the number of primary particulates within the aggregate, the scattering wave vector  $q = \frac{4\pi}{\lambda} \sin(\theta)$  and  $k = 2\pi/\lambda$  are constant throughout the experiment since  $\lambda = 532 \text{ nm}$  and  $\theta = \pi/2$ . The value of the constant  $C$  is discussed in Sorensen (2001) and is set to  $C = 0.77$ . As discussed in Sect. 2 the fractal dimension and the primary particulate diameter are set to  $D_f = 1.8$  and  $d_{p,0} = 0.98 \text{ nm}$ , respectively.

The normalisation factors in Eq. (4) are determined based on the results of our reference case with a silane doping of 3100 ppm and a co-flow temperature of  $T_c = 1500 \text{ K}$  at  $Re_D = 10,000$ . The normalisation factor for the molecular ELS signal is determined to  $a = 6.52374 \cdot 10^{-4}$  such that a value of unity is obtained for the co-flow. The ELS signal from agglomerates is normalised with  $b = 1.01 \cdot 10^{-4}$  to match the same maximum value as the experimental reference case.

Two implications of Eq. (7) are noted:

1.  $C_{\text{sca}}^{\text{agg}}$  scales with  $d_{p,0}^6$ . We may be tempted to assume that the modelling uncertainty with respect to the initial primary particulate size and variations in growth rates may have a very significant non-linear effect on the ELS signal. Indeed, particulate diameters measured at 70 mm downstream can easily vary by a factor of 2. It is hypothesized, however, that particulate number density scales with  $d_{p,0}^{-3}$  and therefore  $S_{\text{ELS}}^{\text{agg}}$  computed by Eq. (6) is much more likely to show a square dependence on the size of the primary particulates. Also note that TEM pictures indicate a very similar mean for the primary particulate size for the entire seedings range. Mean diameters are around 11 nm for 300 ppm and around 14 nm for 3100 ppm, and it may be concluded that primary particulate size is not (primarily nor solely) responsible for the strong non-linear effect observed for the different silane loadings.
2. Effects of agglomeration on the ELS signal are small and inaccuracies in the modelling of collision rates cannot explain the differences between the dependencies of simulations and experiments on silane doping. Agglomeration does not change  $d_{p,0}$ , it decreases  $n_k$  and increases  $N$  and  $R_g$ .  $R_g^{-D_f}$  scales with  $N^{-1}$ . Collision of agglomerates yields changes in  $S_{\text{ELS}}^{\text{agg}}$  proportional to  $n_k N^2 N^{-1}$  which equals unity if two large identical agglomerates collide. The agglomeration of two identical small agglomerates increases  $S_{\text{ELS}}^{\text{agg}}$  by a factor of two (Rayleigh regime) or smaller (Guinier regime).

These observations may not hold in case of significant sintering after collision. However, this is not observed in the current application where primary particulates can easily be identified in the samples collected in the exhaust (cf. Fig. 2d).

## Appendix 2: Calculation of the Laser-Induced Fluorescence (LIF) Signals

The predicted LIF signals are calculated from the molecular concentrations,  $c_i$ , of species  $i$  as:

$$S_i^{\text{LIF}} \propto c_i \frac{f_{v,J}(T)}{Q_i(T)} \quad (8)$$

where  $f_{v,J}(T)$  is the normalised Boltzmann fraction of electrons in the ground level for a transition of quantum numbers  $v, J$  and  $Q_i(T)$  is the normalised collisional quenching rate at temperature  $T$ . The total quenching rate is obtained as

$$Q_i(T) = N_{\text{tot}} \sum_s x_s \sigma_s(T) \left( \frac{8k_B T}{\pi \mu_s} \right)^{\frac{1}{2}} \quad (9)$$

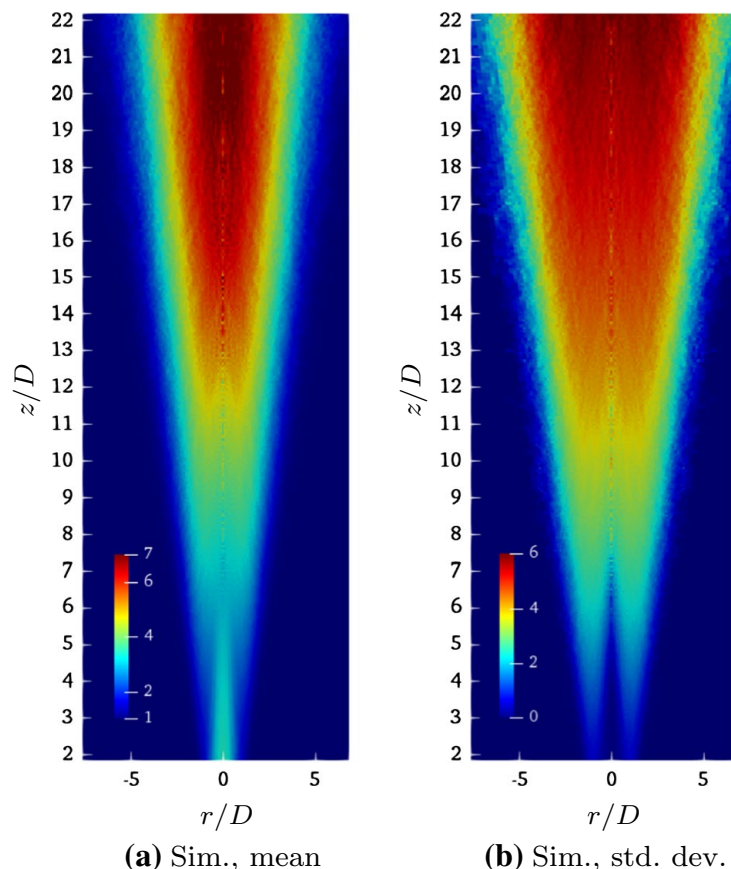
where  $k_B$  is the Boltzmann constant,  $x_s$  is the mole fraction,  $\mu_s$  is the reduced mass and  $\sigma_s$  is the corresponding quenching rate of each collider species  $s$ . Quenching rates for the OH radical under various collider species have been determined by Tamura et al. (1998) where the empirical two-parameter expression is used. In absence of specific quenching rates for SiO, the same rates have been used for the computation of the SiO signal. The Boltzmann fraction for SiO computations was obtained from a *PGOPHER* simulation of this molecule.

### Appendix 3: The Influence of a Mixing Time Scale Modification for the Transported Number Densities of the Discretised Particulate Size Distribution

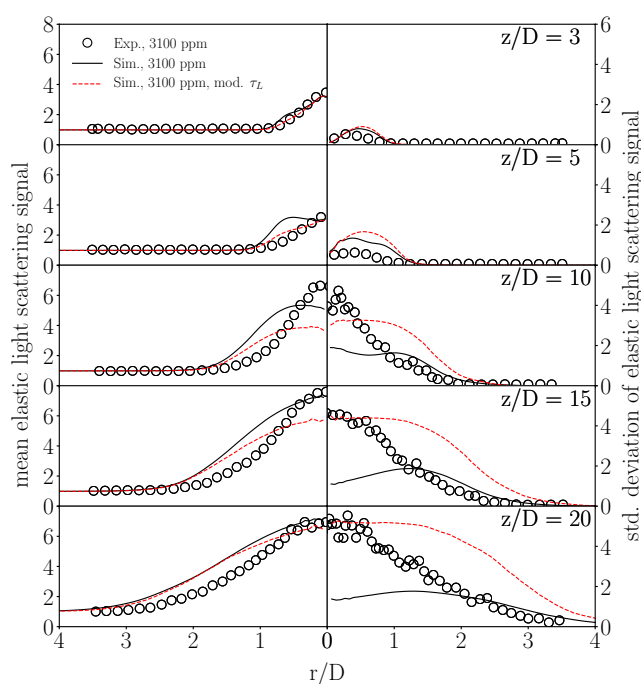
Here, a modification of the Lagrangian mixing time scale is discussed. If unity Lewis number assumptions are invoked, all transported scalars are mixed with a mixing extent calculated on the basis of the anisotropic mixing time scale model proposed by Vo et al. (2017b). Here we show and discuss results obtained with a modification of the Lagrangian mixing time scale for the particulate number densities only, as proposed by Vo et al. (2017a). They showed that for transported particulate matter a modification of the Lagrangian mixing time scale can achieve a significant improvement of the conditional variance. The standard mixing time scale is scaled with the diffusivity of the individual sections in order to reduce the sub-grid mixing of the aerosol,  $\tau_{L,k} = D_k/D \tau_L$ , where  $\tau_{L,k}$  is the mixing time scale of section  $k$ . This emulates reduced mixing rates for large agglomerates. The reference simulation uses the same Lagrangian mixing time scale for all transported scalars including the particulate number densities and has been presented in Sect. 5.1. There, the predicted mean of the ELS signal agrees well with measurements but qualitative differences are observed for the standard deviations (see Fig. 4). It is noted, however, that the location of the peak mean ELS signal moves 5 diameters downstream.

Figure 9 now shows simulated mean and standard deviation of the ELS signal for adjusted mixing time scales mimicking differential diffusion of the particulate matter. All remaining (gas-phase) quantities are mixed with the standard model. Improvements can be observed as (i) particulate nucleation and growth are moved further downstream leading to

**Fig. 9** Contour plots of the normalised elastic light scattering signal for the reference case with a silane loading of 3100 ppm and a co-flow temperature of 1500 K using the modified mixing time scale model



**Fig. 10** Mean and standard deviation of the elastic light scattering signal at different downstream positions for the reference case with a silane doping of 3100 ppm and a modified Lagrangian mixing time for the particulate matter



a reduced ELS signal in the shear layers upstream and (ii) a much better qualitative agreement for the standard deviation is observed (compare Fig. 9b with Fig. 4c).

A more quantitative comparison is provided by Fig. 10 where radial profiles of the ELS signal are shown for different downstream positions. Here, the presence of the ELS signal in the shear layer for the case with equal diffusivities is pronounced and predictions with a modified mixing time scale show improved predictions. Also, the peak values of the standard deviations are much better predicted with the reduced mixing frequencies for the aerosol matter, especially for centerline positions where the peak value are perfectly matched. However, overall agreement does not really improve: the predicted standard deviation profiles are much broader than the measured data and more importantly, the centerline dependence of the mean signal is not captured well. We should point out here that the modifications suggested by Vo et al. (2017a) do not provide a fully consistent differential diffusion model and more sophisticated models as derived e.g. by McDermott and Pope (2007) and Dialameh et al. (2014) should be extended to the present application for accurate predictions of differential diffusion effect. Here, however, we limit ourselves to identify the sensitivities of results on molecular diffusion processes and point out that differential diffusion may need to be properly modelled if agreement with measurements is to be achieved at all positions in the flow.

#### Appendix 4: Discussion of the Influence of Reaction Rate Parameters

In Sect. 5.1 we have shown results of the reference case with a silane doping of 3100 ppm and a co-flow temperature of  $T = 1500$  K. It has been discussed that the computed ELS signal becomes large in the shear layer, whereas this characteristic cannot be observed for the experimental data. There, the ELS signal increases at centerline position in stream-wise direction. One reason could be an incorrect precursor chemistry where chemical reaction rates are overpredicted and inception is too fast. To investigate the influence of

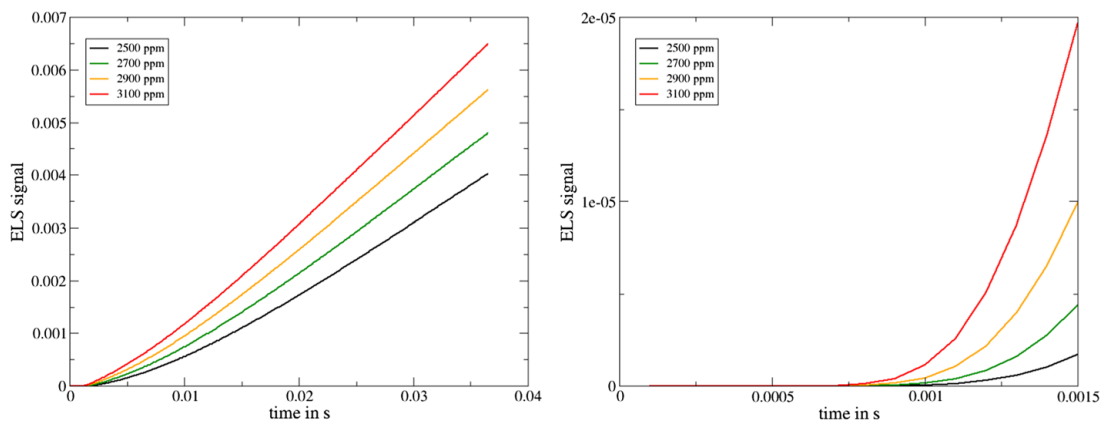
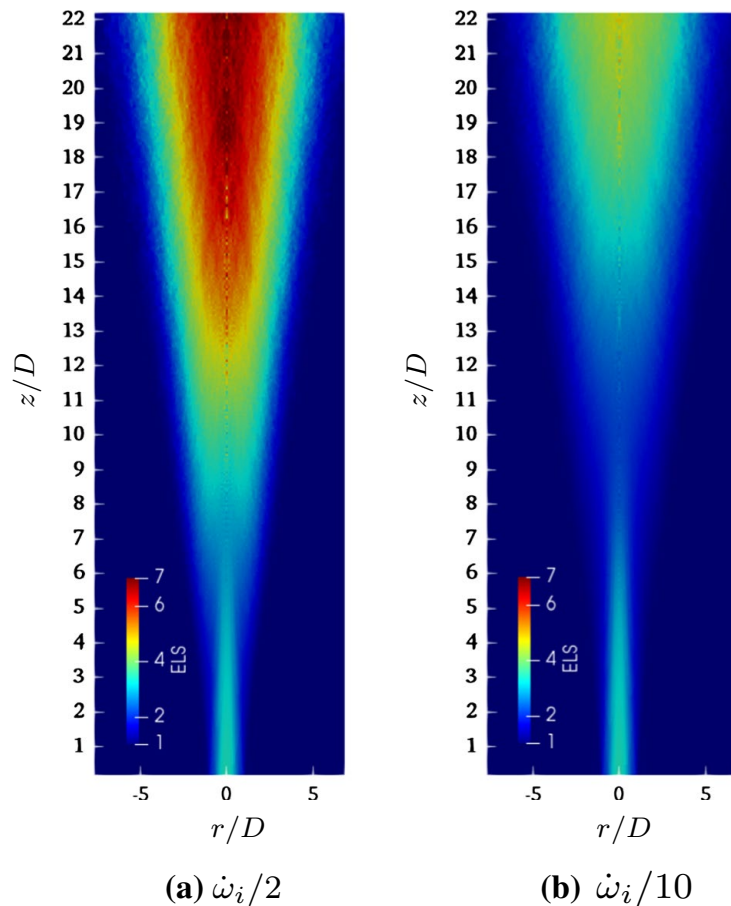


**Fig. 11** ELS signals for different initial silane loadings: entire silicon conversion process (a) and zoom for initial time period of 15 ms (b)

**Fig. 12** Contour plots of the normalised elastic light scattering signal for different reaction rates of the clustering mechanism with a silane loading of 3100 ppm and a co-flow temperature of 1500 K



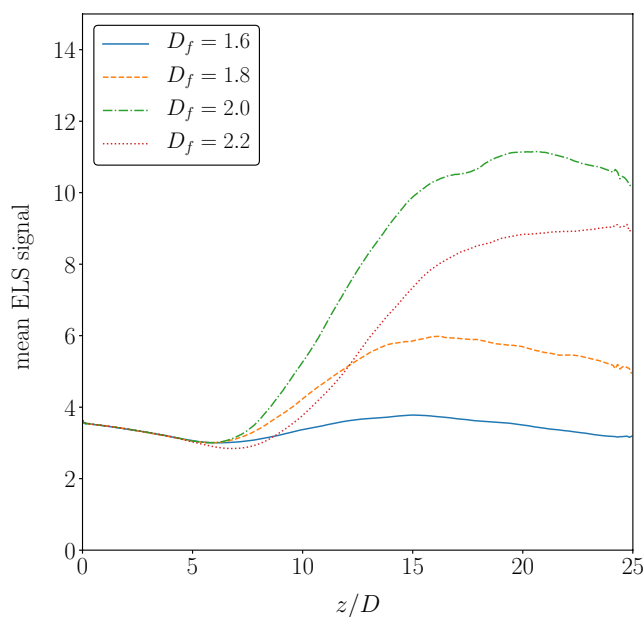
the precursor chemistry we first investigate the time evolution of particulate inception and growth. Figure 11 (left) shows perfectly stirred reactor calculations with different initial silane concentrations. After a transient, the ELS signals are almost linearly dependent on the silane loading. However, during an initial stage (Fig. 11 (right)) the ELS signals are strongly non-linearly dependent and the sensitivity resembles the sensitivity observed in Fig. 7. The rate coefficient for the clustering reactions given in Suh et al. (2002) are estimates and some adjustments seem justified. A reduction in rates may delay

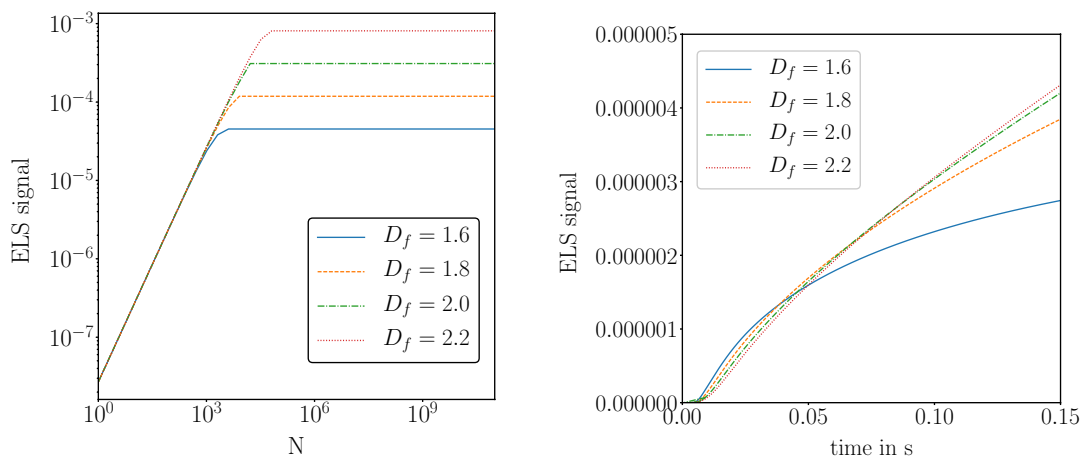
particulate nucleation sufficiently to (i) reduce particulate nucleation in the shear layer and (ii) “freeze” particulate formation sufficiently early due to dispersion and mixing prior to completion of the entire conversion process from silane to silica particulates. Figure 12 shows the mean ELS signal of simulations where the pre-exponential factors of all clustering reactions are divided by 2 and 10, respectively. As expected, the particulate inception is shifted further downstream with negligible particulate formation in the upstream shear layers which is consistent with experiments. Thus, the precursor chemistry model—and uncertainties related with it—can have a strong impact on the particulate evolution processes. We note, however, that the peak ELS signals are shifted further downstream (with the maximum for the  $\dot{\omega}_i/10$  case likely to be located outside the computational domain). The overall agreement with measurements is therefore not improved, and we may postulate a need for improved precursor kinetics if simulations of silica production processes are to be predictive.

## Appendix 5: Investigation of the Influence of the Particulates’ Fractal Dimension on the ELS Signal

The frequency of agglomerate-agglomerate collision is given by the collision kernel. Kernels require the specification of collisional cross-sections that can be parameterized by the agglomerates’ radii of gyration and fractal dimensions. A typical fractal dimension for silica flame synthesis reported in the literature is  $D_f = 1.8$  (Shekar et al. 2012; Schaefer and Hurd 1990) and is assumed to be constant in our sectional approach. However, the fractal dimension may change during the growth process due to collision of different agglomerates (Inci et al. 2017) or due to surface growth and neck formation. To assess the influence of different morphologies Fig. 13 shows the mean ELS signal along the centerline for four MMC-LES simulation of the reference case (as defined in Sect. 5.1). The only change relates to using different—but still constant—values of the fractal dimension. The signal originating from the gas molecules is not affected and signals are nearly equal down to  $z/D=5$  when the first particulates form on the centerline. Then, the ELS signal increases with

**Fig. 13** Mean elastic light scattering signal along the centerline for cases with a co-flow temperature of  $T = 1500$  K and with different (constant) fractal dimensions for the agglomerates’ morphologies





**(a)** ELS signal from  $n_0 = 1 \cdot 10^{20}$  primary particulates dependent on primary particulate number in the agglomerate,  $N$ , for different fixed fractal dimensions,  $D_f$ .

**(b)** ELS signal of perfectly stirred reactor simulations for different fractal dimensions.

**Fig. 14** Influence of the fractal dimension on the elastic light scattering signal

different rates and the signal originating from the solid phase starts to dominate. It can be observed that the maximum signal strength shifts further downstream for larger fractal dimensions. This indicates—as expected—a decreased agglomeration rate for more compact agglomerates. It needs to be noted, however, that the respective maximum values do not reveal a clear dependence on  $D_f$  as the maximum value is observed for  $D_f = 2.0$ .

This non-monotonic dependence on  $D_f$  can be explained with the aid of Fig. 14. To generate Fig. 14a, the ELS signals were computed from agglomerates with a uniform particulate number,  $N$ , and fractal dimension,  $D_f$ , keeping the total number of primary particulates,  $n_0 = 1 \cdot 10^{20}$ , fixed. The figure highlights changes in the ELS signal due to agglomeration and different morphologies. For small and medium sized agglomerates in the Rayleigh and Guinier regime, the signal increases almost linearly with  $N$ . This is consistent with Eqs. (6) and (7) as  $n_k \sim N^{-1}$ . For large agglomerates in the powerlaw regime, the scattering signal remains constant which is in line with our discussion in App. 1. As the scattered signal from large agglomerates is much higher, only the large agglomerates affect the ELS signal. We can also see that the fractal dimension has a strong and non-linear influence on the ELS signal. Here, the scattered light of compact agglomerates is much higher than that of agglomerates with low fractal dimensions. Figure 14b shows the temporal evolution of the ELS signal from a perfectly stirred reactor calculation. The initial composition is given by a burning solution for a mixture fraction of  $Z = 0.35$  of the reactive jet simulations with 3100 ppm silane loading. The simulation time corresponds to the time a fluid element would need to travel along the centerline in our jet configuration described in the main body of the paper, and the PSR simulations thus approximate the time history of a burning notional particle in the absence of mixing. It can be seen that agglomerates with smaller fractal dimensions emit stronger signals at the beginning. After some time, however, this dependence is reversed. This behaviour can now easily be understood with data from Fig. 14a. Initially, agglomerates with small fractal dimension grow faster due to a larger collisional cross section giving faster increases in the ELS signal. After some time, however, scatter is dominated by agglomerates in the power law regime, further growth does not increase the ELS signal, and the increase in the ELS signal considerably slows

(as nucleation is ongoing and smaller agglomerates continue to exist). Since more compact agglomerates with larger fractal dimension tend to yield stronger ELS signals, simulations using larger  $D_f$  will provide larger ELS signals and the initial dependence on  $D_f$  is reversed.

The evolution of the ELS signal observed in Fig. 13 can now be explained: The ELS signals for larger  $D_f$  rise more slowly as agglomeration is delayed. This trend is very quickly reversed for  $D_f < 2.2$  and the more compact agglomerates tend to give larger ELS signals. For the fractal dimension of  $D_f = 2.2$  the results do not quite follow the trend. Upstream, the computed ELS signal is in line with our expectations but further downstream, the signal does not surpass the values computed for  $D_f = 2.0$ . It can be hypothesized here that this is due to broadening effects further downstream. Radial (turbulent and molecular) diffusion and particulate and agglomerate dispersion decrease the local particulate number density and thus the collision frequency and counteract the expected increase in ELS signal.

The discussions with respect to the computed ELS signal show that an unambiguous comparison between measured and computed ELS signals may require a model for the solid phase that includes information not only on mean parameters for particulate number density, radius of gyration, primary particulate diameter and fractal dimension, but also on their distributions and correlations. Such a multi-variate characterisation of the nanoparticles using a sectional approach is currently beyond reach as (i) computational requirements will be huge and (ii) models describing the dynamics within this multi-dimensional space do not exist. Only two-dimensional models based on a multi-sectional moment method were proposed (e.g. Yang and Mueller 2019; Xiong et al. 1993) and may guide future research in the context of MMC-LES-PBE of nanoparticle flame synthesis for improved predictions of particulate characteristics.

## References

- Cabra, R., Myrvoid, T., Chen, J.Y., Dibble, R.W., Karpetis, A.N., Barlow, R.S.: Simultaneous laser Raman–Rayleigh–LIF measurements and numerical modeling results of a lifted turbulent  $\text{h}_2/\text{n}_2$  jet flame in a vitiated co-flow. *Proc. Combust. Inst.* **29**, 1881–1888 (2002). [https://doi.org/10.1016/s1540-7489\(02\)80228-0](https://doi.org/10.1016/s1540-7489(02)80228-0)
- Cleary, M.J., Klimenko, A.Y.: A detailed quantitative analysis of sparse-Lagrangian filtered density function simulations in constant and variable density reacting jet flows. *Phys. Fluids* **23**(11), 115102 (2011). <https://doi.org/10.1063/1.3657085>
- Connelly, B.C., Bennett, B.A.V., Smooke, M.D., Long, M.B.: A paradigm shift in the interaction of experiments and computations in combustion research. *Proc. Combust. Inst.* **32**(1), 879–886 (2009). <https://doi.org/10.1016/j.proci.2008.05.066>
- Curl, R.L.: Dispersed phase mixing: I. Theory and effects of simple reactors. *AIChE J.* **9**(47), 175–181 (1963). <https://doi.org/10.1002/aic.690090207>
- Dialameh, L., Cleary, M.J., Klimenko, A.Y.: A multiple mapping conditioning model for differential diffusion. *Phys. Fluids* **26**(2), 025107 (2014). <https://doi.org/10.1063/1.4864101>
- Dobbins, R.A., Megaridis, C.M.: Morphology of flame-generated soot as determined by thermophoretic sampling. *Langmuir J.* **3**(2), 254–259 (1987). <https://doi.org/10.1021/La00074a019>
- Floyd, J., Kempf, A.M.: Computed tomography of chemiluminescence (CTC): high resolution and instantaneous 3D measurements of a matrix burner. *Proc. Combust. Inst.* **33**, 751–758 (2011). <https://doi.org/10.1016/j.proci.2010.06.015>
- Friedlander, S.K.: *Smoke, Dust and Haze*, 2nd edn. Oxford University Press, Oxford (2000)
- Fuest, F., Barlow, R.S., Chen, J.-Y., Dreizler, A.: Raman/Rayleigh scattering and CO-LIF measurements in laminar and turbulent jet flames of dimethyl ether. *Combust. Flame* **159**(8), 2533–2562 (2012). <https://doi.org/10.1016/j.combustflame.2011.11.001>

- Galindo-Lopez, S., Salehi, F., Cleary, M.J., Masri, A.R., Neuber, G., Stein, O.T., Kronenburg, A., Varna, A., Hawkes, E.R., Sundaram, B., Klimenko, A.Y., Ge, Y.: A stochastic multiple mapping conditioning computational model in OpenFOAM for turbulent combustion. *Comput. Fluids* **172**, 410–425 (2018). <https://doi.org/10.1016/j.compfluid.2018.03.083>
- Iler, R.K.: *The Chemistry of Silica*. Wiley, Hoboken (1979). <https://doi.org/10.1021/ed057pA324.1>
- Inci, G., Kronenburg, A., Weeber, R., Pflger, D.: Langevin dynamics simulation of transport and aggregation of soot nano-particles in turbulent flows. *Flow Turbul. Combust.* **98**, 1065–1085 (2017). <https://doi.org/10.1007/s10494-016-9797-3>
- Janicka, J., Kolbe, W., Kollmann, W.: Closure of the transport-equation for the probability density-function of turbulent scalar fields. *J. Non-Equilib. Thermodyn.* **4**, 47–66 (1979). <https://doi.org/10.1515/jnet.1979.4.1.47>
- Klimenko, A.Y., Pope, S.B.: The modelling of turbulent reacting flows based on multiple mapping conditioning. *Phys. Fluids* **15**(7), 1907–1925 (2003). <https://doi.org/10.1063/1.1575754>
- Kruis, F.E., Kusters, K.A., Scarlett, B., Pratsinis, S.E.: A simple model for the evolution of the characteristics of aggregate particles undergoing coagulation and sintering. *Aerosol Sci. Technol.* **19**(4), 514–526 (1993). <https://doi.org/10.1080/02786829308959656>
- Kruis, F., Maisels, A., Fissan, H.: Direct simulation monte carlo method for particle coagulation and aggregation. *AIChE J.* **46**(9), 1735–1742 (2000). <https://doi.org/10.1002/aic.690460905>
- Link, O., Snelling, D.R., Thomson, K.A., Smallwood, G.J.: Development of absolute intensity multi-angle light scattering for the determination of polydisperse soot aggregate properties. *Proc. Combust. Inst.* **33**, 847–854 (2011). <https://doi.org/10.1016/j.proci.2010.06.073>
- Loeffler, J., Das, S., Garrick, S.C.: Large eddy simulation of titanium dioxide nanoparticle formation and growth in turbulent jets. *Aerosol Sci. Technol.* **45**(5), 616–628 (2011). <https://doi.org/10.1080/02786826.2010.551147>
- Marchisio, D.L., Fox, R.O.: *Computational Models for Polydisperse Particulate and Multiphase Systems*. Cambridge University Press, Cambridge (2013). <https://doi.org/10.1017/CBO9781139016599>
- McDermott, R., Pope, S.B.: A particle formulation for treating differential diffusion in filtered density function methods. *J. Comput. Phys.* **226**, 947–993 (2007). <https://doi.org/10.1016/j.jcp.2007.05.006>
- Neuber, G., Kronenburg, A., Stein, O.T., Cleary, M.J.: MMC-LES modelling of droplet nucleation and growth in turbulent jets. *Chem. Eng. Sci.* **167**, 204–218 (2017). <https://doi.org/10.1016/j.ces.2017.04.008>
- Neuber, G., Garcia, C.E., Kronenburg, A., Williams, B.A.O., Beyrau, F., Stein, O.T., Cleary, M.J.: Joint experimental and numerical study of silica particulate synthesis in a turbulent reacting jet. *Proc. Combust. Inst.* **37**, 1213–1220 (2019a). <https://doi.org/10.1016/j.proci.2018.06.074>
- Neuber, G., Fuest, F., Kirchmann, J., Kronenburg, A., Stein, O.T., Galindo-Lopez, S., Cleary, M.J., Barlow, R.S., Coriton, B., Frank, J.H., Sutton, J.A.: Sparse-Lagrangian MMC modelling of the Sandia DME flame series. *Combust. Flame* **208**, 110–121 (2019b). <https://doi.org/10.1016/j.combustflame.2019.06.026>
- Nicoud, F., Toda, H.B., Cabrit, O., Bose, S., Lee, J.: Using singular values to build a subgrid-scale model for large eddy simulations. *Phys. Fluids* **23**, 085106 (2011). <https://doi.org/10.1063/1.3623274>
- Pesmazoglou, I., Kempf, A.M., Navarro-Martinez, S.: Large eddy simulation of particle aggregation in turbulent jets. *J. Aerosol Sci.* **111**, 1–17 (2017). <https://doi.org/10.1016/j.jaerosci.2017.06.002>
- Pope, S.B.: PDF methods for turbulent reacting flows. *Prog. Energy Combust. Sci.* **11**, 119–192 (1985). [https://doi.org/10.1016/0360-1285\(85\)90002-4](https://doi.org/10.1016/0360-1285(85)90002-4)
- Pope, S.B.: Computationally efficient implementation of combustion chemistry using in situ adaptive tabulation. *Combust. Theor. Model.* **1**, 41–63 (1997). <https://doi.org/10.1080/713665229>
- Prakash, A., Bapat, A., Zachariah, M.: A simple numerical algorithm and software for solution of nucleation, surface growth, and coagulation problems. *Aerosol Sci. Technol.* **37**(11), 892–898 (2003). <https://doi.org/10.1080/02786820300933>
- Pratsinis, S.E.: Simultaneous nucleation, condensation, and coagulation in aerosol reactors. *J. Colloid Interface Sci.* **124**(2), 416–427 (1988). [https://doi.org/10.1016/0021-9797\(88\)90180-4](https://doi.org/10.1016/0021-9797(88)90180-4)
- Schaefer, D.W., Hurd, A.J.: Growth and structure of combustion aerosols: fumed silica. *Aerosol Sci. Technol.* **12**(4), 876–890 (1990). <https://doi.org/10.1080/02786829008959400>
- Seinfeld, J.H.: *Atmospheric Chemistry and Physics of Air Pollution*. Wiley, Hoboken (1986). <https://doi.org/10.1021/es00151a602>
- Seitzman, J.M., Hanson, R.K.: Comparison of excitation techniques for quantitative fluorescence imaging of reacting flows. *AIAA J.* **31**, 513–519 (1993). <https://doi.org/10.2514/3.11359>
- Sewerin, F., Rigopoulos, S.: An LES–PBE–PDF approach for predicting the soot particle size distribution in turbulent flames. *Combust. Flame* **189**, 62–76 (2018). <https://doi.org/10.1016/j.combustflame.2017.09.045>

- Shekar, S., Sander, M., Riehl, R.C., Smith, A.J., Braumann, A., Kraft, M.: Modelling the flame synthesis of silica nanoparticles from tetraethoxysilane. *Chem. Eng. Sci.* **70**, 54–66 (2012). <https://doi.org/10.1016/j.ces.2011.06.010>
- Sorensen, C.M.: Light scattering by fractal aggregates: a review. *Aerosol Sci. Technol.* **35**(2), 648–687 (2001). <https://doi.org/10.1080/027868201316900007>
- Subramaniam, S., Pope, S.B.: A mixing model for turbulent reactive flows based on Euclidean minimum spanning trees. *Combust. Flame* **115**, 487–514 (1998)
- Suh, S.-M., Zachariah, M.R., Girshik, S.L.: Modeling particle formation during low-pressure silane oxidation: detailed chemical kinetics and aerosol dynamics. *J. Vac. Sci. Technol. A* **19**, 940–951 (2001). <https://doi.org/10.1116/1.1355757>
- Suh, S.-M., Zachariah, M.R., Girshik, S.L.: Numerical modeling of silicon oxide particle formation and transport in a one-dimensional low-pressure chemical vapor deposition reactor. *J. Aerosol Sci.* **33**, 943–959 (2002). [https://doi.org/10.1016/s0021-8502\(02\)00047-2](https://doi.org/10.1016/s0021-8502(02)00047-2)
- Tamura, M., Berg, P.A., Harrington, J.E., Luque, J., Jefferies, J.B., Smith, G.P., Crosley, D.R.: Collisional quenching of CH(A), OH(A), and NO(A) in low pressure hydrocarbon flames. *Combust. Flame* **114**, 501–514 (1998). [https://doi.org/10.1016/s0010-2180\(97\)00324-6](https://doi.org/10.1016/s0010-2180(97)00324-6)
- Tornaiainen, E.D., Hinz, A.K., Gouldin, F.C.: Tomographic analysis of unsteady, reacting flows: numerical investigation. *AIAA J.* **36**, 1270–1278 (1998). <https://doi.org/10.2514/2.509>
- Villiermaux, J., Devillion, J.C.: Représentation de la coalescence et de la redispersion des domaines de ségrégation dans un fluide par un modèle d’interaction phénoménologique. In: Proceedings of the Second International Symposium on Chemical Reaction Engineering, pp. 1–13 (1972). <https://doi.org/10.1016/j.ces.2004.09.062>
- Vo, S., Kronenburg, A., Stein, O.T., Cleary, M.J.: Multiple mapping conditioning for silica nanoparticle nucleation in turbulent flows. *Proc. Combust. Inst.* **36**(1), 1089–1097 (2017a). <https://doi.org/10.1016/j.proci.2016.08.088>
- Vo, S., Stein, O.T., Kronenburg, A., Cleary, M.J.: Assessment of mixing time scales for a sparse particle method. *Combust. Flame* **179**, 280–299 (2017b). <https://doi.org/10.1016/j.combustflame.2017.02.017>
- Wang, G., Garrick, S.C.: Modeling and simulation of titania formation and growth in temporal mixing layers. *J. Aerosol Sci.* **37**, 431–451 (2006). <https://doi.org/10.1016/j.jaerosci.2005.04.007>
- Witten, J.T.A., Sander, L.M.: Diffusion-limited aggregation, a kinetic critical phenomenon. *Phys. Rev. Lett.* **47**(19), 1400–1403 (1981). <https://doi.org/10.1103/physrevlett.47.1400>
- Xiong, Y., Akhtar, M.K., Pratsinis, S.E.: Formation of agglomerate particles by coagulation and sintering—part II. The evolution of the morphology of aerosol-made titania, silica and silica-doped titania powders. *J. Aerosol Sci.* **24**(3), 301–313 (1993). [https://doi.org/10.1016/0021-8502\(93\)90004-S](https://doi.org/10.1016/0021-8502(93)90004-S)
- Yang, S., Mueller, M.E.: A multi-moment sectional method (mmsm) for tracking the soot number density function. *Proc. Combust. Inst.* **37**, 1041–1048 (2019). <https://doi.org/10.1016/j.proci.2018.06.107>
- You, J., Yang, Y., Pope, S.B.: Effects of molecular transport in LES/PDF of piloted turbulent dimethyl ether/air jet flames. *Combust. Flame* **176**, 451–461 (2017)

## Affiliations

Gregor Neuber<sup>1</sup> · Andreas Kronenburg<sup>1</sup> · Oliver T. Stein<sup>1</sup> · Carlos E. Garcia<sup>2</sup> · Benjamin A. O. Williams<sup>3</sup> · Frank Beyrau<sup>4</sup> · Matthew J. Cleary<sup>5</sup>

Gregor Neuber  
gregor.neuber@itv.uni-stuttgart.de

Oliver T. Stein  
o.stein@itv.uni-stuttgart.de

Carlos E. Garcia  
c.garcia-gonzalez13@imperial.ac.uk

Benjamin A. O. Williams  
ben.williams@eng.ox.ac.uk

Frank Beyrau  
frank.beyrau@ovgu.de

Matthew J. Cleary  
m.cleary@sydney.edu.au

- <sup>1</sup> Institut für Technische Verbrennung, Universität Stuttgart, Herdweg 51, 70174 Stuttgart, Germany
- <sup>2</sup> Department of Mechanical Engineering, Imperial College London, London SW7 2AZ, UK
- <sup>3</sup> Department of Engineering Science, University of Oxford, Oxford OX1 3PU, UK
- <sup>4</sup> Institute of Fluid Dynamics and Thermodynamics, University of Magdeburg, 39106 Magdeburg, Germany
- <sup>5</sup> School of Aerospace, Mechanical and Mechatronic Engineering, The University of Sydney, Sydney, NSW 2006, Australia

# Chapter 6

## Conclusion & Outlook

### 6.1 Conclusion

The present work has established a novel combined PBE-MMC-LES approach as a powerful solution method for the numerical simulation of particulate flame synthesis in turbulent flows. The efficient modelling includes particulate formation, surface growth and agglomeration of particulates with fractal morphology, thus accounting for the three most important phenomena in particulate synthesis processes. Here, the aerosol phase is described by a sectional method approximating the particulate size distribution, which provides a more detailed insight than, for example, using a moment method. For conventional (dense) PDF models, the inclusion of the particulate size distribution within the transported scalar vector was previously associated with an enormously increased computational effort. This can now be accomplished much more efficiently, since a sparse-Lagrangian MMC method is used for the calculation of the reactive scalar fields and the particulate size distribution. In contrast to conventional stochastic methods, which usually require a considerable number of stochastic particles per LES cell, the MMC method allows for a significant reduction of the number of stochastic particles that are required in the simulations, making the calculation of aerosol dynamics affordable as an additional computational burden. The sparse-Lagrangian particle method is not only much more efficient than other solution methods, but also provides all the desired properties of a mixing model, such as linearity and locality in composition space, among others, as discussed in Sec. 3.2.3.1.

As shown in Chap. 5, compared to conventional methods and with respect to aerosol processes, the PBE-MMC-LES approach can achieve an equivalent result quality with significantly less computational effort. In terms of aerosol processes, this work quantifies the errors that arise when sub-grid contributions of scalar fluctuations are not resolved, and thus shows that these must not be neglected. A validated flow solver has been extended with an additional source code tem-

plate layer to allow for an efficient computation of aerosol dynamics in turbulent, reactive environments, see Sec. 4.3. The full PBE-MMC-LES model was validated by comparison with experimental and numerical data, and it was shown that the numerical scheme can provide excellent results through the application of a newly developed Lagrangian mixing time scale model. It was shown that the use of state-of-the-art models for particulate flame synthesis (cf. Sec. 3.3.3) can generally capture trends under varying boundary conditions. However, this work highlights that there are still some uncertainties regarding the precursor chemistry, that the rigorous assumptions concerning the particulate morphology should be relaxed, and underlines the necessity of an appropriate model for differential diffusion.

## 6.2 Outlook

Based on the discussion of the results in Chap. 5, several pathways for future development emerge, which will be outlined in the following.

### Enhanced simulation of the chemical reaction system

Based on the results presented in Chap. 5, it was shown that the combined PBE-MMC-LES model can generally reproduce the trends observed in the ELS signal; however, the strong non-linearities cannot be reproduced by the numerical model. The related discussion identified, besides differential diffusion and the assumed particle morphology, the chemical reaction mechanism as a potential process that could introduce a non-linearity for the particulate inception rate and thus for the ELS signal. For this reason future work should study a more detailed and validated chemical reaction mechanism for thermal silane decomposition, as particulate formation has been shown to be highly dependent on chemical kinetics. A promising contribution has recently been made by Chatelain *et al.* [246, 247], who have assembled a comprehensive review of suitable decomposition mechanisms for silane chemistry. For an adequate calculation of the precursor chemistry it is necessary to include a very detailed reaction mechanism that may contain up to thousands of chemical reactions. Since such large reaction mechanisms represent a large computational effort even with the sparse-Lagrangian particle method, a tabulated chemistry procedure could be beneficial for this purpose. However, its application is severely limited by the extreme storage and retrieval requirements of this approach. One alternative option would be to reduce the chemical dimension [248] dependent on local conditions in conjunction with a dynamic adaptive chemistry (DAC) approach [249], which provides more chemical detail in regions of interest and allows computational savings in regions of less importance. First simulation results [250] for turbulent reactive

flows using the DAC method in combination with the MMC method are promising, but require further validation work.

### **Application of a minimally-dissipative flow solver**

As discussed in Chap. 5, the implemented density coupling model presented in Sec. 4.2.1 leads to a strong stochastic influence due to the sparse particle distribution, such that strong purely numerically induced density fluctuations can occur which negatively affect the turbulent flow field. Regarding the applied numerical schemes of the finite volume method for LES, Hassanaly *et al.* [217] showed that the applied standard solvers for variable density flows available in OpenFOAM are not fully conservative with respect to momentum. Consequently, Hassanaly *et al.* [217] developed a minimally-dissipative low-Mach number solver within the OpenFOAM framework and confirmed its validity on generic test cases such as the Taylor-Green vortex and a turbulent jet. For this reason, the implementation of the proposed minimally-dissipative solver for low-Mach numbers in the current MMC framework would be extremely useful to provide a robust and fully conservative numerical framework in which the influence of numerically induced density fluctuations is minimised.

Provided that uncertainties in the numerical modelling of the underlying flow field and chemistry are excluded or at least minimised by the previously mentioned approaches, the numerical methods used to represent the aerosol phase still offer potential for improvement at various points, which are discussed in the following:

### **Using an enhanced discretisation scheme for the particulate size distribution**

Since the consideration of a resolved particulate size distribution is not feasible in conventional PDF approaches due to limited computational resources, a moment method is commonly used to model the aerosol dynamics. The application of a sparse-Lagrangian particle method allows the scalars that are required to approximate the particulate size distribution to be added to the transported scalar vector, resulting in much higher accuracy with respect to the representation of aerosol dynamics. In this work, in a first step, a one-dimensional discretisation in particulate volume space was implemented. When considering the size growth of particulates of fractal morphology, this type of discretisation assumes that the fractal dimension does not change during the surface growth process. Here, growth is understood as integral growth, where the volume changes but the particulate morphology itself is preserved. As discussed in Chap. 5, this assumption is of course quite severe and could be one of the reasons why the strong non-linearity of the ELS signals observed in the experiments does not appear in

the simulations. The assumption of a fixed fractal dimension could be overcome by a two-dimensional discretisation - one dimension in particulate volume space and another one in particulate surface space. But this would add another dimension to the discretisation scheme of the PSD and even with a sparse-Lagrangian particle method the computational burden would significantly increase. Consequently, Jeong *et al.* [182] proposed to use two one-dimensional discretisations instead of a two-dimensional discretisation to describe the particulates morphology. There it was shown that the computational savings are substantial, although comparable numerical accuracy can be achieved, such that it is suggested to follow a similar approach here.

### Differential diffusion

As discussed in Sec. 3.3.4 the effect of differential diffusion is an important aspect to consider, especially with the occurrence of larger particulates. In Chap. 5 it was shown that the results differ significantly if a simplistic differential diffusion model is applied. Here, an ad hoc approach was pursued, which has no rigorous derivation and was only intended to unveil that this influence should not be neglected. For this reason, more attention should be paid to the appropriate modelling of differential diffusion, as the large discrepancies between experimental data and numerical results found in this work as well as in the literature [41, 42, 43] may be due to the negligence of differential diffusion effects.

There are only few approaches available to incorporate differential diffusion into a transported stochastic PDF methodology. McDermott & Pope [251] proposed a differential diffusion model based on additional terms within the mixing operator and applied their method to model the Sandia DME flame series [252] showing good results. The method requires smooth Eulerian fields to calculate the additional molecular transport terms. As discussed in Cleary & Klimenko [96], the reconstruction of Eulerian fields in the sparse MMC is subject to a strong stochastic error due to the sparse nature of the approach. Consequently, the conservative formulation of the mixing process would no longer be preserved if the proposed mixing model is applied.

Dialameh & Klimenko [253] developed a differential diffusion model explicitly for MMC, but only for a single species with a higher diffusivity, and the model implementation for species or transported scalars with a lower diffusivity is unclear to date. This issue should be addressed during further model development studies.

Yang *et al.* [254] proposed a comparatively simple differential diffusion model based on a stochastic mass-based implementation and validation was done on a forced homogeneous turbulence setup revealing excellent results for the decay of species variances. A subsequent investigation of a diffusion flame by Zhou *et al.* [255] yields remarkable results for unconditional intermediate species. Due

to its relatively straightforward implementation, the model proposed by Yang *et al.* [254] should also be investigated in the context of the MMC framework.

Dialameh & Klimenko [253] noted that an MMC-consistent treatment of differential diffusion can be achieved with the shadow-position mixing model. Since the shadow-position mixing model has recently been implemented into the MMC framework [124, 125], future research should investigate the possibilities for a subsequent incorporation of differential diffusion effects.

### **Application to more complex problems**

In order to extend the range of application, the combined PBE-MMC-LES model presented in this work should be validated against more complex physical problems. The next logical steps will be to apply the whole PBE-MMC-LES model to more complex geometries or flow conditions, e.g. supersonic flows with high pressure regions, and compare it against other efficient LES methodologies [256]. Another challenge would be to address problems that include spray evaporation in addition to the actual particulate formation, such that the spray droplet size distribution can be represented using the sectional method presented here.

Many recent scientific studies focus on the prediction of soot formation [18, 173, 51, 206]. Since soot – among others – is a strong driver of climate change [7] as well as a hazard to human and animal health, a reduction of soot emission is highly desirable. The models used in the present work with respect to particulate formation have such a generality that they can be applied easily to other problems with different precursors. As such, the prediction of soot formation would be another very interesting application of the presented combined PBE-MMC-LES model.

### **Final Remarks**

In summary, it can be said that the combined PBE-MMC-LES framework represents a major step towards an efficient prediction method for particulate-laden turbulent reactive flows and shows pathways for the development of a robust comprehensive numerical scheme for the simulation of aerosol dynamics in turbulent flows. It thereby contributes to a variety of industrial applications and might help to ensure the product quality of industrially fabricated particulates or to reduce unwanted by-products of combustion such as soot.



# Bibliography

- [1] G. Neuber, F. Fuest, J. Kirchmann, A. Kronenburg, O. T. Stein, S. Galindo-López, M. J. Cleary, R. S. Barlow, B. Coriton, J. H. Frank, and J. A. Sutton. Sparse-Lagrangian MMC modelling of the Sandia DME flame series. *Combust. Flame*, 208:110–121, 2019.
- [2] G. Neuber, A. Kronenburg, O. T. Stein, and M. J. Cleary. MMC-LES modelling of droplet nucleation and growth in turbulent jets. *Chem. Eng. Sci.*, 167:204–218, 2017.
- [3] G. Neuber, C. E. Garcia, A. Kronenburg, B. A. O. Williams, F. Beyrau, O. T. Stein, and M. J. Cleary. Joint experimental and numerical study of silica particulate synthesis in a turbulent reacting jet. *Proc. Combust. Inst.*, 37(1):1213–1220, 2019.
- [4] G. Neuber, A. Kronenburg, O. T. Stein, C. E. Garcia, B. A. O. Williams, F. Beyrau, and M. J. Cleary. Sparse-Lagrangian PDF Modelling of Silica Synthesis from Silane Jets in Vitiated Co-flows with varying Inflow conditions. *Flow Turbul. Combust.*, 106:1167–1194, 2021.
- [5] K. H. Henthorn and S. Lee. *Particle Technology and Applications*. CRC Press, 2012.
- [6] P. Shukla, J. Skea, E. C. Buendia, V. Masson-Delmotte, H.-O. Pörtner, D. C. Roberts, R. S. P. Zhai, S. Connors, R. van Diemen, M. Ferrat, E. Haughey, S. Luz, S. Neogi, M. Pathak, J. Petzold, J. P. Pereira, P. Vyas, E. Huntley, K. Kissick, M. Belkacemi, J. Malley, and (eds.). IPCC, 2019: Climate Change and Land: an IPCC special report on climate change, desertification, land degradation, sustainable land management, food security, and greenhouse gas fluxes in terrestrial ecosystems. Technical report, Intergovernmental Panel on Climate Change, 2019.
- [7] World Health Organization. Ambient air pollution: A global assessment of exposure and burden of disease. Technical report, World Health Organization, 2016.

- [8] H. M. Hulburt and S. Katz. Some problems in particle technology: A statistical mechanical formulation. *Chem. Eng. Sci.*, 19(8):555–574, 1964.
- [9] F. E. Kruis, A. Maisels, and H. Fissan. Direct simulation Monte Carlo method for particle coagulation and aggregation. *AIChE J*, 46(9):1735–1742, 2000.
- [10] F. E. Kruis, J. Wei, T. van der Zwaag, and S. Haep. Computational fluid dynamics based stochastic aerosol modeling: Combination of a cell-based weighted random walk method and a constant-number Monte-Carlo method for aerosol dynamics. *Chem. Eng. Sci.*, 70:109–120, 2012.
- [11] S. E. Pratsinis. Simultaneous nucleation, condensation, and coagulation in aerosol reactors. *J. Colloid Interface Sci.*, 124 (2):416–427, 1988.
- [12] S. K. Friedlander. *Smoke, Dust and Haze*. Oxford University Press, Oxford, New York, second edition, 2000.
- [13] M. K. Akhtar, G. G. Lipscomb, and S. E. Pratsinis. Monte Carlo Simulation of Particle Coagulation and Sintering. *Aerosol Sci. Technol.*, 21(1):83–93, 1994.
- [14] G. Inci, A. Kronenburg, R. Weeber, and D. Pflüger. Langevin Dynamics Simulation of Transport and Aggregation of Soot Nano-particles in Turbulent Flows. *Flow Turbul. Combust.*, 98:1065–1085, 2017.
- [15] H. Dang and M. T. Swihart. Computational Modeling of Silicon Nanoparticle Synthesis: I. A general Two-Dimensional Model. *Aerosol Sci. Technol.*, 43:250–263, 2009.
- [16] S. Rigopoulos. PDF method for population balance in turbulent reactive flow. *Chem. Eng. Sci.*, 62(23):6865–6878, 2007.
- [17] S. Rigopoulos. Population balance modelling of polydispersed particles in reactive flows. *Prog. Energy Combust. Sci.*, 36(4):412–443, 2010.
- [18] S. Rigopoulos. Modelling of Soot Aerosol Dynamics in Turbulent Flow. *Flow Turb. Combust.*, 103:565–604, 2019.
- [19] P. R. Spalart, W. Jou, M. Strelets, and S. Allmaras. Comments of feasibility of LES for wings, and on a hybrid RANS/LES approach. In *International Conference on DNS/LES*, Ruston, Louisiana, Aug. 4-8, 1997.
- [20] M. Franke. *Untersuchung zum Potential höherwertiger Turbulenzmodelle für den aerodynamischen Entwurf*. Phd Thesis, Technische Universität Berlin, Fakultät V - Verkehrs- und Maschinensysteme, 2003.

- [21] R. W. Bilger. Future progress in turbulent combustion research. *Prog. Energy Combust. Sci.*, 26(4-6):367–380, 2000.
- [22] R. W. Bilger, S. B. Pope, K. N. C. Bray, and J. F. Driscoll. Paradigms in turbulent combustion research. *Proc. Combust. Inst.*, 30(1):21–42, 2005.
- [23] N. Peters. *Turbulent Combustion*. Cambridge University Press, 2000.
- [24] A. Y. Klimenko and R. W. Bilger. Conditional moment closure for turbulent combustion. *Prog. Energy Combust. Sci.*, 25:595–688, 1999.
- [25] S. B. Pope. PDF methods for turbulent reacting flows. *Prog. Energy Combust. Sci.*, 11:119–192, 1985.
- [26] S. B. Pope. *Turbulent Flows*. Cambridge University Press, 2000.
- [27] S. Subramaniam and S. B. Pope. A mixing model for turbulent reactive flows based on Euclidean minimum spanning trees. *Combust. Flame*, 115:487–514, 1998.
- [28] C. Celis and L. F. Figueira da Silva. Lagrangian Mixing Models for Turbulent Combustion: Review and Prospects. *Flow Turbul. Combust.*, 94:643–689, 2015.
- [29] S. Mitarai, J. J. Riley, and G. Kosaly. Testing of Mixing Models for Monte Carlo Probability Density Function Simulations. *Phys. Fluids*, 17:047101–1, 2005.
- [30] F. E. Kruis, K. A. Kusters, B. Scarlett, and S. E. Pratsinis. A simple model for the evolution of the characteristics of aggregate particles undergoing coagulation and sintering. *Aerosol Sci. Technol.*, 19(4):514–526, 1993.
- [31] D. L. Marchisio and R. O. Fox. *Computational Models for Polydisperse Particulate and Multiphase Systems*. Cambridge University Press, 2013.
- [32] A. Rittler, L. Deng, I. Wlokas, and A. M. Kempf. Large eddy simulations of nanoparticle synthesis from flame spray pyrolysis. *Proc. Combust. Inst.*, 36:1077–1087, 2017.
- [33] F. Schneider, S. Suleiman, J. Menser, E. Borukhovich, I. Wlokas, A. Kempf, H. Wiggers, and C. Schulz. SpraySyn - A standardized burner configuration for nanoparticle synthesis in spray flames. *Review of Scientific Instruments*, 90(8):085108, 2019.
- [34] M. E. Mueller and H. Pitsch. Large eddy simulation of soot evolution in an aircraft combustor. *Phys. Fluids*, 25(11):110812, 2013.

- [35] T. Chittipotula, G. Janiga, and D. Thévenin. Improved soot prediction models for turbulent non-premixed ethylene/air flames. *Proc. Combust. Inst.*, 33(1):559–567, 2011.
- [36] J. Loeffler, S. Das, and S. C. Garrick. Large Eddy Simulation of Titanium Dioxide Nanoparticle Formation and Growth in Turbulent Jets. *Aerosol Sci. Technol.*, 45(5):616–628, 2011.
- [37] S. C. Garrick and G. Wang. Modeling and simulation of titanium dioxide nanoparticle synthesis with finite-rate sintering in planar jets. *J. Nanopart. Res.*, 13:973–984, 2011.
- [38] S. Das and S. C. Garrick. The effects of turbulence on nanoparticle growth in turbulent reacting jets. *Phys. Fluids*, 22:103303–1–10, 2010.
- [39] J. S. Bhatt and R. P. Lindstedt. Analysis of the impact of agglomeration and surface chemistry models on soot formation and oxidation. *Proc. Combust. Inst.*, 32(1):713–720, 2009.
- [40] Y. Xiong and S. E. Pratsinis. Gas phase production of particles in turbulent reactive flows. *J. Aerosol Sci.*, 22(5):637–655, 1991.
- [41] F. Sewerin and S. Rigopoulos. An LES-PBE-PDF approach for modeling particle formation in turbulent reacting flows. *Phys. Fluids*, 19(10):105105, 2017.
- [42] M. E. Mueller and H. Pitsch. LES model for sooting turbulent nonpremixed flames. *Combust. Flame*, 159(6):2166–2180, 2012.
- [43] P. Donde, V. Raman, M. E. Mueller, and H. Pitsch. LES/PDF based modeling of soot–turbulence interactions in turbulent flames. *Proc. Comb. Inst.*, 34(1):1183–1192, 2013.
- [44] C. E. G. Gonzalez. *Characterization of nanoparticles generated in reacting flows*. PhD Thesis, Imperial College London, 2018.
- [45] S.-M. Suh, M. R. Zachariah, and S. L. Girshick. Modeling particle formation during low-pressure silane oxidation: Detailed chemical kinetics and aerosol dynamics. *J. Vac. Sci. Technol. A*, 19:940–951, 2001.
- [46] S. Shekar, M. Sander, R. C. Riehl, A. J. Smith, A. Braumann, and M. Kraft. Modelling the flame synthesis of silica nanoparticles from tetraethoxysilane. *Chem. Eng. Sci.*, 70:54–66, 2012.
- [47] C. A. Echavarria, A. F. Sarofim, J. S. Lighty, and A. D’Anna. Evolution of soot size distribution in premixed ethylene/air and ethylene/benzene/air

- flames: Experimental and modeling study. *Combust. Flame*, 158(1):98–104, 2011.
- [48] A. Gupta, P. Ifeacho, C. Schulz, and H. Wiggers. Synthesis of tailored  $\text{WO}_3$  and  $\text{WO}_x$  ( $2.9 < x < 3$ ) nanoparticles by adjusting the combustion conditions in a  $\text{H}_2/\text{O}_2/\text{Ar}$  premixed flame reactor. *Proc. Combust. Inst.*, 33(2):1883–1890, 2011.
- [49] T. Blacha, M. D. Domenico, P. Gerlinger, and M. Aigner. Soot predictions in premixed and non-premixed laminar flames using a sectional approach for PAHs and soot. *Combust. Flame*, 159:181–193, 2012.
- [50] S. Tsantilis, H. K. Kammler, and S. E. Pratsinis. Population balance modeling of flame synthesis of titania nanoparticles. *Chem. Eng. Sci.*, 57:2139–2156, 2002.
- [51] P. Rodrigues, B. Franzelli, R. Vicquelin, O. Gicquel, and N. Darabiha. Coupling an LES approach and a soot sectional model for the study of sooting turbulent non-premixed flames. *Combust. Flame*, 190:477–499, 2018.
- [52] S. Yang and M. E. Mueller. A Multi-Moment Sectional Method (MMSM) for Tracking the Soot Number Density Function. *Proc. Combust. Inst.*, 37:1041–1048, 2019.
- [53] T. Poinso and D. Veynante. *Theoretical and Numerical Combustion*. R. T. Edwards, 2001.
- [54] S. R. Turns. *An introduction to combustion: concepts and applications*. Addison-Wesley, Palo Alto, Calif., third edition, 2012.
- [55] S. Arrhenius. Über die Reaktionsgeschwindigkeit bei der Inversion von Rohrzucker durch Säuren. *Z. Phys. Chem.*, 4:226–248, 1889.
- [56] A. R. Masri. Partial premixing and stratification in turbulent flames. *Proc. Combust. Inst.*, 35(2):1115–1136, 2015.
- [57] P. Pradshaw. *An Introduction to Turbulence and its Measurement*. Pergamon, 1971.
- [58] H. C. van de Hulst. *Light scattering by small particles*. New York (John Wiley and Sons), 1957.
- [59] C. M. Sorensen. Light Scattering by Fractal Aggregates: A Review. *Aerosol Sci. Technol.*, 35(2):648–687, 2001.
- [60] M. von Smoluchowski. Versuch einer mathematischen Theorie der Koagulationskinetik kolloider Lösungen. *Z. Phys. Chem.*, 92:129–168, 1917.

- [61] H. Müller. Zur allgemeinen Theorie der raschen Koagulation. *Kolloidchem. Beih.*, 27(6):223–250, 1928.
- [62] V. Raman and R. O. Fox. Modeling of fine-particle formation in turbulent flames. *Annu. Rev. Fluid Mech.*, 48(1):159–190, 2016.
- [63] U. Vogel, K. Savolainen, Q. Wu, M. van Tongeren, D. Brouwer, and M. Berges. *Handbook of Nanosafety: Measurement, Exposure and Toxicology*. Academic Press, 2014.
- [64] S. Park, R. Xiang, and K. Lee. Brownian coagulation of fractal agglomerates: analytical solution using the log-normal size distribution assumption. *J. Colloid Interface Sci.*, 231(1):129–135, 2000.
- [65] E. Otto, H. Fissan, S. Park, and K. Lee. Log-normal size distribution theory of Brownian aerosol coagulation for the entire particle size range: part II—analytical solution using Dahneke’s coagulation kernel. *J. Aerosol Sci.*, 30(1):17–34, 1999.
- [66] M. Yu, J. Lin, J. Cao, and M. Seipenbusch. An analytical solution for the population balance equation using a moment method. *Particuology*, 18:194–200, 2015.
- [67] M. Yu, X. Zhang, J. Lin, J. Cao, and M. Seipenbusch. A new analytical solution for solving the population balance equation in the continuum-slip regime. *J. Aerosol Sci.*, 80:1–10, 2015.
- [68] R. O. Fox. *Computational Models for Turbulent Reacting Flows*. Cambridge University Press, 2003.
- [69] J. Boussinesq. Théorie de l’écoulement tourbillonnant et tumultueux des liquides dans les lits rectilignes à grande section. *Gauthier-Villars et Fils*, 1, 1897.
- [70] J. Smagorinsky. General circulation experiments with the primitive equations. *Monthly Weather Review*, 91:99–164, 1963.
- [71] F. Nicoud, H. B. Toda, O. Cabrit, S. Bose, and J. Lee. Using singular values to build a subgrid-scale model for large eddy simulations. *Phys. Fluids*, 23:085106, 2011.
- [72] M. Rieth, F. Proch, O. Stein, M. Pettit, and A. Kempf. Comparison of the Sigma and Smagorinsky LES models for grid generated turbulence and a channel flow. *Comput. Fluids*, 99:172–181, 2014.
- [73] C. Mockett. *A comprehensive study of detached-eddy simulation*. PhD thesis, Technische Universität Berlin, 2009. PhD Thesis.

- [74] F. Marble and J. Broadwell. The coherent flame model of non-premixed turbulent combustion. *Report TRW-9-PU*, 1977.
- [75] F. Williams. A review of some theoretical combustions of turbulent flame structure. In *AGARD Conference Proceedings II.1*, volume 164, pages 1–25, 1975.
- [76] N. Peters. Laminar diffusion flamelet models in non-premixed combustion. *Prog. Energy Combust. Sci.*, 10:319–339, 1984.
- [77] B. Cuenot and T. Poinso. Effects of curvature and unsteadiness in diffusion flames. Implications for turbulent diffusion flames. *Proc. Combust. Inst.*, 25:1383–1390, 1994.
- [78] C. Kortschik, S. Honnet, and N. Peters. Influence of curvature on the onset of autoignition in a corrugated counterflow mixing field. *Combust. Flame*, 142:140–152, 2005.
- [79] T. Echekki and E. Mastorakos. *Turbulent Combustion Modeling: Advances, New Trends and Perspectives*. Springer Netherlands, 2011.
- [80] C. Y. Ma, T. Mahmud, M. Fairweather, E. Hampartsoumian, and P. H. Gaskell. Lifted methane-air jet flames in vitiated coflow. *Combust. Flame*, 128:60–73, 2002.
- [81] M. Ihme, C. Cha, and H. Pitsch. Prediction of local extinction and re-ignition effects in non-premixed turbulent combustion using a flamelet/progress variable approach. *Proc. Combust. Inst.*, 30(1):793–800, 2005.
- [82] S. Popp, F. Hunger, S. Hartl, D. Messig, B. Coriton, J. H. Frank, F. Fuest, and C. Hasse. LES flamelet-progress variable modelling and measurements of a partially-premixed turbulent dimethyl ether jet diffusion flame. *Combust. Flame*, 162:3016–3029, 2015.
- [83] B. Marracino and D. Lentini. Radiation Modelling in Non-Luminous Non-premixed Turbulent Flames. *Comb. Sci. Technol.*, 128:23–48, 1997.
- [84] A. Y. Klimenko. Multicomponent diffusion of various admixtures in turbulent flow. *Fluid Dyn.*, 25:327–331, 1990.
- [85] R. W. Bilger. Conditional moment closure for turbulent reacting flow. *Phys. Fluids A*, 5:436–444, 1993.
- [86] A. Kronenburg. Double conditioning of reactive scalar transport equations in turbulent non-premixed flames. *Phys. Fluids*, 16, 7:2640–2648, 2004.

- [87] A. Kronenburg and A. Papoutsakis. Conditional moment closure modeling of extinction and re-ignition in turbulent non-premixed flames. *Proc. Combust. Inst.*, 30:759–766, 2005.
- [88] M. Mortensen and R. W. Bilger. Derivation of the conditional moment closure equations for spray combustion. *Combust. Flame*, 156:62–72, 2009.
- [89] S. Ukai, A. Kronenburg, and O. T. Stein. LES-CMC of a dilute acetone spray flame. *Proc. Combust. Inst.*, 34:1643–1650, 2013.
- [90] S. Ukai, A. Kronenburg, and O. T. Stein. Simulation of dilute acetone spray flames with LES-CMC using two conditional moments. *Flow Turbul. Combust.*, 93:405–423, 2014.
- [91] S. Ukai, A. Kronenburg, and O. T. Stein. Large eddy simulation of a dilute acetone spray flame using CMC coupled with tabulated chemistry. *Proc. Combust. Inst.*, 35:1667–1674, 2015.
- [92] A. Kronenburg, R. W. Bilger, and J. H. Kent. Modeling Soot Formation in Turbulent Methane-Air Jet Diffusion Flames. *Combust. Flame*, 121:24–40, 2000.
- [93] A. Kronenburg and R. W. Bilger. Modelling differential diffusion in non-premixed reacting flows: model development. *Combust. Sci. Techn.*, 166:175–194, 2001.
- [94] A. Kronenburg and R. W. Bilger. Modelling differential diffusion in non-premixed reacting flows: application to jet flames. *Combust. Sci. Techn.*, 166:195–227, 2001.
- [95] P. Gerlinger. *Numerische Verbrennungssimulation*. Springer-Verlag Berlin Heidelberg, 2005.
- [96] M. J. Cleary and A. Y. Klimenko. A detailed quantitative analysis of sparse-Lagrangian filtered density function simulations in constant and variable density reacting jet flows. *Phys. Fluids*, 23(11), 2011.
- [97] P. J. Colucci, F. A. Jaber, P. Givi, and S. B. Pope. Filtered density function for large eddy simulation of turbulent reacting flows. *Phys. Fluids*, 10:499–515, 1998.
- [98] W. L. Grosshandler. Radcal: A narrow-band model for radiation calculations in a combustion environment. *NIST Technical Note 1402*, April 1993.
- [99] R. L. Curl. Dispersed phase mixing: I. Theory and effects of simple reactors. *AIChE J.*, 9(47):175–181, 1963.

- [100] C. Dopazo. Probability density function approach for an axisymmetric heated jet: centerline evolution. *Phys. Fluids*, 18:397, 1975.
- [101] C. Dopazo. Relaxation of initial probability density functions in the turbulent convection of scalar fields. *Phys. Fluids.*, 22:20, 1979.
- [102] J. Janicka, W. Kolbe, and W. Kollmann. Closure of the transport equation for the probability density function of turbulent scalar field. *J. Non-Equilib. Thermodyn.*, 4(1):47–66, 1979.
- [103] S. B. Pope. An improved turbulent mixing model. *Combust. Sci. Techn.*, 28:131–145, 1982.
- [104] L. Valiño and C. Dopazo. A binomial sampling model for scalar turbulent mixing. *Phys. Fluids A: Fluid Dynamics*, 2(7):1204–1212, 1990.
- [105] A. T. Norris and S. B. Pope. Turbulent mixing model based on ordered pairing. *Combust. Flame*, 109:198–223, 1997.
- [106] R. O. Fox. The Fokker–Planck closure for turbulent molecular mixing: Passive scalars. *Phys. Fluids A: Fluid Dynamics*, 4:1230, 1992.
- [107] R. O. Fox. On velocity-conditioned scalar mixing in homogeneous turbulence. *Phys. Fluids A: Fluid Dynamics*, 8:2678, 1992.
- [108] S. B. Pope. A model for turbulent mixing based on shadow-position conditioning. *Phys. Fluids*, 25(11), 2013.
- [109] Z. Warhaft and J. Lumley. An experimental study of the decay of temperature fluctuations in grid-generated turbulence. *Journal of Fluid Mechanics*, 88(4):659–684, 1987.
- [110] J. Villiermaux and J. C. Devillion. Représentation de la coalescence et de la redispersion des domaines de ségrégation dans un fluide par un modèle d’interaction phénoménologique. *Proceedings of the Second International Symposium on Chemical Reaction Engineering*, pages 1–13, 1972.
- [111] S. B. Pope. Mapping closures for turbulent mixing and reaction. *Theor. Comput. Fluid Dyn.*, 2:255–270, 1991.
- [112] M. Mortensen and S. M. de Bruyn Kops. Conditional velocity statistics in the double scalar mixing layer - A mapping closure approach. *Combust. Theor. Model.*, 12:929–941, 2008.
- [113] A. Y. Klimenko and S. B. Pope. The modelling of turbulent reacting flows based on multiple mapping conditioning. *Phys. Fluids*, 15(7):1907–1925, 2003.

- [114] R. H. Kraichnan. Closures for probability distributions. *Bull. Amer. Phys. Soc.*, 34:2298, 1989.
- [115] S. S. Girimaji. A mapping closure for turbulent scalar mixing using a time-evolving reference field. *Phys. Fluids A*, 4:2875–2886, 1992.
- [116] L. Valiño and C. Dopazo. Multiscalar mapping closure for mixing in homogeneous turbulence. *Phys. Fluids A: Fluid Dynamics*, 7(144):144–152, 1995.
- [117] A. Y. Klimenko. Matching the conditional variance as a criterion for selecting parameters in the simplest multiple mapping conditioning models. *Phys. Fluids*, 16(12):4754–4757, 2004.
- [118] A. P. Wandel and A. Y. Klimenko. Testing multiple mapping conditioning mixing for Monte Carlo probability density function simulations. *Phys. Fluids*, 17(12):1–4, 2005.
- [119] A. Kronenburg and M. J. Cleary. Multiple mapping conditioning for flames with partial premixing. *Combust. Flame*, 155:215–231, 2008.
- [120] M. J. Cleary and A. Y. Klimenko. A Generalised Multiple Mapping Conditioning Approach for Turbulent Combustion. *Flow. Turbul. Combust.*, 82:477–491, 2009.
- [121] C. B. Devaud, I. Stankovic, and B. Merci. Deterministic Multiple Mapping Conditioning (MMC) applied to a turbulent flame in Large Eddy Simulation (LES). *Proc. Combust. Inst.*, 34(1):1213–1221, 2013.
- [122] M. J. Cleary and A. Y. Klimenko. Multiple Mapping Conditioning: A New Modelling Framework for Turbulent Combustion. In T. Echehki and E. Mastorakos, editors, *Turbulent Combustion Modeling: Advances, New Trends and Perspectives*, pages 143–173. Springer, 2011.
- [123] S. K. Ghai and S. De. Numerical modeling of turbulent premixed combustion using RANS based stochastic multiple mapping conditioning approach. *Proc. Combust. Inst.*, 2018.
- [124] S. Galindo-López, F. Salehi, M. J. Cleary, A. R. Masri, G. Neuber, O. T. Stein, A. Kronenburg, A. Varna, E. R. Hawkes, B. Sundaram, A. Y. Klimenko, and Y. Ge. A stochastic multiple mapping conditioning computational model in OpenFOAM for turbulent combustion. *Comput. Fluids*, 172:410–425, 2018.
- [125] S. Galindo-López. *Modelling of Mixed-mode Combustion using Multiple Mapping Conditioning*. PhD Thesis, School of Aerospace, Mechanical and Mechatronic Engineering, The University of Sydney, 2018.

- [126] A. Kronenburg and M. Kostka. Modeling extinction and reignition in turbulent flames. *Combust. Flame*, 143:342–356, 2005.
- [127] M. J. Cleary and A. Kronenburg. Multiple mapping conditioning. for extinction and reignition in turbulent diffusion flames. *Proc. Combust. Inst.*, 31:1497–1505, 2007.
- [128] M. J. Cleary and A. Kronenburg. ‘Hybrid’ multiple mapping conditioning on passive and reactive scalars. *Combust. Flame*, 51:623–638, 2007.
- [129] A. Y. Klimenko. Matching conditional moments in PDF modelling of non-premixed combustion. *Combust. Flame*, 143(4):369–385, 2005.
- [130] B. Sundaram, A. Y. Klimenko, M. J. Cleary, and Y. Ge. A direct approach to generalised multiple mapping conditioning for selected turbulent diffusion flame cases. *Combust. Theor. Model.*, 20(4):735–764, 2016.
- [131] A. Y. Klimenko. On simulating scalar transport by mixing between Lagrangian particles. *Phys. Fluids*, 19(3), 2007.
- [132] M. J. Cleary, A. Y. Klimenko, J. Janicka, and M. Pfitzner. A sparse-Lagrangian multiple mapping conditioning model for turbulent diffusion flames. *Proc. Combust. Inst.*, 32:1499–1507, 2009.
- [133] A. Y. Klimenko. Lagrangian particles with mixing. I. Simulating scalar transport. *Phys. Fluids*, 21(6), 2009.
- [134] A. Y. Klimenko. Lagrangian particles with mixing. II. Sparse-Lagrangian methods in application for turbulent reacting flows. *Phys. Fluids*, 21(6), 2009.
- [135] A. Y. Klimenko and M. J. Cleary. Convergence to a model in sparse-Lagrangian FDF simulations. *Flow Turbul. Combust.*, 85(3-4):567–591, 2010.
- [136] Y. Ge, M. J. Cleary, and A. Y. Klimenko. Sparse-Lagrangian FDF simulations of Sandia Flame E with density coupling. *Proc. Combust. Inst.*, 33:1401–1409, 2011.
- [137] Y. Ge, M. J. Cleary, and A. Y. Klimenko. A comparative study of Sandia flame series (D–F) using sparse-Lagrangian MMC modelling. *Proc. Combust. Inst.*, 34:1325–1332, 2013.
- [138] S. Vo, O. T. Stein, A. Kronenburg, and M. J. Cleary. Assessment of mixing time scales for a sparse particle method. *Combust. Flame*, 179:280–299, 2017.
- [139] S. Vo, A. Kronenburg, O. T. Stein, and M. J. Cleary. MMC-LES of a syngas mixing layer using a new mixing time scale model. *Combust. Flame*, 189:311–314, 2018.

- [140] N. Branley and W. P. Jones. Large Eddy Simulation of a Turbulent Non-premixed Flame. *Combust. Flame*, 127:1914–1934, 2001.
- [141] M. Muradoglu, S. B. Pope, and D. A. Caughey. The hybrid method for the PDF equations of turbulent reactive flows: Consistency conditions and correction algorithms. *J. Comput. Phys.*, 172(2):841–878, 2001.
- [142] M. Kraft. Modelling of particulate processes. *Kona*, 23:18–35, 2005.
- [143] P. Mitchell and M. Frenklach. Monte Carlo simulation of soot aggregation with simultaneous surface growth—why primary particles appear spherical. *Symp. (Int.) Combust.*, 27(1):1507–1514, 1998.
- [144] P. Mitchell and M. Frenklach. Particle aggregation with simultaneous surface growth. *Physical Review E*, 67:061407, 2003.
- [145] H. J. Schmid, S. Tejwani, C. Artelt, and W. Peukert. Monte Carlo simulation of aggregate morphology for simultaneous coagulation and sintering. *J. Nanoparticle Res.*, 6:613–626, 2004.
- [146] A. Gutsch, S. E. Pratsinis, and F. Löffler. Agglomerate structure and growth-rate by trajectory calculations of monomer-cluster collisions. *J. Aerosol Sci.*, 26(2):187–199, 1995.
- [147] M. Frenklach. Dynamics of discrete distribution for Smoluchowski coagulation model. *J. Colloid Interface Sci.*, 108(1):237–242, 1985.
- [148] E. R. Whitby and P. H. McMurry. Modal Aerosol Dynamics Modeling. *Aerosol Sci. Tech.*, 27(6):673–688, 1997.
- [149] M. Frenklach and S. J. Harris. Aerosol dynamics modeling using the method of moments. *J. Colloid Interface Sci.*, 118(1):252–261, 1987.
- [150] R. McGraw. Description of Aerosol Dynamics by the Quadrature Method of Moments. *Aerosol Sci. Tech.*, 27(2):255–265, 1997.
- [151] F. Gelbard and J. H. Seinfeld. Simulation of Multicomponent Aerosol Dynamics. *J. Colloid Interface Sci.*, 16(78):485–501, 1980.
- [152] M. B. Colket and R. J. Halle. Successes and Uncertainties in Modeling Soot Formation in Laminar, Premixed Flames. *Soot Formation in Combustion, Springer Series in Chemical Physics*, 59:442–470, 1994.
- [153] C. McEnally, A. Schaffer, M. Long, L. Pfefferle, M. Smooke, M. Colket, and R. Hall. Computational and experimental study of soot formation in a coflow, laminar ethylene diffusion flame. *Symp. (Int.) Combust.*, 27(1):1497–1505, 1998.

- [154] M. D. Smooke, C. S. McEnally, L. D. Pfefferle, R. J. Hall, and M. B. Colket. Computational and experimental study of soot formation in a coflow, laminar diffusion flame. *Combust. Flame*, 117(1–2):117–139, 1999.
- [155] M. D. Smooke, M. B. Long, B. C. Connelly, M. B. Colket, and R. J. Hall. Soot formation in laminar diffusion flames. *Combust. Flame*, 143(4):613–628, 2005.
- [156] A. Prakash, A. P. Bapat, and M. R. Zachariah. A simple numerical algorithm and software for solution of nucleation, surface growth, and coagulation problems. *Aerosol Sci. Technol.*, 37(11):892–898, 2003.
- [157] K. E. J. Lehtinen and M. R. Zachariah. Self-Preserving Theory for the Volume Distribution of Particles Undergoing Brownian Coagulation. *J. Colloid Interface Sci.*, 242(2):314–318, 2001.
- [158] R. Bleck. A fast, approximative method for integrating the stochastic coalescence equation. *J. Geophys. Res.*, 75(27):5165–5171, 1970.
- [159] P. Marchal, R. David, J. P. Klein, and J. Villiermaux. Crystallization and precipitation engineering—I. An efficient method for solving population balance in crystallization with agglomeration. *Chem. Eng. Sci.*, 43(1):59–67, 1988.
- [160] M. J. Hounslow, R. L. Ryall, and V. R. Marshall. A discretized population balance for nucleation, growth and aggregation. *AIChE J.*, 34(11):1821–1832, 1988.
- [161] S. Kumar and D. Ramkrishna. On the solution of population balance equations by discretization – I. A fixed pivot technique. *Chem. Eng. Sci.*, 51(8), 1996.
- [162] S. Kumar and D. Ramkrishna. On the solution of population balance equations by discretization—II. A moving pivot technique. *Chem. Eng. Sci.*, 51(8), 1996.
- [163] S. H. Park and S. N. Rogak. A novel fixed-sectional model for the formation and growth of aerosol agglomerates. *J. Aerosol Sci.*, 35(11):1385–1404, 2004.
- [164] R. P. Lindstedt and B. B. O. Waldheim. Modeling of soot particle size distributions in premixed stagnation flow flames. *Proc. Combust. Inst.*, 34(1):1861–1868, 2013.
- [165] J.-L. Consalvi, F. Liu, J. Contreras, M. Kashif, G. Legros, S. Shuai, and J. Wang. Numerical study of soot formation in laminar coflow diffusion flames of methane doped with primary reference fuels. *Combust. Flame*, 162(4):1153–1163, 2015.

- [166] Q. Zhang, H. Guo, F. Liu, G. J. Smallwood, and M. J. Thomson. Implementation of an advanced fixed sectional aerosol dynamics model with soot aggregate formation in a laminar methane/air coflow diffusion flame. *Combust. Theory Model.*, 12(4):621–641, 2008.
- [167] Q. Zhang, H. Guo, F. Liu, G. J. Smallwood, and M. J. Thomson. Modeling of soot aggregate formation and size distribution in a laminar ethylene/air coflow diffusion flame with detailed PAH chemistry and an advanced sectional aerosol dynamics model. *Proc. Combust. Inst.*, 32(1):761–768, 2009.
- [168] Q. Zhang, H. Guo, F. Liu, G. J. Smallwood, and M. J. Thomson. A numerical study of soot aggregate formation in a laminar coflow diffusion flame. *Combust. Flame*, 156(3):697–705, 2009.
- [169] F. Gelbard and J. H. Seinfeld. Numerical solution of the dynamic equation for particulate systems. *J. Comput. Phys.*, 28(3):357–375, 1978.
- [170] S. Rigopoulos and A. G. Jones. Finite-element scheme for solution of the dynamic population balance equation. *AIChE J.*, 49(5):1127–1139, 2003.
- [171] M. Nicmanis and M. J. Hounslow. Finite-element methods for steady-state population balance equations. *AIChE J.*, 44(10):2258–2272, 1998.
- [172] A. I. Roussos, A. H. Alexopoulos, and C. Kiparissides. Part III: Dynamic evolution of the particle size distribution in batch and continuous particulate processes: A Galerkin on finite elements approach. *Chem. Eng. Sci.*, 60(24):6998–7010, 2005.
- [173] A. Liu and S. Rigopoulos. A conservative method for numerical solution of the population balance equation, and application to soot formation. *Combust. Flame*, 205:506–521, 2019.
- [174] D. L. Ma, D. K. Tafti, and R. D. Braatz. High-Resolution Simulation of Multidimensional Crystal Growth. *Ind. Eng. Chem. Res.*, 41(25):6217–6223, 2002.
- [175] S. Qamar, M. P. Elsner, I. A. Angelov, G. Warnecke, and A. Seidel-Morgenstern. A comparative study of high resolution schemes for solving population balances in crystallization. *Comput. Chem. Eng.*, 30(6–7):1119–1131, 2006.
- [176] T. H. Tsang and J. R. Brock. Simulation of Condensation Aerosol Growth by Condensation and Evaporation. *Aerosol Sci. Tech.*, 2(3):311–320, 1983.
- [177] S. Kumar and D. Ramkrishna. On the solution of population balance equations by discretization—III. Nucleation, growth and aggregation of particles. *Chem. Eng. Sci.*, 52(24):4659–4679, 1997.

- [178] F. Sewerin and S. Rigopoulos. An explicit adaptive grid approach for the numerical solution of the population balance equation. *Chem. Eng. Sci.*, 168:250–270, 2017.
- [179] F. Sewerin and S. Rigopoulos. An LES-PBE-PDF approach for predicting the soot particle size distribution in turbulent flames. *Combust. Flame*, 189:62–76, 2018.
- [180] F. Sewerin and S. Rigopoulos. Algorithmic Aspects of the LES-PBE-PDF Method for Modeling Soot Particle Size Distributions in Turbulent Flames. *Combust. Sci. Technol.*, 191(5–6):766–796, 2019.
- [181] M. E. Mueller, G. Blanquart, and H. Pitsch. Hybrid method of moments for modeling soot formation and growth. *Combust. Flame*, 156(6):1143–1155, 2009.
- [182] J. I. Jeong and M. Choi. A sectional method for the analysis of growth of polydisperse non-spherical particles undergoing coagulation and coalescence. *J. Aerosol Sci.*, 32(5):565–582, 2001.
- [183] J. D. Landgrebe and S. E. Pratsinis. A discrete-sectional model for particulate production by gas-phase chemical reaction and aerosol coagulation in the free-molecular regime. *J. Colloid Interface Sci.*, 139 (1):63–86, 1990.
- [184] S.-M. Suh, M. R. Zachariah, and S. L. Girshick. Numerical modeling of silicon oxide particle formation and transport in a one-dimensional low-pressure chemical vapor deposition reactor. *J. Aerosol Sci.*, 33:943–959, 2002.
- [185] M. D. Allendorf, C. F. Melius, P. Ho, and M. R. Zachariah. Theoretical Study of the Thermochemistry of Molecules in the Si-O-H System. *J. Phys. Chem.*, 99:15285–15293, 1995.
- [186] M. R. Zachariah and W. Tsang. Theoretical Calculation of Thermochemistry, Energetics, and Kinetics of High-Temperature  $\text{Si}_x\text{H}_y\text{O}_z$ , Reactions. *J. Phys. Chem.*, 99:5308–5318, 1995.
- [187] V. I. Babushok, W. Tsang, D. R. Burgess, and M. R. Zachariah. Numerical study of low- and high-temperature silane combustion. *Twenty-Seventh Symposium (International) on Combustion*, 27(2):2431–2439, 1998.
- [188] A. Garmory and E. Mastorakos. Aerosol nucleation and growth in a turbulent jet using the Stochastic Fields method. *Chem. Eng. Sci.*, 63(16):4078–4089, 2008.
- [189] F. E. Kruijs and K. A. Kusters. The collision rate of particles in turbulent flow. *Chemical Engineering Communications*, 158(1):201–230, 1997.

- [190] R. W. Mei and K. C. Hu. On the collision rate of small particles in turbulent flows. *J. Fluid Mech.*, 391:67–89, 1999.
- [191] T. Thajudeen, R. Gopalakrishnan, and C. J. H. Jr. The Collision Rate of Nonspherical Particles and Aggregates for all Diffusive Knudsen Numbers. *Aerosol Sci. Technol.*, 46(11):1174–1186, 2012.
- [192] N. A. Fuch. *The Mechanics of Aerosols*. Pergamon Press, 1964.
- [193] C. J. Meyer and D. A. Deglon. Particle collision modeling - A review. *Minerals Engineering*, 24:719–730, 2011.
- [194] M. K. Wu and S. K. Friedlander. Enhanced power-law agglomerate growth in the free-molecule regime. *J. Aerosol Sci.*, 24:273–282, 1993.
- [195] S. Lindsay. *Introduction to Nanoscience*. Oxford University Press, 2009.
- [196] E. Cunningham. On the velocity of steady fall of spherical particles through fluid medium. *Proc. Roy. Soc.*, 83:357–365, 1910.
- [197] B. F. Magnussen and B. H. Hjertager. On mathematical modeling of turbulent combustion with special emphasis on soot formation and combustion. *Symp. (Int.) Combust.*, 16(1):719–729, 1977.
- [198] B. F. Magnussen, B. H. Hjertager, J. G. Olsen, and D. Bhaduri. Effects of turbulent structure and local concentrations on soot formation and combustion in  $C_2H_2$  diffusion flames. *Symp. (Int.) Combust.*, 17(1):1383–1393, 1979.
- [199] K. J. Syed, C. D. Stewart, and J. B. Moss. Modelling soot formation and thermal radiation in buoyant turbulent diffusion flames. *Symp. (Int.) Combust.*, 23(1):1533–1541, 1991.
- [200] S. J. Brookes and J. B. Moss. Predictions of soot and thermal radiation properties in confined turbulent jet diffusion flames. *Combust. Flame*, 116:486–503, 1999.
- [201] D. Aubagnac-Karkar, A. E. Bakali, and P. Desgroux. Soot particles inception and PAH condensation modelling applied in a soot model utilizing a sectional method. *Combust. Flame*, 189:190–206, 2018.
- [202] M. Fairweather, W. P. Jones, H. S. Ledin, and R. P. Lindstedt. Predictions of soot formation in turbulent, non-premixed propane flames. *Symp. (Int.) Combust.*, 24(1):1067–1074, 1992.
- [203] W. Kollmann, I. M. Kennedy, M. Metternich, and J.-Y. Chen. Application of a Soot Model to a Turbulent Ethylene Diffusion Flame. *Soot Formation in Combustion*, 59:503–526, 1994.

- [204] G. Y. di Veroli and S. Rigopoulos. Modeling of aerosol formation in a turbulent jet with the transported population balance equation-probability density function approach. *Phys. Fluids*, 23:043305, 2011.
- [205] M. A. Schiener and R. P. Lindstedt. Joint-scalar transported PDF modelling of soot in a turbulent non-premixed natural gas flame. *Combust. Theory Model.*, 22(6):1134–1175, 2018.
- [206] M. A. Schiener and R. P. Lindstedt. Transported probability density function based modelling of soot particle size distributions in non-premixed turbulent jet flames. *Proc. Combust. Inst.*, 37(1):1049–1056, 2019.
- [207] N. H. Qamar, Z. T. Alwahabi, Q. N. Chan, G. J. Nathan, D. Roekaerts, and K. D. King. Soot volume fraction in a piloted turbulent jet non-premixed flame of natural gas. *Combust. Flame*, 156:1339–1347, 2009.
- [208] M. E. Mueller and H. Pitsch. Large eddy simulation subfilter modeling of soot-turbulence interactions. *Phys. Fluids*, 23(11):115104, 2011.
- [209] K. M. Leung, R. P. Lindstedt, and W. P. Jones. A simplified reaction mechanism for soot formation in nonpremixed flames. *Combust. Flame*, 87(3–4):289–305, 1991.
- [210] G. Wang and S. C. Garrick. Modeling and simulation of titania formation and growth in temporal mixing layers. *J. Aerosol Sci.*, 37:431–451, 2006.
- [211] H. Jasak. *Error Analysis and Estimation for the Finite Volume Method with Applications to Fluid Flows*. PhD Thesis, Imperial College London, 1996.
- [212] H. G. Weller, G. Tabor, H. Jasak, and C. Fureby. A tensorial approach to computational continuum mechanics using object-oriented techniques. *Comput. Phys.*, 12:620, 1998.
- [213] Y. Wang, P. Chatterjee, and J. L. de Ris. Large eddy simulation of fire plumes. *Proc. Combust. Inst.*, 33(2):2473–2480, 2011.
- [214] M. Chapuis, C. Fureby, E. Fedina, N. Alin, and J. Tegner. LES modeling of combustion applications using OpenFOAM. *5th European Conference on Computational Fluid Dynamics*, pages 1–20, 2010.
- [215] G. D’Errico, T. Lucchini, F. Contino, M. Jangi, and X.-S. Bai. Comparison of well-mixed and multiple representative interactive flamelet approaches for diesel spray combustion modelling. *Combust. Theor. Model.*, 18:65–88, 2014.
- [216] H. I. Kassem, K. M. Saqr, H. S. Aly, M. M. Sies, and M. A. Wahid. Implementation of the eddy dissipation model of turbulent non-premixed combustion in OpenFOAM. *Int. Commun. Heat Mass*, 38(3):363–367, 2011.

- [217] M. Hassanaly, H. Koo, C. F. Lietz, S. T. Chong, and V. Raman. A minimally-dissipative low-Mach number solver for complex reacting flows in OpenFOAM. *Comput. Fluids*, 162:11–25, 2018.
- [218] S. Meares and A. R. Masri. A modified piloted burner for stabilizing turbulent flames of inhomogeneous mixtures. *Combust. Flame*, 161(2):484–495, 2014.
- [219] S. Galindo-López, F. Salehi, M. J. Cleary, and A. R. Masri. MMC-LES simulations of turbulent piloted flames with varying levels of inlet inhomogeneities. *Proc. Combust. Inst.*, 36:1759–1766, 2017.
- [220] A. Varna, M. J. Cleary, and E. R. Hawkes. A multiple mapping conditioning mixing model with a mixture-fraction like reference variable. Part 2: RANS implementation and validation against a turbulent jet flame. *Combust. Flame*, 181:354–364, 2017.
- [221] R. S. Barlow and J. H. Frank. Effect of turbulence on species mass fractions in methane/air jet flames. *Proc. Combust. Inst.*, 27:1087–1095, 1998.
- [222] C. Straub, A. Kronenburg, O. T. Stein, G. Kuenne, J. Janicka, R. S. Barlow, and D. Geyer. Multiple mapping conditioning coupled with an artificially thickened flame model for turbulent premixed combustion. *Combust. Flame*, 196:325–336, 2018.
- [223] C. Straub, A. Kronenburg, O. T. Stein, R. S. Barlow, and D. Geyer. Modeling stratified flames with and without shear using multiple mapping conditioning. *Proc. Combust. Inst.*, 37:2317–2324, 2019.
- [224] M. Sontheimer, A. Kronenburg, and O. T. Stein. Two-phase coupling for MMC-LES of spray combustion. *Proc. Comb. Inst.*, 38(2):3361–3369, 2021.
- [225] L. Zhao, M. J. Cleary, O. T. Stein, and A. Kronenburg. A two-phase MMC-LES model for pyrolysing solid particles in a turbulent flame. *Combust. Flame*, 209:322–336, 2019.
- [226] V. Raman, H. Pitsch, and R. O. Fox. Hybrid large-eddy simulation/Lagrangian filtered density function approach for simulating turbulent combustion. *Combust. Flame*, 143:56–78, 2005.
- [227] V. Raman and H. Pitsch. A consistent LES/filtered-density function formulation for the simulation of turbulent flames with detailed chemistry. *Proc. Combust. Inst.*, 31(2):1711–1719, 2007.
- [228] J. J. Monaghan. Smoothed particle hydrodynamics. *Rep. Prog. Phys.*, 68(8):1703, 2005.

- [229] J. L. Bentley. Multidimensional binary search trees used for associative searching. *Commun. ACM*, 18(9):509–517, 1975.
- [230] J. H. Friedman, J. L. Bentley, and R. A. Finkel. An Algorithm for Finding Best Matches in Logarithmic Expected Time. *ACM Trans. Math. Softw.*, 3(3):209–226, 1977.
- [231] X. Wu and P. Moin. A direct numerical simulation study on the mean velocity characteristics in turbulent pipe flow. *J. Fluid Mech.*, 608:81–112, 2008.
- [232] J. Holgate, A. Skillen, T. Craft, and A. Revell. A Review of Embedded Large Eddy Simulation for Internal Flows. *Arch. Computat. Methods. Eng.*, 26:865–882, 2018.
- [233] F. Fuest, R. S. Barlow, D. Geyer, F. Seffrin, and A. Dreizler. A hybrid method for data evaluation in 1-D Raman spectroscopy. *Proc. Combust. Inst.*, 33(1):815–822, 2011.
- [234] F. Fuest, R. S. Barlow, J.-Y. Chen, and A. Dreizler. Raman/Rayleigh scattering and CO-LIF measurements in laminar and turbulent jet flames of dimethyl ether. *Combust. Flame*, 159(8):2533–2562, 2012.
- [235] International Workshop on Measurement and Computation of Turbulent Nonpremixed Flames (TNF). Sandia. available at <http://www.sandia.gov/TNF>, 26th November 2015.
- [236] J. H. Ferziger and M. Perić. *Computational Methods for Fluid Dynamics*. Springer, Berlin, Heidelberg, 2002.
- [237] F. M. White. *Viscous Fluid Flow*. McGraw-Hill, 3rd edition, 2006.
- [238] G. Neuber, Y. Gao, A. Kronenburg, O. T. Stein, and M. J. Cleary. LES-MMC modeling of a partially-premixed turbulent dimethyl ether/air jet flame. In *Proc. of the Australian Combust. Symposium*, Melbourne, Australia, 7. – 9. Dec. 2015.
- [239] G. Neuber, J. Kirchmann, O. T. Stein, A. Kronenburg, and M. J. Cleary. Sparse-Lagrangian MMC modelling of a partially-premixed DME/air flame series. In *11th International ERCOFTAC Symposium on Engineering Turbulence Modelling and Measurements*, Palermo, Italy, 21. – 23. Sep. 2016.
- [240] G. Neuber, A. Kronenburg, O. T. Stein, M. J. Cleary, B. Coriton, and J. H. Frank. Sparse-Lagrangian MMC modelling of the Sandia DME (D-F) jet flames. In *36th Internat. Combust. Symp*, Seoul, Korea, 31. July – 5. August 2016.

- [241] S. Yuan, Z. Zhang, Y. Fan, and X. Zhang. Thermodynamic analysis of droplet nucleation causing liquid-phase precipitation in air-hydrocarbon mixture gas. *Chin. J. Process Eng.*, 21(1):116–124, 2021.
- [242] F. Jia, Z. Y. Li, and D. Y. H. Pui. A detailed numerical study on the evolution of droplet size distribution of dibutyl phthalate in a laminar flow diffusion chamber. *Korean J. Chem. Eng.*, 37(12):423–433, 2020.
- [243] E. D. Tornaiainen, A. K. Hinz, and F. C. Gouldin. Tomographic analysis of unsteady, reacting flows: Numerical investigation. *AIAA Journal*, 36:1270–1278, 1998.
- [244] J. Floyd and A. M. Kempf. Computed Tomography of Chemiluminescence (CTC): High Resolution and Instantaneous 3D Measurements of a Matrix Burner. *Proc. Combust. Inst.*, 33:751–758, 2011.
- [245] B. C. Connelly, B. A. V. Bennett, M. D. Smooke, and M. B. Long. A paradigm shift in the interaction of experiments and computations in combustion research. *Proc. Combust. Inst.*, 32(1):879–886, 2009.
- [246] K. P. Chatelain, Y. He, R. Alharbi, R. Mével, E. L. Petersen, and D. A. Lacoste. Current status of the high-temperature kinetic models of silane: Part I. Pyrolysis. *Combust. Flame*, 227:526–537, 2021.
- [247] K. P. Chatelain, Y. He, R. Alharbi, R. Mével, E. L. Petersen, and D. A. Lacoste. Current status of the high-temperature kinetic models of silane: Part II. Oxidation. *Combust. Flame*, 227:538–549, 2021.
- [248] S. B. Pope. Computationally efficient implementation of combustion chemistry using in situ adaptive tabulation. *Combust. Theory Model.*, 1:41–63, 1997.
- [249] L. Liang, J. G. Stevens, and J. T. Farrell. A dynamic adaptive chemistry scheme for reactive flow computations. *Proc. Comb. Inst.*, 32(1):527–534, 2009.
- [250] Z. Huo, S. Galindo-López, M. J. Cleary, and A. R. Masri. On the validation of the TDAC method for a stochastic turbulent combustion model in OpenFOAM. *12th Asia-Pacific Conference on Combustion*, 2019.
- [251] R. McDermott and S. B. Pope. A particle formulation for treating differential diffusion in filtered density function methods. *J. Comput. Phys.*, 226:947–993, 2007.
- [252] J. You, Y. Yang, and S. B. Pope. Effects of molecular transport in LES/PDF of piloted turbulent dimethyl ether/air jet flames. *Combust. Flame*, 176:451–461, 2017.

- 
- [253] L. Dialameh, M. J. Cleary, and A. Y. Klimenko. A multiple mapping conditioning model for differential diffusion. *Phys. Fluids*, 26(2), 2014.
- [254] T. Yang, H. Zhou, and Z. Ren. A particle mass-based implementation for mixing models with differential diffusion. *Combust. Flame*, 214:116–120, 2020.
- [255] H. Zhou, T. Yang, and Z. Ren. Differential Diffusion Modeling in LES/FDF Simulations of Turbulent Flames. *AIAA Journal*, 57:8, 2019.
- [256] M. Grader, C. Eberle, P. Gerlinger, and M. Aigner. LES of a Pressurized, Sooting Aero-Engine Model Combustor at Different Equivalence Ratios With a Sectional Approach for PAHs and Soot. *Proc. ASME Turbo Expo 2018, Power for Land, Sea and Air*, 11.-15.06.2018, Oslo, Norway, 2018.



# Appendix A

## Silane combustion reaction mechanism

```
!-----  
! SIH4 MECHANISM  
!  
! The complete mechanism is based on following publications:  
!  
! M. D. Allendorf, C. F. Melius, P. Ho, and M. R. Zachariah. Theoretical  
! Study of the Thermochemistry of Molecules in the Si-O-H System.  
! J. Phys. Chem., 99:15285-15293, 1995.  
!  
! M. R. Zachariah and W. Tsang. Theoretical Calculation of  
! Thermochemistry, Energetics, and Kinetics of High-Temperature SixHyOz,  
! Reactions. J. Phys. Chem, 99:5308-5318, 1995.  
!  
! V. I. Babushok, W. Tsang, D. R. Burgess, and M. R. Zachariah. Numerical  
! study of low- and high-temperature silane combustion. Twenty-Seventh  
! Symposium (International) on Combustion, 27(2):2431-2439, 1998.  
!  
! S.-M. Suh, M. R. Zachariah, and S. L. Girshick. Modeling particle  
! formation during low-pressure silane oxidation: Detailed chemical  
! kinetics and aerosol dynamics. J. Vac. Sci. Technol. A,  
! 19:940-951, 2001.  
!  
! S.-M. Suh, M. R. Zachariah, and S. L. Girshick. Numerical modeling of  
! silicon oxide particle formation and transport in a one-dimensional  
! lowpressure chemical vapor deposition reactor.  
! J. Aerosol Sci., 33:943-959, 2002.  
!  
!-----
```

```
ELEMENTS  
AR SI H O N  
END
```

## SPECIES

N2 O2 H2 H2O OH H O H02 H2O2 AR  
 SIH4 SIH3 SIH2 SIH SI SI2 SI3 SI2H2 SI2H3 SI2H5 SI2H6 SI2H4  
 H3SI2H SI3H8 SI3H7 SIH0 SIH20 SIH20-2 SIH30  
 HSI00H HSI00H-2 SI00H SIH30H H2SI0H HSI0H SIH302H SIH302 SI2H  
 SI0 SI0-2 SI0-3 SI0-4 SI0-5 SI0-6 SI0-7 SI0-8 SI0-9 SI0-10  
 SI0-11 SI0-12 SI02 SI02-2 SI02-3 SI02-4 SI02-5 SI02-6 SI02-7  
 SI02-8 SI02-9 SI02-10 SI02-11 SI02-12 SI02-S  
 END

## REACTIONS

! --- H2/O2 system: combination, decomposition  
 H + H + M = H2 + M 1.00E18 -1.00 0.0  
           H2/0/ H20/0/  
 H + H + H2 = 2H2 9.20E16 -0.60 0.0  
 H + H + H2O = H2 + H2O 6.00E19 -1.25 0.0  
 2O + M = O2 + M 1.20E17 -1.00 0.0  
 H2/2.40/ H20/15.40/ AR/0.83/ SIH4/2.00/ SI0/1.75/ SI02/3.60/ SI2H6/3.00/  
 H + OH + M = H2O + M 2.20E22 -2.00 0.0  
 H2/0.73/ H20/3.65/ AR/0.83/ SIH4/2.00/ SI2H6/3.00/  
 O + H + M = OH + M 5.00E17 -1.00 0.0  
 H2/2.00/ H20/6.00/ AR/0.7/ SIH4/2.00/ SI0/1.50/ SI02/2.00/ SI2H6/3.00/  
  
 ! --- H2/O2 system: atom transfers  
 O + OH = O2 + H 4.00E14 -0.50 0.0  
 O + H2 = OH + H 5.06E04 2.67 6290.0  
 2OH = O + H2O 1.50E09 1.14 99.0  
 H2 + O2 = 2OH 1.70E13 0.00 47780.0  
 OH + H2 = H2O + H 1.17E09 1.30 3626.0  
  
 ! --- H2/O2 system: Peroxyl and peroxide  
 H + O2 + M = H02 + M 3.61E17 -0.72 0.0  
 H20/18.6/ H2/2.9/ N2/1.3/ SI02/4.2/ SI0/2.1/  
 H + H02 = H2 + O2 1.25E13 0.00 0.0  
 O + H02 = O2 + OH 1.40E13 0.00 1073.0  
 OH + H02 = O2 + H2O 2.90E13 0.00 -500.0  
  
 2OH (+M) = H2O2 (+M) 7.40E13 -0.37 0.0  
           LOW / 2.300E+18 -0.900 -1700.00/  
           TROE/ 0.7346 94.00 1756.00 5182.00 /  
 H2/2.00/ H20/6.00/ AR/0.7/ SIH4/2.00/ SI0/1.50/ SI02/2.00/ SI2H6/3.00/  
  
 H + H02 = 2OH 1.69E14 0.00 874.0  
 H02 + H = H2O + O 3.01E13 0.00 1721.0  
 2H02 = O2 + H2O2 1.30E11 0.00 -1630.0  
 DUPLICATE  
 2H02 = O2 + H2O2 4.20E14 0.00 12000.0  
 DUPLICATE  
 H2O2 + H = H2O + OH 1.00E13 0.00 3590.0  
 H2O2 + H = H2 + H02 4.79E13 0.00 7950.0

H2O2 + OH = H2O + HO2	1.00E13	0.00	1800.0
H2O2 + O = OH + HO2	9.63E06	2.00	4000.0
! --- SI - H - O reactions			
! --- decomposition, recombination, association			
SIH2 (+M) = SI + H2 + M	9.90E20	-1.76	38240.0
SIH4 (+M) = SIH2 + H2 (+M)	3.12E09	1.70	54710.0
LOW /5.21E30 -3.54 57550.0/			
TROE /-0.4984 888.3 209.4 2760./			
SIH4/4./ SI2H6/4./			
SI2H6 (+M) = SIH4 + SIH2 (+M)	1.81E10	1.70	50203.0
LOW/5.09E53 -10.37 56034.0/			
TROE/4.375E-5 438.5 2726. 438.2/			
SIH4/4./ SI2H6/4./			
SI2H6 (+ M) = H3SI2H + H2 (+M)	9.09E09	1.80	54197.0
LOW/1.94E44 -7.77 59023.0/			
TROE/-0.1224 793.3 2400. 11.39/			
SIH4/4./ SI2H6/4./			
H3SI2H (+M) = SI2H4 (+M)	2.54E13	-0.20	5381.0
LOW/1.1E33 -5.76 9152./			
TROE/-0.4202 214.5 103. 136.3/			
SIH4/4./ SI2H6/4./			
SI2H4 = SIH2 + SIH2	1.00E16	0.00	59000.0
SI2H4 = SI2H2 + H2	3.00E16	0.00	34990.0
SI3H8 (+M) = SIH2 + SI2H6 (+M)	6.97E12	1.00	52677.0
LOW/1.73E69 -15.07 60491.0/			
TROE/-3.47E-5 442. 2412. 128.3/			
SIH4/4./ SI2H6/4./			
SI3H8 (+M) = H3SI2H + SIH4 (+M)	3.73E12	1.00	50850.0
LOW/4.36E76 -17.26 59303.0/			
TROE/0.4157 365.3 3102. 9.72/			
SIH4/4./ SI2H6/4./			
! --- H atom reactions			
SIH4 + H = SIH3 + H2	1.50E13	0.00	2500.0
SIH2 + H = SIH + H2	1.39E13	0.00	2000.0
SIH2 + H = SIH3	3.81E13	0.00	2000.0
SI2H2 + H = SI2H3	8.63E14	0.00	2000.0
SIH2O + H = SIHO + H2	5.40E11	0.58	7230.0
SIH2O + H = H2SIOH	6.50E24	-3.60	8230.0
SIH3OH + H = H2SIOH + H2	1.74E08	1.77	1430.0
SIH3OH + H = SIH3O + H2	2.20E07	1.89	8880.0
SIH3O + H = SIH2O + H2	1.58E18	-1.37	1400.0
SIH3O + H = HSIOH + H2	1.63E18	-1.33	1360.0
SIH3O + H = SIH2 + H2O	9.56E13	-0.34	500.0
SIH3O + H = SIH3OH	1.23E12	0.52	160.0
HSIOOH + H = SIOOH + H2	9.86E07	1.83	1510.0
SIO2 + H = SIOOH	8.50E24	-4.00	5660.0
SIHO + H = SIO + H2	2.00E14	0.00	0.0

SI00H + H = SI02 + H2	1.00E13	0.00	5000.0
H2SI0H + H = SIH20 + H2	3.31E20	-2.04	3540.0
H2SI0H + H = HSI0H + H2	6.16E20	-1.98	3600.0
H2SI0H + H = SIH2 + H20	2.24E15	-0.65	4190.0
SI2H6 + H = H2 + SI2H5	6.98E13	0.00	2635.0
SIH3 + H = SIH2 + H2	1.50E13	0.00	2500.0
SIH302H + H = SIH302 + H2	4.80E13	0.00	7950.0
SIH302 + H = SIH30 + OH	1.00E13	0.00	0.0
SI2 + H = SIH + SI	5.15E13	0.00	5300.0
SI2H2 + H = SI2H + H2	1.50E14	0.00	0.0
SI2H + H = SI2 + H2	1.50E14	0.00	0.0
SI2H4 + H = SI2H5	1.00E13	0.00	0.0
SI3H8 + H = H2 + SI3H7	1.00E14	0.00	1000.0
! --- 0 atom reactions			
SIH4 + 0 = SIH3 + OH	2.00E13	0.00	2762.0
SIH3 + 0 = SIH20 + H	1.30E14	0.00	2000.0
SIH + 0 = SI0 + H	4.00E13	0.00	0.0
SI2H + 0 = SI0 + SI	1.00E13	0.00	2000.0
SI0 + 0 + M = SI02 + M	2.50E15	0.00	4370.0
SIH20 + 0 = SIH0 + OH	1.80E13	0.00	3080.0
SIH0 + 0 = SI0 + OH	1.00E14	0.00	0.0
SIH30H + 0 = H2SI0H + OH	1.70E12	0.00	1730.0
SI2H6 + 0 = OH + SI2H5	1.70E13	0.00	2500.0
SI2H4 + 0 = SIH3 + SIH0	1.00E13	0.00	1500.0
SIH2 + 0 = SI0 + H2	5.00E13	0.00	0.0
! --- OH radical reactions			
SI0 + OH = SI02 + H	1.80E10	0.78	1220.0
SI0 + OH = SI00H	2.10E23	-3.60	1900.0
SIH20 + OH = SIH0 + H20	7.50E12	0.00	170.0
SIH30H + OH = H2SI0H + H20	4.00E12	0.00	1500.0
SIH4 + OH = SIH3 + H20	8.70E12	0.00	95.0
SIH3 + OH = SIH20 + H2	5.00E12	0.00	0.0
SI + OH = SI0 + H	2.00E14	0.00	0.0
SIH0 + OH = SI0 + H20	1.00E14	0.00	0.0
OH + SIH2 = SIH20 + H	1.00E13	0.00	0.0
OH + SI2H6 = SI2H5 + H20	5.00E12	0.00	0.0
OH + SI2H5 = SI2H4 + H20	2.00E13	0.00	0.0
OH + SI2H = SIH2 + SI0	1.00E13	0.00	0.0
! --- H02 radical reactions			
SIH4 + H02 = SIH3 + H202	1.00E13	0.00	14000.0
SIH20 + H02 = HSI00H + OH	1.00E11	0.00	7000.0
SIH20 + H02 = SIH0 + H202	1.00E12	0.00	12000.0
SIH30H + H02 = H2SI0H + H202	6.30E12	0.00	14000.0
SIH302 + H02 = SIH302H + O2	1.00E12	0.00	0.0
H02 + SIH3 = SIH30 + OH	1.00E13	0.00	0.0
H02 + SIH2 = SIH20 + OH	1.00E13	0.00	0.0
SIH30 + H02 = SIH20 + H202	1.00E12	0.00	0.0

## ! --- SIH3 radical reactions

SIH4 + SIH3 = SI2H5 + H2	1.77E12	0.00	4400.0
SIH3 + SIH3 = SIH2 + SIH4	1.80E13	0.00	0.0
SIH3 + SIH3 = SI2H6	4.75E13	0.00	0.0
SIH3 + SIH2 = SI2H5	6.58E12	0.00	2000.0
SI2H5 + SIH3 = SI3H8	3.31E13	0.00	0.0
SIH3OH + SIH3 = H2SIOH + SIH4	1.80E11	0.00	7400.0
SIH3 + O2 = HSI0OH + H	0.80E12	0.00	-760.0
SIH3 + O2 = SIO + H2O + H	0.40E12	0.00	-760.0
SIH3 + O2 = SIH2O + OH	0.60E12	0.00	-760.0
SIH3 + O2 = SIOOH + H + H	0.20E12	0.00	-760.0
SIH3 + O2 + M = SIH3O2 + M	1.00E14	0.00	0.0
SIH3 + SI2H4 = SI3H7	1.00E13	0.00	0.0
SIH3 + SI2H6 = SIH4 + SI2H5	1.00E13	0.00	5000.0
SIH3 + SIH0 = SIH4 + SIO	1.00E13	0.00	0.0
SIH3 + SIH20 = SIH4 + SIH0	4.00E12	0.00	4000.0

## ! --- SIH2 radical reactions

SIH2 + H2O = SIH3OH	2.80E31	-6.37	16140.0
SIH2 + O2 = SIH0 + OH	1.00E14	0.00	3700.0
SIH2 + H2O = SIH2O + H2	3.84E10	-0.61	9720.0
SIH2 + H2O = HSI0H + H2	2.15E10	0.73	9820.0
SIH2 + SI = SI2H2	7.24E12	0.00	2000.0
SIH2 + SI = SI2H + H	1.50E14	0.00	0.0
SIH2 + SI = SI2 + H2	1.50E14	0.00	0.0
SIH2 + SIH = SI2H3	1.26E13	0.00	2000.0
SIH2 + SIH2 = SI2H2 + H2	6.50E14	0.00	0.0
H3SI2H + H2 = SIH2 + SIH4	9.41E13	0.00	4092.3
H3SI2H + SIH4 = SIH2 + SI2H6	1.73E14	0.40	8898.7
SI2 + SIH2 = SI3 + H2	3.55E11	0.00	2000.0
SI3 + SIH2 = SI2 + SI2H2	1.43E11	0.00	16200.0
SIH2 + SIH3O2 = SIH2O + SIH3O	1.00E13	0.00	0.0

## ! --- SIH radical reactions

SIH3 (+M) = SIH + H2 (+M)	4.48E14	-0.55	44690.0
LOW /1.98E26 -3.05 44690./			
SIH4 + SIH = SI2H3 + H2	1.45E12	0.00	2000.0
SIH4 + SIH = SI2H5	1.43E13	0.00	2000.0
SIH4 + SIH = SIH3 + SIH2	1.38E12	0.00	11200.0
SIH + O2 = SIO + OH	1.02E14	0.00	0.0
SIH + H2O = SIH2O + H	3.00E12	0.00	3000.0
SIH + SIH2O = SIH2 + SIH0	1.00E13	0.00	8000.0

## ! --- SI atom reactions

SI3 + SI = SI2 + SI2	2.06E12	0.00	24100.0
SI + SIH4 = SI2H2 + H2	1.50E14	0.00	7290.0
SI + SI + M = SI2 + M	2.47E16	0.00	1180.0
SI + SI2 + M = SI3 + M	2.60E16	0.00	1200.0
SI + O2 = SIO + O	2.00E13	0.00	0.0

SI + H2O	= SIH0 + H	5.00E12	0.00	7000.0
SI + SI2H6	= SIH2 + H3SI2H	1.30E15	0.00	12600.0
SI + H2	= SIH + H	4.00E14	0.00	35990.0
! --- SIH4 reactions				
SIH4 + O2	= SIH3 + H02	7.60E13	0.00	44000.0
SIH4 + O2	= SIH20 + H20	7.60E13	0.00	44000.0
SIH4	= SIH3 + H	3.91E15	0.00	89356.0
! --- SIO reactions				
SIO + M	= SI + O + M	1.00E13	0.00	189000.0
SIO + O2	= SIO2 + O	5.00E12	0.00	30000.0
! --- SIO2 reactions				
SIO2 + M	= SI + O2 + M	1.00E16	0.00	182000.0
! --- SIH0 reactions				
SIH0 + M	= H + SIO + M	5.00E14	0.00	29000.0
SIH0 + O2	= SIO + H02	1.20E14	0.00	3975.0
SIH30 + SIH0	= SIH30H + SIO	1.00E12	0.00	0.0
SIH0 + SIH30H	= SIH20 + H2SIOH	5.00E12	0.00	12000.0
! --- HSI0H reactions				
HSIOH	= SIO + H2	9.40E28	-3.80	38550.0
! --- H2SIOH reactions				
H2SIOH + O2	= HSI00H + OH	1.00E13	0.00	7000.0
H2SIOH	= SIH0 + H2	9.60E27	-3.40	59820.0
H2SIOH + SIH3	= SIH4 + SIH20	2.00E12	0.00	0.0
H2SIOH + SIH2	= SIH20 + SIH3	1.00E12	0.00	0.0
H2SIOH + O	= SIH20 + OH	1.00E13	0.00	0.0
H2SIOH + OH	= SIH20 + H20	1.00E13	0.00	0.0
H2SIOH + H02	= SIH20 + H202	1.00E13	0.00	0.0
! --- SIH30 reactions				
SIH20 + SIH30	= SIH0 + SIH30H	1.20E11	0.00	971.0
SIH4 + SIH30	= SIH3 + SIH30H	2.00E11	0.00	5300.0
SIH30 + O2	= SIH20 + H02	1.00E12	0.00	4500.0
SIH30H + SIH30	= H2SIOH + SIH30H	1.50E12	0.00	5300.0
SIH30	= H2SIOH	1.50E24	-2.60	15420.0
SIH30 + O	= SIH20 + OH	5.00E12	0.00	0.0
SIH30 + OH	= SIH20 + H20	1.00E13	0.00	0.0
SIH30 + SIO	= SIO2 + SIH3	1.00E13	0.00	17000.0
! --- SIH302 reactions				
SIH302	= SIH20 + OH	8.60E14	0.00	40000.0
SIH4 + SIH302	= SIH3 + SIH302H	1.10E13	0.00	18500.0
SIH302 + SIH20	= SIH302H + SIH0	1.30E11	0.00	6800.0
SIH30H + SIH302	= H2SIOH + SIH302H	6.30E12	0.00	14500.0
SIH302 + O	= SIH30 + O2	1.00E13	0.00	0.0

SIH302 + OH	=	SIH30H + O2	1.00E13	0.00	0.0
SIH302 + SIH3	=	SIH30 + SIH30	1.00E13	0.00	0.0
! --- SIH302H reactions					
SIH302H	=	SIH30 + OH	6.50E14	0.00	48700.0
SIH302H + H	=	SIH30 + H2O	1.00E12	0.00	0.0
SIH302H + OH	=	SIH302 + H2O	5.00E12	0.00	0.0
SIH302H + O	=	SIH30 + HO2	1.00E13	0.00	2000.0
SIH302H + SIH3	=	SIH30H + SIH30	3.00E12	0.00	2000.0
SIH302H + SIH2	=	SIH30 + H2SIOH	5.00E12	0.00	4000.0
! --- HSI00H reactions					
HSI00H	=	SIOOH + H	5.00E14	0.00	90000.0
HSI00H	=	SIO + H2O	2.64E35	-6.70	79158.0
HSI00H	=	SIO2 + H2	1.00E10	0.00	54000.0
SIOOH + HO2	=	HSI00H + O2	1.00E13	0.00	0.0
HSI00H + OH	=	SIOOH + H2O	3.00E12	0.00	2000.0
HSI00H + O	=	SIOOH + OH	3.00E12	0.00	2000.0
HSI00H + SIH3	=	SIOOH + SIH4	3.00E12	0.00	9000.0
HSI00H + SIH2	=	SIOOH + SIH3	3.00E12	0.00	20000.0
! --- SIOOH reactions					
SIOOH + O2	=	SIO2 + HO2	1.00E13	0.00	14300.0
SIOOH + M	=	SIO + OH + M	1.00E16	0.00	61000.0
! --- SIH20 reactions					
SIH20	=	SIO + H2	1.00E12	0.00	60800.0
SIH20 + H2O	=	HSI00H + H2	3.60E09	0.43	7690.0
SIH20 + M	=	SI + H2O + M	1.00E16	0.00	77500.0
SIH20 + M	=	SIHO + H + M	5.00E16	0.00	76600.0
SIH20 + O2	=	SIHO + HO2	4.00E14	0.00	35500.0
! --- SIH30H reactions					
SIH30H	=	SIH20 + H2	2.01E27	-4.30	68160.0
SIH30H	=	HSIOH + H2	2.20E26	-4.20	66570.0
SIH30H + O2	=	H2SIOH + HO2	4.00E13	0.00	45000.0
! --- SI2 reactions					
SI2 + H2	=	SIH + SIH	1.54E13	0.00	40000.0
SI2 + H2	=	SI2H2	1.54E13	0.00	2000.0
! --- H3SI2H reactions					
H3SI2H (+M)	=	SI + SIH4 (+M)	1.42E13	0.54	57548.0
		LOW/2.35E42 -7.42 60957./			
		TROE/0.5336 629.2 2190. 626.5/ SIH4/4./ SI2H6/4./			
! --- SI2H3 reactions					
SI2H5	=	SI2H3 + H2	3.16E14	0.00	53000.0
! --- Si2H2 reactions					

---

```

SI2H2 + H2O = SIH2O + SIH2          1.00E10    0.00    10000.0
SI2H2 + H2O = SI0   + SIH4          1.00E09    0.00    10000.0

! --- SIH2O-2 reactions
SIH2O-2 = SIH2O + SIH2O            3.60E25   -6.80    11230.0

! --- HSI00H-2 reactions
HSI00H-2 = HSI00H + HSI00H        1.70E25   -9.60    12300.0

! --- SI3 reactions
SI3 + H2 = SI + SI2H2              9.79E12    0.00    47200.0

! ----- add reaction from Suh's paper -----
! --- SI0 self clustering

SI0-2 = SI0   + SI0                 1.04E15    0.00    49580.0
SI0-3 = SI0-2 + SI0                 3.78E15    0.00    53160.0
SI0-4 = SI0-3 + SI0                 1.49E14    0.00    36670.0
SI0-5 = SI0-4 + SI0                 2.73E14    0.00    51020.0
SI0-6 = SI0-5 + SI0                 2.88E14    0.00    46920.0
SI0-7 = SI0-6 + SI0                 2.88E14    0.00    46920.0
SI0-8 = SI0-7 + SI0                 2.88E14    0.00    46900.0
SI0-9 = SI0-8 + SI0                 2.88E14    0.00    46950.0
SI0-10 = SI0-9 + SI0                2.88E14    0.00    46920.0

! --- irreversible SI0 clustering by (SIH2O)m

SI0   + SIH2O  => SI0-2 + H2         2.00E13    0.00     0.0
SI0   + SIH2O-2 => SI0-3 + 2H2       2.00E13    0.00     0.0
SI0-2 + SIH2O  => SI0-3 + H2         2.00E13    0.00     0.0
SI0-2 + SIH2O-2 => SI0-4 + 2H2       2.00E13    0.00     0.0
SI0-3 + SIH2O  => SI0-4 + H2         3.00E13    0.00     0.0
SI0-3 + SIH2O-2 => SI0-5 + 2H2       3.00E13    0.00     0.0
SI0-4 + SIH2O  => SI0-5 + H2         1.00E14    0.00     0.0
SI0-4 + SIH2O-2 => SI0-6 + 2H2       1.00E14    0.00     0.0
SI0-5 + SIH2O  => SI0-6 + H2         1.00E14    0.00     0.0
SI0-5 + SIH2O-2 => SI0-7 + 2H2       1.00E14    0.00     0.0
SI0-6 + SIH2O  => SI0-7 + H2         1.00E14    0.00     0.0
SI0-6 + SIH2O-2 => SI0-8 + 2H2       1.00E14    0.00     0.0
SI0-7 + SIH2O  => SI0-8 + H2         1.00E14    0.00     0.0
SI0-7 + SIH2O-2 => SI0-9 + 2H2       1.00E14    0.00     0.0
SI0-8 + SIH2O  => SI0-9 + H2         1.00E14    0.00     0.0
SI0-8 + SIH2O-2 => SI0-10 + 2H2      1.00E14    0.00     0.0
SI0-9 + SIH2O  => SI0-10 + H2        1.00E14    0.00     0.0
SIH2O + SIH2O-2 => SI0-3 + 3H2       3.00E13    0.00     0.0

! --- SI02 self-clustering

SI02-2 = SI02   + SI02              1.91E16    0.00    85670.0
SI02-3 = SI02-2 + SI02              4.97E17    0.00   95810.0

```

SI02-4 = SI02-3 + SI02	1.25E17	0.00	94550.0
SI02-5 = SI02-4 + SI02	6.10E17	0.00	94780.0
SI02-6 = SI02-5 + SI02	5.78E17	0.00	94570.0
SI02-7 = SI02-6 + SI02	3.32E17	0.00	92050.0
SI02-8 = SI02-7 + SI02	3.83E17	0.00	93530.0
SI02-9 = SI02-8 + SI02	3.33E17	0.00	93530.0
SI02-10 = SI02-9 + SI02	3.74E17	0.00	93530.0

! --- irreversible SI02 clustering by (HSI00H)m

SI02 + HSI00H => SI02-2 + H2	2.00E13	0.00	0.0
SI02 + HSI00H-2 => SI02-3 + 2H2	2.00E13	0.00	0.0
SI02-2 + HSI00H => SI02-3 + H2	2.00E13	0.00	0.0
SI02-2 + HSI00H-2 => SI02-4 + 2H2	2.00E13	0.00	0.0
SI02-3 + HSI00H => SI02-4 + H2	3.00E13	0.00	0.0
SI02-3 + HSI00H-2 => SI02-5 + 2H2	3.00E13	0.00	0.0
SI02-4 + HSI00H => SI02-5 + H2	1.00E14	0.00	0.0
SI02-4 + HSI00H-2 => SI02-6 + 2H2	1.00E14	0.00	0.0
SI02-5 + HSI00H => SI02-6 + H2	1.00E14	0.00	0.0
SI02-5 + HSI00H-2 => SI02-7 + 2H2	1.00E14	0.00	0.0
SI02-6 + HSI00H => SI02-7 + H2	1.00E14	0.00	0.0
SI02-6 + HSI00H-2 => SI02-8 + 2H2	1.00E14	0.00	0.0
SI02-7 + HSI00H => SI02-8 + H2	1.00E14	0.00	0.0
SI02-7 + HSI00H-2 => SI02-9 + 2H2	1.00E14	0.00	0.0
SI02-8 + HSI00H => SI02-9 + H2	1.00E14	0.00	0.0
SI02-8 + HSI00H-2 => SI02-10 + 2H2	1.00E14	0.00	0.0
SI02-9 + HSI00H => SI02-10 + H2	1.00E14	0.00	0.0
HSI00H + HSI00H-2 => SI02-3 + 3H2	3.00E13	0.00	0.0

! --- irreversible particle formation - Suh, Zachariah, Girshick

SI0-10 + SIO => SI0-11	1.60E13	0.00	0.5
SI0-10 + SIH20 => SI0-11 + H2	1.60E13	0.00	0.5
SI0-9 + SIH20-2 => SI0-11 + 2H2	1.60E13	0.00	0.5
SI0-10 + SIH20-2 => SI0-12 + 2H2	1.60E13	0.00	0.5
SI02-10 + SI02 => SI02-11	1.60E13	0.00	0.5
SI02-10 + HSI00H => SI02-11 + H2	1.60E13	0.00	0.5
SI02-9 + HSI00H-2 => SI02-11 + 2H2	1.60E13	0.00	0.5
SI02-10 + HSI00H-2 => SI02-12 + 2H2	1.60E13	0.00	0.5

END

THERMO ALL

200.000	1000.000	5000.000				
N2	121286N	2	G	298.000	5000.00	1000.00
0.02926640E+02	0.14879768E-02	-0.05684760E-05	0.10097038E-09	-0.06753351E-13		
-0.09227977E+04	0.05980528E+02	0.03298677E+02	0.14082404E-02	-0.03963222E-04		
0.05641515E-07	-0.02444854E-10	-0.10208999E+04	0.03950372E+02			
AR	120186AR	1	G	298.000	5000.00	1000.00
0.02500000E+02	0.00000000E+00	0.00000000E+00	0.00000000E+00	0.00000000E+00		
-0.07453750E+04	0.04366000E+02	0.02500000E+02	0.00000000E+00	0.00000000E+00		

0.00000000E+00	0.00000000E+00	-0.07453750E+04	0.04366000E+02						4
0	L 1/900	1	00	00	00G	200.000	3500.000	1000.000	1
2.56942078E+00	-8.59741137E-05	4.19484589E-08	-1.00177799E-11	1.22833691E-15					2
2.92175791E+04	4.78433864E+00	3.16826710E+00	-3.27931884E-03	6.64306396E-06					3
-6.12806624E-09	2.11265971E-12	2.91222592E+04	2.05193346E+00	6.72540300E+03					4
02	TPIS890	2	00	00	00G	200.000	3500.000	1000.000	1
3.28253784E+00	1.48308754E-03	-7.57966669E-07	2.09470555E-10	-2.16717794E-14					2
-1.08845772E+03	5.45323129E+00	3.78245636E+00	-2.99673416E-03	9.84730201E-06					3
-9.68129509E-09	3.24372837E-12	-1.06394356E+03	3.65767573E+00	8.68010400E+03					4
H	L 7/88H	1	00	00	00G	200.000	3500.000	1000.00	1
2.50000001E+00	-2.30842973E-11	1.61561948E-14	-4.73515235E-18	4.98197357E-22					2
2.54736599E+04	-4.46682914E-01	2.50000000E+00	7.05332819E-13	-1.99591964E-15					3
2.30081632E-18	-9.27732332E-22	2.54736599E+04	-4.46682853E-01	6.19742800E+03					4
H2	TPIS78H	2	00	00	00G	200.000	3500.000	1000.00	1
3.33727920E+00	-4.94024731E-05	4.99456778E-07	-1.79566394E-10	2.00255376E-14					2
-9.50158922E+02	-3.20502331E+00	2.34433112E+00	7.98052075E-03	-1.94781510E-05					3
2.01572094E-08	-7.37611761E-12	-9.17935173E+02	6.83010238E-01	8.46810200E+03					4
0H	RUS 780	1H	1	00	00G	200.000	3500.000	1000.000	1
3.09288767E+00	5.48429716E-04	1.26505228E-07	-8.79461556E-11	1.17412376E-14					2
3.85865700E+03	4.47669610E+00	3.99201543E+00	-2.40131752E-03	4.61793841E-06					3
-3.88113333E-09	1.36411470E-12	3.61508056E+03	-1.03925458E-01	8.81310600E+03					4
H20	L 8/89H	20	1	00	00G	200.000	3500.000	1000.000	1
3.03399249E+00	2.17691804E-03	-1.64072518E-07	-9.70419870E-11	1.68200992E-14					2
-3.00042971E+04	4.96677010E+00	4.19864056E+00	-2.03643410E-03	6.52040211E-06					3
-5.48797062E-09	1.77197817E-12	-3.02937267E+04	-8.49032208E-01	9.90409200E+03					4
H02	L 5/89H	10	2	00	00G	200.000	3500.000	1000.000	1
4.01721090E+00	2.23982013E-03	-6.33658150E-07	1.14246370E-10	-1.07908535E-14					2
1.11856713E+02	3.78510215E+00	4.30179801E+00	-4.74912051E-03	2.11582891E-05					3
-2.42763894E-08	9.29225124E-12	2.94808040E+02	3.71666245E+00	1.00021620E+04					4
H202	L 7/88H	20	2	00	00G	200.000	3500.000	1000.000	1
4.16500285E+00	4.90831694E-03	-1.90139225E-06	3.71185986E-10	-2.87908305E-14					2
-1.78617877E+04	2.91615662E+00	4.27611269E+00	-5.42822417E-04	1.67335701E-05					3
-2.15770813E-08	8.62454363E-12	-1.77025821E+04	3.43505074E+00	1.11588350E+04					4
SIH	121986SI	1H	1		G	298.000	2000.00	1000.00	1
3.11043000E+00	1.09494606E-03	2.89862872E-08	-2.74510414E-10	7.05179865E-14					2
4.51689766E+04	4.19348717E+00	3.83600950E+00	-2.70265667E-03	6.84906991E-06					3
-5.42418421E-09	1.47213123E-12	4.50759297E+04	9.35077846E-01						4
SIH3	42489SI	1H	3		G	298.000	3000.00	1000.00	1
0.05015906E+02	0.03732750E-01	-0.03609053E-05	-0.03729193E-08	0.08468491E-12					2
0.02190233E+06	-0.04291368E+02	0.02946733E+02	0.06466763E-01	0.05991653E-05					3
-0.02218413E-07	0.03052669E-11	0.02270173E+06	0.07347948E+02						4
SIH2	42489SI	1H	2		G	298.000	3000.00	1000.00	1
0.04142390E+02	0.02150191E-01	-0.02190730E-05	-0.02073725E-08	0.04741018E-12					2
0.03110483E+06	0.02930745E+01	0.03475092E+02	0.02139338E-01	0.07672305E-05					3
0.05217668E-08	-0.09898824E-11	0.03147397E+06	0.04436585E+02						4
SIH4	121386SI	1H	4		G	298.000	4000.00	1000.00	1
6.89387369E+00	4.03050054E-03	-4.18331410E-07	-2.29139471E-10	4.38476600E-14					2
1.10703735E+03	-1.74911671E+01	2.47516680E+00	9.00372118E-03	2.18539435E-06					3
-2.68142308E-09	-6.62108064E-13	2.92548804E+03	7.75101471E+00						4
SI2H3	90589SI	2H	3		G	298.000	2000.00	1000.00	1

0.07257627E+02	0.05123859E-01	-0.07633465E-05	-0.06662471E-08	0.02053052E-11	2
0.05062055E+06	-0.10314127E+02	0.03335404E+02	0.02155614E+00	-0.02933937E-03	3
0.02287784E-06	-0.07272827E-10	0.05146157E+06	0.08656853E+02		4
SI	32989SI	1	G	298.000 4000.00 1000.00	1
0.02775845E+02	-0.06213257E-02	0.04843696E-05	-0.12756146E-09	0.11344818E-13	2
0.05339790E+06	0.04543298E+02	0.03113515E+02	-0.02330991E-01	0.03518530E-04	3
-0.02417573E-07	0.06391902E-11	0.05335061E+06	0.03009718E+02		4
SI2H6	90589SI	2H	6	G 298.000 2000.00 1000.00	1
0.08882090E+02	0.11513955E-01	-0.12162159E-05	-0.01905085E-07	0.05542379E-11	2
0.05967241E+05	-0.02265611E+03	0.05301921E+01	0.04184055E+00	-0.04685249E-03	3
0.03179525E-06	-0.09484526E-10	0.07950597E+05	0.01880453E+03		4
SI2H5	90589SI	2H	5	G 298.000 2000.00 1000.00	1
0.08451010E+02	0.09286371E-01	-0.10911831E-05	-0.14423673E-08	0.04250824E-11	2
0.02472718E+06	-0.01710331E+03	0.15788481E+01	0.03549382E+00	-0.04267511E-03	3
0.03059177E-06	-0.09360425E-10	0.02630549E+06	0.16720734E+02		4
SI2H4	S 4/89SI	2H	400 000	OG 298.000 5000.000 1000.00	1
0.74178000E+01	0.75823000E-02	-0.36212000E-06	-0.16579000E-08	0.46739000E-12	2
0.29068000E+05	-0.11186000E+02	0.48078000E+01	0.14031000E-01	-0.20260000E-05	3
-0.72374000E-08	0.38717000E-11	0.29722000E+05	0.22343000E+01		4
H2SI2H2	S 4/89SI	2H	400 000	OG 298.000 5000.000 1000.00	1
0.74178000E+01	0.75823000E-02	-0.36212000E-06	-0.16579000E-08	0.46739000E-12	2
0.29068000E+05	-0.11186000E+02	0.48078000E+01	0.14031000E-01	-0.20260000E-05	3
-0.72374000E-08	0.38717000E-11	0.29722000E+05	0.22343000E+01		4
H3SI2H	S 4/89SI	2H	400 000	OG 300.00 5000.000 1000.00	1
0.72487000E+01	0.72414000E-02	-0.37157000E-06	-0.15919000E-08	0.45055000E-12	2
0.34868000E+05	-0.90435000E+01	0.45964000E+01	0.12892000E-01	-0.13292000E-05	3
-0.60219000E-08	0.28389000E-11	0.35644000E+05	0.49847000E+01		4
SI2H2	90589SI	2H	2	G 298.000 2000.00 1000.00	1
0.05778180E+02	0.04070596E-01	-0.04259125E-05	-0.07920228E-08	0.02379752E-11	2
0.03980520E+06	-0.05392375E+02	0.16247229E+01	0.14871029E-01	-0.08707160E-04	3
-0.01699554E-09	0.10972211E-11	0.04095325E+06	0.16165730E+02		4
SI2	90589SI	2	G	298.000 2000.00 1000.00	1
0.04232196E+02	0.04315355E-02	-0.02964833E-05	0.09823294E-09	-0.12962688E-13	2
0.06964651E+06	0.03308527E+02	0.02993750E+02	0.06053689E-01	-0.10158575E-04	3
0.07909737E-07	-0.02346083E-10	0.06987498E+06	0.09151741E+02		4
SI3	32989SI	3	G	298.000 4000.00 1000.00	1
0.07021584E+02	0.06981538E-02	-0.04818729E-05	0.01720754E-08	-0.01927024E-12	2
0.07429956E+06	-0.08179232E+02	0.05312161E+02	0.05920180E-01	-0.05075224E-04	3
0.05303866E-08	0.07031630E-11	0.07469501E+06	0.04036452E+01		4
SI3H7	BURG89SI	3H	700 000	OG 298.000 5000.000 1406.000	1
0.16485463E+02	0.94436647E-02	-0.31844158E-05	0.48954221E-09	-0.28203292E-13	2
0.26045373E+05	-0.55740306E+02	0.29371333E+01	0.51678716E-01	-0.53929868E-04	3
0.27769071E-07	-0.54890393E-11	0.29712547E+05	0.13301270E+02		4
SI3H8	90589SI	3H	8	G 298.000 2000.00 1000.00	1
0.13422770E+02	0.15636323E-01	-0.01936565E-04	-0.02388329E-07	0.07120030E-11	2
0.09165887E+05	-0.04163000E+03	0.06319791E+01	0.06412995E+00	-0.07772444E-03	3
0.05486969E-06	-0.16460971E-10	0.12092580E+05	0.02133318E+03		4
SIH20	30796H	20	1SI	1 OG 298.000 3000.000 1000.00	0 1
0.35850483E+01	0.83880819E-02	-0.46823699E-05	0.12327730E-08	-0.12511796E-12	2
-0.13326606E+05	0.59446840E+01	0.19649962E+01	0.13285051E-01	-0.10601026E-04	3

0.48593881E-08-0.11099934E-11-0.12891831E+05	0.14235314E+02	4
SIH20-2	101295SI 2H 40 2 G 298.000 3000.00 2000.00	1
1.39725850E+01 7.48814210E-03-2.92057510E-06	5.32497860E-10-3.73370670E-14	2
-8.52831380E+04-4.99955690E+01 0.20512376E+01	0.28732242E-01-0.23774851E-05	3
-0.19760165E-07 0.99057767E-11-0.80128711E+05	0.13885288E+02	4
SIH0	30796H 10 1SI 1 OG 298.000 3000.000 1000.00	0 1
0.38576852E+01 0.43050702E-02-0.24851663E-05	0.67070901E-09-0.69361104E-13	2
0.20943329E+04 0.56646280E+01 0.31372316E+01	0.53986382E-02-0.18072458E-05	3
-0.10840215E-08 0.63433453E-12 0.23399725E+04	0.96178032E+01	4
SIH30	30796H 30 1SI 1 OG 298.000 3000.000 1000.00	0 1
0.38433801E+01 0.11981012E-01-0.66889297E-05	0.17607639E-08-0.17864722E-12	2
0.15200701E+03 0.47134713E+01 0.17619234E+00	0.25227447E-01-0.26169663E-04	3
0.15651673E-07-0.41680718E-11 0.10147120E+04	0.22906490E+02	4
SIH30H	30796H 40 1SI 1 OG 298.000 3000.000 1000.00	0 1
0.50803939E+01 0.12887857E-01-0.67236548E-05	0.16910696E-08-0.16625038E-12	2
-0.36176543E+05-0.18998603E+01 0.17576503E+00	0.32080858E-01-0.36587595E-04	3
0.23458462E-07-0.63580748E-11-0.35117251E+05	0.22011243E+02	4
H2SI0H	30796H 30 1SI 1 OG 298.000 3000.000 1000.00	0 1
0.54165400E+01 0.85418628E-02-0.42990293E-05	0.10522622E-08-0.10133921E-12	2
-0.15236623E+05-0.96346896E+00 0.15634466E+01	0.24418261E-01-0.30066620E-04	3
0.20370623E-07-0.56754136E-11-0.14447307E+05	0.17614220E+02	4
HSI00H	30796H 20 2SI 1 OG 298.000 3000.000 1000.00	0 1
0.64008759E+01 0.73921012E-02-0.37166540E-05	0.91103419E-09-0.87961357E-13	2
-0.59123231E+05-0.68493506E+01 0.84650357E+00	0.30332170E-01-0.40649068E-04	3
0.28173146E-07-0.78033556E-11-0.58000538E+05	0.19886511E+02	4
HSI00H-2	zach SI 2H 40 4 OG 298.000 4000.000 1000.00	1
0.19514769E+02 .64274929E-02-0.20058889E-05	.28175472E-09-0.14160852E-13	2
-0.17650975E+06-0.74545852E+02 .19514769E+02	.64274929E-02-0.20058889E-05	3
0.28175472E-09-0.14160852E-13-0.17650975E+06	-0.74545852E+02	4
SI00H	30796H 10 2SI 1 OG 298.000 3000.000 1000.00	0 1
0.64981916E+01 0.34222132E-02-0.15371997E-05	0.34510638E-09-0.31179579E-13	2
-0.39984706E+05-0.56480532E+01 0.24684717E+01	0.20083835E-01-0.27999655E-04	3
0.19404030E-07-0.52595504E-11-0.39184036E+05	0.13711989E+02	4
HSI0H	30796 H 20 1SI 1 OG 298.000 3000.000 1000.00	0 1
0.48597322E+01 0.54931697E-02-0.26612995E-05	0.63436147E-09-0.59994357E-13	2
-0.12775548E+05-0.39218673E+00 0.11583361E+01	0.20649678E-01-0.26759036E-04	3
0.18165894E-07-0.49489026E-11-0.12024928E+05	0.17446894E+02	4
SIH302H	SI 1H 40 2 OG 298.000 5000.000 1434.000	1
1.47264815E+01 3.93537438E-03-1.43018295E-06	2.31215230E-10-1.37984022E-14	2
-3.67891192E+04-5.44899015E+01 7.48977124E+00	1.90370336E-02-1.20459856E-05	3
2.83994528E-09-8.04501066E-14-3.41811791E+04	-1.51264812E+01	4
SIH302	SI 1H 30 2 OG 298.000 5000.000 1336.000	1
8.53368584E+00 6.64665749E-03-2.36417403E-06	3.76778379E-10-2.22618909E-14	2
-1.58369978E+04-2.21892869E+01 4.73366694E+00	9.88277794E-03 1.32668928E-06	3
-4.32539392E-09 1.26521586E-12-1.39328821E+04	2.55947074E-01	4
SI2H	ZAC89SI 2H 1 G 298.000 5000.00 1000.00	1
4.42768812E+00 2.21626856E-03-6.04895263E-07	9.88251703E-11-7.35117957E-15	2
5.79041484E+04-1.19944179E+00 3.05066776E+00	6.05167449E-03-4.95663426E-06	3
2.80415913E-09-8.19333208E-13 5.79001094E+04	5.95436096E+00	4
SI0	J 9/67SI 10 100 000 OG 298.000 5000.000 4000.00	1

3.70917120E 00	9.06972840E-04	-4.23304730E-07	9.03440730E-11	-7.28025760E-15	2
-1.34940450E 04	3.18421880E 00	0.32528276E 01	0.41823126E-03	0.37806202E-05	3
-0.51024483E-08	0.19471317E-11	-0.13090340E 05	0.66485803E 01		4
SI0-2	msw SI 20	2 0 OG	298.000	4000.000 2000.00	1
9.76258470E+00	-1.59353080E-04	2.31807220E-07	-7.57209880E-11	7.77168600E-15	2
-5.33710790E+04	-2.30217600E+01	0.92417820E+00	0.32980940E-01	-0.51830190E-04	3
0.38738640E-07	-0.11215970E-10	-0.51126570E+05	0.20120830E+02		4
SI0-3	msw SI 30	3 0 OG	298.000	4000.000 2000.00	1
1.56134860E+01	-2.21169110E-04	3.45236710E-07	-1.13962780E-10	1.17410590E-14	2
-9.50701140E+04	-4.97466280E+01	.21152430E+01	.50626100E-01	-0.80051180E-04	3
0.60249350E-07	-0.17563970E-10	-0.91662460E+05	.16063000E+02		4
SI0-4	msw SI 40	4 0 OG	298.000	4000.000 1000.00	1
2.11570120E+01	2.07394160E-04	1.79942680E-07	-8.45013870E-11	9.74073920E-15	2
-1.28311320E+05	-7.05609390E+01	.54219200E+01	.58099300E-01	-0.89181270E-04	3
0.65612680E-07	-0.18785080E-10	-0.12426260E+06	.59483540E+01		4
SI0-5	zach SI 50	5 0 OG	298.000	4000.000 1000.00	1
0.26191211E+02	.13338465E-02	-0.32827956E-06	.17492749E-10	.21543416E-14	2
-0.16850283E+06	-0.88299259E+02	.26191211E+02	.13338465E-02	-0.32827956E-06	3
0.17492749E-10	.21543416E-14	-0.16850283E+06	-0.88299259E+02		4
SI0-6	zach SI 60	6 0 OG	298.000	4000.000 1000.00	1
0.31851958E+02	.15028756E-02	-0.30125048E-06	-0.10515966E-10	.61345351E-14	2
-0.20694060E+06	-0.10970323E+03	.31851958E+02	.15028756E-02	-0.30125048E-06	3
-0.10515966E-10	.61345351E-14	-0.20694060E+06	-0.10970323E+03		4
SI0-7	zach SI 70	7 0 OG	298.000	4000.000 1000.00	1
0.37512704E+02	.16719046E-02	-0.27422140E-06	-0.38524681E-10	.10114729E-13	2
-0.24537973E+06	-0.13110721E+03	.37512704E+02	.16719046E-02	-0.27422140E-06	3
-0.38524681E-10	.10114729E-13	-0.24537973E+06	-0.13110721E+03		4
SI0-8	zach SI 80	8 0 OG	298.000	4000.000 1000.00	1
0.43173451E+02	.18409336E-02	-0.24719233E-06	-0.66533396E-10	.14094922E-13	2
-0.28380506E+06	-0.15251118E+03	.43173451E+02	.18409336E-02	-0.24719233E-06	3
-0.66533396E-10	.14094922E-13	-0.28380506E+06	-0.15251118E+03		4
SI0-9	zach SI 90	9 0 OG	298.000	4000.000 1000.00	1
0.48834197E+02	.20099626E-02	-0.22016325E-06	-0.94542112E-10	.18075115E-13	2
-0.32226095E+06	-0.17391515E+03	.48834197E+02	.20099626E-02	-0.22016325E-06	3
-0.94542112E-10	.18075115E-13	-0.32226095E+06	-0.17391515E+03		4
SI0-10	zach SI 100	10 0 OG	298.000	4000.000 1000.00	1
0.54494944E+02	.21789916E-02	-0.19313418E-06	-0.12255083E-09	.22055309E-13	2
-0.36070173E+06	-0.19531913E+03	.48834197E+02	.20099626E-02	-0.22016325E-06	3
-0.12255083E-09	.22055309E-13	-0.36070173E+06	-0.19531913E+03		4
SI02	J 9/67SI 10	200 000 OG	298.000	5000.000 4000.00	1
6.20905340E 00	1.36310434E-03	-5.94220510E-07	1.19915530E-10	-9.22823080E-15	2
-3.55487970E 04	-8.42874470E 00	0.32628058E 01	0.85016584E-02	-0.57388144E-05	3
0.12896573E-10	0.97544976E-12	-0.38035971E 05	0.66549123E 01		4
SI02-S	msw8/99SI 120	24 0 OS	298.000	3000.000 1000.00	1
0.59601470E+01	.44202120E-02	-0.26370670E-05	.74432140E-09	-0.79310880E-13	2
-0.11133540E+06	-0.30331350E+02	-0.18425620E+02	.12796220E+00	-0.24167100E-03	3
0.20738990E-06	-0.66847150E-10	-0.10735050E+06	.81904590E+02		4
SI02-2	zach SI 20	4 0 OG	298.000	4000.000 1000.00	1
0.14124110E+02	.15950164E-02	-0.54220059E-06	.82032840E-10	-0.44677341E-14	2
-0.11532942E+06	-0.45435969E+02	.14124110E+02	.15950164E-02	-0.54220059E-06	3

```

0.82032840E-10-0.44677341E-14-0.11532942E+06-0.45435969E+02      4
SI02-3      zach  SI  30   6   0   OG  298.000  4000.000 1000.00      1
0.22459020E+02 .19173620E-02-0.53221537E-06 .53174897E-10-0.44334868E-15      2
-0.20054665E+06-0.88541520E+02 .22459020E+02 .19173620E-02-0.53221537E-06      3
0.53174897E-10-0.44334868E-15-0.20054665E+06-0.88541520E+02      4
SI02-4      zach  SI  40   8   0   OG  298.000  4000.000 1000.00      1
0.30789209E+02 .22504993E-02-0.52885450E-06 .25942087E-10 .34393352E-14      2
-0.28512765E+06-0.12932230E+03 .30789209E+02 .22504993E-02-0.52885450E-06      3
0.25942087E-10 .34393352E-14-0.28512765E+06-0.12932230E+03      4
SI02-5      zach  SI  50  10   0   OG  298.000  4000.000 1000.00      1
0.39111755E+02 .25928812E-02-0.53027648E-06-0.13783655E-12 .72174148E-14      2
-0.36982254E+06-0.17095038E+03 .39111755E+02 .25928812E-02-0.53027648E-06      3
-0.13783655E-12 .72174148E-14-0.36982254E+06-0.17095038E+03      4
SI02-6      zach  SI  60  12   0   OG  298.000  4000.000 1000.00      1
0.47385779E+02 .30157212E-02-0.57997804E-06-0.13830300E-10 .98447246E-14      2
-0.45438869E+06-0.21224988E+03 .47385779E+02 .30157212E-02-0.57997804E-06      3
-0.13830300E-10 .98447246E-14-0.45438869E+06-0.21224988E+03      4
SI02-7      zach  SI  70  14   0   OG  298.000  4000.000 1000.00      1
0.37967736E+02 .33222336E-01-0.18762707E-04 .47009253E-08-0.43291249E-12      2
-0.52959089E+06-0.15320877E+03 .37967736E+02 .33222336E-01-0.18762707E-04      3
0.47009253E-08-0.43291249E-12-0.52959089E+06-0.15320877E+03      4
SI02-8      zach  SI  80  16   0   OG  298.000  4000.000 1000.00      1
0.37534746E+02 .48331588E-01-0.27772963E-04 .70286348E-08-0.65123762E-12      2
-0.60965897E+06-0.14514804E+03 .37534746E+02 .48331588E-01-0.27772963E-04      3
0.70286348E-08-0.65123762E-12-0.60965897E+06-0.14514804E+03      4
SI02-9      zach  SI  90  18   0   OG  298.000  4000.000 1000.00      1
0.37101755E+02 .63440840E-01-0.36783218E-04 .93563443E-08-0.86956276E-12      2
-0.68972705E+06-0.13708732E+03 .37101755E+02 .63440840E-01-0.36783218E-04      3
0.93563443E-08-0.86956276E-12-0.68972705E+06-0.13708732E+03      4
SI02-10     zach  SI 100  20   0   OG  298.000  4000.000 1000.00      1
0.36668764E+02 .78550092E-01-0.45793473E-04 .11684054E-07-0.10878879E-11      2
-0.76979513E+06-0.12902659E+03 .36668764E+02 .78550092E-01-0.45793473E-04      3
0.11684054E-07-0.10878879E-11-0.76979513E+06-0.12902659E+03      4
SI0-11      zach  SI 110  11   0   OG  298.000  4000.000 1000.00      1
0.54494944E+02 .21789916E-02-0.19313418E-06-0.12255083E-09 .22055309E-13      2
-0.36070173E+06-0.19531913E+03 .48834197E+02 .20099626E-02-0.22016325E-06      3
-0.12255083E-09 .22055309E-13-0.36070173E+06-0.19531913E+03      4
SI0-12      zach  SI 120  12   0   OG  298.000  4000.000 1000.00      1
0.54494944E+02 .21789916E-02-0.19313418E-06-0.12255083E-09 .22055309E-13      2
-0.36070173E+06-0.19531913E+03 .48834197E+02 .20099626E-02-0.22016325E-06      3
-0.12255083E-09 .22055309E-13-0.36070173E+06-0.19531913E+03      4
SI02-11     zach  SI 110  22   0   OG  298.000  4000.000 1000.00      1
0.36668764E+02 .78550092E-01-0.45793473E-04 .11684054E-07-0.10878879E-11      2
-0.76979513E+06-0.12902659E+03 .36668764E+02 .78550092E-01-0.45793473E-04      3
0.11684054E-07-0.10878879E-11-0.76979513E+06-0.12902659E+03      4
SI02-12     zach  SI 120  24   0   OG  298.000  4000.000 1000.00      1
0.36668764E+02 .78550092E-01-0.45793473E-04 .11684054E-07-0.10878879E-11      2
-0.76979513E+06-0.12902659E+03 .36668764E+02 .78550092E-01-0.45793473E-04      3
0.11684054E-07-0.10878879E-11-0.76979513E+06-0.12902659E+03      4

```

END

# Appendix B

## Data storage

Table A1: Case and code used to produce results of Neuber *et al.* [1]. The corresponding repository is `ssh://git@git.itv.uni-stuttgart.de:itv-publications/2019-Neuber-CNF.git`

2019_Neuber_CNF		
Data on storage	Cases	SHA
.../JOURNAL/2019_Neuber_CNF/	all	6e1c9a63

Table A2: Case and code used to produce results of Neuber *et al.* [2]. The corresponding repository is `ssh://git@git.itv.uni-stuttgart.de:itv-publications/2017_Neuber_CES.git`

2017_Neuber_CES		
Data on storage	Cases	SHA
.../JOURNAL/2017_Neuber_CES/	all	79c54334

Table A3: Case and code used to produce results of Neuber *et al.* [3]. The corresponding code repository is `ssh://git@git.itv.uni-stuttgart.de:2222/itv-publications/2019_Neuber_PCI.git`

2019_Neuber_PCI		
Data on storage	Cases	SHA
.../JOURNAL/2019_Neuber_PCI/	all	dc128fd4

Table A4: Case and code used to produce results of Neuber *et al.* [4]. The corresponding code repository is `ssh://git@git.itv.uni-stuttgart.de:2222/itv-publications/2020-Neuber-FTC.git`

2020_Neuber_FTC		
Data on storage	Cases	SHA
.../JOURNAL/2020_Neuber_FTC	all	460f6222